

# Selective electrical and optical neuromodulation of the central nervous system with conformable microfabricated implants

THÈSE N° 7628 (2017)

PRÉSENTÉE LE 12 AVRIL 2017

À LA FACULTÉ DES SCIENCES ET TECHNIQUES DE L'INGÉNIEUR  
CHAIRE FONDATION BERTARELLI DE TECHNOLOGIE NEUROPROSTHÉTIQUE  
PROGRAMME DOCTORAL EN BIOTECHNOLOGIE ET GÉNIE BIOLOGIQUE

ÉCOLE POLYTECHNIQUE FÉDÉRALE DE LAUSANNE

POUR L'OBTENTION DU GRADE DE DOCTEUR ÈS SCIENCES

PAR

**Amélie Anne GUEX**

acceptée sur proposition du jury:

Prof. T. Lasser, président du jury  
Prof. S. Lacour, directrice de thèse  
Prof. C. McKay, rapporteuse  
Prof. T. Moser, rapporteur  
Prof. Ph. Renaud, rapporteur



ÉCOLE POLYTECHNIQUE  
FÉDÉRALE DE LAUSANNE

Suisse  
2017



# Acknowledgements

This thesis would not have been possible without the contribution of many people, who provided me with great help, support and advice throughout these four years.

First of all, I want to warmly thank my thesis director, Prof. Stéphanie P. Lacour, for giving me the opportunity to work in the laboratory for soft bioelectronic interfaces (LSBI) and for her continuous support and invaluable advice throughout this thesis. Her guidance allowed me to continuously move forward in this thesis and helped me face the challenges along the way with confidence.

I would like to thank my thesis committee, Profs. Theo Lasser, Philippe Renaud, Colette M. McKay and Tobias Moser for taking the time to critically review my work.

I also would like to thank the Fondation Bertarelli for providing the funding for this thesis.

My thanks also go to our collaborators of the ABI lab, at the Massachusetts Eye and Ear Infirmary in Boston, and in particular to Dr. Daniel J. Lee and Prof. M. Christian Brown for supporting me in my various trips to Boston, making sure I had the best possible working conditions, and more generally for very helpful discussions and guidance in this project. My thanks also go to A. Edward Hight for performing the implantation surgeries, optimizing the data acquisition system and for the many conversations we had about project design, stimulation protocol, data analysis and interpretation. I also want to thank Evan Foss, Kenneth E. Hancock and Ishmael Stefanov for prompt and efficient technical assistance, as well as current and past members of the ABI lab, Rohit U. Verma for his continuous support and friendship and for taking time off to do surgeries in the first year of the project, Shreya Narasimhan for assistance during experiments, and also Elliott Kozin, Kristen Babicz and Michael Slama.

I want to thank Prof. Grégoire Courtine for his support and guidance in the spinal cord optical stimulation project and Leonie Asboth for the discussions and collaboration in the project design, data acquisition, analysis and interpretation. My thanks also go to Jérôme Gandar for the microCT scans and Natalia Pavlova and Polina Shkorbatova for the surgeries.

## Acknowledgements

---

I warmly thank also the staff of the center for micronanotechnologies at EPFL (CMi) for their highly efficient technical support, and in particular Giancarlo Corradini for his excellent work with the wire-bonding of the LEDs. I also would like to thank Prof. Nicolas Grandjean and Jean-Michel Lamy for their work on the LED project.

The LSBI has been a great place to work in the past four years thanks to all its past and present members. My warm thanks go to all of them for good times spent in and outside the lab. In particular, I want to thank Nicolas Vachicouras for many helpful discussions about the project, great help in many aspects of my work and review of several chapters of this thesis; Frédéric Michoud, Aaron Gerratt and Florian Falleger for thesis reviews; Pierre Joris for his tremendous help with the microfabrication at the beginning of the project; Hadrien Michaud for help with the thermal simulation model; Martin Jobin for the custom-built current source; Jennifer, Laurent, Giuseppe, Arthur, Sandra, Aaron, Xiaoyang, Ivan, Kate, Cédric, Alessia, Alba, Christina, Kristie and all the others for great scientific and lunchtime conversations.

Last but not least, my deepest gratitude goes to my family and friends: to my parents, for nearly 29 years of unconditional love and encouragements; to Jérôme, Antoine, Alicia and the newcomer Thibault, for always reminding me to take some perspective; to all my friends at home and all over the world for their continuous support.

*Lausanne, 23 Decembre 2016*

Amélie Guex

# Abstract

Neuroprosthetic systems are designed to interface with the nervous system, for the replacement or restoration of damaged functions in the motor and/or sensory systems. In order to have an efficient communication with the nervous tissue leading to optimized clinical outcomes, achieving neural stimulation with high selectivity is essential. This thesis aims at finding technological routes to enable spatial, structural and cell-type selective surface neuromodulation using electrical and optogenetic stimulation and to validate them in in vivo models.

Thin and conformable electrode arrays enable close contact with the target tissue, thereby leading to minimal distances with the target neurons and maximal spatial selectivity. Flexible polymer technologies based on polyimide (PI) are used to design thin ( $< 10 \mu\text{m}$  thick) electrode arrays with small feature size ( $< 100 \mu\text{m}$ ), resulting in miniaturized conformable arrays for surface stimulation. PEDOT conducting polymer coatings are used on the miniaturized electrical stimulation sites ( $100 \mu\text{m}$  diameter) to improve their charge injection properties. This implant is used for auditory brainstem stimulation in a rat model, and is shown to generate robust activation of the auditory system. Analysis of the multiunit recordings obtained from the inferior colliculus (IC), an auditory structure of the midbrain, led to the identification of different phases in the responses, with various frequency tuning properties. The stimulation configuration is shown to influence the tonotopic organisation of the frequency-tuned responses. Bipolar stimulation with small interelectrode distances ( $400 \mu\text{m}$ ) is shown to generate responses that are more frequency-selective than with larger interelectrode distances ( $800 \mu\text{m}$ ). The orientation of the electrode pair and the waveform of stimulation current are also shown to influence the response properties. An updated design of the clinical auditory brainstem implant (ABI) is then proposed, integrating higher electrode density and guidelines for a more tissue-conformal format. The main steps in the road towards improvement of ABI outcomes are then discussed, with proposed changes in the stimulation protocol and electrode array in parallel.

Another approach to cell-specific neuromodulation is the implementation of optogenetics. This requires not only genetic engineering of the neurons but also the manufacturing of implantable light-emitting devices. Here, we introduce a fabrication process for the integration of thin ( $50 \mu\text{m}$ ) LEDs into a polyimide-based device. A proof-of-concept in vivo study

## Acknowledgements

---

shows that stimulation of the spinal cord of a mouse model generates robust EMG responses in both legs over the course of several weeks. The walking integrity is confirmed, showing the absence of functional damages to the spinal cord. These results show that the presented LED array can provide a way of stimulating key elements of the locomotor neural circuitry, potentially leading to a greater understanding of the role of each neuronal subtypes in the spinal cord.

Through the applications of ABI and spinal cord stimulation, this thesis thus highlights the importance and potential use of specifically tailored technologies enabling selective surface stimulation of the nervous system.

Keywords: neuroprostheses, auditory brainstem implant, flexible electronics, conductive polymers, spinal cord stimulation, electrical stimulation, optogenetics

## Résumé

Les neuroprothèses sont des interfaces avec le système nerveux utilisées pour le remplacement ou la restauration de fonctions endommagées des systèmes moteurs et/ou sensoriels. Pour avoir une communication efficace avec le tissu nerveux et générer des résultats cliniques optimaux pour les patients, une grande sélectivité de stimulation est essentielle. Cette thèse a pour but de développer des technologies permettant une stimulation de surface du tissu nerveux avec une sélectivité spatiale, structurelle ainsi qu'une sélectivité des types de neurones stimulés en utilisant une stimulation électrique ou optique, et de valider ces technologies dans des modèles in vivo.

Les champs d'électrodes fins et conformes permettent un contact optimal avec le tissu nerveux, générant donc une distance minimale avec les neurones à stimuler et une sélectivité spatiale maximale. Des technologies basées sur le polyimide (PI), un polymère flexible, sont utilisées pour fabriquer des champs d'électrodes fins ( $< 10 \mu\text{m}$  d'épaisseur) avec des très petites dimensions ( $< 100 \mu\text{m}$ ), ce qui permet d'obtenir des champs d'électrodes conformes pour la stimulation de surface. Une couche de polymère conducteur est déposée sur les sites de stimulation électrique miniaturisés ( $100 \mu\text{m}$  de diamètre) pour améliorer les propriétés d'injection des charges. Cet implant est utilisé pour la stimulation du tronc cérébral auditif dans un modèle de rat, et il est montré qu'une activation robuste du système auditif peut être générée. L'analyse des enregistrements obtenus dans le colliculus inférieur (IC), une structure auditive du mésencéphale, permet d'identifier différentes phases de réponses avec des propriétés variables de sélectivité fréquentielle. La configuration des électrodes de stimulation a une influence sur l'organisation tonotopique des réponses avec une haute sélectivité fréquentielle. Il est démontré que la stimulation bipolaire avec des paires d'électrodes de faible espacement ( $400 \mu\text{m}$ ) génère des réponses avec une meilleure organisation tonotopique que les paires d'électrodes plus distantes ( $800 \mu\text{m}$ ). L'orientation des paires d'électrodes ainsi que la forme de l'impulsion de courant électrique ont aussi une influence sur les propriétés de la réponse du système auditif. Un nouveau design clinique d'implant auditif sur le tronc cérébral (ABI) intégrant une plus haute densité d'électrodes ainsi qu'un substrat conforme au tissu neuronal est donc proposé. Les étapes principales qui permettront d'améliorer les performances cliniques de cet implant sont discutées, intégrant en parallèle des changements dans le protocole de stimulation et dans le champ d'électrodes.

## Acknowledgements

---

Une autre approche pour la stimulation de types de neurones spécifiques est l'optogénétique. Cette technique nécessite, en plus de l'ingénierie génétique des neurones, le développement de dispositifs implantables pour l'illumination du tissu nerveux. Ici, nous présentons un procédé de fabrication pour l'intégration de diodes (LEDs) fines ( $50\ \mu\text{m}$ ) sur un substrat en polyimide. Une preuve de principe *in vivo* montre que la stimulation optique de la moelle épinière d'une souris génère des réponses EMG robustes dans les deux jambes, pendant plusieurs semaines. L'intégrité de la marche est confirmée, ce qui montre que le dispositif ne génère pas de dommages fonctionnels à la moelle épinière. Ces résultats démontrent que le champ de diodes développé peut fournir un moyen de stimuler des éléments clés du circuit neuronal de la locomotion, ce qui peut mener à une meilleure compréhension du rôle de chaque type de neurones dans la moelle épinière.

À travers les applications de stimulation du tronc cérébral auditif et de la moelle épinière, cette thèse met donc en évidence l'importance et l'utilité potentielle de technologies ciblées pour chaque application permettant une stimulation sélective de la surface du tissu nerveux.

Mots-clés : neuroprothèses, implant auditif sur le tronc cérébral, électronique flexible, polymères conducteurs, stimulation de la moelle épinière, stimulation électrique, optogénétique



# Contents

<b>Acknowledgements</b>	<b>i</b>
<b>Abstract (English/Français)</b>	<b>iii</b>
<b>List of figures</b>	<b>xi</b>
<b>List of tables</b>	<b>xv</b>
<b>1 Introduction</b>	<b>1</b>
1.1 The need for selectivity in the context of neuroprosthetics . . . . .	2
1.2 Surface electrical stimulation . . . . .	4
1.2.1 Mechanisms of electrical stimulation . . . . .	4
1.2.2 Selectivity of electrical stimulation . . . . .	5
1.3 Optical stimulation . . . . .	6
1.3.1 Optogenetic stimulation of neural tissue . . . . .	6
1.3.2 Selectivity of optogenetic stimulation . . . . .	7
1.4 Technological requirements . . . . .	8
1.5 Outline of the thesis . . . . .	9
1.5.1 Chapter 2: Technologies for conformal surface neural stimulation . . . . .	9
1.5.2 Chapter 3: New generation auditory brainstem implant . . . . .	9
1.5.3 Chapter 4: Optogenetic stimulation of the spinal cord . . . . .	10
<b>2 Technologies for conformable surface neural stimulation</b>	<b>11</b>
2.1 Introduction . . . . .	12
2.1.1 Interfacing with the central nervous system . . . . .	12
2.1.2 Technologies for conformable implants . . . . .	12
2.1.3 Electrical stimulation . . . . .	14
2.1.4 Optical stimulation . . . . .	18
2.1.5 Goals of the project . . . . .	22
2.2 Electrical stimulation implant . . . . .	22
2.2.1 Polyimide electrode array fabrication . . . . .	22
2.2.2 PEDOT electropolymerization . . . . .	22
2.2.3 Electrochemical impedance spectroscopy . . . . .	24
2.2.4 Cyclic Voltammetry / CSCc . . . . .	26

## Contents

---

2.2.5	Pulse test / CIC	26
2.2.6	Bending tests	27
2.2.7	Coating reliability	28
2.3	Optoelectronic implant	29
2.3.1	Fabrication	29
2.3.2	Electrical characterization	29
2.3.3	Optical power characterization	30
2.3.4	Thermal dissipation model	31
2.4	Discussion	34
2.4.1	Electrical implant	34
2.4.2	Optoelectronic implant	35
<b>3</b>	<b>New Generation Auditory Brainstem Implant (ABI)</b>	<b>39</b>
3.1	Introduction	40
3.1.1	Auditory brainstem implants	40
3.1.2	Neurophysiology of the cochlear nucleus	45
3.1.3	Hypotheses for ABI improvements	48
3.1.4	Assessment of auditory system activation properties	51
3.1.5	Goals of the project	53
3.2	Methods	53
3.2.1	Acute in vivo experiments	53
3.2.2	Signal processing	55
3.3	Acoustic stimulation results	57
3.4	Electrode array design	59
3.4.1	14-electrodes array with 200 $\mu\text{m}$ spaced pairs	60
3.4.2	20-electrode array with hexagonal configuration	61
3.4.3	Packaging for in vivo acute testing	62
3.5	Electrically generated ABRs	62
3.5.1	eABRs parameters extraction	62
3.5.2	Effect of stimulation location on eABRs characteristics	63
3.5.3	Effect of stimulation pair configuration on eABRs characteristics	66
3.5.4	Comparison between monopolar and bipolar stimulation	67
3.5.5	Discussion	69
3.6	IC response maps post-processing	70
3.6.1	IC response maps characterization	70
3.6.2	Location-specific activity	74
3.6.3	Early and late phases of activity	76
3.6.4	Combined processing - average subtraction on the early phase of activity	83
3.6.5	Synthesis	85
3.7	Effect of stimulation level	86
3.7.1	Characteristic frequency	86
3.7.2	Intensity parameters	86

3.7.3 Synthesis . . . . .	88
3.8 Stimulation pairs orientations and interelectrode distances . . . . .	88
3.8.1 14-electrode array with 200 $\mu\text{m}$ spaced pairs . . . . .	89
3.8.2 20-electrode array with hexagonal configuration of electrodes . . . . .	92
3.9 Comparison between monopolar and bipolar stimulation . . . . .	96
3.9.1 Effect on tonotopic organisation of responses . . . . .	96
3.9.2 Effect on intensity parameters . . . . .	98
3.9.3 Synthesis . . . . .	98
3.10 Using alternative stimulation pulse waveforms . . . . .	98
3.10.1 Range of tested waveforms . . . . .	98
3.10.2 IC response maps characterization . . . . .	100
3.10.3 Effect of polarity on symmetric pulses . . . . .	100
3.10.4 Effect of phase duration on symmetric pulses . . . . .	102
3.10.5 Asymmetric stimulation pulses . . . . .	103
3.10.6 Triphasic stimulation pulse . . . . .	106
3.10.7 Synthesis . . . . .	106
3.11 Discussion . . . . .	107
3.11.1 Electrodes configuration effect on the tonotopic organisation of responses	107
3.11.2 Neurophysiology . . . . .	109
3.11.3 eABRs vs IC . . . . .	112
3.11.4 Potential for translation of results for clinical use . . . . .	113
<b>4 Optogenetic stimulation of the spinal cord</b>	<b>115</b>
4.1 Introduction . . . . .	116
4.1.1 Optogenetics in the context of spinal cord damage and repair . . . . .	116
4.1.2 Challenges associated to chronic optogenetic stimulation of the spinal cord	117
4.1.3 Goals of the study . . . . .	117
4.2 Optoelectronic device for spinal cord stimulation . . . . .	118
4.2.1 Device with 4 LEDs for lateral spinal cord stimulation . . . . .	118
4.2.2 Experimental model . . . . .	119
4.2.3 Characterization of device placement . . . . .	119
4.3 Functional validation . . . . .	120
4.3.1 Experimental setup and stimulation protocol . . . . .	120
4.3.2 Raw EMG responses . . . . .	120
4.3.3 EMG parameters characterization . . . . .	122
4.3.4 Parametric study . . . . .	124
4.4 Chronic stability and safety . . . . .	127
4.4.1 EMG parameters chronic variations . . . . .	127
4.4.2 Integrity of the walking functionality . . . . .	129
4.4.3 Histological analysis . . . . .	130
4.5 Discussion . . . . .	130
4.5.1 Optical power and thermal heating . . . . .	130

## Contents

---

4.5.2	Device . . . . .	131
4.5.3	Potential applications . . . . .	132
<b>5</b>	<b>Discussion</b>	<b>135</b>
5.1	Selectivity of stimulation . . . . .	135
5.2	Strategies towards an improvement of ABI outcomes . . . . .	136
5.2.1	Substrate . . . . .	136
5.2.2	Electrode sites diameter . . . . .	137
5.2.3	Density of electrode sites . . . . .	138
5.2.4	Stimulation electrode material . . . . .	139
5.2.5	Stimulation protocol . . . . .	140
5.2.6	Clinical validation . . . . .	141
5.3	Clinical translation of optogenetics . . . . .	142
5.4	Clinical translation of microfabricated implants . . . . .	143
5.5	Outlook: towards closed-loop sensory neuroprostheses . . . . .	144
	<b>Bibliography</b>	<b>166</b>
	<b>Curriculum Vitae</b>	<b>167</b>

# List of Figures

1.1	Examples of clinical implantable neuroprostheses . . . . .	2
1.2	Schematic illustration of the spatial, structural and cell-type selectivity of stimulation . . . . .	3
1.3	Illustration of the three main types of opsins . . . . .	6
1.4	Illustration of cell type selectivity in optogenetics . . . . .	8
2.1	Flexible polymer-based devices . . . . .	13
2.2	Charge transfer mechanisms . . . . .	15
2.3	PEDOT and PSS formulas . . . . .	17
2.4	Fiber-based optical implants . . . . .	18
2.5	LED-based optical implants . . . . .	19
2.6	Attenuation spectrum of the neural tissue . . . . .	21
2.7	Process flows for the fabrication of electrical and optoelectronic devices . . . . .	23
2.8	Optical imaging of PEDOT films . . . . .	24
2.9	Electrochemical properties of PEDOT films . . . . .	25
2.10	Bending test . . . . .	27
2.11	PEDOT reliability after in vivo acute tests . . . . .	28
2.12	Electrical properties of the optical device . . . . .	30
2.13	Optical power characterization . . . . .	31
2.14	Thermal characterization of the optical device . . . . .	33
3.1	Schematic of the peripheral and central auditory systems . . . . .	40
3.2	Main ascending auditory pathways . . . . .	41
3.3	Clinical ABI devices . . . . .	42
3.4	Illustration of the ABI implantation . . . . .	43
3.5	Structure of the human cochlear nucleus complex . . . . .	46
3.6	Structure of the rat cochlear nucleus complex . . . . .	47
3.7	Neurophysiological organisation of the dorsal cochlear nucleus in mammals . . . . .	48
3.8	Examples of human and rat ABRs . . . . .	52
3.9	Experimental setup . . . . .	53
3.10	Stimulation protocol and signal processing . . . . .	55
3.11	IC response map features extraction . . . . .	56
3.12	Response maps following acoustic stimulation . . . . .	58

## List of Figures

---

3.13	Correspondance between characteristic frequency and IC recording site . . . . .	59
3.14	14-channels stimulation array . . . . .	60
3.15	20-channels electrode array . . . . .	61
3.16	Packaging for acute in vivo experiments . . . . .	62
3.17	Peak labeling of electrically-generated ABRs . . . . .	63
3.18	Raw eABRs in individual rats . . . . .	64
3.19	Effect of stimulation position on eABRs . . . . .	65
3.20	Effect of inter-electrode distance on eABR parameters . . . . .	67
3.21	eABR parameters generated by monopolar and bipolar stimulation . . . . .	68
3.22	Raw IC response maps in individual rats . . . . .	71
3.23	Characteristic frequency variations of raw IC responses . . . . .	72
3.24	IC map parameters variations for individual rats . . . . .	73
3.25	Tonotopic organisation of responses before and after average subtraction . . . . .	75
3.26	IC map parameter variations for the different types of processing . . . . .	77
3.27	Examples of PSTH and cutoff between early and late activity . . . . .	78
3.28	PSTHs of the early phase of response . . . . .	79
3.29	Timing properties of the late phase of responses . . . . .	80
3.30	Tonotopic organisation of early and late phases of response . . . . .	82
3.31	Tonotopic organization of responses after combined processing . . . . .	84
3.32	Effect of stimulation level on the IC map parameters . . . . .	87
3.33	Effect of orientation and distance of electrode pairs in the 14-electrode array . . . . .	90
3.34	Orientations and interelectrode distances with the 20-electrodes array . . . . .	92
3.35	Effect of orientation and distance on raw IC response map parameters . . . . .	93
3.36	Effect of orientation and distance on IC response map parameters after combined processing . . . . .	94
3.37	Raw IC response maps following monopolar and bipolar stimulation . . . . .	96
3.38	IC response map parameters following monopolar and bipolar stimulation . . . . .	97
3.39	Illustration of the 8 tested waveforms . . . . .	99
3.40	Effect of symmetrical waveforms on tonotopic organisation of responses . . . . .	101
3.41	Effect of waveform on IC response map properties . . . . .	102
3.42	Effect of asymmetrical waveforms on tonotopic organisation of responses . . . . .	104
3.43	Effect of triphasic waveforms on tonotopic organisation of responses . . . . .	105
4.1	Optical stimulation device . . . . .	118
4.2	MicroCT confirmation of LED device placement . . . . .	120
4.3	Raw EMG recordings following spinal cord optical stimulation . . . . .	121
4.4	Effect of LED stimulation on EMG parameters . . . . .	123
4.5	Lateral selectivity of activation . . . . .	124
4.6	Effect of stimulation pulse width on the EMG parameters . . . . .	125
4.7	Effect of stimulation pulse rate on EMG parameters . . . . .	127
4.8	Chronic variation of EMG parameters . . . . .	128
4.9	Integrity of walking functionality and histological analysis . . . . .	130

5.1	Proposed clinical ABI design . . . . .	139
5.2	Closed-loop CI and ABI systems . . . . .	145





# List of Tables

2.1	Properties for the different materials used in the thermal dissipation model . . .	32
3.1	Orientations and distances with the 14-electrode array . . . . .	61
3.2	P-values of the statistical tests of single rats . . . . .	74



# 1 Introduction

Implantable neuroprostheses are an ensemble of systems engineered to provide an interface between the central or peripheral nervous systems and man-made devices. They can include stimulation and/or recording capabilities, and are used for the replacement or restoration of damaged sensory or motor function. They have thus a great therapeutic potential for many patients suffering from chronic nervous system deficits<sup>[100]</sup>.

The multitude of neuroprosthetic devices currently used in clinics or in research can be of several different types. Sensory neuroprostheses seek to replace damaged function in the sensory system. The cochlear implant is the most successful sensory neuroprosthesis on the market with more than 300'000 implanted patients<sup>[143,183]</sup> (Fig. 1.1A). Retinal implants were recently approved for clinical use (Argus II retinal prosthesis system, CE mark in 2011 and FDA approval in 2013, Fig. 1.1B), and are implanted in more than 100 patients<sup>[116]</sup>. Auditory brainstem implants<sup>[201]</sup> (Fig. 1.1C) and spinal cord stimulation implants to alleviate chronic neuropathic pain<sup>[191]</sup> (Fig. 1.1D) have also been used clinically for several years.

Alternatively, motor neuroprostheses are used to improve or replace motor functions. Deep brain stimulation (DBS) of the subthalamic nucleus can be used to reduce drug-resistant motor symptoms in patients with Parkinson's disease<sup>[146]</sup> (Fig. 1.1E). The use of electrochemical neuroprostheses in rehabilitation following spinal cord injuries has also been the subject of intense research<sup>[30,198]</sup>. Some neuroprostheses consist of a bidirectional interface, such as the system allowing simultaneous motor control and sensory feedback of a robotic arm in amputee patients, which is the subject of a clinical trial<sup>[160]</sup>. Other applications include vagus nerve stimulation for the treatment of epilepsy and mood disorders<sup>[67,182]</sup> (Fig. 1.1F) and sacral nerve stimulation for the treatment of bladder dysfunction<sup>[82]</sup>. In addition to reducing Parkinson's disease motor deficits, DBS is also envisioned to treat other conditions, such as bipolar disorder<sup>[58]</sup>, obsessive compulsive disorder<sup>[6]</sup> or Tourette syndrome<sup>[179]</sup> by targeting different parts of the brain.

All the mentioned neuroprostheses share some common features in terms of technology,

## Chapter 1. Introduction

in order to achieve safety and efficiency of stimulation and long-term durability. Since they all aim at providing an interface with the nervous system, technological improvements, methods or protocols developed for one specific application can potentially be transferred to other applications.

### 1.1 The need for selectivity in the context of neuroprosthetics

When trying to replace or restore lost function, the first challenge is to understand with precision the system to stimulate, including its normal function but also the potential changes due to injury and the mechanisms of recovery of the system<sup>[131,162]</sup>. This step is of critical importance in complex systems, in order to identify which neuronal populations are linked to the function to restore and to select the best targets for artificial stimulation. This includes the selection of the structure to stimulate (in the central or peripheral nervous system), as well as the target neuronal population within that structure.

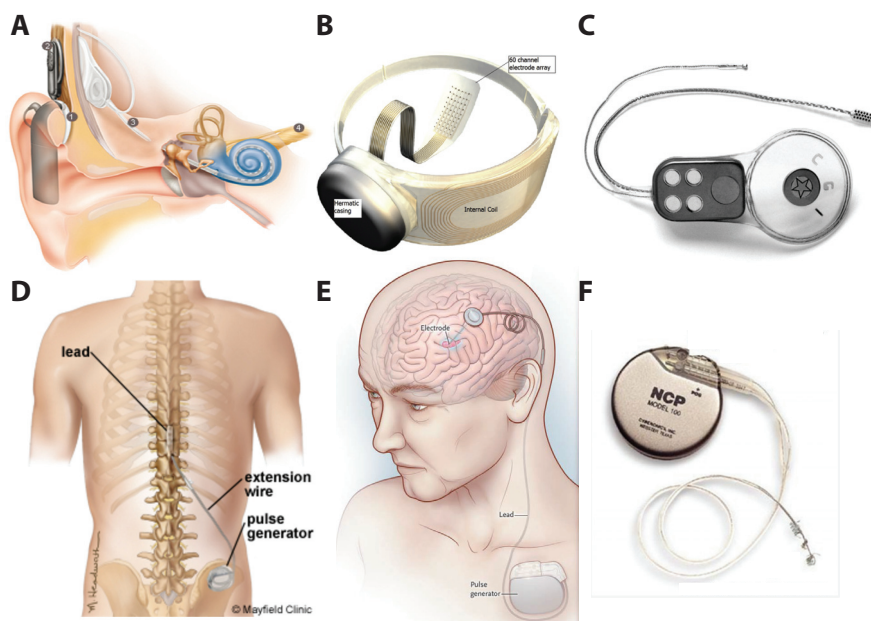


Figure 1.1: Examples of clinical implantable neuroprostheses A) Cochlear implant (Cochlear corp.)<sup>[48]</sup>, B) Argus II retinal prosthesis<sup>[116]</sup>, C) Auditory brainstem implant (Cochlear corp.)<sup>[180]</sup>, D) Spinal cord stimulator for neuropathic pain<sup>[118]</sup>, E) Deep brain stimulation device<sup>[146]</sup>, F) Vagus nerve stimulator<sup>[182]</sup>

In order to reach high levels of performance, the neuroprosthetic interface must communicate efficiently with the nervous system. Usually, that means developing a stimulation protocol that corresponds as closely as possible, in space and time, to the natural activation of the system. The ultimate goal is to mimic the natural function, but this is currently often impossible to

## 1.1. The need for selectivity in the context of neuroprosthetics

achieve due to the great complexity of most neural systems and the limited numbers of channels available. A neural mechanism that is of critical importance in this context is the neural plasticity, the ability of the brain to adapt and reorganize in a stimulus-dependent way<sup>[158]</sup>. This mechanism is responsible for the neuronal reorganization following injury<sup>[47,175,195]</sup> and for the adaptation to the artificial stimulus<sup>[47,131,154]</sup>. It enables an optimization of the performance of the stimulation even if the stimulus is not exactly similar to the natural activation of the system. Neuroplasticity is influenced by many factors, such as the duration and onset of injury and the time of implantation<sup>[47]</sup>. However, even with efficient neuroplasticity, the final performance achieved with a neuroprosthetic device is highly dependent on the quality and resolution of the artificial stimulation<sup>[56,103]</sup>.

One of the keys for improving the detailed understanding of a neural system and achieving a stimulation that is as close as possible to the natural function of the tissue is the selectivity of stimulation, or the ability to stimulate a specific neuronal element without stimulating the rest of the tissue.

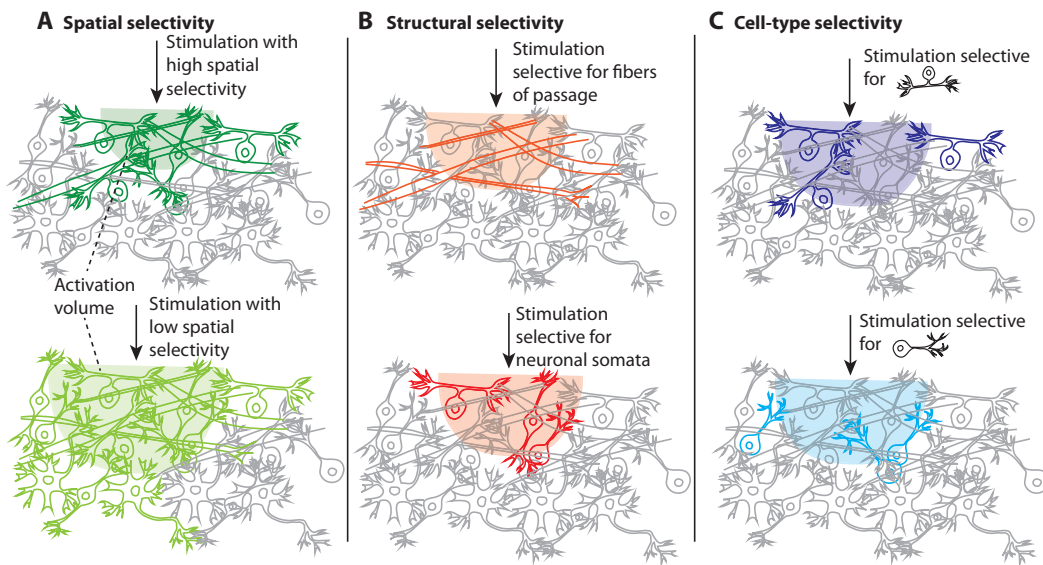


Figure 1.2: Schematic illustration of the spatial (A), structural (B) or cell-type (C) selectivity of stimulation of neural tissue showing the volume of activation and the activated neuronal elements in color. A) Stimulation with high and low spatial selectivity, resulting in activation of different volumes of tissue. B) Illustration of a stimulation protocol with structural selectivity for fibers of passage and for neuronal somata. C) Illustration of cell-type selective stimulation of two different neuronal type.

Spatial selectivity refers to the ability to stimulate a specific volume of tissue without stimulating neighbouring areas, as illustrated in figure 1.2A<sup>[134]</sup>. It is for instance important in cochlear stimulation, to avoid channels interaction<sup>[190]</sup>, and in deep brain stimulation, to

avoid stimulation of off-target areas<sup>[95]</sup>. Structural selectivity is the preferential stimulation of specific tissue structures, including neuronal somata, axons, or fibers of passage of specific diameters<sup>[124]</sup> (Fig. 1.2B). It can be for example useful to target neuronal somata in a tissue with mixed neuronal somata and fibers of passage. Most neural tissue being composed of a mix of different neuronal types, cell-type selectivity refers to the targeting of a specific neuronal type (Fig. 1.2C), thus potentially activating only a specific function in a network of interconnected neurons<sup>[50]</sup>. Exploring ways to optimize selectivity in its different aspects is of critical importance and can lead to the improvement of many neuroprosthetic devices.

Electrical and optical stimulation are two of the main modes of stimulation of neural tissue, with possibilities to achieve various levels of spatial, structural and cell-type selectivity. In this thesis, these two modes of stimulation will be considered, to investigate whether a more selective stimulation can improve existing functionality, or even lead to new functionalities. To achieve this goal, it is first necessary to review the mechanisms of neural stimulation with each of these two modes of stimulation.

## 1.2 Surface electrical stimulation

### 1.2.1 Mechanisms of electrical stimulation

The transmembrane potential of a neuron, the difference between the extracellular and intracellular membrane potentials, is controlled by both passive mechanisms, the capacitive effect of the lipid bilayer, and active mechanisms, through the ion channels (mainly  $\text{Na}^+$  and  $\text{K}^+$  channels)<sup>[134]</sup>. If the extracellular potential is driven negative compared to the intracellular potential, the neuron is depolarized and an action potential (AP) can be generated if the depolarization threshold is reached<sup>[193]</sup>. The AP is generated by the sequential activation and inhibition of the different membrane ion channels, as described in the Hodgkin-Huxley model<sup>[84]</sup>.

As charge is injected into the tissue during neural stimulation, the resulting change of extracellular potential can artificially induce the generation of APs in neighboring neurons through a depolarization of portions of the axon membrane<sup>[84,134]</sup>. In the simplest case of a current source  $I$  (A) being placed near an isotropic excitable tissue of conductivity  $\sigma$  (S/m), the extracellular potential  $V_e$  at a distance  $r$  from the current source can be modeled as  $V_e = \frac{I}{4\pi r\sigma}$ . The activating function, describing the activation of the neurons, was shown to vary with the second derivative of this potential<sup>[161]</sup>. However, real stimulation conditions are very different due to the complex structure of most neural tissue, constituted of a mix between neuronal cell bodies and fibers of passage, in different proportions and orientations. For instance, the conductivity of the white matter and gray matter are very different, the gray matter having an isotropic conductivity of about 0.2 S/m, and the white matter having a higher conductivity in the direction of the fibers (1 S/m) than across the fibers (0.1 S/m)<sup>[95]</sup>. The size and orientation of the fibers, as well as the membrane properties of different neuronal types can also result in a

complex electric field distribution, altering the response properties of a neural tissue<sup>[125] [213]</sup>. The excitability of each neuronal type thus have to be taken into account in order to optimize the efficiency of stimulation<sup>[197]</sup>.

### 1.2.2 Selectivity of electrical stimulation

Spatial selectivity, determined by the volume of activation (Fig. 1.2A), is strongly dependent on the efficiency of stimulation to generate activation in the target neuronal elements. An efficient stimulation will generate activity at smaller current levels, thus generating less current spread. Spatial selectivity can be influenced by many parameters, including geometrical and stimulation protocol parameters.

First, geometrical parameters of the stimulation electrode influence the spatial selectivity, as the distance to the target neurons is a critical factor determining the necessary current level<sup>[15,214]</sup>. Here, two main categories of geometries can be discriminated. First, penetrating electrodes have small areas (usually below  $10'000 \mu\text{m}^2$ ) and can be implanted in close proximity to the target neurons. A high spatial selectivity can thus be achieved because of the low current thresholds. However, a major drawback of penetrating electrodes is that rigid shanks are usually used, inducing chronic inflammation due to micromotion-induced tissue damage<sup>[71]</sup>. Second, macroelectrodes located at the surface of the tissue have geometrical areas usually larger than  $0.001 \text{ cm}^2$  and are less invasive than penetrating electrodes<sup>[44]</sup>. However, because of the greater distance to the target neurons and the higher electrode area compared to penetrating electrodes, current thresholds are higher and spatial selectivity is lower. An implant with the low invasiveness of surface electrodes and the spatial selectivity of penetrating electrodes would combine the advantages of both approaches. An optimization of surface stimulation combining minimally invasive, safe and efficient stimulation with close contact to the tissue and a high density of electrode sites is thus the approach chosen here.

In addition to the geometrical parameters, the current level used for stimulation also depends on the stimulation protocol. The structure and composition of the target elements in the tissue have a large influence on the most efficient stimulation protocol to use, as fibers of different diameters and cell somata do not have the same response properties to electrical stimulation<sup>[125]</sup>. For instance, high frequency stimulation was shown to generate greater neuronal output in fibers of passage than in local cells, whereas specifically designed asymmetric pulses could efficiently target local cell bodies<sup>[124,125]</sup>. Some level of fiber diameter selectivity is also possible since thicker fibers can be stimulated with lower currents than thinner fibers<sup>[125,173]</sup>.

This variability in excitability properties enables a certain level of structural selectivity during electrical stimulation. This, in turn, can achieve some cell-type selectivity depending on the properties of the target tissue. A true cell-type selectivity is however not achievable with electrical stimulation, which is one of the reasons of the development of optogenetics, as

described in the next section.

### 1.3 Optical stimulation

#### 1.3.1 Optogenetic stimulation of neural tissue

Optogenetics is a technology that enables cell-type specific, millisecond-scale control of neural activity. It is based on genetic targeting and modification of specific neuronal types with a light-sensitive ion channel, followed by optical illumination of the neural tissue. This control is possible in intact brain tissue and in freely moving animals<sup>[50]</sup>.

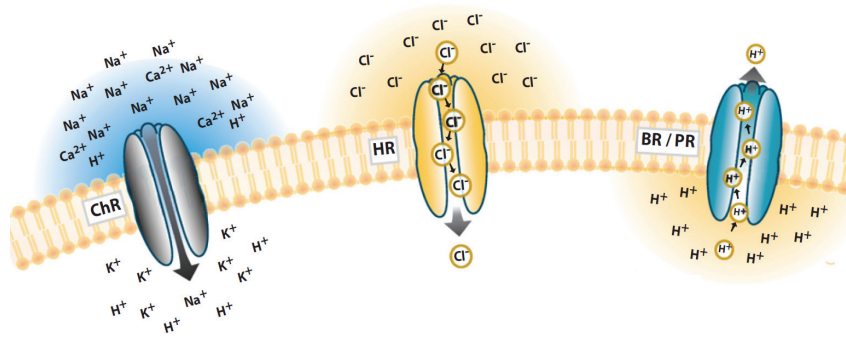


Figure 1.3: Illustration of the three main types of opsins: Channelrhodopsin (ChR), a cation channel (peak absorption: 473 nm); Halorhodopsin (HR), a chloride pump (peak absorption: 570 nm); Bacteriorhodopsin (BR), a proton pump (broad spectrum, peak absorption: 570 nm)<sup>[215]</sup>

The light-sensitive ion channels used in optogenetics originate from microbial opsins, light-gated ion channels present in the membrane of some microorganisms. Three main types of opsins, channelrhodopsin (a cation channel), bacteriorhodopsin (a proton pump) and halorhodopsin (a chloride pump) can be used for precise activation or inhibition of neurons<sup>[50]</sup> (Fig. 1.3). From the initially discovered versions of these three different types of opsins, genetic engineering lead to an expansion of the library of available opsin properties. Specifically tailored opsins for defined physiologic effect with various kinetic properties, light-sensitivities and wavelength sensitivities are thus available<sup>[215]</sup>. Widely used in neuroscience, type 2 channelrhodopsin (ChR2) can be used for fast excitation of neurons, is characterized by a  $\tau_{off}$  time constant of about 10 ms, and is sensitive to blue light (peak sensitivity at 473 nm). Due to its fast kinetics and high light sensitivity, it was selected for the experiments presented in this thesis.

The cell type selectivity of optogenetics is enabled by genetically targeting the expression of



light-gated proteins. To achieve this, the gene coding for the light-sensitive protein (ChR2 here) is placed under the control of a cell type specific promoter. Only the neurons corresponding to the cell type selectivity of the promoter will thus express ChR2. Transfection can be achieved through several different techniques, including but not limited to viral promoters (lentiviral vectors or adeno-associated vectors) or transgenic approaches<sup>[215]</sup>. While viral promoters are injected locally, transgenic approaches generate ChR2 expression in specific cell-types in the entire animal, and light can be delivered at any location. For instance, a mouse line expressing ChR2 under the control of the Thy1 promoter was developed (Thy1::ChR2-EYFP). This mouse line expresses ChR2 in projection neurons, and can be used in the study of several different systems involving stimulation of these neurons<sup>[215]</sup>.

Successful optogenetic stimulation is also critically dependent on the light delivery system. First, the wavelength of the delivered light must correspond to the wavelength sensitivity of the selected light-sensitive protein. The intensity of the light must also be sufficient to generate activation of the ion channels. As an example, the peak of wavelength sensitivity of ChR2 is 473 nm, and the threshold of activation of single proteins is 1-5 mW/mm<sup>2</sup><sup>[215]</sup>. Light power decreases exponentially with tissue depth, so in vivo experiments require higher light power to compensate for the losses when the target neurons are not located at the surface of the tissue. In vivo optogenetics thus requires the use of devices enabling chronic, localized, temporally determined, safe and efficient light delivery<sup>[153]</sup>. These requirements will be further detailed in Chapter 2 of this thesis.

#### 1.3.2 Selectivity of optogenetic stimulation

The activation or inhibition evoked by optogenetic stimulation can be specific to any neuronal type (Fig. 1.4), provided that the opsin gene can be put under the control of a cell-type specific promoter. Although a lot of work in the genetics field is required to enable the targeting of each specific cell type, many possibilities for targeting neuronal types already exist.

Since light does not spread in the same manner as electrical current (Fig. 1.4), only the neurons in the beam of light are stimulated during optical illumination. The spatial selectivity of optogenetics can thus be very high, and is strongly dependent on the focusing of the light. The volume of activation is also dependent on the optical properties of the tissue and the wavelength of the light, which both influence the exponential decay of light in the tissue<sup>[1,215]</sup>.

A 'natural' structural selectivity is present in optogenetics, where fibers of smaller diameter are usually recruited before fibers of larger diameter<sup>[110]</sup>, an order of recruitment similar to physiological recruitment. In contrast, electrical stimulation usually generates activation of larger diameter fibers before smaller diameter fibers<sup>[125]</sup>. In addition, structural selectivity can result from cell-type selectivity, if the different structural elements can be genetically targeted independently. Since the optical threshold of activation is also dependent on the level of expression of ChR2 on the membrane, structural selectivity could also be achieved by

targeting discrete subcellular domains, such as the soma or the dendrites<sup>[62]</sup>.

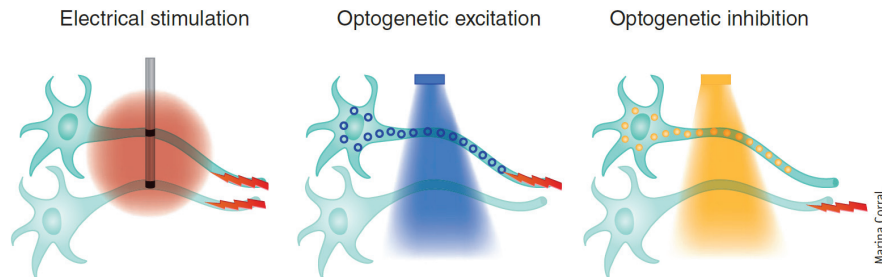


Figure 1.4: Illustration of cell type selectivity in optogenetics, with possibilities to activate or inhibit specific cell types, as opposed to unspecific electrical stimulation<sup>[50]</sup>

The spatial and cell type selectivity achievable with optogenetics has generated a lot of interest from a variety of different fields, including neuroprosthetics. In auditory prostheses, the number of channels and resulting spectral resolution of stimulation are often limited by the spread of electrical current. Thus, optogenetics is investigated as a way to improve stimulation, in the peripheral<sup>[140]</sup> and central<sup>[76]</sup> auditory systems. In the field of retinal prostheses, optogenetics is also a promising technique to increase spatial selectivity, to target specific cells types in the retina, but also to selectively induce inhibition of certain cell types<sup>[19]</sup>, and is the subject of a recently initiated clinical trial<sup>[163]</sup>. A better understanding of the underlying neural mechanisms of DBS<sup>[60]</sup> is also an example of an application enabled by optogenetic targeting of the different neural components.

### 1.4 Technological requirements

As mentioned in the previous sections, achieving a high spatial selectivity with electrical and optical stimulation is dependent on two essential points: a close proximity to the target tissue and a high density of stimulation sites. Most structures of the human body have curvilinear shapes. Examples of radii of curvature found in the central nervous system are 1.5 mm for the brainstem<sup>[167]</sup>, ~9 mm for the cortex<sup>[24]</sup> and ~10 mm for the spinal cord<sup>[34]</sup>. A technological requirement to be in close proximity to the target tissue for surface implants is thus the conformability of the substrates.

In addition, the necessity for a high density of stimulation sites, in order to have many spatially addressable stimulation sites and to increase the spatial resolution, is linked to a miniaturization of the design of the stimulation devices. As detailed in the second chapter of this thesis, minimal feature sizes lower than 100  $\mu\text{m}$  are often required.

Technologies for conformable arrays enabling feature sizes smaller than 100  $\mu\text{m}$  are thus necessary in order to develop high quality interfaces with the nervous system tissue. The development and tailoring of such technologies for specific applications in the central nervous system is the main focus of this thesis.

## 1.5 Outline of the thesis

### 1.5.1 Chapter 2: Technologies for conformal surface neural stimulation

The second chapter of this thesis presents the development of conformable devices designed for surface electrical and optical neuromodulation. The technical challenges for improved electrical and optical stimulation are presented, and designs are proposed for each application. For electrical stimulation, the use of small electrode sites requires the implementation of a coating on the electrode sites in order to achieve safe and efficient neural stimulation. For optical stimulation, a device integrating an array of LEDs for spatially addressable stimulation is presented.

### 1.5.2 Chapter 3: New generation auditory brainstem implant

The third chapter presents an application of surface electrical stimulation for a sensory neuro-prosthesis: the auditory brainstem implant (ABI). The ABI is an alternative hearing strategy for patients suffering from sensorineural hearing loss who cannot benefit from cochlear implants (CIs) because of a disconnection between the peripheral and central auditory systems. ABIs provide auditory sensations and help with lipreading for most patients. However, speech hearing performance is relatively poor compared to the high outcomes obtained in most patients with CIs. One hypothesis for this is the spread of electric current leading to low spatial selectivity and stimulation of extra-auditory neurons, causing side-effects. Based on this hypothesis, improving the spatial selectivity of stimulation is a route for improving the ABI clinical outcomes.

Using a high-density microfabricated ABI array with the flexible implant technology presented previously, the possibility to generate frequency-tuned responses with spatially selective stimulation is investigated. Different components of the multiunit recordings obtained from an animal model are separately analyzed, in order to improve the understanding of the neural correlates of the auditory brainstem stimulation. The effect of stimulation electrode configuration and of the waveform of stimulation on the tonotopic organization of responses are tested.

### 1.5.3 Chapter 4: Optogenetic stimulation of the spinal cord

The fourth chapter presents a proof of principle for chronic optical stimulation of the spinal cord with a LED-based optical stimulation array. Optogenetics, as mentioned earlier, enables cell type selectivity, which is not achievable with electrical stimulation. This technique could lead to a better understanding of the spinal cord circuits and of the role of each neuronal type in the recovery, and potentially also to improved recovery following spinal cord injury.

These experiments are performed using a transgenic mouse model (Thy1:ChR2) showing high levels of expression of channelrodopsin in projection neurons, and, as a result, low activation thresholds. Evoked motor responses are recorded in the leg muscles, and the effect of stimulation with a single LED or with pairs of LEDs is investigated. Optical stimulation of the spinal cord is also characterized by analyzing the lateral selectivity of stimulation and the effect of changing stimulation parameters (LED current, pulse rate and duration). Chronic variations of stimulation thresholds and other parameters over time as well as safety of stimulation are also analyzed and discussed in this chapter.

## 2 Technologies for conformable surface neural stimulation

### Abstract

Surface neuromodulation implants enable minimally invasive stimulation of neural tissue compared to penetrating implants in many neuroprosthetic devices. However, there are unique challenges associated with this type of stimulation, both in electrical and optical stimulation. In electrical stimulation, the stiffness of the traditional silicon substrates ( $> 100$  GPa) prevents a good conformability to soft neural tissues ( $\sim 1$ - $100$  kPa) that often have complex shapes. Additionally, safe stimulation requires relatively large electrode sites (several hundreds of  $\mu\text{m}$ ) due to the limited charge injection properties of the stimulation electrode materials. These two elements lead to high current thresholds and low spatial selectivity of stimulation. In optical stimulation, laser-fiber coupled implants provide the highest optical power (tens of mW), but they cannot be fully implanted and are highly limited in the number of channels. LEDs-based implantable devices with multiple spatially addressable channels must combine a sufficient optical power in order to stimulate target neurons that might not be at the surface of the tissue with limited thermal heating ( $< 2^\circ\text{C}$ ) to avoid chronic thermal damage at the surface of the tissue.

In this chapter, we present a technology for conformal surface stimulation implants based on thin polyimide substrate, combining the advantages of a stable microfabrication process with small feature sizes and conformability due to the flexible substrate. A coating based on PEDOT:PSS, a conducting polymer with high effective area and efficient charge transduction properties is presented as a means to improve the transduction of charges at the electrode/tissue interface, enabling high safe injectable charge with small electrode areas. For optical stimulation, a fabrication process for the integration of thin ( $50\ \mu\text{m}$ ) LEDs on a flexible polyimide substrate is presented. The parameter space allowing thermally safe chronic optical stimulation is identified with a model of thermal heating of the tissue.

**Publication:** Guex, A., Vachicouras, N., Hight, A.E., Brown, M.C., Lee, D.J., Lacour, S.P., Conducting polymer electrodes for auditory brainstem implants, *J. Mat. Chem. B* (2015)

### 2.1 Introduction

#### 2.1.1 Interfacing with the central nervous system

The human body, and particularly the nervous system, is composed of soft tissues with complex shapes. In the central nervous system, the Young's modulus of the brain tissue is  $\sim 1$ - $10$  kPa<sup>[36]</sup> and that of the spinal cord is  $\sim 100$  kPa<sup>[74]</sup>. The radii of curvature can be as small as  $\sim 1.5$  mm for the brainstem<sup>[167]</sup>,  $\sim 9$  mm for the cortex<sup>[24]</sup> and  $\sim 10$  mm for the spinal cord<sup>[34]</sup>. Interfacing with these specific structures thus requires materials that can conform to curvilinear shapes, making traditional hard electronics ( $> 100$  GPa) not adapted for this purpose.

In addition, in many aspects of neural surface stimulation in the context of neuroprosthetics, spatial resolution is a key feature to generate the desired function. In retinal implants, increasing the stimulation resolution is a very important challenge in order to improve visual acuity<sup>[103]</sup>. In spinal cord stimulation, spatial selectivity is critical to activate specific segments that generate the desired motor function in flexor or extensor muscles<sup>[206]</sup>. In the auditory system, the different frequencies of the sound are encoded in different locations, an organization called 'tonotopy' that is conserved along the entire auditory pathway<sup>[84]</sup>. A high spatial resolution is then required to stimulate independent frequency channels.

Most present clinical technologies are based on thick platinum or platinum-iridium electrodes ( $> 1 \mu\text{m}$ ) with stimulation electrode areas larger than  $0.2 \text{ mm}^2$  and stainless-steel wires embedded in millimeter-thick silicone matrix<sup>[100,201]</sup>. These properties make them not able to conform to small radii of curvature and complex shapes found in the nervous system or to achieve high spatial resolution in stimulation. Technologies for conformable surface implants allowing a very small minimal feature size are thus necessary in order to develop efficient interfaces with the nervous system.

#### 2.1.2 Technologies for conformable implants

Several technologies can be considered to fabricate a conformable surface implant. The main solution is the use of soft substrates with Young's moduli as similar as possible to the tissue to interface. Among these materials, we can cite elastomers ( $\sim$  MPa) or flexible polymers, such as polyimide or parylene (3-5 GPa).

Elastomeric materials can be used to develop devices that can conform to complex surfaces with non-gaussian curvatures.<sup>[71]</sup> Polydimethylsiloxane (PDMS) is one of the main materials used as an elastomeric substrate. Several techniques can be used to deposit stretchable metallization onto the substrate in order to fabricate stretchable implants for neuroprosthetic applications. These techniques include the evaporation of a microcracked gold film<sup>[54,99,129]</sup>, or the design of serpentine structures of metal<sup>[53]</sup>.

One major challenge of these approaches is the feature size limitation of about  $100\ \mu\text{m}$ . As mentioned earlier, when using surface stimulation with a high density of spatially distributed electrodes, the fabrication technique needs to accommodate small feature sizes (below  $100\ \mu\text{m}$ ), especially in a research context where the target structures are often much smaller in animal models than in humans<sup>[100]</sup>.

Despite their higher Young's modulus compared to elastomeric materials, flexible polymer substrates such as polyimide or parylene are of high interest here because they are adapted to standard microfabrication processes and can have micrometer-size features. Flexible implants can be used as penetrating implants inserted into neural tissue<sup>[35,132]</sup> (Figure 2.1A) or as surface electrodes<sup>[78,142,171]</sup> (Figure 2.1B-E). The presented examples are fabricated with parylene<sup>[55,166]</sup> or polyimide<sup>[2,35,78,88,132,142,171]</sup> of various thicknesses.

Several different strategies can be used to compensate for the higher Young's modulus of flexible polymer substrates compared to elastomers. First, the bending stiffness ( $S$ ) can be decreased by reducing the thickness ( $t$ ) of the substrates, as shown by the bending stiffness equation :

$$S = \frac{E \times t^3}{12 \times (1 - \mu^2)}$$

Where  $E$  = Young's modulus of the substrate and  $\mu$  = Poisson ratio

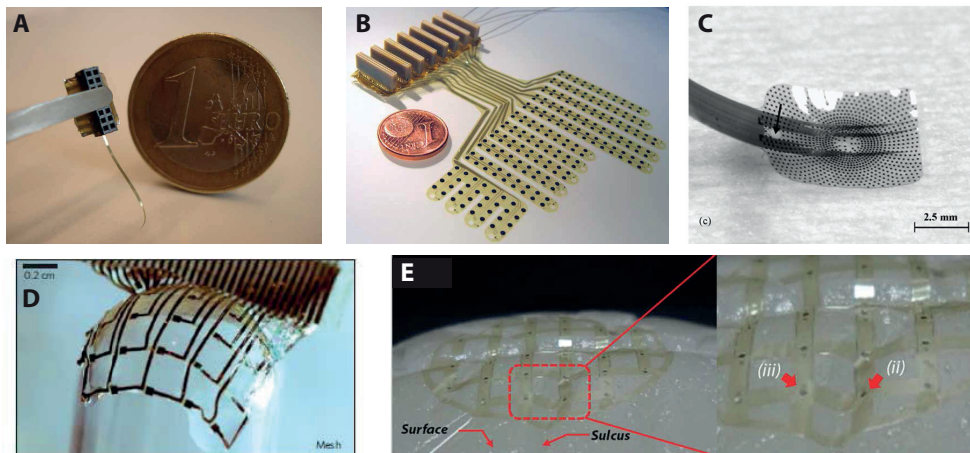


Figure 2.1: Flexible polymer devices. A) Polyimide neural probe ( $20\ \mu\text{m}$  thick)<sup>[132]</sup>. B) Polyimide ECoG ( $10\ \mu\text{m}$  thick)<sup>[171]</sup>. C) Parylene retinal implant ( $15\ \mu\text{m}$  thick)<sup>[166]</sup>. D) Polyimide mesh electrode array ( $7\ \mu\text{m}$  thick) with dissolvable silk fibroin membrane<sup>[88]</sup>. E) Polyimide mesh electrode array ( $6\ \mu\text{m}$  thick)<sup>[14]</sup>.

To maximize the conformability of the substrate and adapt it to each application, the thickness

can thus be reduced to the minimum allowing correct handling of a free-standing film in the absence of a carrier substrate. As seen in figure 2.1D-E, mesh-like structures can also be designed to further increase conformability of devices, particularly around non-gaussian curvatures<sup>[14,88]</sup>.

In the context of surface neural stimulation, using a thin polyimide-based substrate thus combines several advantages, while limiting the drawbacks due to its relatively high Young's modulus. Its compatibility with standard microfabrication processes and possibility to design small feature sizes (down to the  $\mu\text{m}$ ) can be used to quickly fabricate prototypes with a very high design flexibility.

### 2.1.3 Electrical stimulation

#### Electrodes diameter

In order to investigate the limits of spatial selectivity achievable with surface implants, the density of electrodes on the array is increased, taking advantage of the small feature sizes enabled by the microfabrication technique described earlier. An increase in the density of electrode sites has to be associated to a decrease in their area, which raises new challenges.

A major limitation to reducing electrode area is the associated higher density of charges sent through the electrode-electrolyte interface for the same total charge, which leads to lower damage thresholds. In order to design a safe, efficient and selective neural stimulation protocol, it is essential to understand the electrode-electrolyte interface, where complex electrochemical and physiological processes are occurring.

#### The electrode/tissue interface

At the electrode-electrolyte interface, a transduction of charge carriers from electrons in the electrode to ions in the extracellular fluid occurs during stimulation.<sup>[44]</sup> This transduction can happen through two main mechanisms. First, the capacitive, or non-faradaic charge transfer is associated to a redistribution of charges on both sides of the interface, without any electrons being transferred. It is a fully reversible process. Second, the faradaic charge transfer involves electrons transfer at the interface through oxidation and reduction reactions (Figure 2.2).

The rate of these reactions is defined by the reaction kinetics, at potentials close to equilibrium, and by the mass transport rate, when the potential is driven far away from equilibrium. The reversibility of the reaction is determined by the relative rate between kinetics and mass transport. Indeed, a fast kinetics induces a reversible reaction, all the reaction products staying close to the interface, whereas a slow kinetics induces the reaction products to diffuse away, making the reaction irreversible. In this case, a change in the chemical environment is induced and can lead to damages to the tissue or the electrode<sup>[134]</sup>. The mechanisms involved in charge



transfer in each case are highly dependent on the electrode material, the electrochemical potential and the waveform used for stimulation.

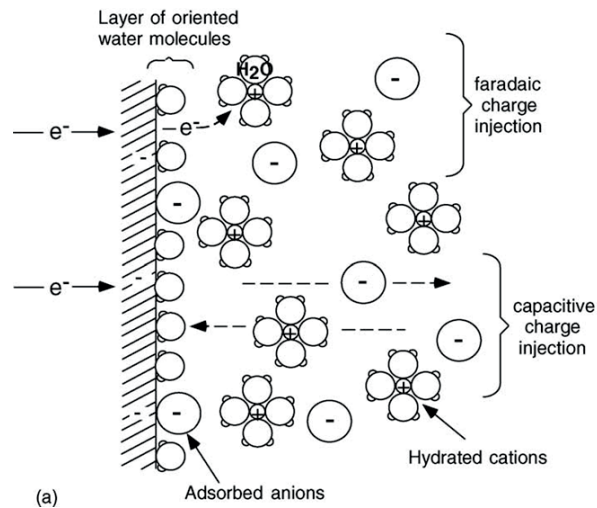


Figure 2.2: Illustration of the faradaic and capacitive charge transfer mechanisms<sup>[134]</sup>.

Electrode sites are usually characterized using several different methods. Electrochemical impedance spectroscopy (EIS) describes the complex impedance modulus and phase over the frequency spectrum and can help determine whether the charge injection mechanism is capacitive or faradaic for the different frequencies. Cyclic voltammetry (CV) is used to determine the cathodic charge storage capacity of an electrode during a slow potential sweep between the limits of water electrolysis, -0.6 and 0.8 V.

The cyclic voltammetry is often used to characterize the total cathodic charge that can be stored at the interface. However, it is poorly relevant for electrical stimulation as it is a slow sweep, whereas the changes in current during stimulation pulses are very rapid, allowing only the very rapid charge transfer reactions to happen. The charge available during electrical stimulation (or charge injection capacity, CIC) will thus be dependent on the stimulation pulse parameters, and can be characterized by analyzing voltage transients associated to specific stimulation pulses<sup>[44,205]</sup>. The voltage transients are composed of several phases, including the ohmic drop, the initial voltage drop due to the resistance of the solution, and the overpotential. The overpotential of the interface depends on many parameters, including the electrode material properties, the pulse waveform and frequency and the electrolyte composition. During neural stimulation, the overpotential has to be kept within safe limits to avoid irreversible reactions, usually defined by the limits of water electrolysis, -0.6 and 0.8 V ('water window')<sup>[193]</sup>. The CIC is the maximal charge generating an overpotential of the interface that remains within the water window, and is defined for each specific waveform.

The CIC is expressed in charge density because of its dependence on the area of contact

## Chapter 2. Technologies for conformable surface neural stimulation

---

between the electrode material and the electrolyte. Reducing the diameter of stimulation sites thus induces a decrease in this contact surface, resulting in an increase in impedance and a decrease in charge injection capacity. Since the charge injection capacity highly depends on the material, it can be increased by using materials with highly efficient charge injection mechanisms. Particular care thus has to be taken when selecting the electrode material in order to ensure a charge injection capacity that is high enough to allow safe charge injection at efficient levels with small electrode areas.

### Stimulation electrode material

The material chosen for the electrodes must have a satisfying charge injection capacity and not be damaged or induce damage upon electrical stimulation<sup>[134]</sup>. The electrode material is also chosen depending on the mechanism used to inject charges. Capacitive mechanisms, fully reversible and non-damaging, are the most desirable mechanisms. However, the maximal double layer charge density is very limited. Faradaic reactions, based on reduction and oxidation reactions, can induce changes in the electrochemical environment that can lead to tissue damage if the overpotential is driven too far from the resting potential<sup>[44]</sup>.

Noble metals, including platinum or platinum/iridium alloys, are the most common materials for neural stimulation<sup>[44]</sup>. They use both capacitive and faradaic charge injection mechanisms, but show limited charge injection capacity of about 0.05 - 0.15 mC/cm<sup>2</sup>. In order to increase the electrochemical surface area, platinum can be electroplated on the electrode sites, forming platinum black. This results in a decrease of impedance and an increase in charge injection capacity. Platinum black is the most widely used electroplated platinum coating, although its structural stability is weak and its use for neural stimulation is limited. Another version based on a slower electroplating protocol has been developed, platinum grey, and shows better structural stability. This coating is the subject of a patent (US 6974533 B2) and is used in the clinically-approved Argus II retinal implant<sup>[116]</sup>.

Iridium oxide coatings, either formed by activation of the iridium surface (AIROF), electrodeposition (EIROF), sputtering (SIROF) or thermal deposition (TIROF) were also shown to greatly increase the charge injection capacity of electrode sites compared to platinum or platinum/iridium metals, with values up to 5 mC/cm<sup>2</sup><sup>[44]</sup>. The charge injection mechanism of this coating is based on reversible reduction and oxidation reactions between the Ir<sup>3+</sup> and Ir<sup>4+</sup>, and on an increased effective surface area thanks to its porous microstructure. However, a positive inter-pulse bias must be used to reach high CIC values, which is not advantageous in terms of safety and requires more complex current sources<sup>[43]</sup>.

### Conducting polymer coatings

Conducting polymers (mainly Polypyrrole, PPy, and poly(3,4-ethylenedioxythiophene), PEDOT) have gained substantial interest over the past ten years for recording and stimulation

electrodes<sup>[10]</sup>. Although PPy properties have been extensively studied in the literature, PEDOT is generally preferred for biomedical applications because of its higher electrochemical stability<sup>[49]</sup> (Figure 2.3).

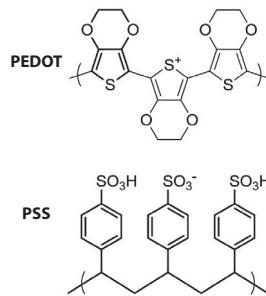


Figure 2.3: PEDOT and PSS formulas<sup>[202]</sup>

The surface of a PEDOT film is usually rough, resulting in an increase of the surface of contact with the electrolyte<sup>[10]</sup>, and an increase in charge injection capacity compared to a smooth surface. The conductivity of PEDOT (and other conducting polymers) is linked to the conjugated double bonds, allowing charge mobility along its backbone. However, without the presence of a doping ion, this mobility is limited because of an energy gap in the electronic spectrum and the polymer is not conductive. Doping introduces charge carriers that neutralize the unstable polymer backbone, allowing charge mobility and generating electrical conductivity<sup>[69,85?]</sup>. The conductivity thus has electronic and ionic components, and the charge transfer is highly efficient because of the high mobility of the electrons.

PEDOT coatings under stimulation conditions show excellent biocompatibility, with good neuronal adhesion and growth *in vitro*<sup>[164]</sup> and *in vivo*<sup>[114]</sup>. *In vivo* PEDOT electropolymerization has also been demonstrated, with good electrical performance and no impairment of function<sup>[150]</sup>. PEDOT has also been used to improve electrode properties for auditory system applications. In the cochlea, PEDOT was integrated with a functionalized alginate hydrogel for low impedance electrodes with concurrent drug delivery<sup>[37]</sup>. PEDOT-coated microelectrodes provided efficient microstimulation of the auditory cortex<sup>[92]</sup>. PEDOT was also shown to improve the recording SNR of hydrogel-coated electrodes in the auditory cortex<sup>[89]</sup>. The possibility to functionalize PEDOT coatings with bioactive molecules is also of high interest for many applications<sup>[10]</sup>. Although some studies report on a limited stability of PEDOT under repeated pulsing in chronic conditions<sup>[61]</sup>, it appears as a good alternative to metal films in an acute application aiming at improving charge transduction properties of electrode sites.

Implementing PEDOT-coated electrode sites can thus enable safe neural stimulation with small electrode sites at efficient current levels. This in turn allows for the design of an electrode array with small and dense electrode sites on a thin flexible substrate, thus combining of minimal invasiveness, maximal conformability and maximal electrode density. An implant

## Chapter 2. Technologies for conformable surface neural stimulation

with such properties will have a close proximity to the target neurons, leading to an optimal level of spatial selectivity.

### 2.1.4 Optical stimulation

Optogenetics is a very important tool when trying to achieve cell-type and spatial selectivity in neural stimulation. However, the development of optogenetics and its use for chronic stimulation in animals is highly dependent on the development of safe and efficient light delivery devices. High optical power, low energy, high spatio-temporal resolution and good integration in the tissue are necessary features to achieve successful chronic optical stimulation.

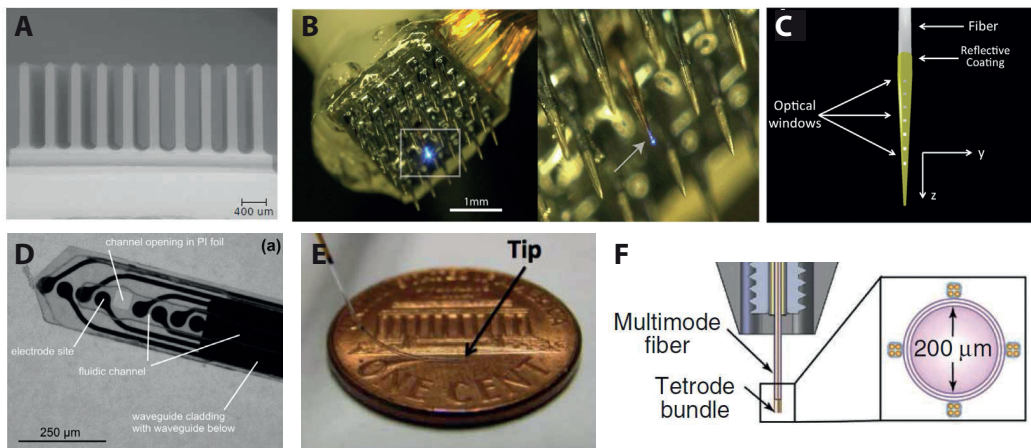


Figure 2.4: Fiber-coupled optical stimulation devices. A) Glass optrode array<sup>[1]</sup>. B) Hybrid optrode-MEA device<sup>[203]</sup>. C) Multipoint-emitting optical fiber<sup>[155]</sup>. D) Polymer-based device with fluidic channel, waveguide and recording electrodes<sup>[172]</sup>. E) Flexible optrode<sup>[109]</sup>. F) Optrode for combined optical fiber stimulation and four tetrode bundles readout<sup>[8]</sup>.

### Laser fiber devices

The first category of systems for optogenetic stimulation consists of a laser fiber that can be coupled to a waveguide penetrating into the tissue to deliver the light close to the target neurons<sup>[1,27]</sup> (Figure 2.4). These interfaces can be developed with the possibility to simultaneously readout the generated neuronal activity (Figure 2.4B,F)<sup>[8,28,203]</sup>, and also to inject viruses at the same location for transfection of neurons prior to optical stimulation (Figure 2.4D)<sup>[172]</sup>. Flexible probes have also been developed (Figure 2.4E)<sup>[28,109]</sup>, as well as multipoint fibers, allowing the addressing of neurons at several different depths in the tissue with a single shank device (Figure 2.4C)<sup>[155]</sup>.

Although these interfaces have the possibility to bring high power in close proximity to the neurons, there are several different limitations. First, the number of channels is very limited, as one laser fiber per channel must be present. In the case of multipoint fibers, several depths

can be accessed with the same fibers, but the number of independently controlled emitting point is very limited<sup>[155]</sup>. Additionally, an efficient coupling between the laser fiber and the waveguide is challenging, and losses occur at the interface<sup>[172,203]</sup> and in the waveguide itself<sup>[1]</sup>. Finally, developing a chronic interface based on a laser fiber is challenging because the laser sources are not fully implantable. All chronic systems of this kind will thus remain tethered, unless miniaturized implantable laser sources are developed.

### LEDs-based devices

Substrate-integrated light-emitting diode (LED) arrays can potentially overcome the challenges associated to fiber-based devices. Each LED being individually addressable, different volumes of tissue can be targeted. It is also possible to develop fully implantable systems, since a laser is not required. Losses due to coupling with the laser source are also avoided. Figure 2.5 shows examples of LED-based optogenetic stimulation arrays.

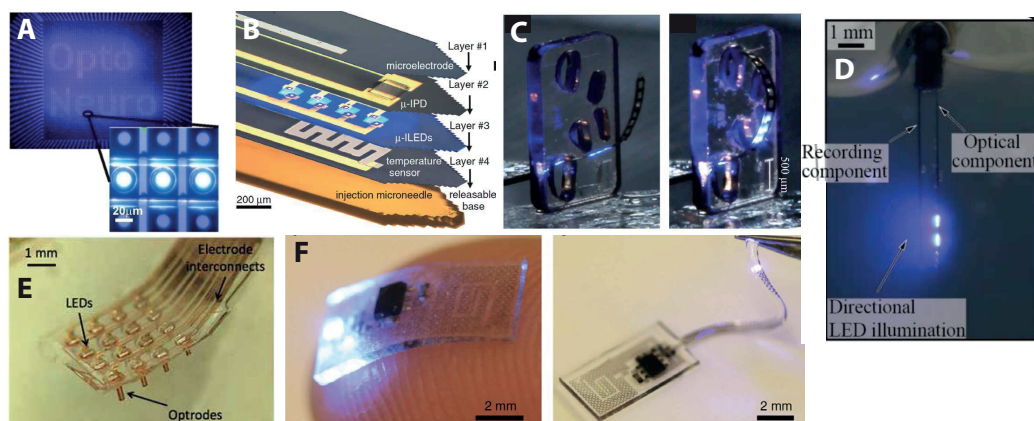


Figure 2.5: LED-based optical stimulation devices. A) LED array for in vitro neurons stimulation<sup>[65]</sup>. B) Injectable multimodal probe<sup>[90]</sup>. C) Flexible LED array for cochlear stimulation<sup>[59]</sup>. D) 3D optrode for optogenetic stimulation and electrophysiological recording<sup>[12]</sup>. E) Slanted optrode array<sup>[98]</sup>. F) Soft wireless optoelectronic system<sup>[151]</sup>.

The possibility to optogenetically stimulate neurons with an LED array was validated in vitro (Figure 2.5A)<sup>[65]</sup> and can help dissect the neural circuits. Devices for in vivo implantation can be divided into two categories: penetrating and surface arrays. Penetrating probes with optical stimulation and electrophysiological recording capabilities open a wide range of potential applications (Figure 2.5B,D)<sup>[12,90,120]</sup> since the light is delivered in close proximity to the target neurons. However, the invasive nature of penetrating probes can be a limitation, and lead to the development of surface LED arrays.

In the cochlear implant application, the spiral ganglion neurons (SGN) can be targeted by

## Chapter 2. Technologies for conformable surface neural stimulation

---

the light, provided that the LED array can be inserted in the complex shaped cochlea. A flexible device integrating a linear array of LEDs ( $50 \times 50 \mu\text{m}^2$  each) was then developed (Figure 2.5C)<sup>[59]</sup>. A fully implantable system with LEDs, and a stretchable wireless radio power and controls system, integrated into a PDMS substrate was developed and tested on the sciatic nerve and the spinal cord, showing the possibility to modulate the pain response of a mouse (Figure 2.5F)<sup>[151]</sup>. This option presents a soft device that can be used wirelessly, with however a relatively large thickness ( $700 \mu\text{m}$ ).

One of the challenges with surface stimulation is that the target neurons are often not in the first layer of the tissue. The optical power necessary to stimulate the target neurons is thus higher, due to the light dissipation through tissue (this will be described in the next section). In the cases where the optical power is not sufficient, it is thus necessary to penetrate through the first layers of tissue. To this purpose, an optrode array was developed with a waveguide under each LED (Figure 2.5E)<sup>[98]</sup>. This however reduces the chronic integration of the implant in the tissue, due to the stiff implanted waveguides. Another strategy to optimize the optical power extraction is to add a reflecting micromirror at the back of the device, and a focusing microlens in front of the LED, resulting in an increase of about 70% of excitable tissue<sup>[21]</sup>. A tradeoff must then be found between efficiency and invasiveness, depending on the specific application and the location and accessibility of the target neurons.

### Attenuation of optical power through neural tissue

In order to develop an efficient surface LED array, the delivered light must be sufficient to stimulate neurons at the required depth. The attenuation of optical power through tissue is due to absorption and scattering, both being dependent on the composition and structure of the tissue, as well as on the wavelength of stimulation. The wavelength of interest here is 460-470 nm, corresponding to the peak of wavelength sensitivity of the channelrodopsin used in the experiments presented in chapter 4 of this thesis. At this wavelength, tissue absorption is dominated by hemoglobin and melanin, but the overall power attenuation is largely dominated by scattering (Figure 2.6). Other versions of photosensitive opsins with different wavelength sensitivities can be used, and the attenuation of optical power through tissue can vary and has to be taken into account.

The optical transmittance of the tissue as a function of depth follows an exponential decay<sup>[4]</sup>. Scattering is highly influenced by the structure of the tissue, so it is important to consider the type of tissue targeted by the stimulation to obtain the parameters of the exponential decay. For instance, grey matter, consisting primarily of neuronal somata, and white matter, consisting primarily of axons, have very different scattering properties.

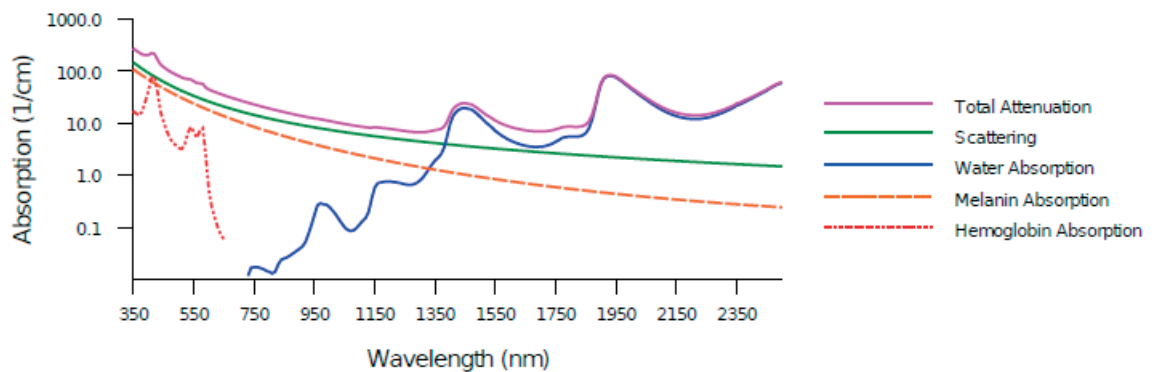


Figure 2.6: Tissue attenuation spectrum showing absorption and scattering properties of neural tissue components (from Abaya, 2012). Scattering is dominant in the wavelength of interest for optogenetics (460-470 nm).

Optical properties of mouse<sup>[4]</sup> and human<sup>[212]</sup> brain tissue of different types were estimated. Knowing the estimated power dissipation parameters of the target tissue and the depth of the target neurons, it seems then possible to estimate the power needed at the surface of the tissue. This is a good estimation for the activation of single neurons, but for behavioral responses the minimal volume of activation necessary to generate a measurable response depends on the application and has to be characterized experimentally. Despite the tools available to predict the necessary power for an optogenetic application, an experimental step is thus necessary for a reliable estimation of the threshold.

### Thermal dissipation of LEDs

When powered, LEDs generate significant thermal heating, which has to be taken into consideration when the device is located against the tissue. Indeed, a chronic increase in temperature of the tissue can induce profound physiological changes, even without leading to cell damage. Chronic thermal heating above 1°C has been shown to generate physiological differences in neuronal activity<sup>[51,119]</sup>. Official regulations for biomedical devices prevent chronic heating above 2°C (ISO 14708-1:2014). Thermal heating at the tissue surface thus has to be measured and controlled when using LEDs-based devices.

Measurements of thermal heating at the surface of a device is usually performed with a thermal camera. This technique is however not possible to measure temperature in the tissue. A finite element model (FEM) can be developed, approximating a solution to the heat equation<sup>[51,104,119,188]</sup>. Direct measurements with a thermocouple can also confirm the FEM results.<sup>[51,104]</sup>

The temperature in the tissue for a given device can be influenced by the power and the duty cycle, which is determined by the pulse duration and frequency. Changes on the device

## Chapter 2. Technologies for conformable surface neural stimulation

---

can be made to decrease the heating of the tissue. For instance, coating the device with a thermal insulator, like PDMS, or optimizing the light extraction of the LEDs can help having efficient stimulation at acceptable levels of thermal heating.

### 2.1.5 Goals of the project

- Design and fabricate conformal electrical surface stimulation implants based on thin polyimide technologies.
- Develop and characterize electropolymerized PEDOT:PSS coatings on the platinum electrode sites, in order to improve the electrode/tissue interface.
- Design, fabricate and characterize optical stimulation implants integrating an array of LEDs on a thin polyimide substrate.
- Develop a model for the characterization of the average increase in temperature at the surface of the tissue generated by the LEDs.

## 2.2 Electrical stimulation implant

### 2.2.1 Polyimide electrode array fabrication

The electrode arrays were fabricated using standard microfabrication processes<sup>[132,170]</sup> (Figure 2.7A). A sacrificial layer of Ti(25 nm)/Al(100 nm) was first deposited by evaporation on a silicon wafer. A first layer of polyimide (PI2611, HD Microsystems GmbH, Germany) was then spin-coated and cured (soft bake, 5 min at 120°C followed by hard bake for 2 hours at 300°C in a N<sub>2</sub> oven). The interconnects layer (Ti/Pt/Ti, 75/350/75 nm) was then sputtered after O<sub>2</sub> plasma surface activation and patterned by photolithography and ion beam etching (IBE). A second layer of PI was subsequently spin-coated and cured. In the cases where the polyimide was too thick to be directly patterned (>12 μm), a 500 nm SiO<sub>2</sub> layer was deposited and patterned to serve as an etch mask. Patterning of the SiO<sub>2</sub> film and the PI defined both the electrode active sites and the implant external shape. The oxide and polyimide films were etched by reactive ion etching (RIE). The electrode arrays were subsequently released from the wafer by anodic dissolution of the Al layer (1 V bias, in saturated NaCl solution)<sup>[132]</sup>.

### 2.2.2 PEDOT electropolymerization

PEDOT:PSS was electropolymerized from a solution of EDOT (3,4-ethylenedioxythiophene, 0.1%w/v) and PSS (polystyrene sulfonate, 0.2%w/v) (both purchased from Sigma Aldrich). Prior to electropolymerization, the electrodes were cleaned with an air plasma treatment at 100W for 30s. Electropolymerization was performed galvanostatically at 0.75 mA/cm<sup>2</sup> with a platinum counterelectrode and an Ag/AgCl reference electrode. PEDOT:PSS coatings were electropolymerized with different deposition charges (75-600 mC/cm<sup>2</sup>) by increasing the



## 2.2. Electrical stimulation implant

deposition time. After electropolymerization, the devices were rinsed in dH<sub>2</sub>O and air dried.

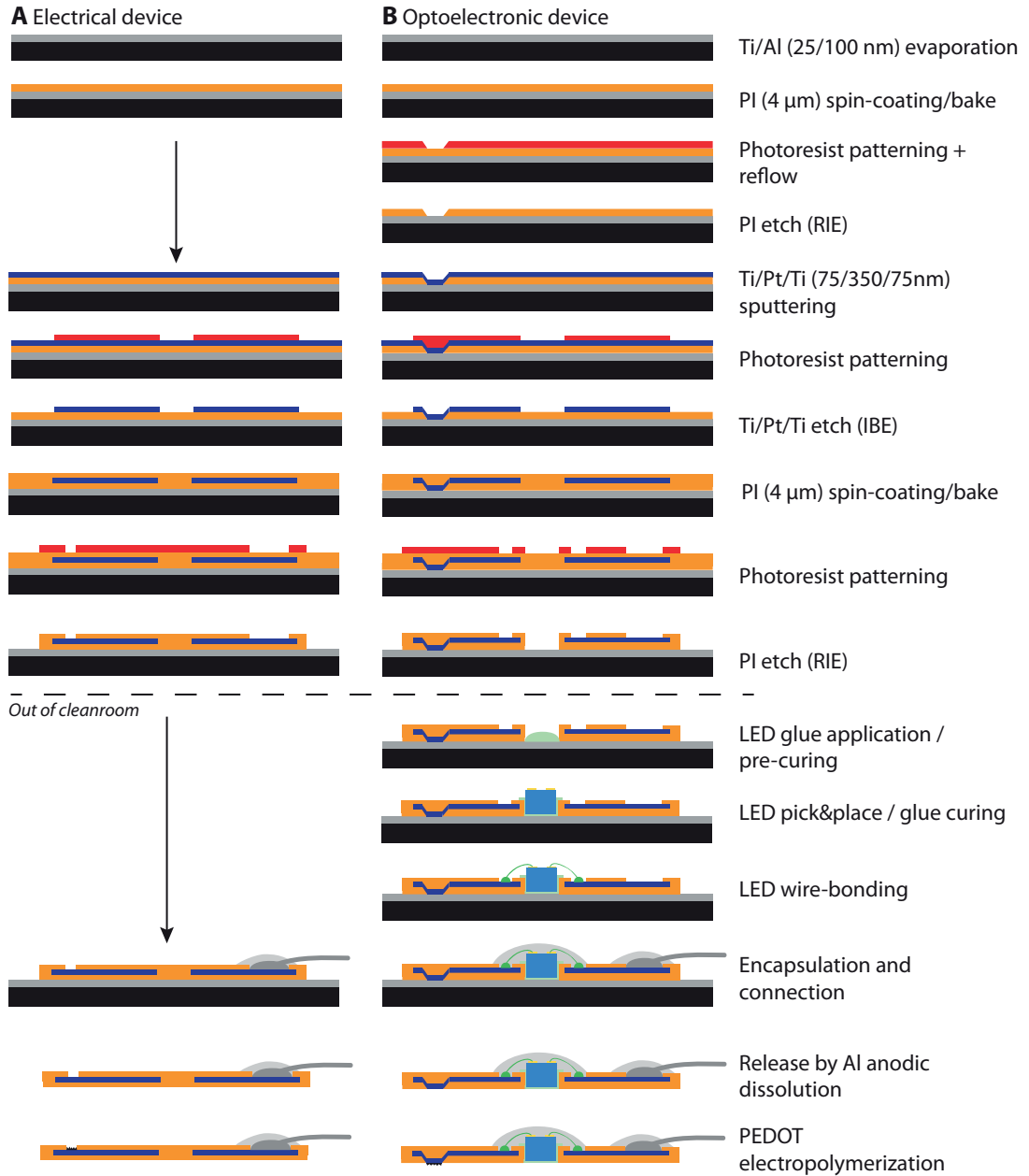


Figure 2.7: Process flows for the fabrication of the electrical and optoelectronic devices

For the first phase of experiments, PEDOT was electropolymerized on platinum embedded in thick (44  $\mu\text{m}$ ) polyimide. Deposition charges of 75, 150, 300, 450 and 600  $\text{mC}/\text{cm}^2$  were tested. The thickness of the coating, measured by mechanical profilometry, varied with the deposition charge, from 0.6  $\mu\text{m}$  at 75  $\text{mC}/\text{cm}^2$  to 3  $\mu\text{m}$  at 600  $\text{mC}/\text{cm}^2$  (Figure 2.8). For the in

## Chapter 2. Technologies for conformable surface neural stimulation

vivo experiments, a polyimide thickness of  $8\ \mu\text{m}$  was selected to optimize the conformability of the substrate. With this increased flexibility, thick coatings delaminated from the platinum when the polyimide substrate was free-standing. This is likely due to the increased stress in the film. A deposition charge of  $75\ \text{mC}/\text{cm}^2$  was then selected, as it did not delaminate from the substrate.

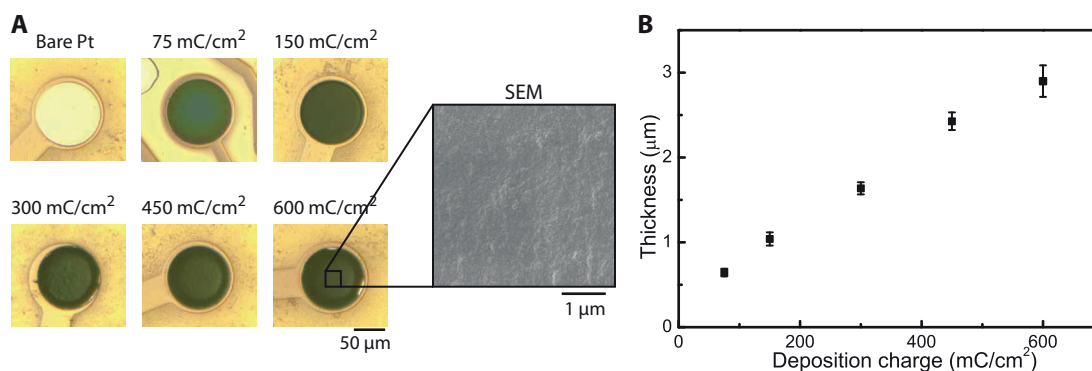


Figure 2.8: A) Optical imaging of PEDOT with various deposition charges, and SEM image showing the surface roughness of the PEDOT coating. B) Thickness of the PEDOT film at different deposition charges.

### 2.2.3 Electrochemical impedance spectroscopy

#### Methods

All electrochemical measurements were made in a 3-electrode setup with a potentiostat (Gamry Reference 600, Gamry Framework) with a large area platinum counterelectrode and an Ag/AgCl reference electrode. Measurements were performed at room temperature, in phosphate-buffered saline (PBS, pH:7.4). Complex impedances were measured by electrochemical impedance spectroscopy (EIS), with an AC voltage of 5 mV RMS and no DC bias, between 100 Hz and 1 MHz.

#### Results

PEDOT:PSS coating induced a decrease in impedance modulus at 1 kHz of more than one order of magnitude (from  $45.27 \pm 2.62\ \text{k}\Omega$  for Pt to  $2.6 \pm 0.66\ \text{k}\Omega$  for PEDOT:PSS of  $0.6\ \mu\text{m}$  thickness) (Figure 2.9A,B). Moreover, the phase of the impedance is close to zero over the entire range of measured frequencies, indicating a resistive behaviour associated with PEDOT:PSS charge-injection mechanism. The change of impedance between the different deposition conditions is not significant (one-way Anova,  $p > 0.05$ ), indicating a negligible effect of the PEDOT:PSS thickness on the impedance modulus and phase.

## 2.2. Electrical stimulation implant

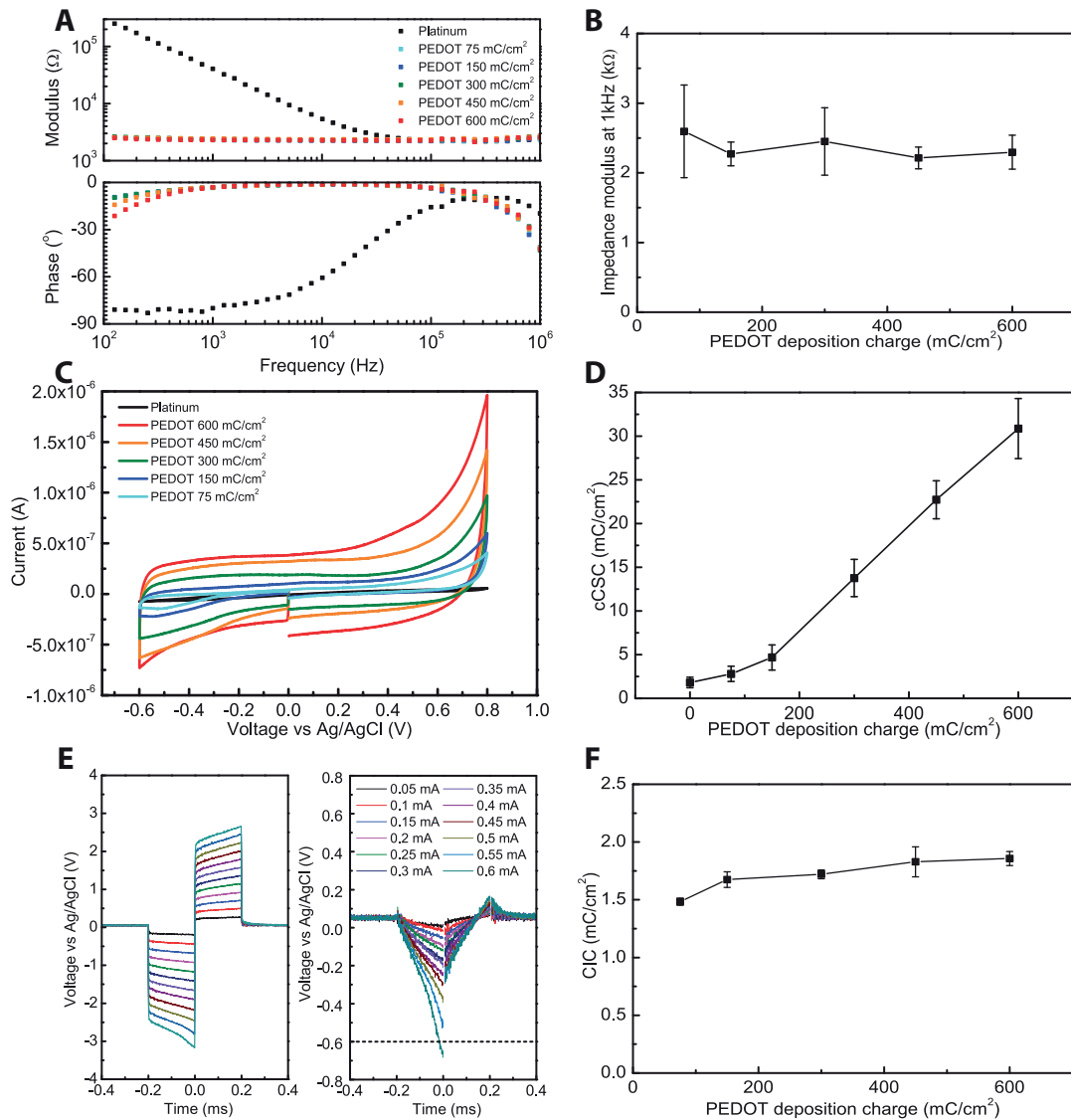


Figure 2.9: A) Electrochemical impedance spectra and B) impedance modulus at 1 kHz following PEDOT:PSS deposition with different deposition charges on 200  $\mu\text{m}$  diameter electrodes ( $N=5$ ). C) Cyclic voltammograms of 200  $\mu\text{m}$  diameter PEDOT:PSS coated electrodes and D) cOSC of PEDOT:PSS films prepared with increasing deposition charges ( $N=5$ ). E) Voltage transients measured during biphasic current pulses and recorded with increasing stimulation currents, before (left) and after (right) removal of the ohmic drop on 100  $\mu\text{m}$  diameter electrodes. F) Average CIC of PEDOT at different deposition charges ( $N=5$ ).

### 2.2.4 Cyclic Voltammetry / CSCc

#### Methods

Cyclic voltammetry was performed with the same 3-electrode setup as EIS, by cycling the potential between the limits of water electrolysis (typically -0.6 to 0.8 V) at a speed of 50 mV/s. Cathodic charge storage capacity (cCSC) was calculated by integration of the cathodic current over one cycle of CV.

#### Results

A non significant increase in cCSC between the platinum electrode and the thinnest coating is obtained (one-way Anova and post-hoc Tukey-Kramer test,  $p > 0.05$ ) (Figure 2.9C,D). Larger charge deposition generated a substantial and steady increase in cCSC (one-way Anova and post-hoc Tukey-Kramer test,  $p < 0.05$  for all conditions).

### 2.2.5 Pulse test / CIC

#### Methods

Charge injection capacity (CIC) is defined as the maximum charge that can be injected without the overpotential of the interface going beyond the limits of the water window. It was measured with the same 3-electrode setup as EIS, for a particular pulse waveform and frequency by increasing the current level step by step and measuring the voltage transients. This transient is composed for each phase of several components. The initial quasi-instantaneous drop is called the ohmic drop and is due to the resistance of the circuit and solution. It was defined as the drop in potential occurring during the first  $10\mu\text{s}$  of the pulse. The potential at the interface after subtraction of the ohmic drop, or overpotential, was used to measure CIC, the maximum charge for which the negative and positive potentials remain within the electrochemically safe window<sup>[43]</sup>.

#### Results

Figure 2.9E displays an example of charge injection capacity measurement with a biphasic cathodic-first pulse at 20 Hz and 0.2 ms/phase. The voltage transients following current pulses of increasing amplitudes (0.05 to 0.6 mA) before and after subtraction of the ohmic drop are plotted. Figure 2.9F shows the behavior of the CIC of PEDOT:PSS-coated electrode sites with different deposition charges for 100  $\mu\text{m}$  diameter electrode sites. A significant effect of the PEDOT:PSS deposition charge on CIC is obtained (one-way Anova,  $p < 0.05$ ). A Tukey-Kramer post-hoc test determined that only the 75  $\text{mC}/\text{cm}^2$  condition is significantly different from other conditions (450 and 600  $\text{mC}/\text{cm}^2$ ) ( $p < 0.05$ ).

### 2.2.6 Bending tests

#### Methods

One important feature of the polyimide array is its flexibility. The PEDOT:PSS coating of the electrode sites must therefore remain intact upon bending to a radius of curvature corresponding to the estimated minimal bending radius of the rat cochlear nucleus, about 1.65 mm in the auditory brainstem stimulation experiments presented in the second chapter of this thesis. This value was determined from the 3D reconstruction of a rat brainstem (Fig. 2.10A) [200].

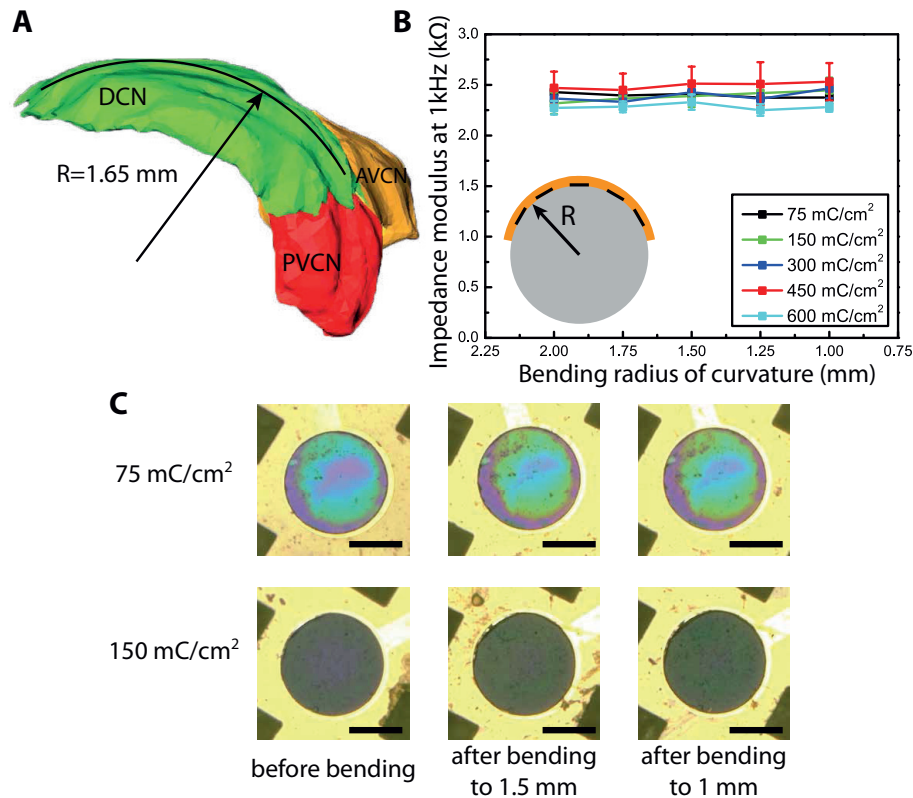


Figure 2.10: A) 3D reconstruction of a rat cochlear nucleus. The dorsal cochlear nucleus has an approximate radius of curvature of 1.65 mm [200]. DCN: dorsal cochlear nucleus, AVCN: anteroventral cochlear nucleus, PVCN: posteroventral cochlear nucleus. B) Impedance modulus at 1kHz of PEDOT:PSS coated electrodes (diameter = 200  $\mu$ m) after increasing compressive bending. C) Optical images of two electrode sites before bending, after bending to 1.5 mm radius and to 1 mm radius indicating the absence of cracks or delamination of the coating. Scale bars: 100  $\mu$ m

To perform bending tests, the PEDOT coated devices were bent around rods of radius of curvature ranging from 2, 1.75, 1.5, 1.25 down to 1 mm. The complex impedance spectrum of the electrodes was measured before the test and immediately after, and so on until the

smallest bending radius. The coatings were also inspected with an optical microscope to detect potential cracks or delamination.

### Results

Results of the bending tests show no significant change in impedance modulus at 1 kHz of the coated electrode sites, in all deposition charge conditions (One-way Anova,  $N=5$ ,  $p>0.05$ ) (Fig. 2.10B). Furthermore, no cracks nor delamination of the coating were observed during any tested bending conditions (Fig. 2.10C).

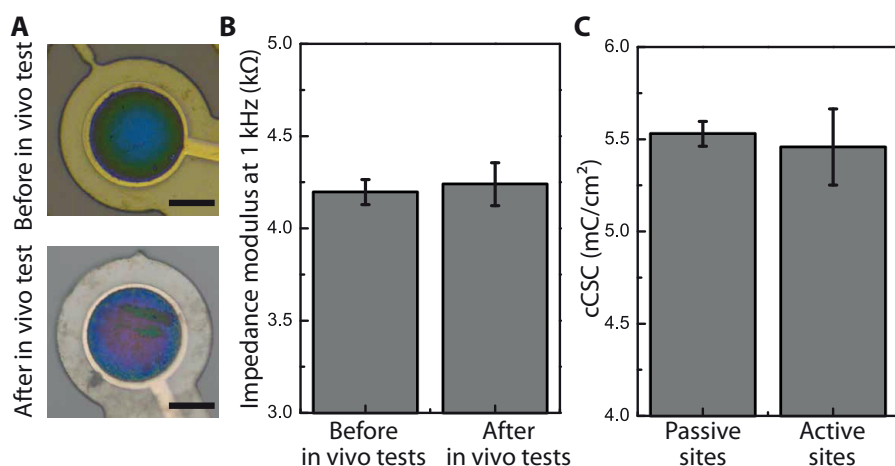


Figure 2.11: A) Optical images of PEDOT films on 100  $\mu\text{m}$  diameter electrode sites before and after in vivo tests. Scale bars: 50  $\mu\text{m}$ . B) Impedance modulus at 1 kHz before and after in vivo tests showing no significant difference ( $p>0.05$ ,  $N=19$ ). C) cCSC of passive and active sites after explantation, showing no significant difference in the electrochemical properties of the PEDOT:PSS film. ( $p>0.05$ ,  $N=7$  for passive sites,  $N=19$  for active sites)

### 2.2.7 Coating reliability

Electrode sites from 3 different arrays were analyzed after the acute in vivo tests (see chapter 2) to confirm integrity of the PEDOT:PSS coating. On the 20 explanted electrode sites, 19 appeared intact on the microscope while one PEDOT:PSS coating appeared delaminated and was not considered for further analysis. Electrochemical tests (EIS and CV) were subsequently performed on these 19 electrode sites. No significant change in impedance modulus at 1kHz was observed after the in vivo test compared to that of the pristine electrodes (One-way Anova,  $N=19$ ,  $p>0.05$ , Figure 2.11). Furthermore, cCSC after explantation of active (stimulated) sites and passive (non-stimulated) sites showed no significant change, indicating no loss in electroactivity of the coating due to stimulation (One-way Anova,  $N=7$  for passive sites and  $N=19$  for active sites,  $p>0.05$ ).

## 2.3 Optoelectronic implant

### 2.3.1 Fabrication

#### Clean room fabrication process

The microfabrication process to fabricate the optoelectronic array is different from the purely electrical array, to allow for openings on both sides (electrodes on one side, and contacts for the LEDs wire-bonding and connection pads on the other side) (Figure 2.7B). The electrical process is then modified by adding a patterning step of the first PI layer, to open electrodes on the backside of the device. A reflow of photoresist is used here to obtain angled PI walls of about 40°, thus guaranteeing a continuous metal film, despite the 4 μm PI step. The rest of the process is similar to the electrode array fabrication. A window is designed in the PI at the position of the LED, so that the light can shine through the device without power losses due to polyimide absorption (transmittance of 460 nm light through 10 μm thick PI film was measured to be only 60-70%).

#### LEDs integration and encapsulation

After the microfabrication steps, the LEDs (Cree CxxxTR2227-Sxx00) are integrated. First, some glue (Epotek 302-3M) is dispensed on the windows in the PI with a pick-and-place machine. The glue is then pre-cured for 15 minutes at 65°C. The LEDs are pick-and-placed in the windows, and the curing is completed for 3 hrs at 65°C. The LEDs are then wire-bonded. An adhesion promoter is applied (Epotek AP-100), followed by an encapsulation (Epotek 353ND) to mechanically protect the wires. In order to guarantee a good electrical insulation, the devices are then dip-coated with PDMS (Sylgard 184, 1:10) mixed with heptane (25 wt%) to decrease its viscosity. After 10 min at room temperature to let the heptane evaporate, the PDMS was cured for 2 hrs at 80°C

### 2.3.2 Electrical characterization

An electrical characterization of the LEDs integrated in the polyimide device was performed (Figure 2.12). Current was varied between 0 and 20 mA and voltage was measured, for a single LED and two LEDs in series. The device used for this characterization is presented in chapter 3 of this thesis. For the characterization of a single LED, the switch on voltage is about 2.7 V, as specified in the LED datasheet.

### 2.3.3 Optical power characterization

#### Methods

The optical power generated by the devices at a wavelength of 460 nm was measured with an optical power sensor (Thorlabs S170C). In order to measure the intensity of pulses, the console was connected to an oscilloscope where the power of the pulses over time was obtained. Because of the relatively slow response of the power sensor, the power of short pulses (below 20 ms) was obtained by fitting an exponential curve and using the asymptote of this curve as the maximal power. This approach was confirmed by comparing the measurements of short pulses with exponential fit to the ones of long pulses.

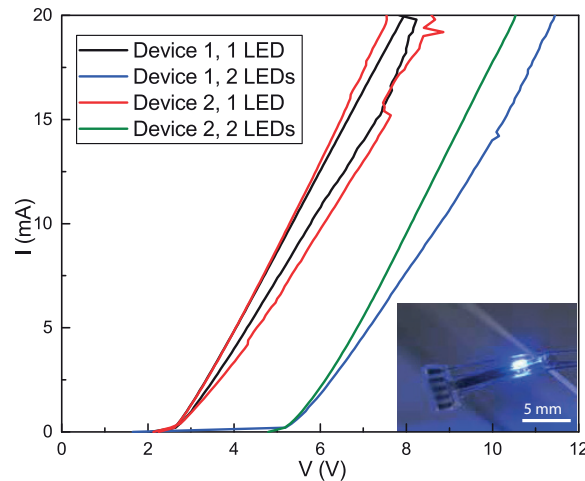


Figure 2.12: I/V curves for two different devices, with one LED or two LEDs in series. Inset: device for optical stimulation of the spinal cord (see chapter 4) with activation of 2 LEDs in series at 5 mA.

#### Results

The optical power at different current levels, for several different LEDs is shown on figure 2.13. The power in a pulsed regime was measured, with typical pulses of 5-20 ms. Measurements recorded with such short pulses show an exponentially growing curve that does not reach saturation. Assuming perfectly squared current pulses, an exponential fit is performed on the response of the power sensor, with the equation  $y = a \cdot (1 - e^{-b \cdot (x-c)})$ , with  $a$ ,  $b$  and  $c$  the fitted parameters. The asymptote of this fit is used as the power value. To confirm this strategy, measurements with identical power of pulses of 20, 50 and 80 ms were performed. When the pulses are long enough (50 or 80 ms), the reached plateau corresponds almost exactly to the exponential fit of shorter pulses, thus validating the exponential fit method.



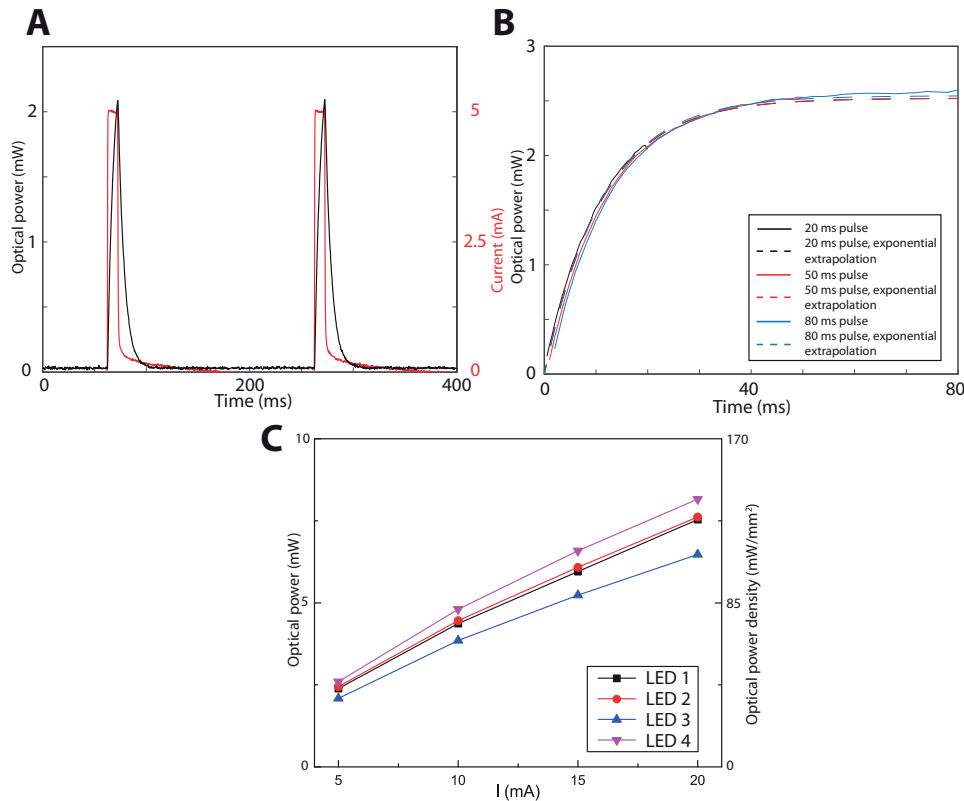


Figure 2.13: A) Response of the optical power sensor (black) following 20 ms, 5 mA square current pulses at 2.5 Hz (red). B) Response of the optical power sensor to a 20, 50 and 80 ms pulse, with exponential fit used to estimate pulse peak power. C) Peak power (in mW) and peak power density (in  $\text{mW}/\text{mm}^2$ ) of 20 ms pulses of four individual LEDs, at increasing current levels.

### 2.3.4 Thermal dissipation model

#### Methods

Temperature change at the surface of the device was measured with a thermal camera (FLIR A325sc), before PDMS encapsulation. The thermal camera is sensitive to wavelengths 7.5 - 13  $\mu\text{m}$ . The PDMS being partly transparent to these wavelengths<sup>[26]</sup>, the measurements at the surface of the PDMS were not reliable. A bio-heat transfer model was performed with Comsol (COMSOL Multiphysics 4.3a) to estimate the temperature at the surface of the tissue when implanted (at body temperature,  $37^\circ\text{C}$ ) from the thermal camera measurements at the surface of the device (before PDMS encapsulation). A steady-state model was chosen, although the measured temperature at the surface of the LED is time-dependent. The assumption was made that the PDMS encapsulation of the device dampens the variations of temperature on a small timescale. Moreover, the parameter that has to be controlled to avoid physiological changes in the neuronal activity due to chronic heating of the tissue is the average increase in

## Chapter 2. Technologies for conformable surface neural stimulation

---

temperature.

A first model was developed to estimate the thermal power generated by the LED that leads to the temperature increase measured by the thermal camera at the surface of the device, at room temperature and in the presence of convective cooling at the surfaces in contact with air. An axisymmetric model was used, and a circular LED of same area than the rectangular LED used was defined, with  $50\mu\text{m}$  thickness. Since the LED is fabricated on SiC substrate, the LED was approximated as a volume with SiC thermal properties. The glue was defined as a  $2\mu\text{m}$  thick layer below the LED, and the encapsulation epoxy as a  $50\mu\text{m}$  thick layer on the back and on the sides of the LED. The back of the devices was placed against a glass slide during thermal camera measurements, so this glass slide was added to the model. The materials used were SiC 6H for the LED, Silica glass for the glass slide, and the glue and encapsulation were estimated with standard non thermally conductive epoxy thermal properties (Table 2.1). The boundary conditions were 1. Room temperature ( $20^\circ\text{C}$ ) on the back and on the sides of the glass slide. 2. Convective cooling at all surfaces in contact with air (surface of the glue, sides of the encapsulation). The heat source was modeled as a surface with defined power at the top surface of the LED (p/n junction). The temperature in the model was estimated at a point on the axis of symmetry, at the surface of the glue below the LED. A parametric sweep of the LED power was performed, from 0.1 to 12 mW, with steps of 0.1 mW. The equation solved by the model is the equation for stationary heat transfer in solids:  $\rho c \nabla T = \nabla(k \nabla T) + Q$ , with  $\rho$ : density,  $c$ : specific heat capacity,  $k$ : thermal conductivity and  $Q$ : LED heat source. The LED power corresponding to each measured temperature could then be estimated.

Material	$k$ [ $\text{Wm}^{-1}\text{K}^{-1}$ ]	$c$ [ $\text{Jkg}^{-1}\text{K}^{-1}$ ]	$\rho$ [ $\text{kgm}^{-3}$ ]
SiC 6H	370	690	3211
Silica glass	1.38	703	2203
Epoxy	0.2	1000	1030
Tissue <sup>[51]</sup>	0.5	3650	1050

Table 2.1: Properties for the different materials used in the thermal dissipation model

A second model was then designed to simulate in vivo conditions, with the device previously encapsulated in PDMS. The PDMS layer was measured to be about  $60\mu\text{m}$  thick, so  $30\mu\text{m}$  on each side. A  $30\mu\text{m}$  thick PDMS layer was then added on each side of the device. The glass slide was removed, and instead a large volume of tissue was defined around the device. Its dimensions are large enough to remove potential boundary effects on temperature. The boundary condition is body temperature at the borders of the tissue. A parametric sweep of the LED power was again defined, from 0.1 mW to 12 mW with steps of 0.1 mW. The temperature of the model was this time probed at the surface of the tissue, below the  $30\mu\text{m}$  PDMS encapsulation layer, on the axis of symmetry of the model. Increases in temperature were thus obtained for each LED power, and linked to the original measurements of the temperature change at the surface of the device made with the thermal camera.

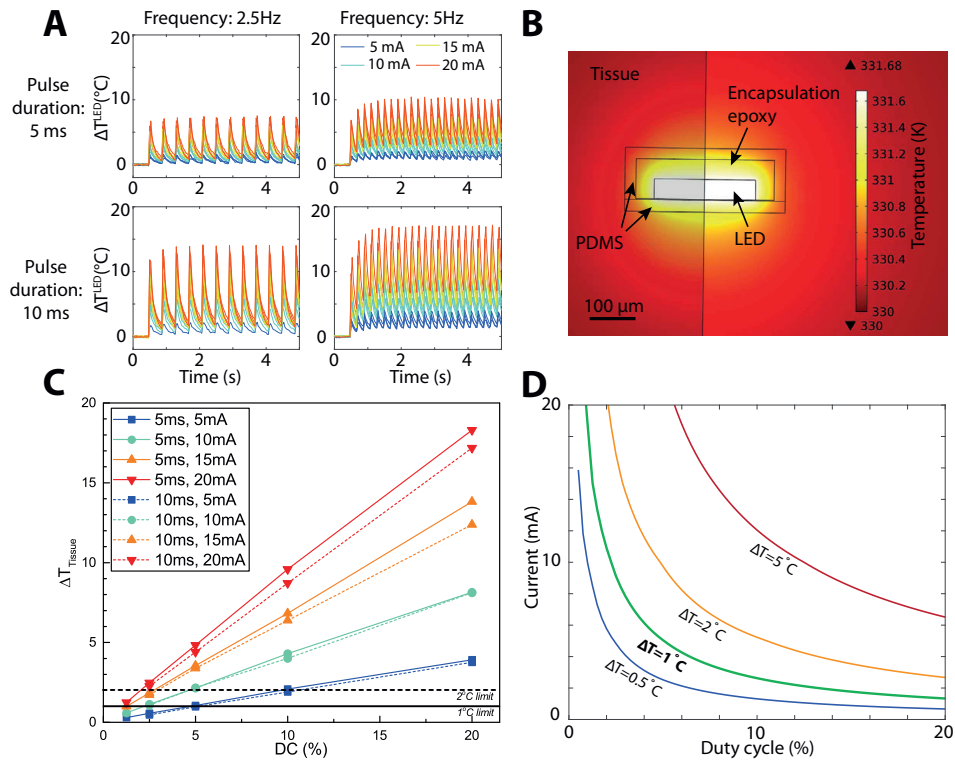


Figure 2.14: A) Thermal camera measurements at the surface of the device (before PDMS encapsulation) at different frequencies, pulse durations and current levels. B) Thermal dissipation model used to estimate the increase in temperature at the surface of the tissue. Result with a LED thermal power of 0.78 mW, corresponding to a maximal heating of the tissue of 1°C. C) Increase in temperature at the surface of the tissue mainly depends on the duty cycle and the current in the LED. D) Parameter space generating an average increase of temperature in the tissue lower than 0.5°C (blue line), 1°C (green line), 2°C (orange line) or 5°C (red line)

## Results

The thermal camera measurements of increases of temperature are shown on Figure 2.14A. They show a time-dependent pattern, with variations depending on the current, pulse duration and pulse frequency. An average increase of temperature in the first pulses was measured, followed by a stabilization. Mesh convergence analysis showed convergence of the solution for both models. The complete mesh consisted of 14661 elements for the first model, and of 6022 elements for the second model. Figure 2.14B shows an image of the thermal dissipation model with temperatures in K at each point of the model, in the condition with LED power of 0.78 mW, the power leading to a 1°C increase at the surface of the tissue. The temperature at the surface of the tissue mainly depends on the duty cycle (DC) and the LED power, with small variations due to the pulse width, as shown in figure 2.14C. Figure 2.14D shows the parameters leading to a temperature increase in the tissue lower than 1°C, defining a safe

range of parameters for chronic stimulation.

## 2.4 Discussion

### 2.4.1 Electrical implant

The fabrication process for a flexible implant based on platinum tracks embedded in polyimide shows good stability and reliability. Furthermore, the resulting device is implantable, and a large freedom in design is possible, thanks to the small feature size achievable by the photolithography process. The tunable thickness of polyimide leads to devices with various flexibility levels, thus adaptable to different applications. If the application requires implantation into tissue without buckling, the substrate will be thicker. On the contrary, if the application requires bending around a structure, especially on soft tissue like neural tissue, the chosen thickness will be smaller. A mesh-like structure can even be used to further increase conformability of the device<sup>[88]</sup>. In a situation where the array needs to be pushed in the tissue (like in penetrating microelectrode arrays), a strategy can be envisioned where the probe is temporarily stiffened by a bioresorbable film.

Results of the tests with the conducting polymer PEDOT:PSS electropolymerized on a platinum substrate showed a large decrease of impedance and increase in CIC. This enables safe and efficient stimulation with small electrode sites, allowing for a study of electrical stimulation with high spatial selectivity, with small diameters and high density of electrode sites. The low thickness ( $\mu\text{m}$ ) and resulting high flexibility of the substrate create a mechanically challenging environment for the PEDOT:PSS coating. A  $75 \text{ mC}/\text{cm}^2$  deposition charge was selected, and proved to have electrical properties, as well as size, thickness and bendability suitable for surface neural stimulation.

In these experiments, the charge injection capacity was calculated according to the standard water window limits (-0.6 to 0.8 V), which is a simplification of the real electrochemical window limits. They are often considered to be between -0.6 and 0.8 V for platinum and -0.6 to 0.8 V or -0.9 to 0.5 V for PEDOT:PSS<sup>[43,61]</sup>. Moreover, these limits highly depend on the conditions such as the temperature, the electrolyte composition and pH and the counterelectrode material. In order to measure them on a case-by case basis, CV cycles can be performed with very wide voltage limits. The negative voltage where the current drops and the positive voltage where the current quickly rises reflect water electrolysis and are the true limits of the water window. However, water window limits determined *in vitro* for this application will still be different from *in vivo* limits. The choice was then made to measure all electrochemical properties with respect to the -0.6 to 0.8 V limits. These values are quite conservative and widely used in the literature.

The electrochemical limit is not the only safety limit to consider for chronic stimulation. There is another limit of charge density above which the chronic overstimulation of neurons

induces neuronal damage, first described by McCreery and coworkers<sup>[122,134]</sup>. This limit can be calculated with the formula  $\log\left(\frac{Q}{A}\right) = k - \log(Q)$ , with  $Q$ : charge per phase,  $A$ : electrode geometrical area and  $k$ : a factor varying between 1.5 and 2 depending on the experimental conditions<sup>[185]</sup>. With 100  $\mu\text{m}$  diameter electrodes and a standard charge-balanced biphasic symmetric pulse waveform with 0.2 ms/phase and using a conservative value of  $k = 1.5$ , this limit corresponds to a current level of about 0.25 mA. This current might not be sufficient to generate efficient stimulation in some applications. In those cases, developing a chronic stimulation device would then require the use of larger stimulation sites.

Another issue for developing a chronic device is the stability of the coating. Electrochemical properties of PEDOT:PSS coatings electrodeposited on smooth platinum surface have been shown to degrade over time<sup>[61]</sup>. Because of the electrochemical safety of stimulation and the limited chronic stability of PEDOT:PSS electropolymerized on smooth platinum substrate, the presented array may not be adapted for use in a chronic neural stimulation model. However, for short-term experiments, like the one presented in chapter 3 of this thesis, the properties of this stimulation array are ideal. This is confirmed by the coating reliability studies, showing that most electrode site properties remain unchanged after acute implantation in a rat, with 28 Hz stimulation for several hours at current levels up to 2 mA.

Several modifications of the PEDOT:PSS coating resulting in improved chronic stability are being investigated. One potential solution is to roughen the underlying platinum metal with a laser prior to deposition, which has been shown to reduce delaminations<sup>[61]</sup>. However, laser roughening of the metal surface is challenging on thin films because of the low thickness (about 400 nm) of the metal layer. Other solutions include the use of other doping agents for the PEDOT. Particularly, pTS (para-toluene sulfonate) has been shown to improve chronic electrochemical stability of the coating under stimulation conditions<sup>[61]</sup>. Composites of conducting polymers with other polymers<sup>[85]</sup> or carbon nanotubes (CNT)<sup>[10,115]</sup> are also investigated as a means to improve chronic stability of the coatings. Stabilizing the structure might be an efficient way to increase the electrochemical stability of conducting polymers, as the main hypotheses of failure mechanisms are the stress in the film or volume changes due to ion transport<sup>[10]</sup>.

### 2.4.2 Optoelectronic implant

The fabrication process for the optoelectronic implant leads to devices with stable performance. Functional validation is demonstrated in chapter 4 of this thesis. The developed device is fabricated with a thin polyimide (8  $\mu\text{m}$ ) polyimide substrate encapsulated in a PDMS layer estimated to 60  $\mu\text{m}$ , except at the locations of the LEDs. At these locations, the thickness is much more important, with the 50  $\mu\text{m}$  of the LED, and the space of the wires for the wire-bonding, plus the epoxy encapsulation for mechanical protection of the wires. The total thickness is estimated to about 150  $\mu\text{m}$ . Adding a PDMS layer further increases this thickness

## Chapter 2. Technologies for conformable surface neural stimulation

---

to about  $200\mu\text{m}$ , but as a counterpart decreases the stiffness of the surface felt by the tissue. It also avoids having to add more epoxy encapsulation layers that would guarantee the electrical insulation but would make the device much thicker. However, the large total thickness of the device at the LED locations might generate some damage to the tissue, a point that will be investigated during functional validation of the device.

Limitations on the density of LEDs are intrinsic to the fabrication process. Due to the integration process of the LEDs with wire-bonding, two pads need to be designed next to each LED, leading to a limitation in the density of LEDs. Using an alternative technique than wire-bonding to connect the LEDs, like eutectic bonding, would allow a greater maximal density of LEDs, as it does not require the wire-bonding pads that increase the necessary footprint of each LED. However, increasing the spatial selectivity is also linked to the size of the light beam. That will thus be associated to a decrease of the size of the LEDs. One possible solution for this would be to combine growth of the LEDs and device fabrication on the same wafer, in order to avoid manual manipulation of LEDs<sup>[59]</sup>. A focusing of the light would also be necessary here, as the light emitted by these LEDs is not directional, and the lateral stimulation generates an overlap of the light of closely spaced pairs of LEDs. Better focusing of the light can for example be achieved by adding a lens in front of the LED<sup>[21]</sup>. This technique however has the disadvantage of increasing the thickness of the device with a  $100\mu\text{m}$  thick SU8 polymer lens.

The presented process has a single metallic layer, which means that there can be no overlap between the pad and tracks of the LEDs and the electrodes, even if the openings for the electrodes are on the backside. Optical and electrical stimulation can thus not exactly be at the same place. However, a bimodal implant with optical and electrical contacts interfacing with the exact same area can be used to have a local measurement of the optically-generated activity<sup>[98]</sup> or to directly compare electrical and optical stimulation. Such devices require multiple active layers, with at least one layer for the electrodes and one layer for the LEDs, generating more complexity in the fabrication process. Since the LEDs and electrode sites are at the same locations, the electrodes layer as well as the substrate must be transparent, in order to limit the optical power losses. Simultaneous stimulation and measurements are possible in that case, despite the presence of a light-induced artefact on the recording electrodes, the photoelectric effect<sup>[93]</sup>.

The power generated by these devices is more limited than with laser fibers, but is well above the ChR2 activation threshold. At 20 mA, the power generated by a single LED is about 7.5 mW. Considering the area of illumination of the LED,  $190 \times 230\mu\text{m}^2$ , it corresponds to a power density of about  $64\text{ mW}/\text{mm}^2$ . At the cellular level, activation of the ChR2 protein occurs at about  $1\text{ mW}/\text{mm}^2$ . In between these two values, there are other elements to consider, including power losses due to diffraction of the light in the layer of glue or of PDMS and scattering in the tissue, which depends on its optical properties and the depth of the target neurons. Additionally, the stimulation threshold also depends on the ChR2 expression level, and the minimal amount of activated neurons that are necessary to generate the desired

functionality. All the power generated by the LED is also not directional and focused, which decreases the actual power density at a certain location in the tissue. Functional validation is thus necessary to characterize the activation threshold, and assess the possible use of this LED array in each considered application.

Another critical element to consider is the safety for the tissue, especially with respect to temperature changes generated by the LEDs. This depends mainly, as shown in this chapter, on the current level and the duty cycle. The limitations in the parameters to guarantee efficiency of the device are first the pulse width, since it cannot be lower than the activation time constant of the ChR2 (2-3 ms)<sup>[108]</sup>. Then, the current must be higher than threshold (although the threshold can also depend on the pulse width and frequency of stimulation). Limiting the frequency is thus important, in order not to exceed a certain duty cycle, as shown in the thermal heating model.

There are several potential sources of imprecision in the presented model of thermal heating. The first one is the fact that a stationary model was used, instead of a time-dependent model. This choice was made because the main interest here is to limit the average increase of temperature in the tissue. However, since pulsed current is used to power the LEDs, peaks of temperature that are higher than the mentioned values can be reached. Other imprecisions in the model could be due to differences in materials properties or layers thicknesses. For instance, a total PDMS thickness of 60  $\mu\text{m}$  was used, but this does not take into account the potential variations from device to device. This study also assumes a homogeneous tissue, and does not consider the blood flow. However, blood flow was shown to act as a heat sink and to reduce the heating of the tissue in a similar thermal simulation study<sup>[51]</sup>. All these sources of imprecision of the model could modify the results. This is why the threshold of 1°C was chosen as the limit, compared to the official limits of 2°C for chronic heating of biomedical devices. This conservative limit should guarantee that, even considering the imprecisions of the model, the 2°C limit of chronic tissue heating is not reached.

Optogenetics, as mentioned earlier, can potentially be used with several independent wavelengths simultaneously, with for instance the activation and inhibition of two neuronal populations present in the same tissue and transfected with opsins of different wavelength sensitivities. With LEDs, it could be through the integration of LEDs of different colors on the same array. However, two LEDs wouldn't stimulate exactly the same area. Technologies for multicolor optoelectrodes based on injection laser diodes are being developed and can allow multicolor stimulation of the same location<sup>[83]</sup>.

Finally, developing fully implantable devices is also a very important step to achieve chronic optogenetic studies with freely moving animals. It is a challenging problem, especially with implantable active electronics, requiring more energy than passive devices. Fully implantable RF-powered systems have been developed and were shown to be suitable to use in optogenetics<sup>[138,152]</sup>. Particularly, a soft stretchable antenna for RF power harvesting was shown<sup>[152]</sup>.

## **Chapter 2. Technologies for conformable surface neural stimulation**

---

Further development of these techniques will thus enable the powering of several LEDs simultaneously, necessary for the spatiotemporal control of stimulation.

In order to achieve higher power and to limit thermal heating, the development of fully implantable laser sources might also be envisioned. This could be based on VECSELs (vertical-external-cavity surface-emitting lasers), a type of lasers allowing a great control on emission wavelength, a high power and efficiency and a compact size (down to a 1.5 cm footprint cavity)<sup>[97,218]</sup>. However, these lasers are designed for high power applications (in the order of W), and implantable versions with low power consumption are still to be developed.

### **Contributions**

The work on PEDOT:PSS coatings was built upon two students semester projects performed in our lab by D.Watson and N.Vachicouras. Optimization of part of the clean room process for the optoelectronic implant was performed by P.Joris.



# 3 New Generation Auditory Brainstem Implant (ABI)

## Abstract

The auditory brainstem implant (ABI) is a neuroprosthesis that provides sound sensations to patients who cannot benefit from a cochlear implant (CI) because of a disconnection between the peripheral and central auditory systems due to tumours, cochlea or cochlear nerve aplasia or traumas. The ABI stimulation array is placed at the surface of the cochlear nucleus (CN), the first auditory processing nucleus in the central auditory system. The ABI provides useful hearing sensations to most patients, with however much poorer outcomes than in CIs, and particularly low spectral resolution in most cases. In this chapter, we explore the different hypotheses for the limited performance of ABIs, including the lack of spatial selectivity of stimulation and the low understanding of the neural targets of the ABIs and their neurophysiological properties. Using the flexible surface implant technology with increased electrode density presented in Chapter 2 of this thesis, the effect of higher spatial selectivity of stimulation of the brainstem in a rat model are investigated.

Results show that CN electrical stimulation with the microfabricated electrode array generates multiunit activity recorded from the inferior colliculus (IC), as well as auditory brainstem responses (ABRs). The pattern of IC recordings initially shows a high variability, but upon further analysis, different components of the response showing tonotopic cues are isolated. Bipolar stimulation with small interelectrode distances provides better tonotopic cues that with large interelectrode distance. Additionally, the waveform of stimulation is shown to have an important effect on activation thresholds and response properties. Analysis of timing of responses and effect of stimulation current lead to hypotheses about the neuronal populations contributing to the different components of the response. Finally, possible modifications of the ABI array and stimulation protocol are proposed to optimize the spectral cues and hopefully result in improvement of hearing outcomes for ABI patients.

**Publication:** Guex, A., Hight, A.E., Narasimhan S., Vachicouras N., Lee, D.J., Brown, M.C., Lacour, S.P., Auditory brainstem stimulation with a conformable microfabricated array elicits responses with tonotopically organized components, *submitted*

### 3.1 Introduction

#### 3.1.1 Auditory brainstem implants

##### The auditory system

The auditory system is composed of several structures sequentially stimulated when activated by an auditory stimulus. First, the peripheral auditory system (Figure 3.1A) transduces the sound from a pressure wave in the external and middle ear to fluid motion in the cochlea. This motion then induces movement of the ciliae of the inner hair cells, generating a depolarization that propagates to the spiral ganglion neurons, which give rise the VIII<sup>th</sup> cranial nerve, the vestibulocochlear nerve. In the cochlea, a decomposition of the sound into different frequencies occurs, and high frequencies generate activation of the basal inner hair cells, while low frequencies generate activation of the apical inner hair cells. This correspondence between sound frequency ('tono') and location of activity ('topo') is called tonotopy, and is conserved throughout the auditory system<sup>[42,176]</sup>.

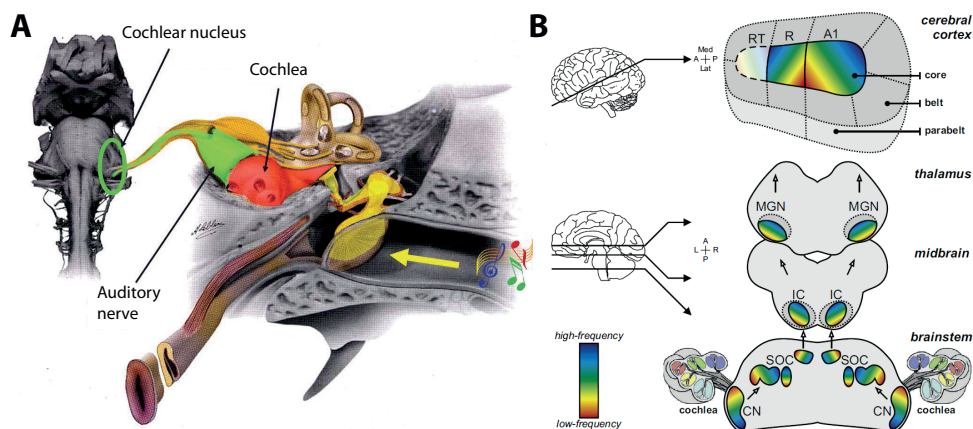


Figure 3.1: A) Schematic of the peripheral auditory system<sup>[94]</sup>; B) Schematic of the central auditory system showing the main auditory nuclei and their tonotopic organisation<sup>[176]</sup>.

The vestibulocochlear nerve enters the central nervous system at the level of the cochlear nucleus (CN), at the surface of the brainstem, which is the first relay station for all ascending auditory information. The cochlear nucleus is organized in different subunits, the dorsal, anteroventral and posteroventral cochlear nucleus (DCN, AVCN and PVCN), each with different structures, functions, organizations and types of neurons.<sup>[187]</sup> When entering the cochlear nucleus, the auditory nerve fiber shows a branching pattern with fibers projecting to the three subunits.<sup>[121]</sup> A parallel processing then occurs, and each of these subunits has its own tonotopic organization, that is conserved from the vestibulocochlear nerve through the branching pattern, as shown in figure 3.1B<sup>[42,121,201]</sup>. Thus, a tonotopic organization is present in the DCN, AVCN and PVCN. In the DCN, this tonotopy is present with lower to higher frequencies

being represented in the ventrolateral to dorsomedial axis<sup>[42,121,174]</sup>. The projections from different cell populations in the dorsal and ventral CN give rise to several parallel auditory pathways (Figure 3.2). They project to higher auditory structures, including the contralateral cochlear nucleus, the superior olive, the lateral lemniscus and the inferior colliculus on the ipsilateral or contralateral sides. Third order neurons then project to the thalamus and to the primary auditory cortex.<sup>[29,84,158]</sup>

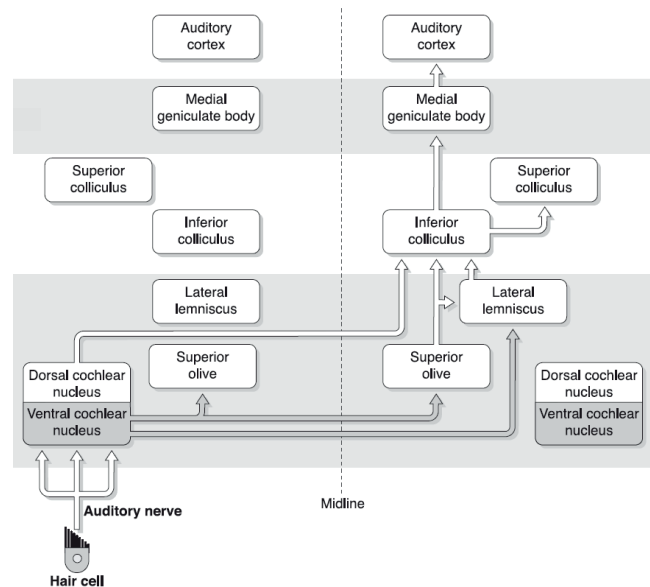


Figure 3.2: Schematic of the main ascending central auditory pathways<sup>[66]</sup>

### Deafness and auditory implants

Different types of hearing loss result from the dysfunction of various structures of the auditory system. Conduction hearing loss is defined as hearing loss due to a defect in the external or middle ear affecting sound conduction to the cochlea. External hearing aids, middle ear implants or BAHA (bone-anchored hearing aids) can be used to restore function of the middle ear and transmission of the sound vibrations to the cochlea.

Hearing loss due to a defect in the sensory cells or in the nerve cells is called sensorineural hearing loss. The most common solution for the patients suffering from profound sensorineural hearing loss is the cochlear implant, a neuroprosthetic device consisting of multiple electrical stimulation sites along a single shank inserted along the tonotopic axis of the cochlea. It electrically stimulates the spiral ganglion neurons, thus bypassing the inner hair cells. The cochlear implant is the most successful neuroprosthetic device currently available on the market. To this day, more than 300'000 children and adults worldwide suffering from profound sensorineural hearing loss, mostly due to damage to the hair cells, have benefited from this technology<sup>[183]</sup>.

### Chapter 3. New Generation Auditory Brainstem Implant (ABI)

Despite the outstanding outcomes associated with the cochlear implant, some patients having a disconnection between the peripheral and central auditory systems cannot benefit from it. These patients most commonly suffer from Neurofibromatosis type 2 (NF2), an autosomal dominant condition occurring in 1 in 40'000 births and characterized by the bilateral growth of tumors along the vestibulocochlear nerve. [45] Removal or growth of these tumors causes the destruction of the auditory nerve. Other conditions include cochlear aplasia, cochlear nerve agenesis or VIII<sup>th</sup> nerve sectioning due to traumas. These patients can be implanted with an auditory brainstem implant (ABI), a type of auditory implant that bypasses the auditory nerve and directly stimulate the cochlear nucleus (CN) [133].

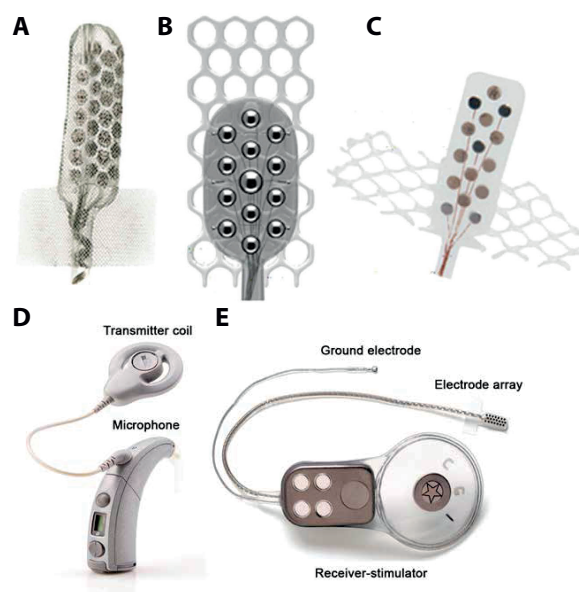


Figure 3.3: A-C) Photographs of the three main clinical ABI arrays, from Cochlear (A), Med-El (B) and Oticon Medical (C); D) External and E) implanted parts of the Cochlear ABI device(modified from [201]).

The first auditory brainstem implant was developed at the House Ear Institute in Los Angeles, in the late 1970s and consisted of a pair of ball electrodes [201]. Since then, the number of electrodes was progressively increased and integrated into an array of about 3-by-8 mm<sup>2</sup>, roughly corresponding to the available surface of the CN [45]. Figure 3.3 shows pictures of the ABI arrays currently used in the clinics by the three main ABI companies, Cochlear (A), Med-El (B) and Oticon Medical (C). Worldwide, more than 1500 people have already benefited from this technology [121,181]. In the US, the ABI is currently clinically approved only for adults with NF2, because the device can be implanted in the same surgery as the tumor resection, generating minimal additional surgical risk [180]. In Europe, the ABI is also approved for non-tumor patients [46], as well as for congenitally deaf children for whom the CI is not an option [183]. A clinical trial for pediatric ABIs is ongoing in the US [144,157].

### The ABI : implantation and outcomes

Contemporary ABI devices are very similar to CIs except for the electrode array, and consist of an externally worn microphone and processor (Figure 3.3D), and an internal receiver and stimulator connected to the ABI electrode array (Figure 3.3E). The array is placed on the CN surface<sup>[201]</sup>, located at the dorsolateral surface of the brainstem, at the junction between the medulla and the pons (Figure 3.4A). During surgery, the electrode array is inserted into the lateral recess of the fourth ventricle and placed over the surface of the CN.<sup>[45]</sup> This structure is not directly accessible and the approach is blind, as illustrated in figure 3.4B. Due to the complex shape of the cochlear nucleus complex and the anatomical locations of the different CN subunits, the structures targeted by the ABI are the DCN and part of the PVCN, the rest of the CN complex being located too deep into the brainstem and thus being unreachable by a surface implant.<sup>[167,201]</sup> The DCN seems to be the primary target because the depth of the PVCN may vary and the DCN is larger<sup>[201]</sup>.

6 to 8 weeks after implantation, the implant is turned on. Several programming steps are necessary here. First, electrode sites that generate useful auditory stimulation with no side effects are selected. Then, for each of these electrodes, the threshold (T) and comfort (C) current levels are determined and the electrodes are pitch ranked at C level and the device is programmed<sup>[113,201]</sup>.

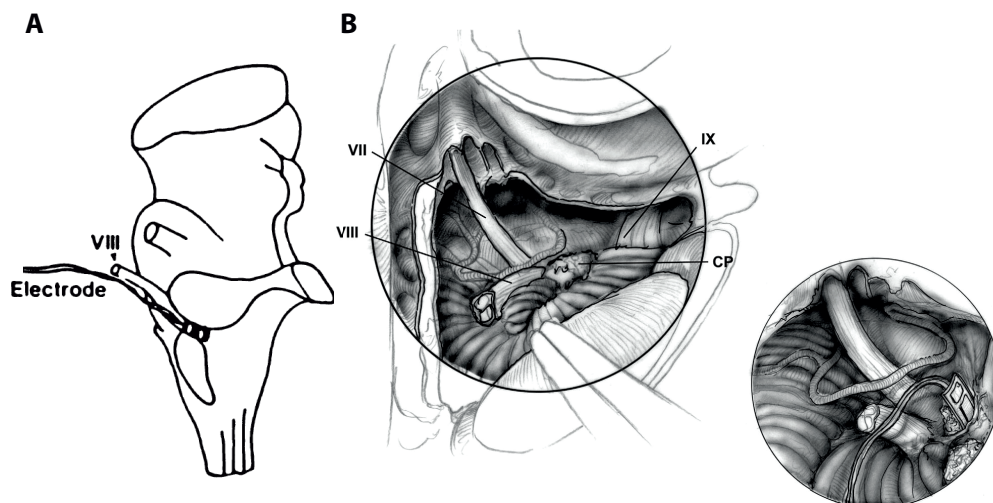


Figure 3.4: A) Approximate placement of the ABI array at the surface of the brainstem, on the cochlear nucleus<sup>[201]</sup>. B) Drawings showing the anatomy (with VII<sup>th</sup>, VIII<sup>th</sup> and IX<sup>th</sup> cranial nerves, as well as the choroid plexus (CP)) and implantation location of the ABI array<sup>[180]</sup>.

In the great majority of cases, ABI patients report useful auditory sensations from their implant. In pediatric ABIs, most of the patients show improvements in cognitive development, and some of them can even have a normal auditory development.<sup>[183]</sup> However, the clinical out-

### Chapter 3. New Generation Auditory Brainstem Implant (ABI)

---

comes of ABIs are in general not comparable to CIs, with lower word recognition scores with ABI alone. Except for a few patients showing excellent outcomes and good speech understanding, most patients use their implant for sound awareness, environmental cues and as a help for lipreading.<sup>[201] [121]</sup> Some patients can pitch-rank their electrodes, showing a possibility of access to some distinct frequencies.<sup>[121]</sup> ABI users performed much poorer than CI users at discriminating between frequencies (i.e. spectral cues)<sup>[121,184]</sup>. If initially the overall results seemed poorer for NF2 patients than for non-NF2 patients, suggesting a damage of the CN due to the tumor or its removal<sup>[121]</sup>, other results reported some cases with excellent performances in NF2 patients with the 12-electrodes Med-El implant.<sup>[201]</sup> These results suggest that the surgical approach, implant type and processing might affect the outcome more than the disease itself.<sup>[183]</sup>

The overall performance is not necessarily linked to the number of electrodes. Indeed, some patients using a low number of channels showed good perceptual performance<sup>[201]</sup>. However, experience with CIs shows that at least 4 channels are necessary for good speech understanding in quiet, and that this number increases in the presence of background noise<sup>[201]</sup> or for understanding of spectral content of speech<sup>[211]</sup>. Accurate frequency encoding might then be the main culprit for reduced speech comprehension in ABI users.

#### Challenges faced with ABIs

One of the challenges with the current ABIs is the extra-auditory side-effects often generated by some of the electrodes, which need to be deactivated. These side effects can include dizziness, tingling in the leg or in the tongue, and are due to current spread inducing stimulation of the neighbouring non-auditory structures by the ABI electrodes, including the VII<sup>th</sup> or IX<sup>th</sup> cranial nerves<sup>[201] [184]</sup> and other brainstem nuclei. This phenomenon decreases the number of usable electrodes, thus preventing the use of electrodes that would potentially give good auditory sensations.

Additionally, poor spectral resolution seen among ABI users may be the result of electrical stimulation failing to stimulate independent populations of auditory neurons along the tonotopic axis<sup>[46]</sup>. This may be the result of poor spatial selectivity and current spread, due to the relatively large electrode sites used in the contemporary ABIs and the high current thresholds. These high current thresholds can be partly explained by the fact that the electrode arrays used in clinical ABIs are thick (0.6 mm) and not very flexible, and they might not be able to conform to the curvilinear cochlear nucleus surface<sup>[167]</sup>, thus increasing the distance with the target neurons. The poor frequency selectivity of stimulation might also be due to the neurophysiological properties of the stimulated structures and their respective frequency tuning properties. Stimulation of a population of neurons with wide frequency tuning would lead to a lack of spectral definition, even in the presence of spatially specific stimulation. If the ABI induces stimulation of a mix of several neuronal populations with various frequency tuning properties, as suggested by the CN neurophysiology, it could be an explanation for the

mixed outcomes of spectral resolution. It was also suggested that some parts of the frequency spectrum might not be accessible by surface stimulation<sup>[167]</sup>.

Another possible explanation for the poor outcomes of the current ABIs is the bypass of the processing steps occurring in the CN. Indeed, it is impossible to stimulate the CN neurons in the same way than the auditory nerve would in a healthy patient, so some processing would necessarily be bypassed. Important information about sound modulation and periodicity, or sound onset and offset might then be lost.<sup>[45]</sup> Moreover, the processing in the three subunits of the CN occurs in parallel, so at least some of it is bypassed by stimulating mainly the DCN<sup>[137]</sup>. The question here is: is this bypassed processing so important that no good speech understanding is achievable with an ABI? It does not seem to be the case since some patients achieve good speech understanding with ABIs<sup>[201]</sup>.

Finally, the processing strategies used in contemporary ABIs could help explain the modest outcomes. The Med-El ABI uses the CIS (continuous interleaved sampling) strategy, using high fixed rate stimulation (600-1800 Hz) to a small number of channels in a nonoverlapping fashion, in order to avoid channel interactions. It is adapted to a stimulation giving very precise temporal information to a low number of independent frequency channels. The Cochlear ABI device is based on the SPEAK (spectral peak coding) processing strategy, which analyses the intensity and frequency of the sound and dynamically selects the electrodes to stimulate, and uses 250-300 Hz stimulation or on the ACE (advanced combination encoder) strategy, a high pulse rate version of the SPEAK strategy<sup>[111,113]</sup>. These processing strategies were developed for cochlear implants, and although some good outcomes were reported using the Med-El implant<sup>[113,181]</sup>, they might not be optimal for auditory brainstem stimulation. Indeed, the cochlea and cochlear nucleus are fundamentally different in several ways including their structure, tonotopic organisation, neuronal properties and role in the auditory system. Successful ABI stimulation might require targeting of a subset of neuronal types or structures with specifically-designed protocols. It is then essential to adapt the processing strategy to the cochlear nucleus structure and function<sup>[13,201]</sup>, which requires an in-depth study of its different neuronal populations, their projections and properties.

#### 3.1.2 Neurophysiology of the cochlear nucleus

The CN is a very important relay station in the auditory pathway, but also includes a lot of processing of the sound. Its size has been measured to 8 mm x 1.53 mm x 3.76 mm at the maximum in humans<sup>[167]</sup>. Its complex shape, as well as the volume ratio of 1:5 between the dorsal and ventral parts has to be considered during the design of a new ABI<sup>[167]</sup> (Figure 3.5).

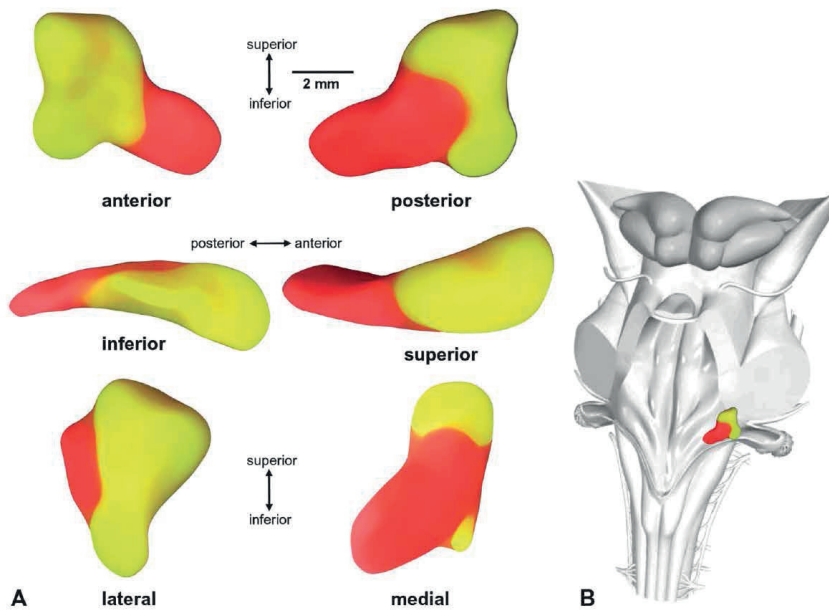


Figure 3.5: A) Views of the right human cochlear nucleus complex, showing the dorsal (red) and ventral (yellow) cochlear nucleus substructures. B) Dorsolateral view of the human brainstem, showing the position of the cochlear nucleus complex (from <sup>[167]</sup>).

The neurophysiology of the CN has been thoroughly characterized in animal models, and compared to the human in some studies <sup>[16,17,139]</sup>. Many different neuronal types can be identified in the CN that differ in their localizations, frequency tuning properties, projections, temporal patterns of responses to tone burst and functions <sup>[201]</sup>. We will take a particular interest in the principal neurons, those that have direct projections to higher auditory structures, which have been reviewed in several papers <sup>[29,121]</sup>. Many more types of neurons are involved in internal processing and are important for the functionality of the CN, but will not be discussed in depth here.

The AVCN and PVCN contain various types of projecting neurons. The spherical and globular bushy cells present in the AVCN are thought to be important for sound localization and binaural hearing <sup>[29,121,201]</sup>. The type I multipolar cells in higher mammals and humans (probably corresponding to the T-stellate cells in rodents), located in the central region of the VCN, are narrowly tuned to sound frequency and project directly to the IC. Their response properties suggest that they are specialized in amplifying and extracting the envelope of the sound, and thus that they encode temporal features of sound and are important for speech perception. <sup>[121,137]</sup> The octopus cells present in the caudal PVCN respond to tone bursts with very precise timing and are thought to encode broadband temporal timing information <sup>[121]</sup>.



The organization of the DCN shows more distinct differences between animal models such as cats and rats, and humans. The DCN shows a laminar structure in most animals, composed of three main layer, the molecular, the fusiform and the deep layer (Figure 3.7). The first layer includes the parallel fibers, composed of axons from the granule cells and other sources. Below, the fusiform cell layer and deep layer present many different types of neurons involved in the internal processing of the CN. The DCN contains two main types of neurons projecting to the higher auditory structures. First, the pyramidal (fusiform) cells located in the fusiform cell layer, below the parallel fibers, receive excitatory input from tonotopically organized auditory nerve fibers and inhibitory input from tonotopically organized vertical cells<sup>[216]</sup>. They also receive excitatory and inhibitory inputs from the parallel fibers, the stellate cells and the cartwheel cells that might be less tonotopically organized, and integrate these inputs into direct, fast-conducting, tonotopically-organized projections to the contralateral IC via the dorsal acoustic stria<sup>[16,121,216]</sup>. Second, the giant cells, located in the deep layer of the DCN, project to the contralateral IC but also to the contralateral CN.<sup>[29]</sup> These neurons are located deeper and are much less numerous than the pyramidal neurons.

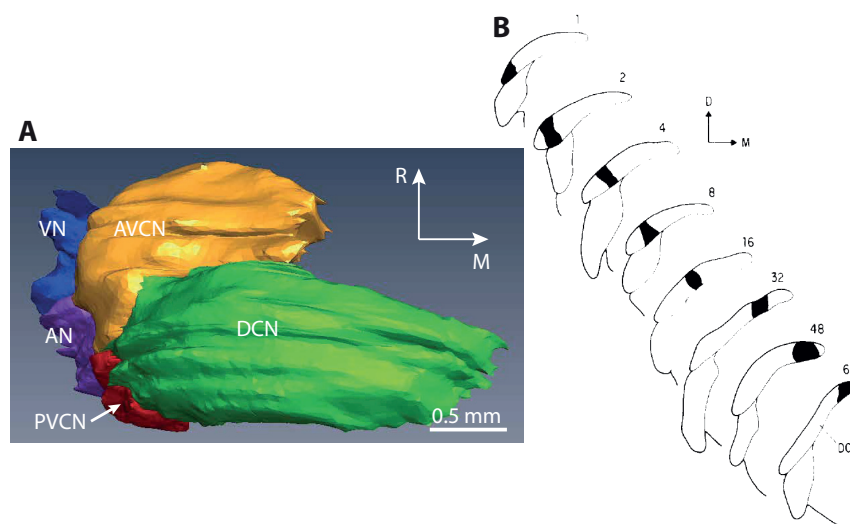


Figure 3.6: A) 3-dimensional reconstruction of a rat CN, as in<sup>[200]</sup>, showing the three subunits (anteroventral (AVCN), posteroventral (PVCN) and dorsal (DCN) cochlear nucleus), as well as the auditory nerve (AN) and vestibular nerve (VN) entrances into the CN. B) Tonotopic organisation of the rat DCN<sup>[174]</sup>.

The role of the DCN in humans is not clear, as it differs in its cytoarchitecture compared to other mammals<sup>[16,139]</sup>. Particularly, some neuronal cell types involved in internal processing of the DCN in animals, such as cartwheel cells, might not be present in humans<sup>[139]</sup>. Part of the stratified structure observed in most mammale is however present<sup>[17]</sup>. Its relatively low number of projections compared to the VCN suggests an important role in the processing of sounds<sup>[121]</sup>, and in particular the coding of sound elevation<sup>[145]</sup>.

It is difficult to identify the precise neuronal targets of the ABI since little is known about the CN physiology, about the precise role of the different neuronal types, but also about the non-projecting neurons and the nature of the connections between the different subunits of the CN<sup>[121]</sup>. However, the pyramidal neurons are a potential target in the DCN as they are located not far from the surface, are more numerous than the giant cells and have direct, tonotopic projections to the contralateral IC. In the VCN, the type I multipolar cells are also a potential target, since they are thought to be critically important for speech understanding and have direct, tonotopically-organized projection to the IC<sup>[29]</sup>.

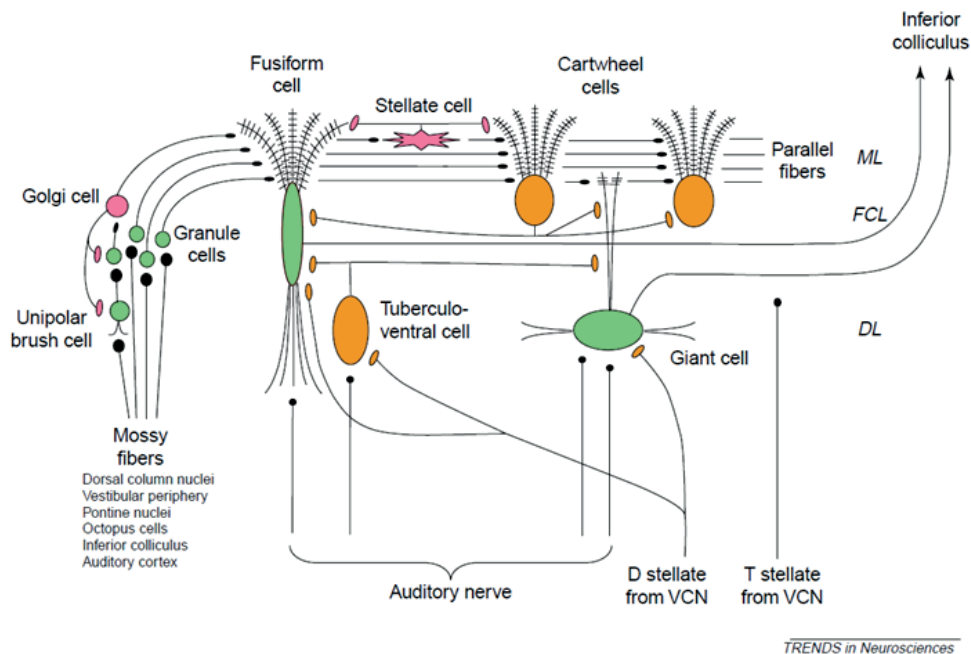


Figure 3.7: Neurophysiological organisation of the DCN in mammals showing the main cell types and connections in the three layers (ML: molecular layer; FCL: fusiform cell layer; DL: deep layer) and the projections to the IC of the two principal cell types, fusiform cells and giant cells<sup>[145]</sup>.

### 3.1.3 Hypotheses for ABI improvements

#### Targeting neurons in the VCN

In ABIs, unlike in CIs, the tonotopic axis is difficult to access since higher frequencies are located deeper in the DCN.<sup>[183]</sup> Since more narrowly frequency tuned neurons seem to be present deep in the VCN with direct projections to the IC, penetrating ABIs (PABIs) were developed. The advantages of using microstimulation within the CN were thought to be multiple and to include particularly better access to the tonotopically-organized Type 1 multipolar cells and lower current thresholds resulting in lower extra-auditory side effects, and ultimately better frequency selectivity and speech understanding.<sup>[123]</sup> Clinical trials showed

that, if indeed lower currents could be used, this did not result in improvement of speech understanding.<sup>[149]</sup> Moreover, specific problems associated with PABI were described. First, the accurate placement of the PABI is more difficult due to anatomical variations between patients. Additionally, unlike with surface ABIs, there is no possibility to intraoperatively probe and change its placement if it is not optimal. Non-auditory sensations were also generated and the PABI was found more likely to stimulate the deep fibers in the CN instead of the single neurons, resulting in lack of tonotopic selectivity in some cases.

For these reasons, an optimization of the surface approach is chosen. In some cases, ABI patients have very satisfying hearing outcomes with access to different frequencies and good speech understanding. These patients show the possibility to generate useful auditory stimulation with surface ABIs, and work is required to understand what is different in these patients compared to the ones with low hearing outcomes, as well as what is the potential for improvement of the surface ABI.

#### **Increasing spatial selectivity of surface stimulation**

One of the strategies envisioned to improve surface ABIs is to optimize spatial selectivity of stimulation. There are two main reasons for this. First, one of the main issues with contemporary ABIs is the generation of side-effects due to stimulation of neighbouring non-auditory structures. Increasing the spatial selectivity of stimulation will allow to limit the current to the auditory portion of the brainstem, particularly at the edges. Second, decreasing the volume of activated neurons with spatially specific stimulation may allow an optimization of the number of frequencies that can be accessed, thus maximally taking advantage of the tonotopic organization of the DCN. This will hopefully increase the number and independence of frequency channels, leading to higher spectral content in the new generation ABI.

There are several directions to improve the ABI's stimulation selectivity. Contemporary ABI arrays consist of electrodes on a rigid backing (0.6 mm thickness) that conforms only minimally or not at all to the curvature of the brainstem surface<sup>[167]</sup>. Using a thin flexible stimulation array would lead to an implant that conforms to the the CN surface<sup>[68]</sup>, thus minimizing the distance to the target neurons and the stimulation thresholds.

Decreasing the diameters of electrode sites and increasing their density can also contribute to an increased spatial selectivity. Clinical ABI arrays consist of electrodes with diameters varying between 550 and 700  $\mu\text{m}$  and inter-electrode distances of typically 1 mm (center-to-center)<sup>[186,201]</sup>. Decreasing electrode diameters and increasing their density can provide a platform to study the limits of spatial selectivity achievable with electrical stimulation. Additionally, bipolar stimulation may produce a more focused excitation volume of neural tissue in cochlear stimulation<sup>[135,190,219]</sup> and deep brain stimulation<sup>[95,148]</sup> compared to monopolar stimulation, currently used in ABIs for power reasons<sup>[75]</sup>. Although bipolar stimulation is not always associated with functional benefits in these studies, it can potentially reduce the

### Chapter 3. New Generation Auditory Brainstem Implant (ABI)

---

lateral spread of stimulation current, both perpendicular to the electrode pair and deep into the tissue<sup>[22]</sup> and might thus be beneficial.

#### **Adapting the stimulation strategy to the CN neurophysiology**

Even if the CIs and ABIs target fundamentally different structures, as seen before, all existing ABI devices use processing algorithms that are CI-specific, even though the stimulated neurons do not have the same response properties than the spiral ganglion cells targeted by CIs.<sup>[201]</sup> This is a major issue in current ABIs, and a lot of work would be required to precisely identify the targeted structures and their properties within the CN, so that a new and optimized processing algorithm can be developed.

In this context, investigating the effect of different waveforms of stimulation on the auditory system responses is a first step to understand how to stimulate the CN neurons in order to optimize the tonotopic organisation and the frequency selectivity of stimulation. This strategy is well known from the literature, and different waveforms of stimulation have shown to provide various spatial or structural selectivity properties.

For instance, short phase durations have shown to be associated to lower thresholds (in charge per phase) than longer phase durations<sup>[91]</sup>. Asymmetric pulses were also tested and waveforms that stimulated preferentially neuronal somata over fibers of passage, or the opposite, were shown in a simulation study<sup>[124]</sup>. A strategy to inverse the current-distance relationship, inactivating neurons close to the electrode site while stimulating further neurons was also presented in an in vitro model<sup>[63]</sup>. Testing these different waveforms and their effects on the activation properties of the auditory system might thus enable a better understanding of the stimulated neurons, and a targeting of neuronal populations with specific properties.

#### **Improving the ABI placement and the intraoperative assessment**

Another issue affecting ABI outcomes is the difficulty of reliable placement of the electrode array during surgery. Even if the placement can be probed by assessing the presence of ABRs after stimulation from the different electrodes of the array, a good placement is not guaranteed. Several elements can explain this. First, the approach is blind, and the surgeon has to “slide” the implant between the cerebellum and the brainstem, within the lateral recess of the 4<sup>th</sup> ventricle to reach the CN surface (Figure 3.4).<sup>[45]</sup> Very few surgical landmarks are available, and for NF2 patients, the structures might appear very distorted due to the tumor.<sup>[149]</sup> Second, the “ABR probing” done intraoperatively is very crude: the electrodes are tested in a bipolar configuration to minimize the stimulation artefact in the recording and optimize the time of testing, whereas they are most often used in a monopolar configuration when the implant is switched on.<sup>[180]</sup> This can induce important differences in the generation of auditory sensations, but also extra-auditory side-effect, which are often not detectable intraoperatively. Moreover, the correspondance between the generation of ABRs intraoperatively and the pres-

ence of auditory sensations in stimulation conditions is not automatic<sup>[75,180]</sup>. It is not clear why this is the case, however it is known that the anesthesia has a big influence on the ABRs and the electrode array position might not be fully stable during the recovery time.<sup>[137]</sup>

An improvement of ABI performances will thus most likely be linked to an improvement both on the array and on the processing side. It is also intrinsically linked to a good understanding of the physiology of the stimulated system and the precise targeted neurons. It is our hope in this project to improve the understanding of the stimulated neurons, as a step in this direction.

#### 3.1.4 Assessment of auditory system activation properties

##### The auditory brainstem response

The auditory brainstem response (ABR) is a far-field measurement of the auditory system activation along the brainstem and midbrain, up to the auditory cortex following an auditory stimulus. In animal models, it is recorded with three subcutaneous electrodes placed at the vertex, behind the ipsilateral ear and on the back of the animal. Evoked potentials are recorded following stimulation of the auditory system by subtracting the signal obtained from the ear electrode to the signal obtained from the vertex electrode, each relative to the reference electrode on the back of the animal.

The recorded auditory evoked potential can last for several seconds, and the first 10ms correspond to the ABR. This multi-peaked response can be measured following acoustic stimulation (aABR) or electrical stimulation (eABR) (Figure 3.8) and the amplitudes and latencies of the different peaks can provide information about the auditory system activation. Five different peaks can usually be identified in acoustically-generated ABRs. It is generally accepted that they correspond to the sequential activation in the auditory nerve (I), the cochlear nucleus (II+III), the superior olive (IV), the lateral lemniscus and the inferior colliculus (V), although it may be more complex<sup>[130]</sup>.

As it is an indirect measure of activity, it has a poor selectivity. In particular, no information about the frequency selectivity of auditory system activation can be obtained. However, it is the only method that can be used clinically during ABI implantation surgery to intraoperatively assess the correct positioning of the ABI and reposition it if necessary<sup>[75]</sup>. It is thus an important recording method to consider in the design of a new ABI.

##### Multiunit recordings along the auditory pathway

Multiunit recordings along the auditory pathways can provide very precise information on the auditory system activation following acoustic or electrical stimulation in animal models. Thanks to the tonotopic organization conserved from the cochlea throughout the auditory

### Chapter 3. New Generation Auditory Brainstem Implant (ABI)

system up to the auditory cortex, information about the frequency content and selectivity of stimulation can be obtained [11,57,117,165]. The central nucleus of the inferior colliculus (IC) provides two main advantages for recording. First, it is tonotopically organised in isofrequency laminae along a dorsal-to-ventral axis, with deeper layers corresponding to higher acoustic frequencies, and shallower layers corresponding to lower frequencies. Thus, by introducing a single shank multichannel electrode array along this axis, information about the frequency selectivity of auditory stimulation can be obtained. The second advantage is that most of the projections from the CN to the higher auditory structures pass, directly or indirectly, via the IC [29].

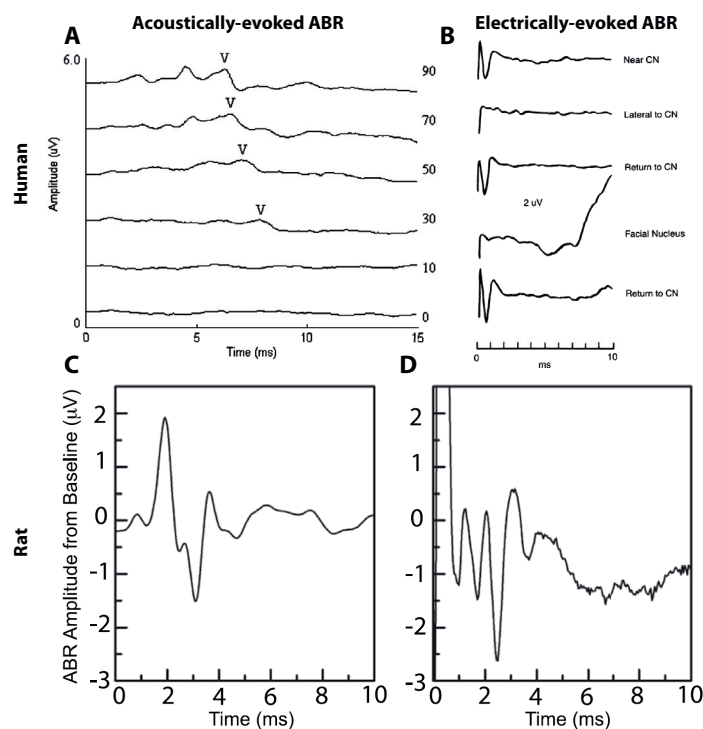


Figure 3.8: A) Example of acoustically-evoked ABRs in a human at different stimulation levels, with wave V marked, the main wave used for ABR-based diagnosis of various conditions [208]. B) Electrically-evoked ABR during ABI implantation surgery at different locations on and near the CN [180]. C-D) Acoustically (C) and electrically (D) evoked ABRs in a rat model following 40dB SPL click stimulus (C) and 0.4 mA stimulation on the DCN (D) [200].

The exact link between multiunit recordings from the IC and audiologic perception of speech and sounds is unclear, as there is some extra processing occurring in higher auditory structures than the IC including the thalamus, the primary auditory cortex and higher cortical areas. However, IC multiunit recordings are the best available measure to estimate the frequency selectivity in animal models and can provide useful information on the activation of the auditory system.

### 3.1.5 Goals of the project

- Use a conformable microfabricated array to stimulate the cochlear nucleus surface in a rat model and record the evoked activity of the auditory system.
- Investigate whether the tonotopy of the CN can be accessed by this spatially selective stimulation, by analyzing the different components of the response.
- Develop hypotheses on the neural correlates of the different components of the response.
- Investigate the effect of electrodes configuration (bipolar vs monopolar) and in the case of bipolar stimulation, the effect of distance between the two sites of the stimulation electrode pair and orientation of the electrode pair
- Investigate the effect of the waveform of stimulation on the parameters of activation and access to different frequencies.
- Draw guidelines on how to translate the obtained results into improvement of the ABI array for human use.

## 3.2 Methods

### 3.2.1 Acute in vivo experiments

#### Surgery

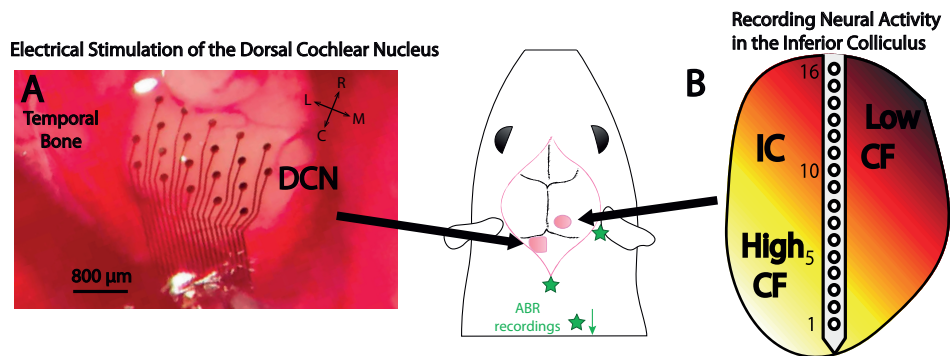


Figure 3.9: Experimental setup with stimulating array in the left DCN (A) and recording probe in the contralateral (right) IC (B). Lateral (L), medial (M), rostral (R) and caudal (C) directions on the DCN surface are indicated. In the IC, the tonotopic axis runs from low CF dorsolateral to high CF ventromedial. ABRs are recorded with three subcutaneous wires, indicated by the green stars, on the vertex, behind the right ear and on the back of the animal.

All experimental procedures were performed in accordance with the National Institute of Health guidelines for the care and use of laboratory animals as well as approved animal care

### **Chapter 3. New Generation Auditory Brainstem Implant (ABI)**

---

and use protocols at the Massachusetts Eye and Ear Infirmary, Boston, MA. In vivo tests were performed on male Sprague-Dawley rats (350-500 g) within a sound-attenuating chamber. Animals were anesthetized with Ketamine (100 mg/kg) and Xylazine (20 mg/kg) for the duration of the experiment. Normal function of the cochlea at all frequencies of the rat hearing range was checked by measuring the distortion product otoacoustic emissions (DPOAEs). A left occipital craniectomy was performed and a small portion of the ipsilateral cerebellum was aspirated. A second craniectomy was performed over the right temporo-parietal suture, to access the surface of the contralateral IC (Figure 3.9).

#### **Electrical stimulation protocol**

The array (described in section 3.4) was placed on the surface of the DCN. Electrical stimulation was induced with custom-made current sources. Stimuli were current-controlled but expressed in voltage levels due to the presence of a 2 k $\Omega$  resistor in parallel with the output during the experiments. The stimuli were pulse trains (train duration, 500 ms; trains repeated 1/s). Within a train, the pulses consisted of charge-balanced biphasic symmetric pulses at 0.2 ms/phase and 28 pulses/s with alternate polarity unless otherwise specified (Figure 3.10A). Stimulation level ranged from 0 to 4 V in steps of 0.5 V. Bipolar stimulation was applied between two electrode sites of the array, whereas monopolar stimulation was applied between one electrode of the array and a reference electrode (stainless steel needle placed in the neck muscles of the animal). Averages of 30 repetitions of 500 ms pulse trains were obtained for each condition. All runs were performed in a pseudo-random order.

#### **Auditory brainstem responses (ABRs) recordings**

Electrically evoked auditory brainstem responses (eABRs) were recorded. These recordings were made by differentially recording signals from two subcutaneous stainless steel needle electrodes, one placed on the vertex and the other behind the ipsilateral pinna of the animal, with a ground electrode placed on the back of the animal. The signals were filtered with an analog bandpass filter (30 Hz to 3 kHz) amplified by 60 dB before A/D conversion with a sampling frequency of 25 kHz (Ithaco Model 1201, DL Instruments, Ithaca NY) and averaged over all stimulus presentations.

#### **Multiunit recordings from the inferior colliculus (IC)**

A 16-channel penetrating recording probe (A1x16-5 mm-150-177, Neuronexus, Ann Arbor, MI) was inserted into the central nucleus of the IC. Multiunit recordings from the IC were obtained simultaneously from 16 recording sites along the silicon shank of the probe with a 25 kHz sampling frequency. Recording site diameter was 15  $\mu\text{m}$  and center-to-center spacing was 150  $\mu\text{m}$ . The average signal of all sites was used as a global reference.



### Characterization of electrode array position

Accurate placement of the ABI electrode on the DCN surface was confirmed by inserting pins (0.1 mm diameter Minutien) at the corners of the array and subsequently recovering the pin-holes in Nissl-stained frozen sections during post-experiment histology.

### 3.2.2 Signal processing

#### Data pre-processing

Processing of the data was performed with MATLAB software (The Mathworks Inc., Natick, MA). The first 1 ms of each recording following each stimulus pulse onset was discarded to eliminate the stimulation artefact. A forward and reverse bandpass Butterworth filter of order 5 was applied, with cut-off frequencies of 500 Hz and 3 kHz. The filter was also applied on the baseline activity. Threshold for spike detection was set to three times the standard deviation of the filtered baseline. The spike rate was determined after subtraction of the baseline spike rate, for the 30 ms after stimulus (Figure 3.10).

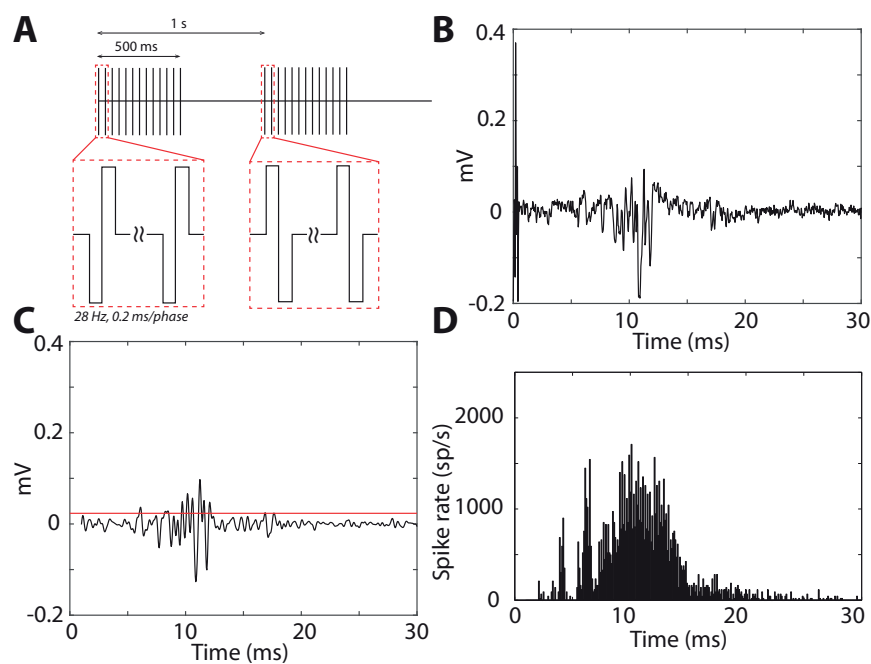


Figure 3.10: A: Illustration of the stimulation protocol with alternate polarity. B: Raw IC recording. C: IC recording after deletion of the first millisecond of recordings containing the stimulation artefact, and filtering. The threshold for spike detection is shown in red. D: Post-stimulus time histogram (PSTH) following spike count for all 30 averages

Post-stimulus time histograms (PSTHs) were obtained for each condition with a temporal resolution of 0.1 ms. Spikes were then averaged over a defined time interval for each IC

### Chapter 3. New Generation Auditory Brainstem Implant (ABI)

recording site and stimulation level to generate IC response maps. Significance of activation for each condition was determined by a student's t-test between the spike rate of the different repetitions, and the same data at the zero stimulation level. A p-value < 0.001 was used as the significance criterion. Spike rate of non-significant conditions were put to zero.

#### Response maps parameters measurements

The best threshold of activation was determined for each map as the lowest stimulation level generating significant activity on at least one of the recording sites. For each level  $l$  above best threshold, the centroid of activity  $C_l$  and the width of activation  $W_l$  were calculated with the following formulas ( $k$ : IC recording sites;  $MAP$ : 2-dimensional IC response map) [52]:

$$C_l = \frac{\sum_k k * MAP(k, l)}{\sum_k MAP(k, l)}$$

$$W_l = 2 * \sqrt{\frac{\sum_k (k - C_l)^2 * MAP(k, l)}{\sum_k MAP(k, l)}}$$

The centroid for electrical and acoustic stimulation were defined slightly above threshold, in order to provide a greater stability in the measurements. The centroid for electrical stimulation was defined at a level of 1 V above the best threshold for each IC response map (Figure 3.11). The centroid for acoustic stimulation was defined at 10 dB SPL above threshold for each acoustic frequency.

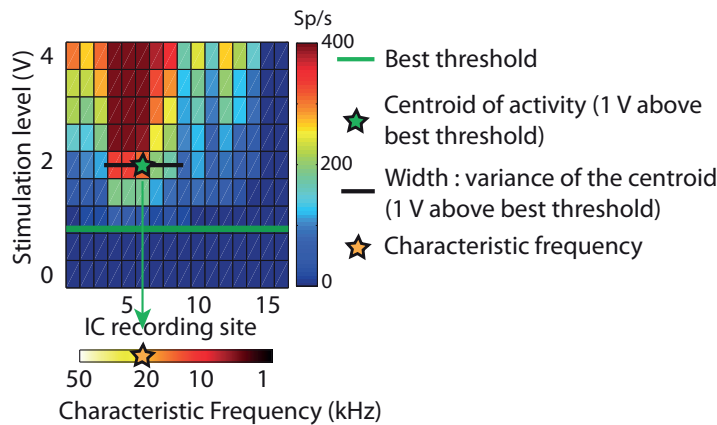


Figure 3.11: Example response area to illustrate the features that were extracted for analysis. Scale at bottom shows relationship between IC recording site and characteristic frequency, which was determined for each animal using acoustic stimulation.

Rate level curves were obtained using the average spike rates at the centroid  $\pm 1/2$  width. Spike rates were normalized for each rat to the maximum of the rate level curves across all stimulation conditions. Spike counts were obtained for each run and stimulation level by adding the spikes recorded from each IC recording site. The range  $R$  between two characteristic frequen-

cies  $CF_{min}$  and  $CF_{max}$  was expressed in octaves, following the equation  $R = \log_2\left(\frac{CF_{max}}{CF_{min}}\right)$ . The common activity was calculated by averaging IC response maps with significant activity evoked by all electrode pairs across the DCN. This average map was calculated separately for the different inter-electrode distances.

### 3.3 Acoustic stimulation results

Recordings of IC activity following acoustic stimulation is performed at the beginning of each experiment after insertion of the multichannel recording probe. The probe placement along the tonotopic axis of the IC can be confirmed and corrected if necessary before starting electrical stimulation. Tone pips of 20 ms duration are sent to the contralateral ear, between 1 and 46.5 kHz at 2 steps per octave, between 0 and 80 dB SPL (sound pressure level).

Recorded maps show strong activity in the IC following acoustic stimulation at all tested frequencies (with a few exceptions, for example the 32 kHz run in rat 3)(Figure 3.12). Stimulation with high acoustic frequencies induce activity in the low-numbered recording sites (located ventromedially in the IC); as frequency is decreased, the activity progressively shifts to higher-numbered sites (more dorsolateral in the IC). Generated data show variable maximal spike rates (between 247 and 613 sp/s) and best thresholds (between 10 and 40 dB SPL) in the different rats.

The shift in activity along the array with sound acoustic frequency is very reliable(Figure 3.13), but the width of activity varies from rat to rat. A general trend to extract from this data in several rats (1 to 5) is the lower threshold in the middle frequency range (8 - 16 kHz) than in the low or high frequencies. This trend highlights the range of highest hearing sensitivity in this species of rats<sup>[86]</sup>.

The centroid of activity following stimulation with each of the acoustic frequencies is calculated, then a logarithmic fit is used to obtain the characteristic frequency associated with each IC recording site (Figure 3.13). This logarithmic function is then used as the correspondence between IC recording site and characteristic frequency in the analysis of electrically-generated data. Information on the frequency content and selectivity of the IC multiunit activity generated by electrical stimulation of the DCN is thus possible. Only the IC recording sites for which acoustically-evoked activity is recorded are considered for analysis of the electrically-generated data.

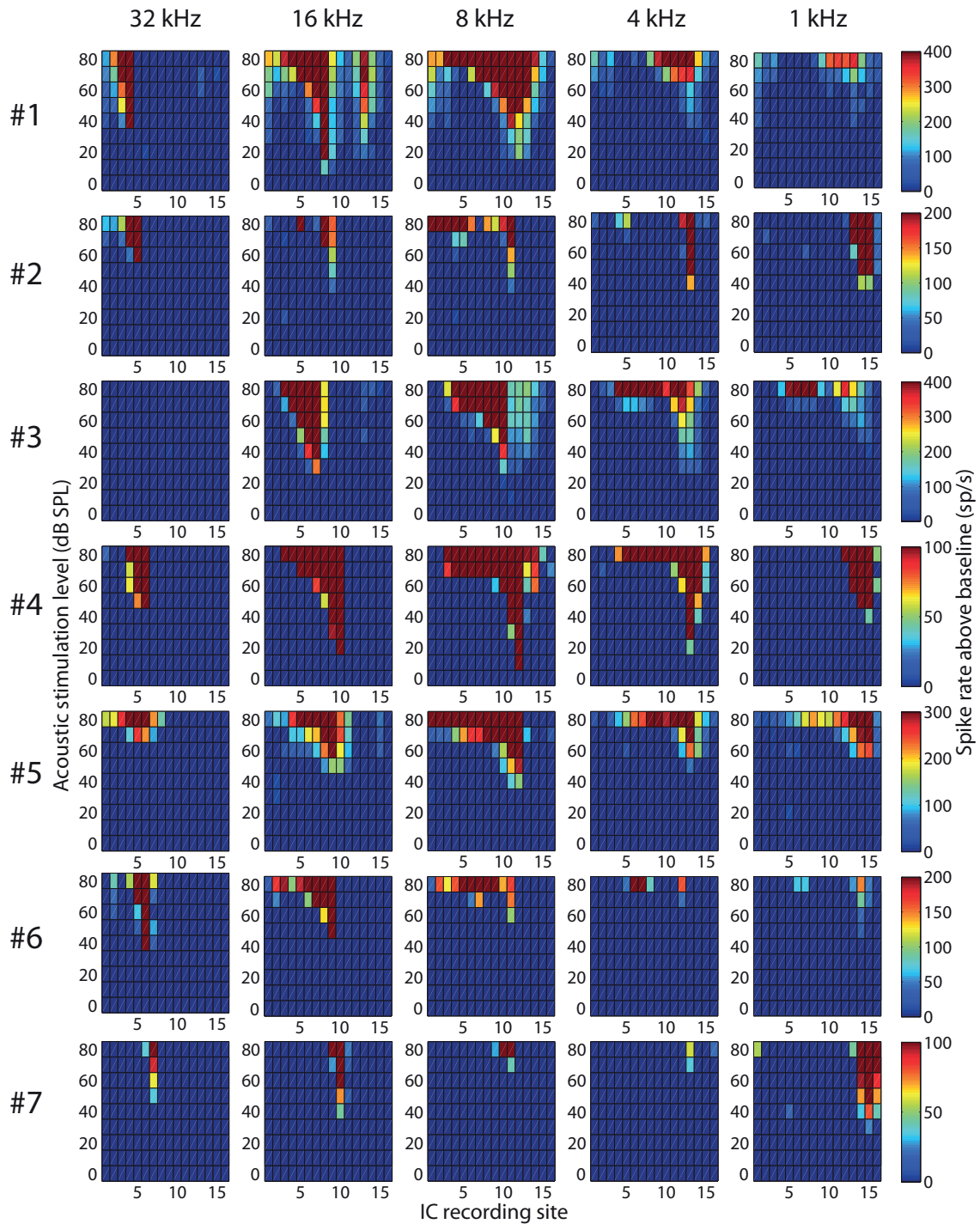


Figure 3.12: Multichannel recordings from the IC following acoustic stimulation at 1, 4, 8, 16 and 32 kHz shown for each of the seven rats. A shift in activity along the recording probe is observed, from low site numbers at high frequency to high site numbers at low frequency.

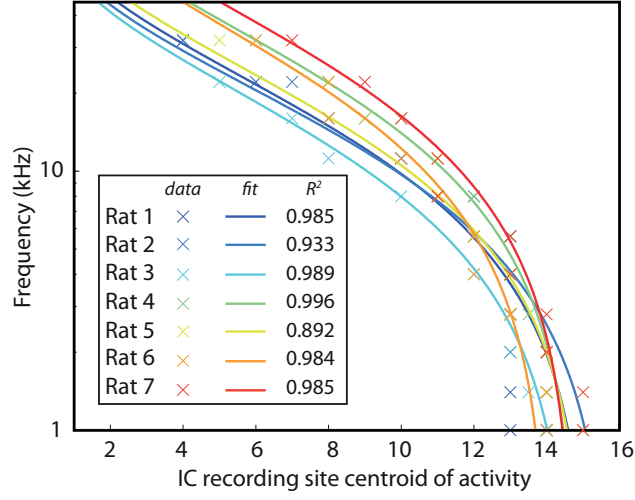


Figure 3.13: Correspondence between centroid of activity and CF is given by a logarithmic fit of the data obtained with acoustic stimulation for each rat.

### 3.4 Electrode array design

The thickness of the polyimide has to be small enough for the device to conform to the DCN surface, which radius of curvature has been estimated to 1.65 mm<sup>[68]</sup>. The thickness  $h_{max}$  at which the capillary forces are sufficient for a thin film of Young's modulus  $E$  and Poisson coefficient  $\nu$  to conform around a cylinder of radius  $R$  wetted by a liquid of surface tension  $\gamma$

can be expressed with the formula:  $h_{max} = \sqrt[3]{\frac{R^2 \cdot 24(1 - \nu^2)\gamma}{E}}$ <sup>[159]</sup>. For the values  $E = 3.2 \text{ GPa}$  and  $\nu = 0.34$  for the polyimide thin film and  $\gamma = 72 \cdot 10^{-3} \text{ N/m}$  for the surface tension of water,  $h_{max} = 10.8 \mu\text{m}$ . Following this calculation, a polyimide thickness of 8  $\mu\text{m}$  is selected for in vivo tests.

A finger-like design is used in order to further optimize the conformability of the array (Figure 3.14A and 3.15A). In the context of this application, one desired feature is a high density of electrodes on the available 1-by-2 mm surface of the surgically exposed rat CN, in order to be able to precisely tune the stimulation location. An electrode diameter of 100  $\mu\text{m}$  is selected for this purpose. Under these conditions, PEDOT:PSS with 75  $\text{mC/cm}^2$  deposition charge is selected for further testing. Indeed, the low thickness of the polyimide substrate induces mechanically challenging conditions, and coatings with higher deposition charges tend to crack and delaminate from the substrate. As mentioned in the previous chapter, selecting a 0.6  $\mu\text{m}$  thick coating provides a sufficient mechanical stability without compromising the electrochemical properties and the safety of stimulation. A plot of the complex impedance spectrum of over 100 sites before and after coating with PEDOT:PSS at 75  $\text{mC/cm}^2$  shows repeatability of PEDOT:PSS coating impedance characteristics (Figure 3.14B).

For both array designs presented below, the stimulation electrode sites are characterized by their position on the lateral-to-medial axis (x-axis of the coordinate system) and the caudal-to-rostral axis (y-axis of the coordinate system), with the origin of the coordinate system at the center of the array.

### 3.4.1 14-electrodes array with 200 $\mu\text{m}$ spaced pairs

A 14-electrode array is specifically designed to test the effect of stimulation with close (200  $\mu\text{m}$  distance) pairs. Seven pairs of electrodes are distributed on the whole CN surface with an emphasis on the lateral-to-medial axis distribution. A center-to-center distance of 200  $\mu\text{m}$  is selected for these close pairs, and several other distances (400, 500, 640, 800, 1200 and 1600  $\mu\text{m}$ ) can be tested. A range of orientations of the pairs can also be tested with this array. All the close pairs have an orientation of  $90^\circ$ , but larger interelectrode distances have orientations of  $0^\circ$ ,  $\pm 14^\circ$ ,  $\pm 36^\circ$ ,  $\pm 51^\circ$  and  $90^\circ$ .

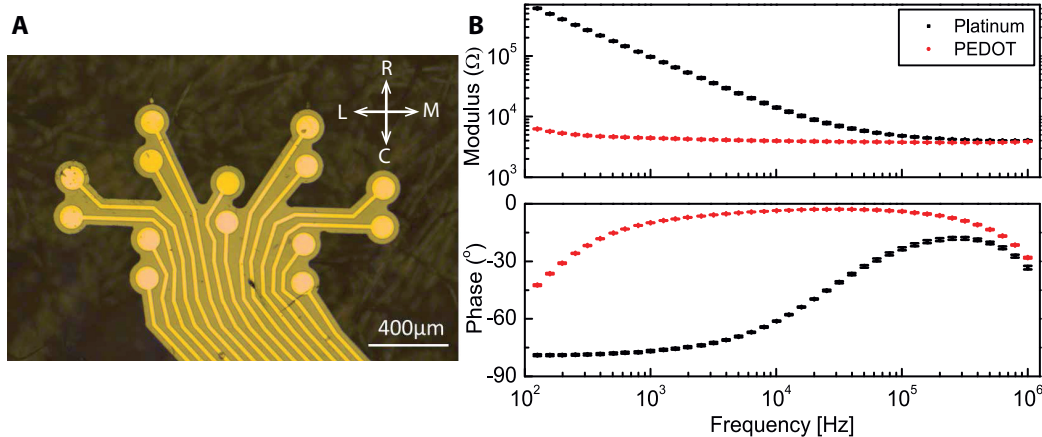


Figure 3.14: A) Picture of the 14-channels stimulation array. Lateral (L), medial (M), rostral (R) and caudal (C) directions are indicated. B) Impedance modulus and phase spectra of bare Pt and PEDOT:PSS coated electrodes (diameter = 100  $\mu\text{m}$ ). The small values of error bars for the PEDOT:PSS coated electrodes demonstrate great repeatability of the coating.

One of the limitations with this design when trying to investigate the effect of distance and orientation of the stimulation electrode pair is the impossibility to decorrelate one from the other. Indeed, as mentioned before, all 200  $\mu\text{m}$  distance pairs have an orientation of  $90^\circ$ . For higher distance pairs, two orientations can be tested : 400-412  $\mu\text{m}$  are associated to orientations of  $90^\circ$ , or close to  $0^\circ$  ( $\pm 14^\circ$ ). 500  $\mu\text{m}$  are associated to orientations of  $\pm 36^\circ$ . 640  $\mu\text{m}$  are associated to orientations of  $\pm 51^\circ$  (Table 3.1). Some information can thus already be obtained by comparing groups of pairs with the same distance and different orientations, but the dependence between the two variables to study, orientation and distance, makes any statistical analyses complicated. Despite this limitations, this design is suitable to investigate

### 3.4. Electrode array design

whether such an array can generate significant activation of the auditory system, and whether 200  $\mu\text{m}$  distance pairs can generate tonotopically organized activity in the IC.

The second limitation of this array is the limited coverage of the DCN, particularly in the corners. The pairwise organisation of electrode sites prevents a regular coverage of the surface and the axes (with the exception of the lateromedial axis) are difficult to characterize.

	200 $\mu\text{m}$	400 $\mu\text{m}$	412 $\mu\text{m}$	500 $\mu\text{m}$	600 $\mu\text{m}$	640 $\mu\text{m}$	800 $\mu\text{m}$
-51.3°	-	-	-	-	-	4	-
-36.8°	-	-	-	8	-	-	-
-14°	-	-	4	-	-	-	-
0°	-	-	-	-	-	-	4
14°	-	-	4	-	-	-	-
36.8°	-	-	-	8	-	-	-
51.3°	-	-	-	-	-	4	-
90°	7	2	-	-	4	-	2

Table 3.1: Number of tested electrode pairs for different stimulation configurations, described by their orientation and by the distance between the two electrodes of the pair.

#### 3.4.2 20-electrode array with hexagonal configuration

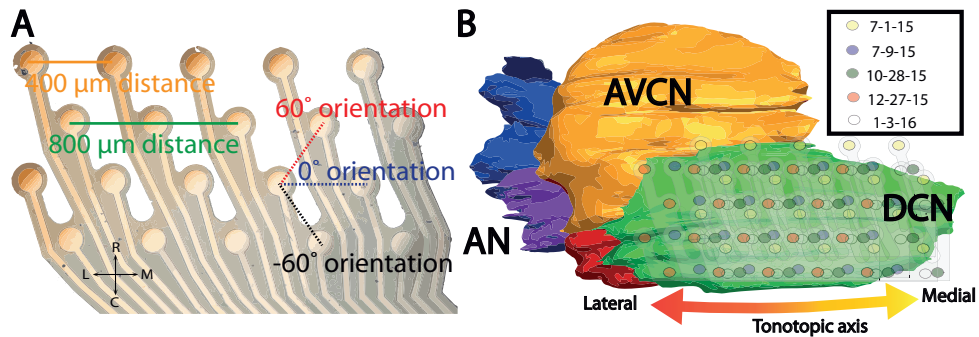


Figure 3.15: A) Photograph of the 20-channels stimulating electrode array. Lateral (L), medial (M), rostral (R) and caudal (C) directions are indicated. B) Overlaid array schematics from 5 rats, pictured on a colored CN reconstruction (from Verma et al., 2014). Schematics are positioned according to post-experiment histology.

A 20-electrodes array is developed to provide a regular coverage of the entire DCN surface and study the independent effect of orientation and distance in a bipolar stimulation configuration, in comparison with monopolar stimulation. The array hosts 20 microelectrodes patterned in a hexagonal configuration, with 4 rows, each of 5 electrodes (Figure 3.15). The total surface of the array is 1.1 mm by 1.9 mm. Each electrode's diameter is 100  $\mu\text{m}$ . Orientations of -60°, 0° and 60° (with respect to the lateromedial axis) and interelectrode distances of 400 and 800

$\mu\text{m}$  can be studied independently, and linked to the position of the pairs on the surface of the DCN.

### 3.4.3 Packaging for in vivo acute testing

Acute experiments require a specific packaging geometry with the following characteristics: possible access from the outside of the animal's head with a rigid shaft, at an orientation of about  $70^\circ$  (elevation), and  $45^\circ$  (compared to lateromedial axis). The polyimide device is composed of three sections. First, the connector section is located outside the skull where a pin connector is glued, each pin corresponding to one electrode site. Then, the tracks link the connector to the electrode array on the brainstem. This section is glued to a rigid shaft, in order to allow easy manipulation during surgery. Lastly, the electrode array is designed at an angle of  $45^\circ$  compared to the tracks, and a bending in the polyimide is induced (by thermal bending or physical gluing to the shaft). The thermal bending is about  $50^\circ$ , while the bending by gluing on the shaft induces a larger bending of  $70\text{-}90^\circ$ . Experiments showed that the latter allows a greater ease of placement with no need to widen the opening in the skull of the animal. In both case, the active part of the array is free-standing and can be positioned on the DCN surface.



Figure 3.16: Illustration of the packaging used for acute experiments in rats.

## 3.5 Electrically generated ABRs

### 3.5.1 eABRs parameters extraction

In this section, results following stimulation with the 20-electrode array (section 3.4.2) are presented. Recorded eABRs averaged over the different repetitions are digitally filtered with a Butterworth bandpass filter of order 5, with cutoff frequencies of 20 Hz and 2 kHz. For each run, the eABR threshold is visually determined as the first stimulation level with visible peaks.

Labeling of eABR peaks is done manually, after observation of the general pattern of a large number of recordings. Inspiration was taken from the peaks labeling of human eABRs, as shown in <sup>[75]</sup>. Five main positive peaks are identified, with a range of latencies following the pattern illustrated in Figure 3.17



Following peak labeling, several parameters are extracted from the signals: latency and amplitude of each peak (amplitude is defined as the difference between a local maximum - a positive peak, and the next local minimum - a negative peak), number of peaks, total amplitude and RMS energy of the signal. For all parameters, the value at a stimulation level of 1 V above threshold is used in the following analyses.

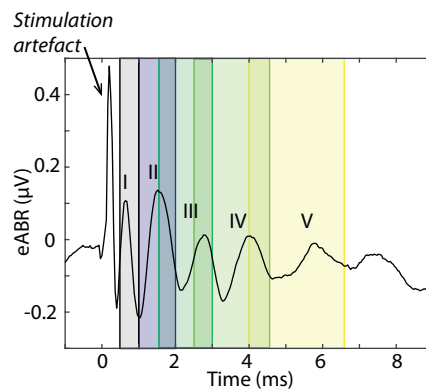


Figure 3.17: Electrically-generated ABR following DCN surface bipolar stimulation showing the five identified peaks and their respective latency ranges (shaded areas shown in black (Peak I - 0.3 to 1 ms), blue (Peak II - 1 to 2 ms), dark green (Peak III - 1.5 to 3 ms), light green (Peak IV - 2.5 to 4.5 ms) and yellow (Peak V - 4 to 6.5 ms)).

Figure 3.18 shows examples of eABRs generated by bipolar stimulation pairs located at different positions on the surface of the DCN. The first observation is the presence of the multi-peaked waveform characteristic of the ABRs on most of the runs. Variations in general pattern of the ABRs and in the properties of the individual peaks can be observed. Extraction and analysis of the parameters will allow the study of the effect of stimulation configuration and location on eABRs parameters across all rats.

#### 3.5.2 Effect of stimulation location on eABRs characteristics

The first phase of the eABR analysis attempts to identify potential effects of the location of stimulation on the different parameters. Figure 3.19A shows color-coded visualizations of eABR threshold for each individual rat, and figure 3.19B shows three eABR parameters following stimulation with all the neighbouring pairs of electrodes at the surface of the DCN (averaged between the different rats). A strong effect of the stimulation pair rostrocaudal position on the DCN surface is visible on the threshold, amplitude, number of peaks and RMS. For this reason, the more detailed analysis on the individual peaks properties focuses on the effect of location on the rostrocaudal axis.

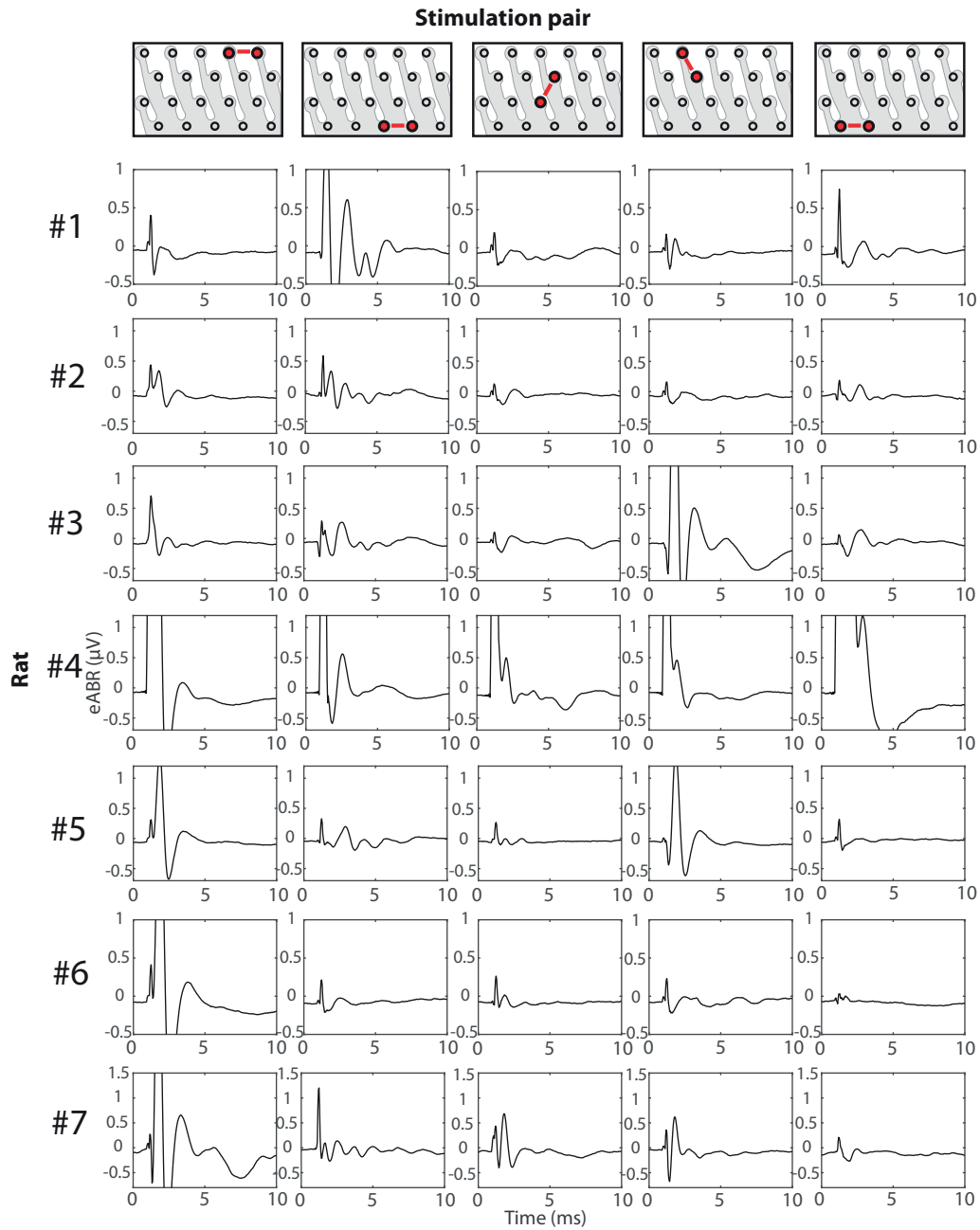


Figure 3.18: Electrically-evoked auditory brainstem responses (eABRs) for CN electrical stimulation in 7 rats. Top: Five bipolar pairs of stimulating electrodes (red) located at various positions on the DCN surface. Bottom: Responses to the five bipolar pairs in seven rats following 4 V stimulation.

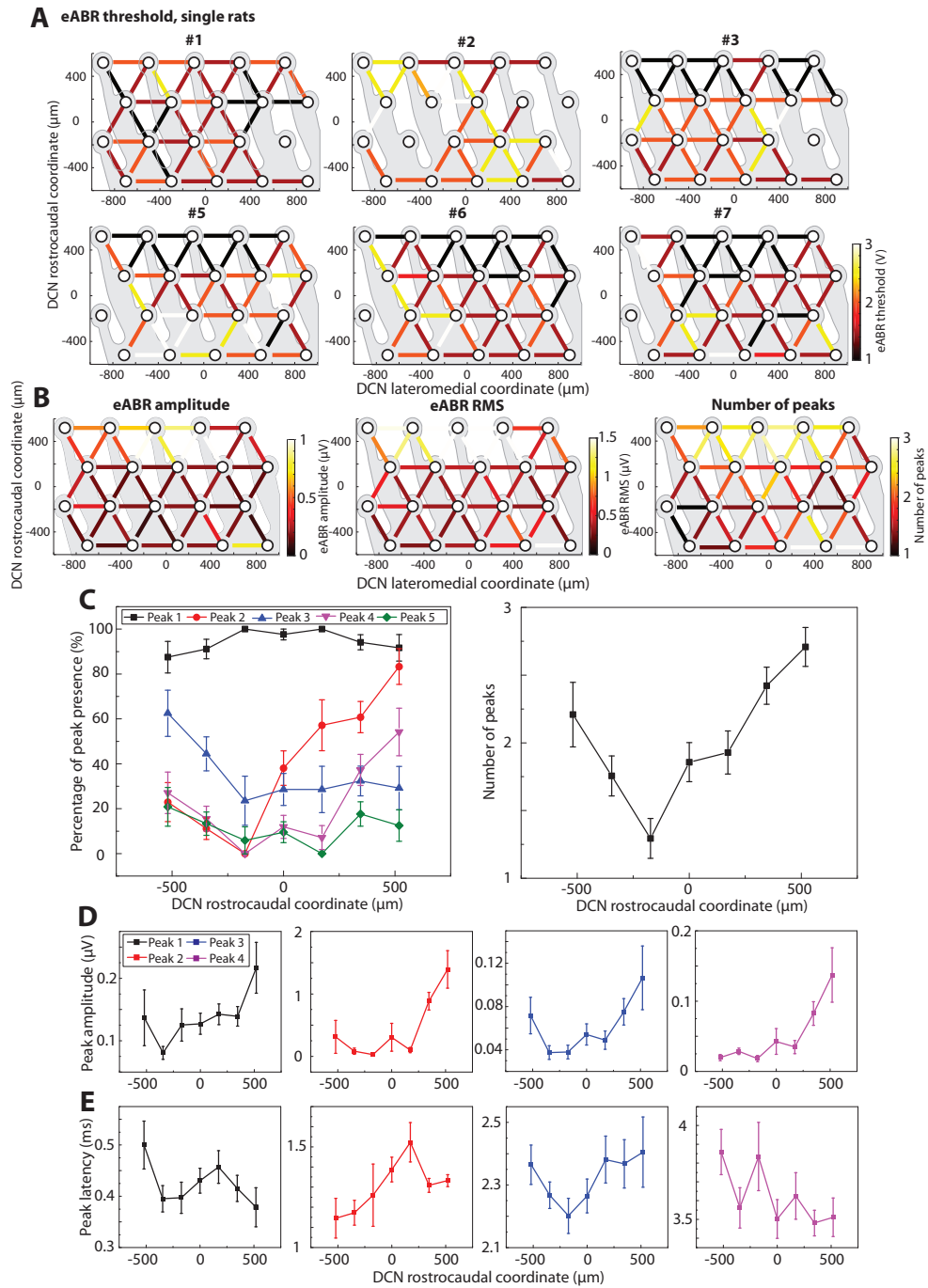


Figure 3.19: Effect of stimulation position on eABRs. A) Variations of eABR threshold with cochlear nucleus lateromedial and rostrocaudal position, for each rat. B) Variations with cochlear nucleus lateromedial and rostrocaudal position of the eABR, number of peaks, total amplitude and RMS, averaged over the 6 rats. C) Left: Effect of rostrocaudal position of stimulation on the fraction of runs presenting each individual peak. Right: Effect of rostrocaudal position of stimulation on the average number of peaks in the generated eABR. D-E) Effect of rostrocaudal position of stimulation on the amplitude (D) and the latency (E) of the first four peaks of the eABR.

### Chapter 3. New Generation Auditory Brainstem Implant (ABI)

---

The analysis of the presence of peaks 1 to 5 as a function of rostrocaudal position (Figure 3.19B) shows that the percentages of presence of peaks 2 and 4 are significantly higher at rostral locations (mult.lin.reg, N=6,  $p < 0.05$ ). P3 however shows an opposite effect, with higher percentage of presence on caudal locations (mult.lin.reg, N=6,  $p < 0.05$ ). No rostrocaudal effect was identified on P1 and P5 (mult.lin.reg, N=6,  $p > 0.05$ ). The effect of rostrocaudal location on the number of peaks is statistically significant (mult.lin.reg, N=6,  $p < 0.05$ , Figure 3.19C).

Rostrocaudal effects on the individual peaks amplitudes and latencies are also identified. The amplitude of several peaks (P1-P4) is significantly larger at rostral locations (mult.lin.reg, N=6,  $p < 0.05$  for P1-P4, Figure 3.19D). The latency of P2 is significantly larger on rostral locations, and the latency of P4 shows an opposite effect, with larger values at caudal locations (mult.lin.reg, N=6,  $p < 0.05$  in both cases).

None of the mentioned parameters (eABR amplitude, number of peaks, threshold, RMS or peaks presence, latency and amplitude) show any significant effect of lateromedial position of the stimulation pair (mult.lin.reg, N=6,  $p > 0.05$  in all cases), confirming that the rostrocaudal axis is the main axis of variations of recorded eABRs. The absence of lateromedial effect, particularly on the threshold of activation, is a very important effect as it shows a similar efficiency of stimulation along the longest dimension of the array. This is very likely associated to a close contact between the array and the underlying DCN, a property due to the flexibility of the electrode array.

#### 3.5.3 Effect of stimulation pair configuration on eABRs characteristics

With the tested electrode array design, the orientations of the pairs are correlated with their rostrocaudal locations. Specifically, all pairs at the most rostral and the most caudal locations ( $\pm 520 \mu\text{m}$ ) are oriented along the lateromedial axis. Considering the important rostrocaudal effect on eABR parameters highlighted in the previous section, an independent study of the effect of electrode pair orientation cannot be achieved. For this reason, only the effect of distance between the two electrodes of a stimulation pairs is investigated here.

The percentage of eABR presenting each peak for the two different distances (Figure 3.20A) shows that P2-P5 are present more often with an interelectrode distance of  $800 \mu\text{m}$  compared to  $400 \mu\text{m}$ . This difference is significant for P2 (mult.lin.reg, N=6,  $p < 0.05$ ), but does not reach significance for P3, P4 and P5 (mult.lin.reg, N=6,  $p > 0.05$  in the three cases). The total number of peaks is also significantly larger with the larger distance (mult.lin.reg, N=6,  $p < 0.05$ ; Figure 3.20B).

The study of the amplitude of individual peaks shows that all 5 peaks have slightly larger amplitudes with  $800 \mu\text{m}$  distance compared to  $400 \mu\text{m}$ . However, the significance is not reached in any of the peaks, or in the RMS energy of the signal (mult.lin.reg, N=6,  $p > 0.05$  in all cases; Figure 3.20C-D).

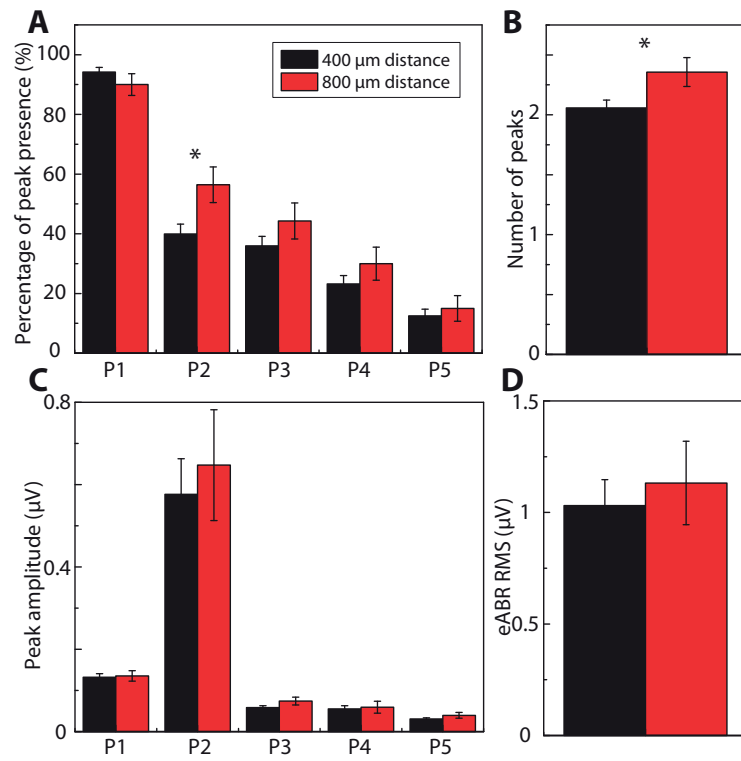


Figure 3.20: Effect of inter electrode distance on the fraction of runs presenting each peak (A), the number of peaks of the eABR (B), the amplitude of each peak (C) and the eABR RMS (D). Significant differences between the two distances are indicated with a star.

### 3.5.4 Comparison between monopolar and bipolar stimulation

When comparing eABRs generated by monopolar and bipolar stimulation, the first element that needs to be considered is the large stimulation artefact generated by monopolar stimulation (Figure 3.21A), which may also be partly myogenic activity. The two examples shown here are representative of this effect consistently present across all rats. This artefact contaminates P1 and also possibly P2, making the analysis of early peaks amplitude and latency very challenging. Analysis of properties of the later peaks and of the presence of the different peaks can however still be relevant for the comparison of monopolar and bipolar stimulation.

The latencies of P1-P4 present a significant difference between monopolar and bipolar stimulation. Monopolar stimulation induces earlier P1, P2 and P4, but later P3 than bipolar stimulation (mult.lin.reg, N=6,  $p < 0.05$  in all 4 cases; Figure 3.21B). The amplitude of P4 is larger following monopolar stimulation than bipolar stimulation (mult.lin.reg., N=6,  $p < 0.05$ ; Figure 3.21C).

### Chapter 3. New Generation Auditory Brainstem Implant (ABI)

The percentage of eABRs presenting each individual peak also shows differences between monopolar and bipolar stimulation, with P2 and P4 being more often present following monopolar stimulation than bipolar stimulation (mult.lin.reg.,  $N=6$ ,  $p < 0.05$  in both cases; Figure 3.21D). This difference is also reflected in the number of peaks, with significantly more peaks present after monopolar stimulation than bipolar stimulation (mult.lin.reg.,  $N=6$ ,  $p < 0.05$ ; Figure 3.21E). These results highlight differences in the pattern of generated eABRs with monopolar and bipolar stimulation.

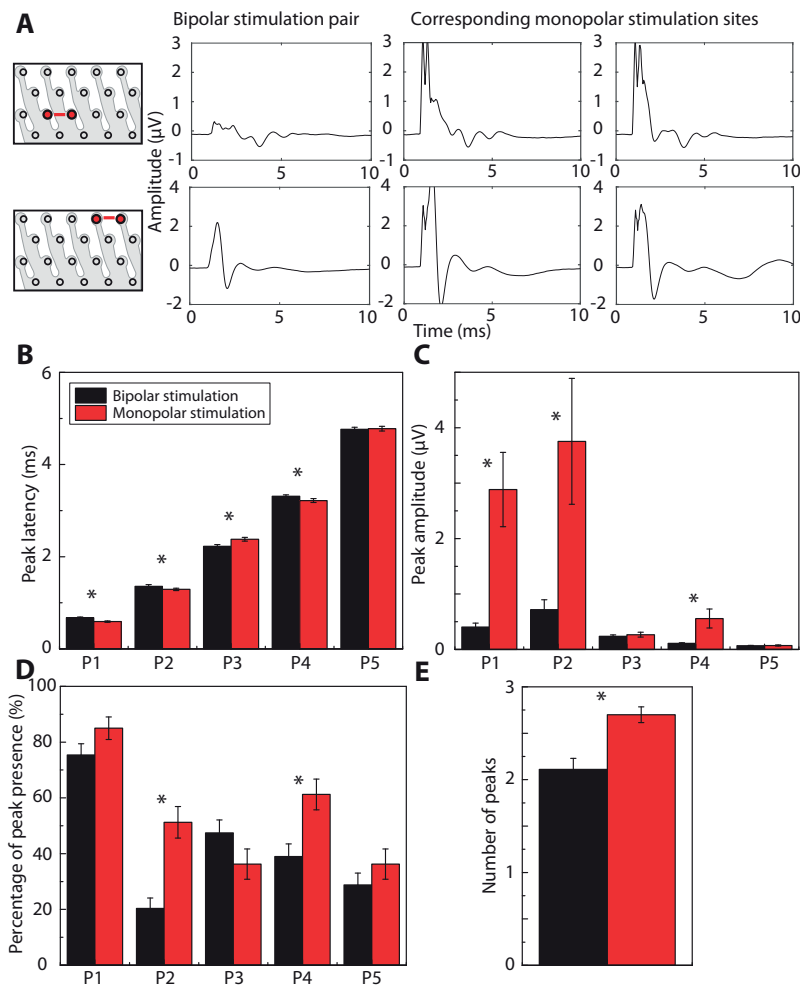


Figure 3.21: A) Examples of eABRs generated with two bipolar pairs and their corresponding monopolar stimulation sites (first line is from rat 10, second line is from rat 8). B-E) Comparison of monopolar and bipolar stimulation on the following eABR parameters: the latency of each peak (B), the amplitude of each peak (C), the percentage of eABRs presenting each peak (D) and the average number of peaks (E).

#### 3.5.5 Discussion

Several effects are identified on the parameters of the eABRs generated by electrical stimulation of the DCN surface. Stimulation with bipolar pairs with 800  $\mu\text{m}$  distance generate eABRs with a larger number of peaks than 400  $\mu\text{m}$  distance. Monopolar stimulation generates larger stimulation artefacts than bipolar stimulation, but also eABRs with a larger number of peaks. Larger eABR peak amplitudes and number of peaks are also obtained following stimulation at rostral DCN locations .

The larger eABRs generated at 800  $\mu\text{m}$  interelectrode distances and monopolar stimulation might correspond to a larger volume of activation, compared to bipolar stimulation with close pairs. The increase in number of peaks however raises more questions, because the peaks are thought to be generated by specific structures of the auditory system, suggesting that the stimulated pathways are different. In acoustically-generated ABRs in rats, five different waves can usually be identified, wave II being the most reliable wave and presenting the largest amplitude. It is generally accepted that the waves I to V are mainly generated by sequential activation of neurons in the auditory nerve (I), the CN (II and III), the superior olive (SO, IV), the lateral lemniscus (LL, V), and the IC (V) [7,72,130,156].

It is difficult to match the identified peaks from the eABRs to the generally accepted pattern of acoustically-generated ABR waves. One hypothesis can be based on the fact that in the recorded data, peak 2 has the largest amplitude and is followed by peak 3, that has the smallest amplitude. P2 and P3 of the eABRs would then correspond to waves II and III of aABRs in rats. The presence of peak 1 is then a question, since the auditory nerve is supposed to be bypassed. In these recordings however, its presence is close to 100%. It might correspond to local activation of the CN, while peak 2 might be activation of the whole cochlear nucleus complex. This hypothesis is supported by the fact that P2 presence and amplitude are much higher at rostral DCN positions, close to the AVCN, so in a better position to stimulate bushy cells, a neuronal type that is hypothesized to be important for ABR generation [130]. The potential correlation of the later waves of the eABRs to IC activity might provide more information on the origin of the eABR peaks.

One hypothesis for the increased number of peaks at rostral locations, with larger interelectrode distances or with monopolar stimulation is that these types of stimulation more efficiently stimulate the bushy cells, and activate a different pathway (VCN-SO-LL-IC pathway) than the direct DCN-IC pathway activated by local stimulation (Figure 3.2), thus generating more peaks. It is then not excluded that the wave corresponding to IC activity varies depending on the pathway that is primarily activated.

Even if specific conclusions on the stimulated neural populations that generate the recorded eABRs might be difficult to reach, the fact that multi-peaked eABRs are generated in most cases is important to consider in a clinical context, as eABR recordings are used intraoperatively as a

guide for the correct positioning of the ABIs. As the ABI is tentatively positioned on the CN surface, stimulation is induced with different pairs across the array, and eABRs are recorded. If one side of the array does not generate any eABRs, its position can be corrected by the surgeon. However, although this technique is very useful, the link between eABRs presence and auditory sensations generated by a given electrode site is not direct. There is some suggestion that auditory sensations can be better predicted by the presence of a certain peak in the eABR, rather than by the presence of the eABR itself<sup>[75]</sup>. In this context, investigating the link between the eABR parameters and the properties of the direct multiunit recordings from the inferior colliculus is thus clinically relevant.

### 3.6 IC response maps post-processing

#### 3.6.1 IC response maps characterization

##### IC maps and PSTH characteristics

In this section, results following stimulation with the 20-electrode array (section 3.4.2) are presented. Electrical stimulation using 400  $\mu\text{m}$  spaced bipolar pairs of the array evokes activity in the IC. These responses are significantly larger than spontaneous activity (t-test,  $N=30$  repetitions, see methods for details) in the great majority of runs (372 out of 398, across all rats and conditions (93.5%)). Activity following each single pulse spans about 20-30 ms after stimulus onset, with a pattern that varies between runs and IC recording sites.

In most cases, the activity is composed of two specific phases, a first phase with one or several bursts of sharp, time-aligned spikes, followed by a phase with a wider, longer-lasting activity (Figure 3.27, on page 78). The average spike rate over the 30 ms time period after stimulus is calculated and color-coded, for each IC recording site and stimulation current level, to generate the IC response maps (Figure 3.22).

Example IC response maps in response to stimulation with 5 electrode pairs illustrate the variety of observed patterns across and within animals (Figure 3.22 shows results for the 7 individual rats). For example, Rat 1 has broad activity and high spike rates in response to most of the 5 stimulation pairs, whereas Rat 6 has narrow activity with moderate spike rates. Within a single rat, responses to different pairs can be broad or narrow (e.g., Rat 3). There are some differences across rats in the evoked spike rates (100 – 400 spikes/s) in response to the highest stimulation level (4 V). The pattern of thresholds across the DCN (Fig. 3.24) was in some cases remarkably even (Rats 1-3), and in others there were “clumps” of electrodes with low thresholds with increased thresholds elsewhere (Rats 5, 6). Electrode pairs with the highest thresholds or no responses were almost always located on the rostral (Rats 5, 6, 7) or medial (1, 2, 3) edges of the array, indicating that they might be located outside the DCN surface.



### 3.6. IC response maps post-processing

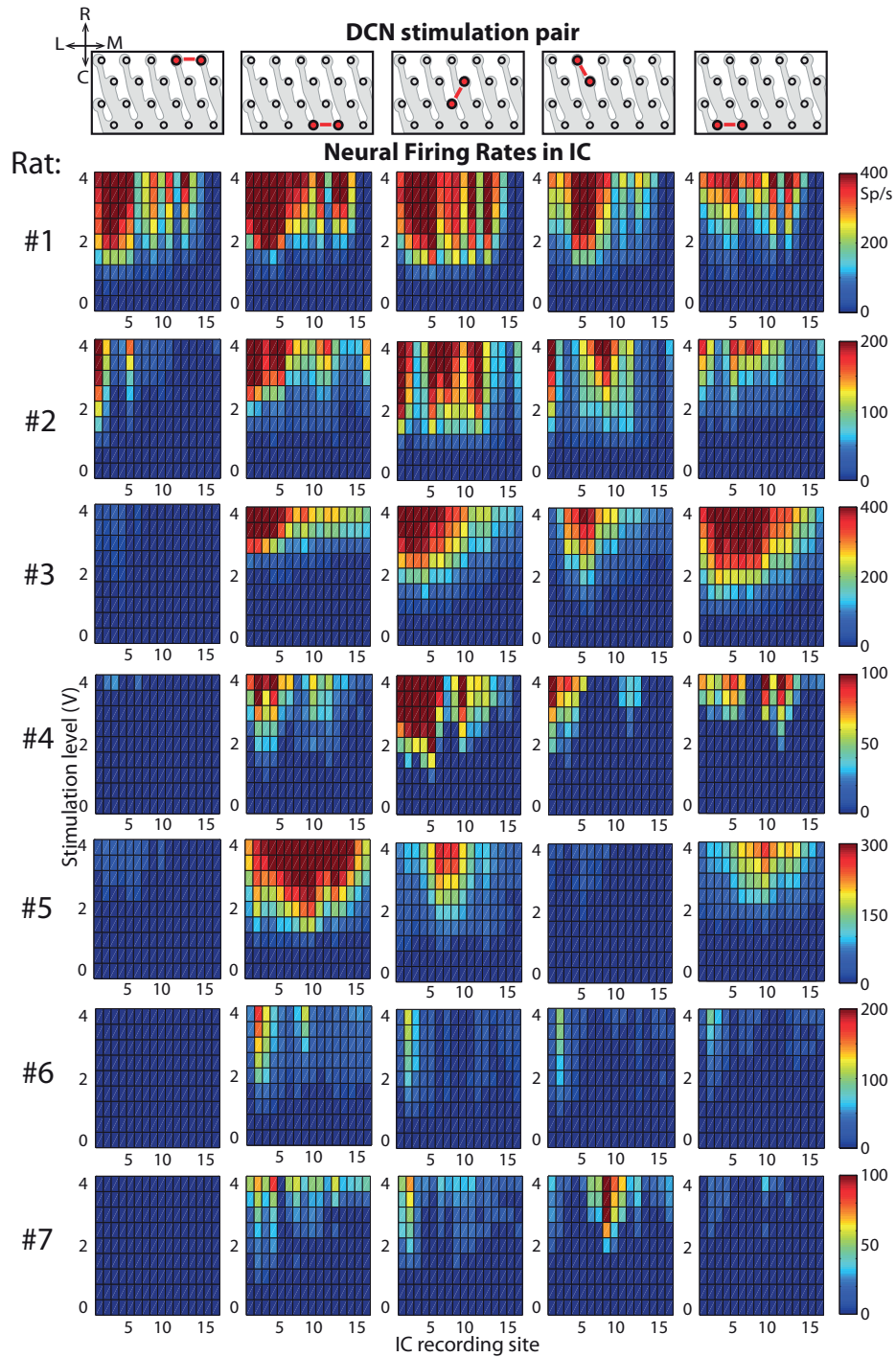


Figure 3.22: Top: Five bipolar pairs of electrodes (red) stimulating different locations on the DCN surface. Rostal (R), caudal (C), lateral (L) and medial (M) directions are indicated. Bottom: Responses to the five bipolar pairs in seven rats. Responses are firing rates (color scales) as a function of stimulation current plotted at each of the 16 IC recording sites.

**Tonotopic organisation**

The stimulating electrode pair position was varied in the ventrolateral-to-dorsomedial dimension (simplified as 'lateromedial'), the tonotopic axis of the DCN<sup>[141,192,200]</sup> and along the rostrocaudal dimension, although that dimension has shorter distances across the DCN and array. For each stimulation pair, the centroid is measured from the IC response maps (Fig. 3.11, Methods). The CF of that recording site, as determined from acoustic responses, is plotted as a function of lateromedial and rostrocaudal position (Figure 3.23). The correlation between the CF and the stimulation pair position along the lateromedial and rostrocaudal dimensions are determined with multiple regression (Table 3.2). The CFs are positively correlated with the pair's lateromedial positions in 4/7 rats (2, 3, 4 and 5) and with the rostrocaudal position in 6/7 rats (1 to 6), as indicated by p-values smaller than 0.05. In the multiple regression analysis, the factor of interaction between lateromedial and rostrocaudal position is significant in rat 1 (Table 3.2). In the other cases, correlations are not significant ( $p > 0.05$ ). In most cases, CFs span the middle part of the rat hearing range, with no access to the low frequencies (1-10 kHz), and very low access to the high frequencies (>32 kHz).

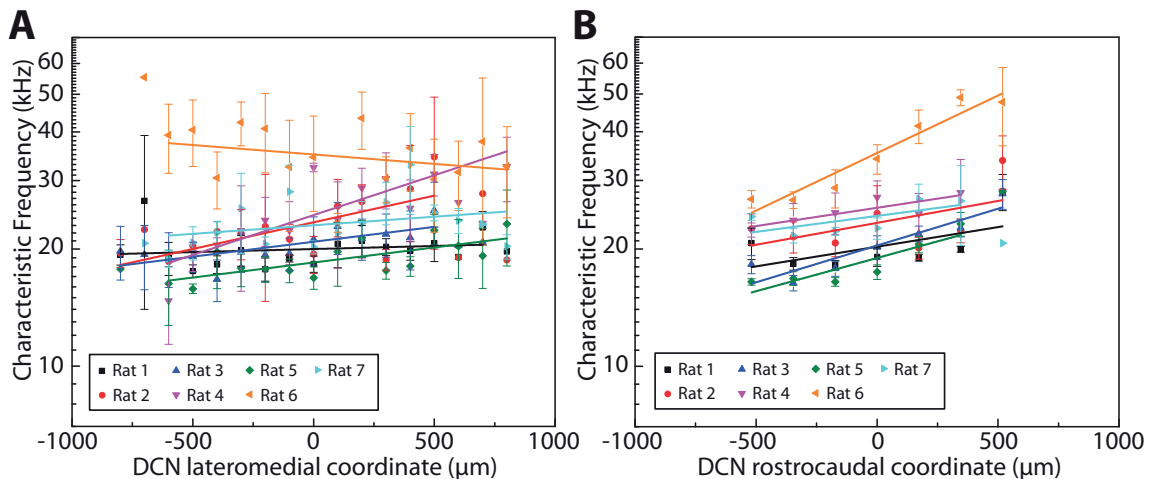


Figure 3.23: Characteristic frequencies (CFs) as a function lateromedial (A) and rostrocaudal (B) dimensions for all DCN stimulation bipolar pairs.

**Intensity parameters**

Variations of the intensity parameters (best threshold, normalized spike rate and width) for individual rats are shown in Fig. 3.24. The correlation between the intensity parameters and the stimulation pair position along the lateromedial and rostrocaudal dimensions are determined with multiple regression (Table 3.2). The correlation between the best threshold and

at lateral positions ( $p < 0.05$  in both cases), but not for the 5 other rats ( $p > 0.05$ ). For rats 4 to 7, the best threshold is significantly correlated to the rostrocaudal positions ( $p < 0.05$  in all 4

cases), with larger threshold at rostral sites.

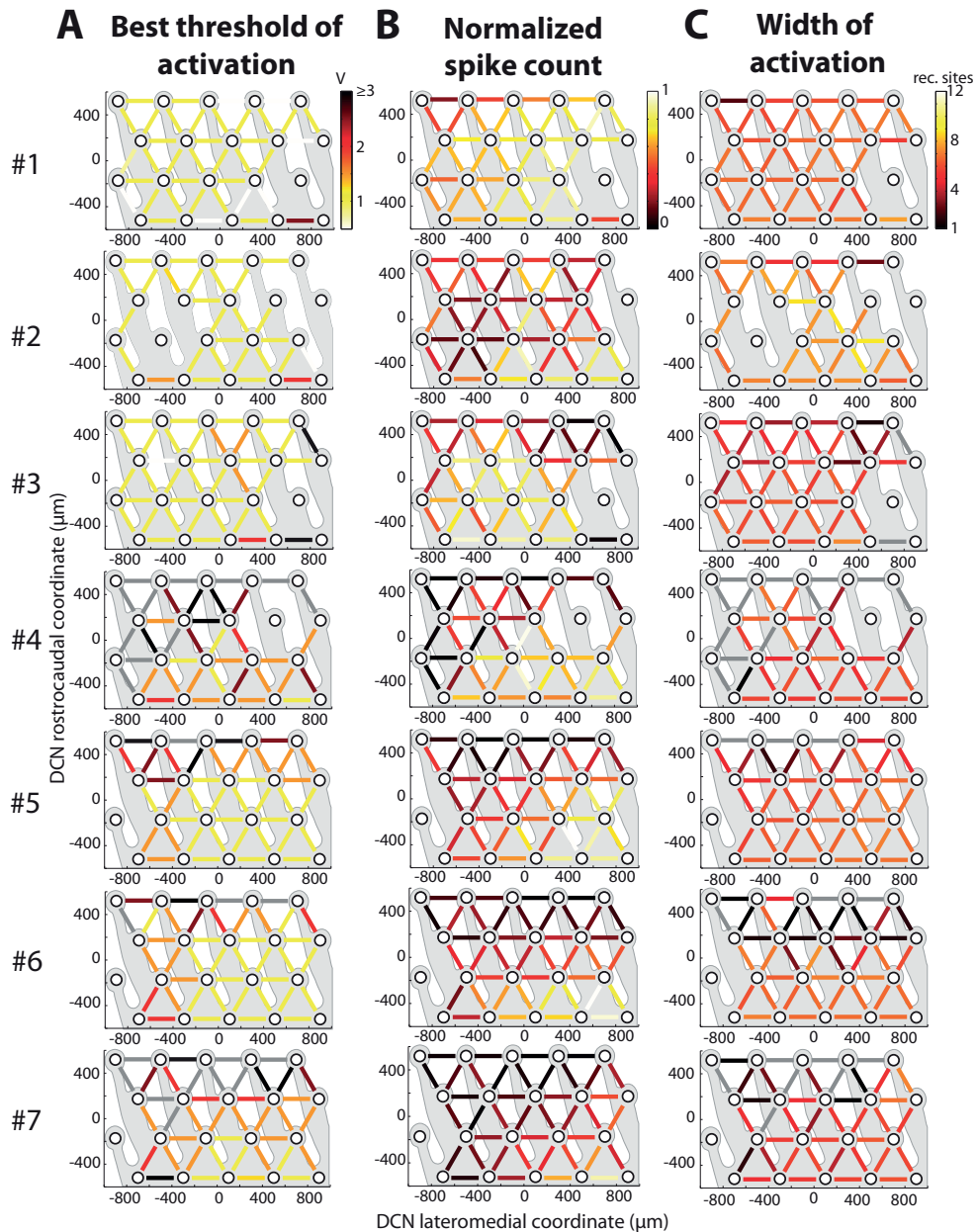


Figure 3.24: IC map parameters variations over the DCN surface for each individual rat. Color-coded values of best threshold (A), normalized spike count (B) and width of activation (C) for all tested pairs of stimulation on the CN surface, for each of the seven rats.

Spike counts are significantly correlated with lateromedial and rostrocaudal positions in all rats ( $p < 0.05$  in all cases), with maximal values on the medial-caudal corner. Width of activation is significantly correlated to lateromedial position in rats 5 and 7 ( $p < 0.05$  in both cases), with a lower width on the lateral part of the implant. Width has significant rostrocaudal

### Chapter 3. New Generation Auditory Brainstem Implant (ABI)

dependence for 6/7 rats (all except 4,  $p < 0.05$  in the 6 cases), with narrower width on the rostral side of the implant.

These analyses show primarily a rostrocaudal effect on the intensity of activation, present in most rats. Stimulation at rostral locations generates activity with lower spike counts, lower widths and higher thresholds than stimulation at caudal locations. Rostral locations are also associated to higher CFs. Overall, the parameters are more stable along the lateromedial dimension, the long dimension of the array. Particularly, 6/7 rats show threshold variations of at most 1 voltage step along the lateromedial dimension (when considering the pairs located centrally, between  $-200$  and  $200\mu$ , along the rostrocaudal axis). This might be resulting from a good contact of the array along the lateromedial axis, a clear advantage of using a conformable array.

	CF LM	CF RC	CF int	W LM	W RC	W int
1	0.218	3.9e-3	1e-4	0.102	7.7e-3	5.7e-3
2	3.1e-3	2.1e-3	0.092	0.060	5.6e-3	0.079
3	0.029	9e-8	0.752	0.281	1.2e-7	0.060
4	1.7e-5	0.023	0.073	0.308	0.661	7.5e-3
5	8.9e-5	1.4e-8	0.102	5.5e-4	1.2e-8	0.368
6	0.079	8.8e-8	0.647	0.461	2.3e-6	0.809
7	0.144	0.155	0.564	3.9e-4	0.030	0.382
	T LM	T RC	T int	N LM	N RC	N int
1	0.505	0.382	0.015	1.4e-5	0.034	0.030
2	0.543	0.174	0.550	0.010	0.024	5.8e-3
3	0.078	0.316	0.202	0.021	1.6e-4	0.833
4	0.220	0.021	0.478	1.4e-4	3.7e-5	0.065
5	3.8e-3	3.5e-6	0.750	1.4e-9	2.2e-13	2.0e-3
6	2.3e-3	2.6e-3	0.920	5.2e-9	5.6e-22	1.9e-3
7	0.536	4.1e-3	0.027	4.1e-8	1.4e-7	1.2e-4

Table 3.2: P-values of the statistical tests of single rats p-values of the multiple regression analyses of characteristic frequency (CF), width (W), best threshold (T) and spike count (N) for each single rat. For each test, the p-value for the lateromedial (LM) and rostrocaudal (RC) position factors, as well as for the interaction factor are shown. Significant values ( $p < 0.05$ ) are shown in blue.

### 3.6.2 Location-specific activity

#### Average subtraction

This section presents a processing strategy that refines the response maps by subtracting their average activity. This strategy was employed because IC response maps from electrode pairs located at different lateral-to-medial positions show a common pattern of activity with similar CFs. Subtraction of this common pattern might highlight location-specific components that

### 3.6. IC response maps post-processing

are present but masked in the raw IC response maps. The average activity, calculated by averaging all IC response maps with significant activity for each rat, was subtracted from each individual response map. Averages of all maps (for each rat) had CFs of  $22.4 \pm 1.5$  kHz and width of activations of  $6.4 \pm 0.3$  recording sites. In the example shown here (Fig. 3.25A), the two IC response maps show stronger pattern variations after average subtraction than in the raw data.

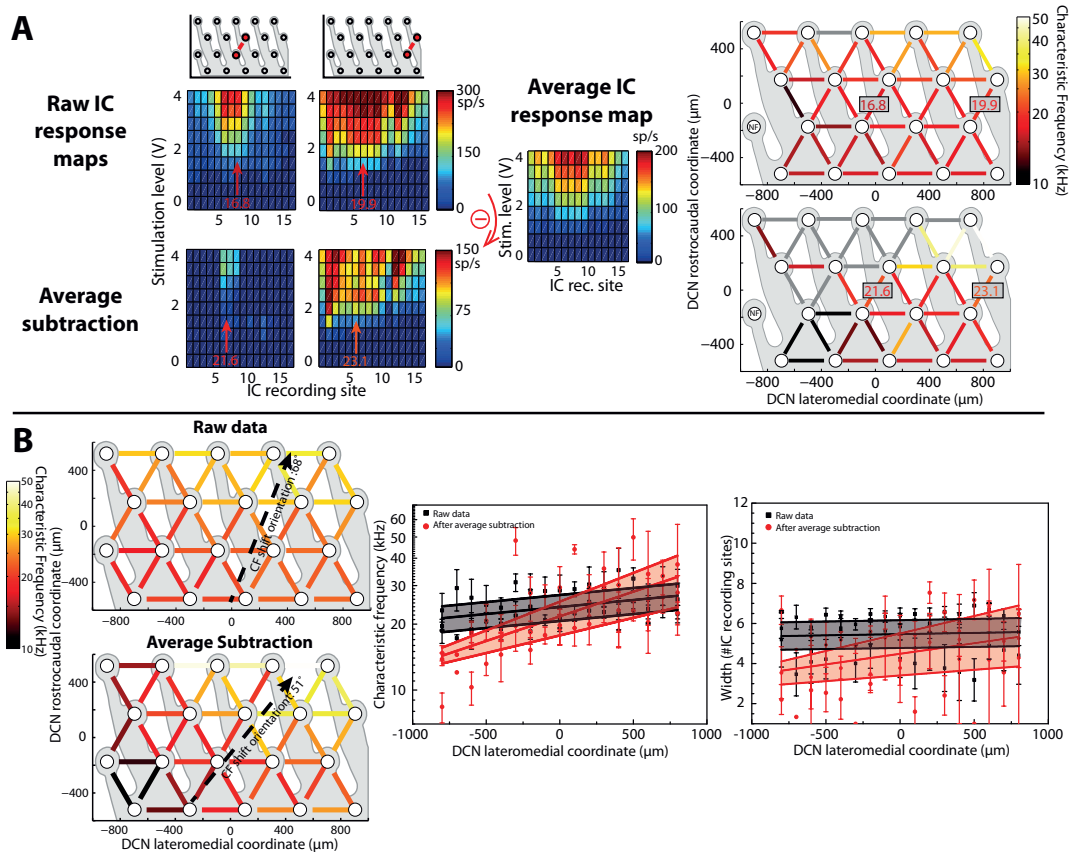


Figure 3.25: Subtraction of average activity reveals tonotopic shift of CF. A) Top: Two bipolar pairs of stimulating electrodes (red) chosen because they differ in lateromedial position along the DCN's tonotopic axis. In response to these stimulating pairs, the color plots show the raw response maps and the maps after subtraction of the average activity. CFs for all electrode pairs are plotted in the matrices on the right, with color-coded segments (see scales) between the two electrodes of each pair, across the DCN's lateromedial (x axis) and rostrocaudal (y axis) dimensions. Some maps with raw activity below average show no remaining activity after average subtraction (grey segments). B) Color-coded matrices of CFs (left) before (top) and after (bottom) subtraction of average activity, averaged across all rats. The preferred orientations of the CF shift are indicated by the dotted lines. Plot of CF (middle) before and after average subtraction and for all pairs and their lateromedial position. Plot of width of activation (right) before and after average subtraction for all pairs and their lateromedial position. Shaded areas are calculated with the regression of the top and bottom of the standard errors.

### **Tonotopic organisation before and after average subtraction**

After average map subtraction, the response CF of individual maps is positively correlated with the electrode pair position along the lateromedial axis in 5/7 rats (vs. 4/7 before subtraction, multiple linear regression,  $p < 0.05$  in 5 significant cases). Multiple regression analyses with the data from the 7 rats demonstrate significant interactions between before vs. after average subtraction and the lateromedial coordinate ( $p < 0.05$  for the interaction factor,  $N=7$ ). Such interaction resulted in a greater range of CFs after average subtraction than for the raw data. In one example (Fig. 3.25A), the range of CFs found in the IC was larger after average subtraction (8.1 to 51.4 kHz, 2.67 octaves) compared to the raw data (12 to 31.6 kHz, 1.4 octaves). Data from all subjects (Fig. 3.25B, middle panel) after average subtraction also showed a greater range of CFs (8.4 to 49.9 kHz, 2.57 octaves) compared before average subtraction (17.2 to 35.3 kHz, 1.04 octaves). We define a vector across the DCN characterizing the orientation of the CF variations. The orientation of this vector, the “CF shift orientation” is determined by performing a linear regression of corresponding CF values of IC responses according to the electrode pair position along the lateromedial and rostrocaudal axes of the DCN (Fig. 3.25B, left panels). The orientation is  $68^\circ$  for the raw data, and  $51^\circ$  after average subtraction, with respect to the lateromedial axis.

### **Intensity parameters before and after average subtraction**

The width of activation is on average lower after subtraction of the average activity than in raw data (multiple linear regression,  $N=7$  rats,  $p < 0.05$ ), showing higher frequency selectivity in the IC (Figure 3.25B, right panel and 3.26C). These findings suggest that the common activity is widespread, because the subtraction of the average map results in more frequency-specific, narrower widths of activation. In addition, the width of activation shows a significant correlation with the lateromedial position of the stimulating electrode after average subtraction (multiple linear regression,  $N=7$ ,  $p < 0.05$ ).

After subtraction of average activity, best thresholds are on average higher and spike counts are lower than in raw data (multiple linear regression,  $N=7$ ,  $p < 0.05$  in both cases; Figure 3.26A-B). The analysis of these parameters shows a lower intensity of the activity after average subtraction than in the raw data, consistent with the fact that the location-specific represents a subset of the raw activity.

### **3.6.3 Early and late phases of activity**

#### **Separation between early and late spikes**

This section presents a processing strategy that refines the response map by segregating the responses into two temporal windows. This strategy is employed because the responses, as measured by poststimulus time histograms (PSTHs), show an early phase with a sharp,

time-aligned pattern and a later phase with a wider, longer-lasting pattern (Fig. 3.27).

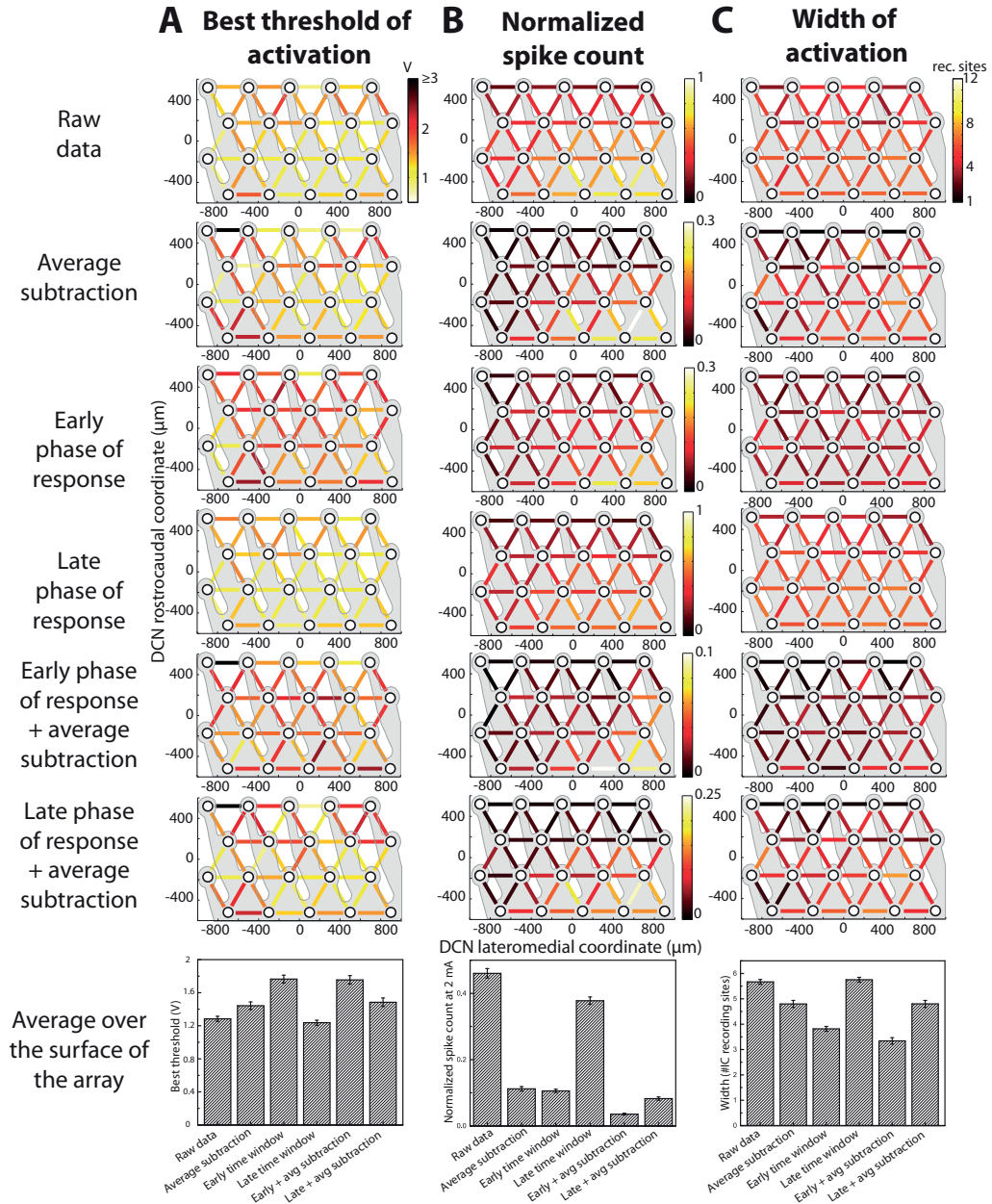


Figure 3.26: Average IC map parameters variations over the CN surface following different processing types. Color-coded values of threshold (A), normalized spike count (B) and width of activation (C) for all tested pairs of stimulation on the CN surface. Bottom: Average over surface and standard errors of the same parameters, for each processing type.

Despite the consistency of this pattern, the limit between the early and late phases is variable across runs between and within animals. An automatization of the limit determination is

### Chapter 3. New Generation Auditory Brainstem Implant (ABI)

excluded because of this variability, so the limit is individually fixed for each run and each IC recording site. This limit is determined at the transition between the early and late phases, knowing that in most cases some minimal overlap is present.

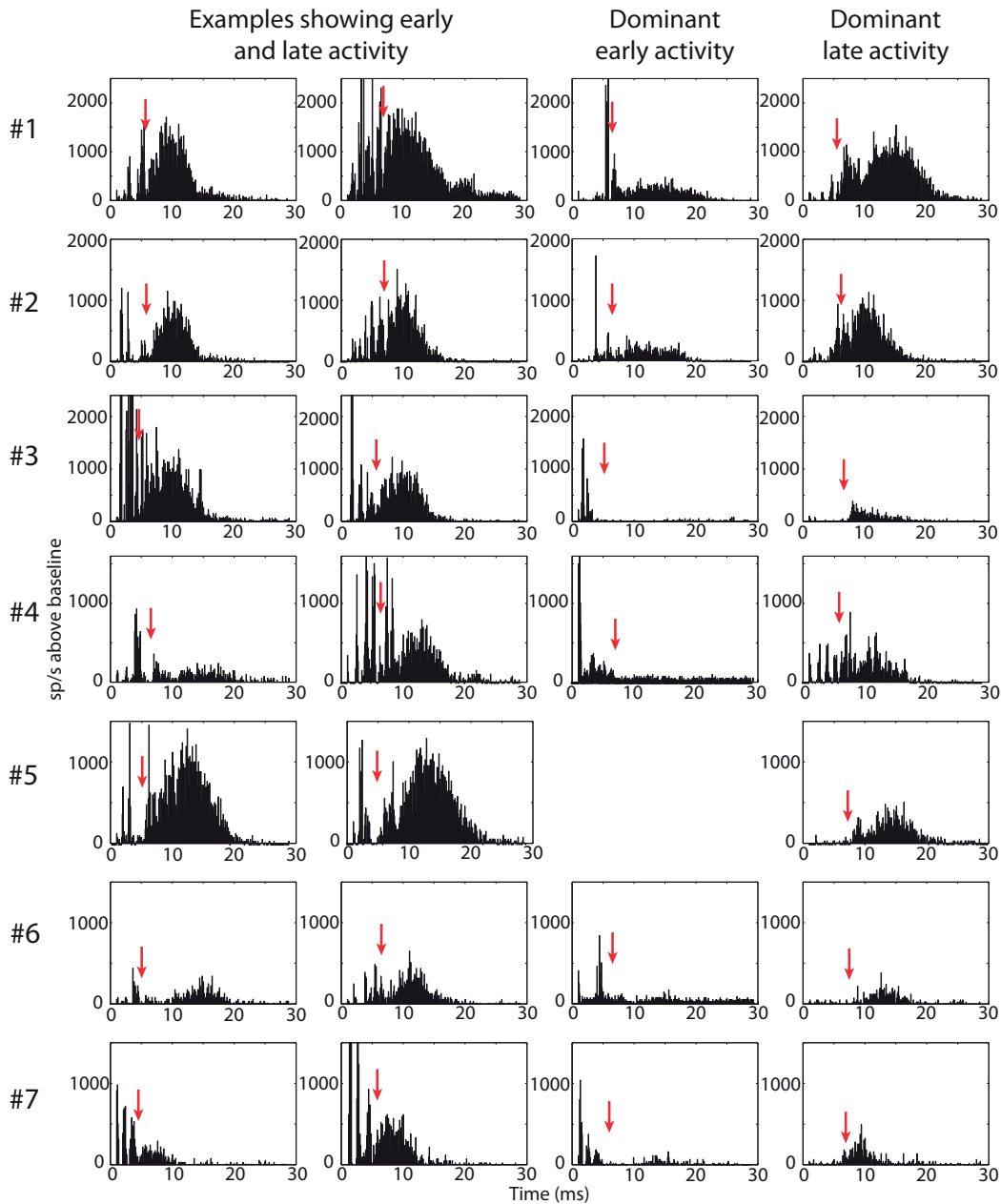


Figure 3.27: Post-stimulus time histograms (PSTH) from IC recording sites for various stimulation pairs for the seven rats. Cutoff time between early and late activity are indicated by the red arrows. Columns 1 and 2 show typical patterns of response with early and late activity clearly discernable. Column 3 shows examples of PSTHs with strong early activity, and weak or absent Gaussian-shaped late activity. Column 4 shown examples of PSTHs with weak or absent early activity.



Average cutoff times across all runs and IC recording sites in each of the 11 rats ranged from 6.91 to 7.39 ms post stimulus. A significant effect of the IC recording site on the cutoff time was observed in 3 rats out of 11 (one-way Anova, N=55 runs,  $p < 0.05$  in these 3 cases), with low IC recording site numbers (high acoustic frequencies) having earlier cutoffs than high IC recording site numbers (low acoustic frequencies). The maximal difference in cutoff time across all recording sites for a single rat was 0.81 ms. For the remaining 8 rats, no effect of the IC recording site was obtained (one-way Anova, N=55,  $p > 0.05$  in the 8 cases).

**Timing properties of the early phase of activity**

Figure 3.28 shows post-stimulus time histograms (PSTH) of early phase of responses of five different IC recording sites, following stimulation with five different pairs at the surface of the DCN. Responses have a variety of shapes and timings, but are most often organised in one or several time-aligned bursts of spikes.

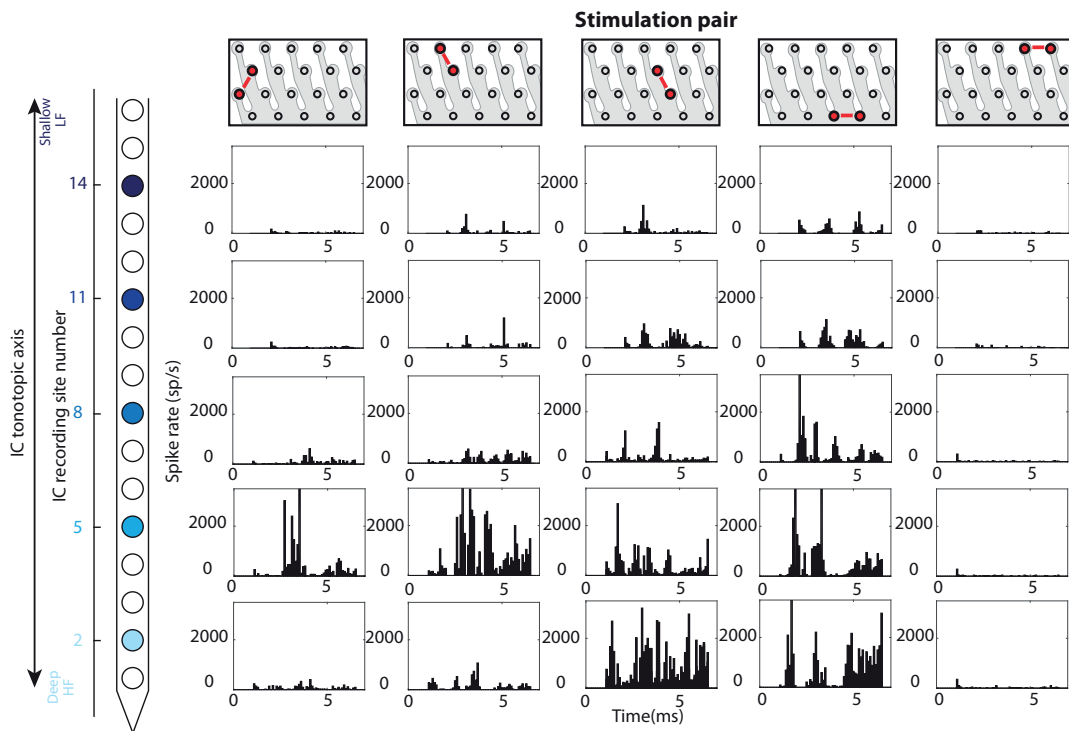


Figure 3.28: PSTHs of the early phase of response of five IC recording sites following DCN surface stimulation with five different stimulation pairs (from rat 3).

In the example shown here, shallow IC recording sites (corresponding to low CFs) have weaker responses than deep IC recording sites (corresponding to high CFs). In addition, the stimulation pair located on the rostro-medial edge of the array generates very weak activity. The responses thus show a dependence on the IC recording site, as well as on the stimulation

location.

### Timing properties of the late phase of activity

The timing of the late, gaussian-shaped activity is analyzed by extracting the time centroid of this activity (Figure 3.29A). This parameter is extracted for each run at each level and IC recording site, and the values at a stimulation level 1 V higher than threshold are considered for further analysis.

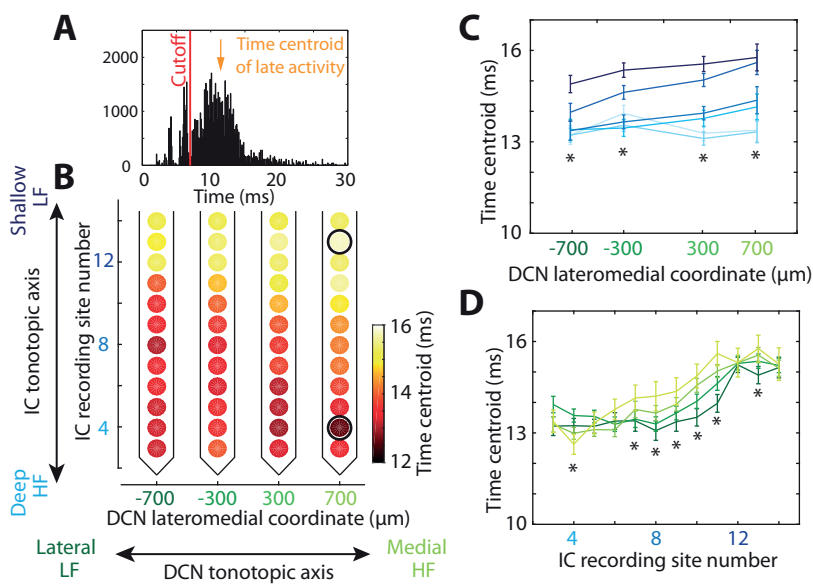


Figure 3.29: A: PSTH showing the early and late activity, and the measured time centroid of the late activity. B: Time centroid of late activity along the 16 IC recording sites, following DCN surface stimulation at different lateromedial positions. Maximal and minimal values of time centroid are shown with a black circle. C-D: Same data as B plotted as a function of DCN lateromedial coordinate for different IC recording sites (C), and as a function of IC recording site for different lateromedial positions (D). Significant differences between the IC recording sites (C) or DCN stimulation lateromedial positions (D) (multiple linear regression,  $p < 0.05$ ) are indicated with a star.

The time centroid of activity following DCN surface stimulation at different locations along the lateromedial axis and recorded from all IC recording sites is color-coded and displayed on Figure 3.29B. The activity is occurring later at shallow IC locations, corresponding to low frequency fibers activity, than at deep IC locations, corresponding to high frequency fiber activity, for all lateromedial stimulation locations (multiple linear regression,  $N=7$ ,  $p < 0.05$  for the IC recording site factor in all cases). Figure 3.29C shows the time centroid values for 6 IC recording sites at all lateromedial locations. The increase in time centroid with IC recording

site is significant for all lateromedial positions, indicated with a star.

The second effect is highlighted in Figure 3.29D, showing the time centroid variations with IC recording site number for all lateromedial locations. It shows that at low IC recording sites (high frequencies), the time centroid is smaller for medial stimulation sites (high frequencies) than for lateral stimulation sites. This effect is significant for IC recording site 4 (multiple linear regression,  $N=7$ ,  $p < 0.05$  for the lateromedial position effect, for the IC recording site 4). On the other hand, for high IC recording site numbers (low frequencies), the time centroid is lower for lateral stimulation locations (low frequencies) than for medial stimulation locations. Significance is reached for IC recording sites 7,8,9,10,11 and 13 (multiple linear regression,  $N=7$ ,  $p < 0.05$  for the lateromedial position effect, for the IC recording sites 7-10 and 12). Overall, it means that the time centroid of late activity is minimal when the characteristic frequency of the IC recording site matches that of the stimulation location on the DCN.

These results mean that IC neurons with low characteristic frequency respond slower than IC neurons with high characteristic frequency. This might be because of different speeds of fibers, or because they are activated in different ways, direct or indirect. The small lateromedial location dependence effect can be linked to the small lateromedial location dependence of other studied parameters in the late activity (CF, width...), described in the next section. This confirms that the great majority of activity in the late phase of responses is likely not location specific.

#### **Tonotopic organisation of the early and late phases of response**

Compared to the late phase of response, the early phase shows more correlation of response CF with the electrode pair position along the lateromedial axis (positive correlation in 7/7 rats vs. 4/7 rats in the late phase of response, multiple linear regression,  $p < 0.05$  in all cases). Considering data from one rat (Fig. 3.30A, left), the range of CF shift is greater than seen with the late phase of response (8.1 to 51.4 kHz, 2.66 octaves vs. 14 to 36.1 kHz, 1.37 octaves). Considering all seven rats (Fig. 3.30B), the early phase of response shows an access to the mid-frequency range (15.3 to 35.8 kHz, 1.23 octaves), only slightly larger than the range of CFs accessed in the late phase of responses (17.2 to 35.1 kHz, 1.03 octaves). However, the early and late phases of response vary dramatically in their CF shift orientation ( $4^\circ$  orientation for the early phase of responses and  $76^\circ$  orientation for the late phase of responses). There is a larger CF change with lateromedial position for the early vs. the late phase of response (Fig. 3.30B, middle panel; mult.lin.reg,  $N=7$ ,  $p < 0.05$  for the interaction between latency and position). The late phase of responses shows a pattern that is very close to the raw data, both in the range of accessed CFs (17.2 to 35.1 kHz vs 17.2 to 35.3 kHz, 1.03 vs 1.04 octaves) and in the CF shift orientation ( $76^\circ$  vs  $68^\circ$ ).

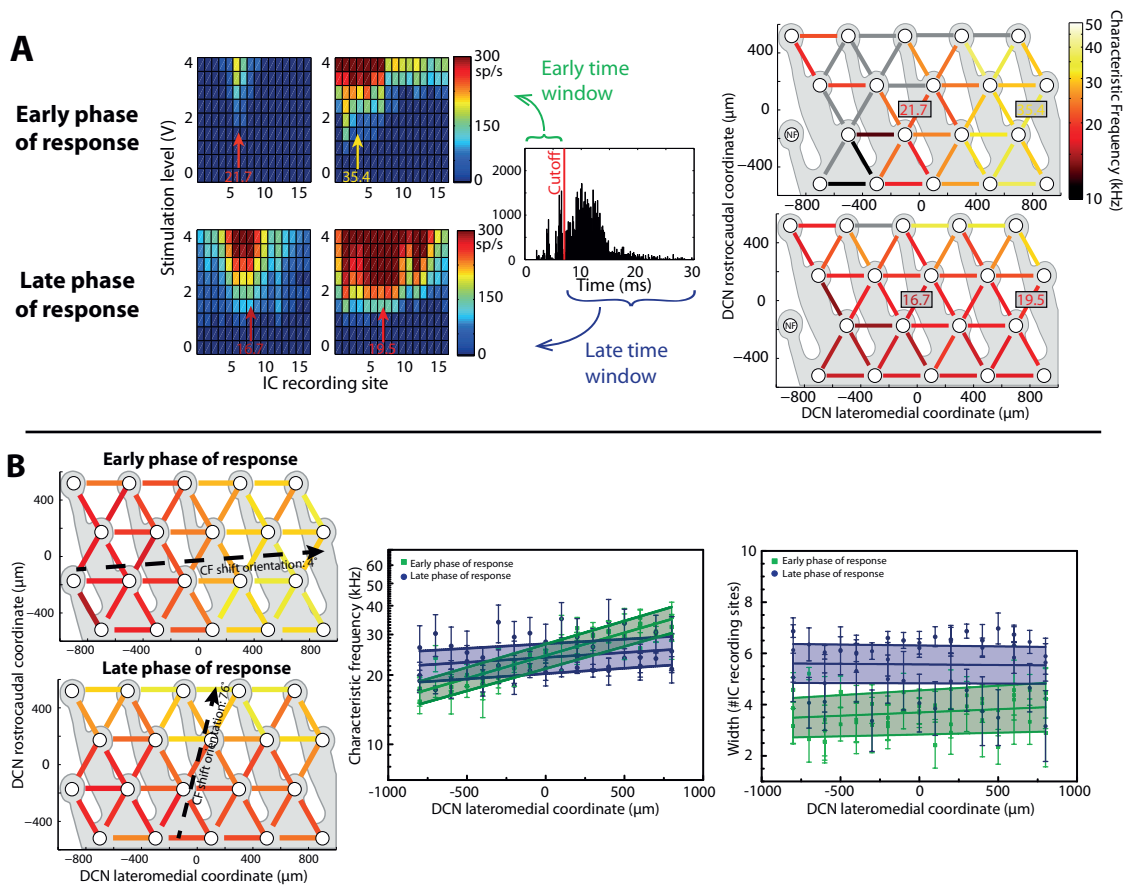


Figure 3.30: Tonotopic shift of CF in early and late phases of response. A) Top: Two bipolar pairs of stimulating electrodes (red) chosen because they differ in lateromedial position along the DCN's tonotopic axis. In response to these stimulating pairs, the color plots show the response maps of early and late phases of activity. CFs for all electrode pairs are plotted in the matrices on the right, with color-coded segments (see scales) between the two electrodes of each pair, across the DCN's lateromedial (x axis) and rostrocaudal (y axis) dimensions. Some maps show no significant activity (grey segments). B) Color-coded matrices of CFs (left) in the early (top) and late (bottom) phases of activity, averaged across all rats. The preferred orientations of the CF shift are indicated by the dotted lines. Plot of CF (middle) for the early and late phases of response, for all pairs and their lateromedial position. Plot of width of activation (right) for the early and late phases of response, for all pairs and their lateromedial position. Shaded areas are calculated with the regression of the top and bottom of the standard errors.

### Intensity parameters of the early and late phases of response

In the early phase of responses, the width of activation is significantly correlated with the rostrocaudal location of stimulation, with lower values on the rostral side of the array (mult.lin.reg,  $N=7$ ,  $p < 0.05$  for the rostrocaudal location factor). Multiple linear regression analysis of the

normalized spike count shows a significant effect of the lateromedial position, the rostrocaudal position as well as a significant interaction factor between the two ( $p < 0.05$  for all 3 factors). The highest spike counts are observed at the medial-caudal corner of the array. The best threshold of activation does not show any significant correlation with the position of the stimulation pair (Figure 3.26, page 77) (mult.lin.reg,  $p > 0.05$  for the lateromedial and rostrocaudal position factors, and for the interaction factor).

In the late time window, the width of activation is significantly correlated with the rostrocaudal location of stimulation, with lower values on the rostral side of the array, similarly to the early phase of responses (mult.lin.reg,  $N=7$ ,  $p < 0.05$  for the rostrocaudal position factor). The normalized spike count also shows a similar behavior than in the early phase of responses, with all three factors of the multiple regression analysis being significant ( $N=7$ ,  $p < 0.05$  for the lateromedial and rostrocaudal position and their interaction). The best threshold however shows a different behavior than in the early time window and is significantly correlated to the rostrocaudal position of stimulation, with larger threshold values on the rostral part of the array (mult.lin.reg,  $N=7$ ,  $p < 0.05$  for the rostrocaudal position factor).

In the comparison of both phases of responses, the width of activation is significantly lower for the early phase compared to the late phase of responses (Figure 3.26 and 3.30B, right; mult.lin.reg,  $N=7$ ,  $p < 0.05$ ), showing a higher frequency selectivity in the IC. Both phases show no significant dependence on lateromedial position (mult.lin.reg,  $N=7$ ,  $p > 0.05$  for the lateromedial position factor in both cases). In the early phase of responses, the best threshold of activation is significantly higher than in the late phase of responses and the normalized spike count is significantly lower (mult.lin.reg,  $N=7$ ,  $p < 0.05$  in both cases).

#### 3.6.4 Combined processing - average subtraction on the early phase of activity

##### Why combine both types of processing?

Previous analyses show that average subtraction and extraction of the early phase of response isolates activity with different properties from all the IC recorded spikes. Location-specific spikes obtained after average subtraction show a large range of CFs over the surface, but an orientation of the CF shift that does not match the underlying DCN tonotopic organisation. Spikes recorded in the early phase of activity show a CF shift over the array surface that is in the same orientation as the DCN tonotopic organisation. The range of CFs obtained by stimulating at different locations on the surface is however smaller. In addition, both processings generate a lower width of activation in the IC than raw data and late phase of responses.

Here, we propose a combination of the two processing strategies, namely subtraction of the average map of the early phases of responses. If the early phase of responses consists of a mix between location-specific and general activity, this combined strategy will allow an extraction of the location-specific spikes within the early phase of activity that might show a

tonotopic organisation closely matching that of the DCN.

### Tonotopic organisation after combined processing

After a combined processing strategy that subtracts the average IC response map of only the early phase of response, there was better correlation of the response CF with the electrode pair position (now in 5/7 rats vs. 4/7 rats before, mult.lin.reg,  $p < 0.05$  for 5 significant cases). The correlation between the CF and the lateromedial position is significantly different between the combined processing and each individual processing (Fig. 3.31A, mult.lin.reg,  $p < 0.05$  for the interaction between the lateromedial position and the processing type in both cases). The range of CFs obtained across the DCN, 8.34 to 39.4 kHz (2.24 octaves), is larger than for the early phase of response, 15.3 to 35.8 kHz (1.23 octaves), but slightly smaller than for the average subtraction, 8.4 to 49.9 kHz (2.57 octaves). The preferred orientation of the CF shift is  $12^\circ$  (Fig. 5A, inset), close to the CF shift orientation obtained with the early phase of response ( $4^\circ$ ) but very different than raw data ( $68^\circ$ ) and average subtraction ( $51^\circ$ ).

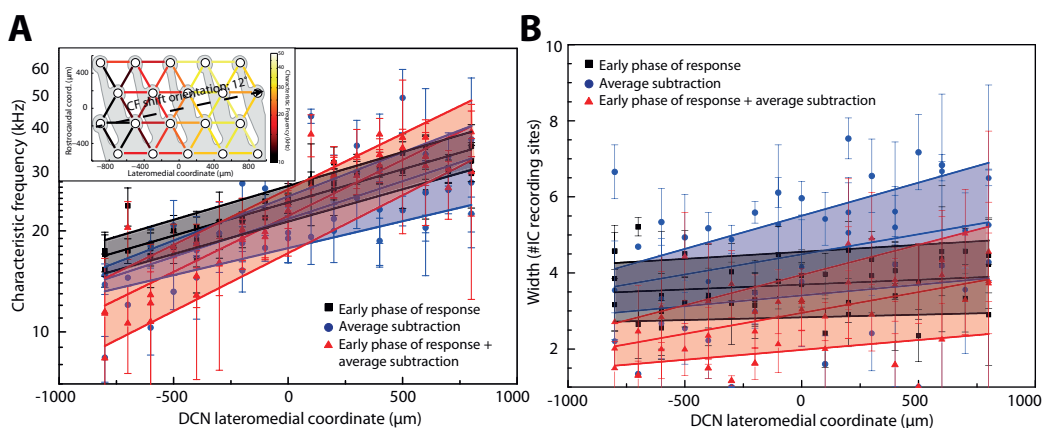


Figure 3.31: A) Plot of CF after extraction of the early phase of responses, after subtraction of the average activity, and after both processing types combined for all pairs and their lateromedial position. Inset: Color-coded matrices of CFs after extraction of early activity and subtraction of average activity. B) Plot of width of activation for the same processing types as in A for all pairs and their lateromedial position.

### Intensity parameters after combined processing

The width of activation after combined processing is narrower than after each individual processing (mult.lin.reg,  $N=7$ ,  $p < 0.05$  in both cases), confirming that this processing extracts the spikes with the most frequency specific activation in the IC. After combined processing, it is significantly correlated to the lateromedial and the rostrocaudal positions of the stimulation pair (mult.lin.reg,  $N=7$ ,  $p < 0.05$  for the lateromedial and rostrocaudal position factors). The best threshold of activation after combined processing is significantly higher than after average subtraction (mult.lin.reg.,  $N=7$ ,  $p < 0.05$ ), but similar to the early phase of responses

(mult.lin.reg.,  $N=7$ ,  $p > 0.05$ ). Similarly to the early phase of responses, the best threshold after combined processing is not significantly correlated to the position of the stimulation pair (mult.lin.reg.,  $N=7$ ,  $p > 0.05$  for the lateromedial and rostrocaudal position factors). The normalized spike count is significantly lower than after both individual processing types (mult.lin.reg.,  $N=7$ ,  $p < 0.05$  in both cases), and corresponds to a small portion of the total generated spikes. It is correlated to both the lateromedial and the rostrocaudal positions of stimulation (mult.lin.reg.,  $N=7$ ,  $p < 0.05$  for the lateromedial and rostrocaudal position factors).

#### 3.6.5 Synthesis

The different processing strategies presented are tools to better understand the different components of the multiunit activity generated in the IC following electrical stimulation of the DCN surface. The structures that are stimulated are likely to be a mix between wide and narrow frequency tuned neurons, fibers of passage and neuronal somata, fast and slow conducting axons, and monosynaptic and polysynaptic pathways. Thus, extracting location-specific activity, and discriminating between the early and late phase of responses depending on the timing pattern of activity generated in the IC allows the extraction of different components of this response.

The comparison of early and late time windows is particularly interesting to consider in this respect, as it shows that both phases of responses have different patterns of activation and tonotopic organisations. Particularly, the early phase of responses consists of one or several short, time-aligned bursts of spikes starting as early as 1-2 ms after stimulus, and having a lateromedial tonotopic organisation covering part of the rat hearing range. The late phase of responses shows a very different pattern with wider activity and a larger number of spikes spanning a longer time interval, with a rostrocaudal range of CFs. The time centroid of activity shows mainly a dependence on the IC recording site, and only minimally on the lateromedial location of stimulation. These different behaviors suggest that the two phases of responses might be generated by the activation of different neuronal populations. This will be further discussed in the general discussion of this chapter.

One of the main interests of this study is the quantification of the access to the tonotopic axis of the DCN: what is the range of frequencies that can be accessed, what is the width of activity in the IC? It is known that the tonotopic axis of the DCN follows a lateromedial orientation, and this information is used as a guide during analysis. Overall, combining both strategies allows a maximization of the range of CFs and a minimization of the width of activation in the IC, with a (close to) lateromedial orientation of the CF shift. Because of these properties, it is hypothesized that the extracted spikes following combined analysis are generated by the frequency-tuned neurons along the lateromedial tonotopic axis of the DCN. For these reasons, this combined processing strategy is used in sections 3.8 and 3.9, where the effects of different stimulation parameters and stimulation electrodes configurations on the access to tonotopy

are investigated.

### 3.7 Effect of stimulation level

#### 3.7.1 Characteristic frequency

The effect of increasing stimulation level on the characteristic frequency of IC response maps is shown on figure 3.32A, for the different types of processing presented earlier. The general observed effect is a decrease in CF at increasing stimulation level. In the raw data and the late phase of responses, this effect is significant at nearly all lateromedial locations (mult.lin.reg,  $N=7$ ,  $p < 0.05$ ). In the types of processing that were shown to extract spikes with better tonotopic organisation however (average subtraction, early phase of responses and combined processing), the decrease is significant only at some medial locations (indicated with a star on figure 3.32A) but not at lateral locations.

#### 3.7.2 Intensity parameters

The width of IC activity (Figure 3.32B) significantly increases with stimulation level for all types of processing (mult.lin.reg,  $N=7$ ,  $p < 0.05$ ), following a close to logarithmic increase. A higher saturation level might be reached in the early phase of responses than in the other types of processing, and the corresponding curve shows a close to linear increase in width with stimulation level.

It is interesting to notice here that the average subtraction has a greater effect at high stimulation levels than at low stimulation levels on the width. Indeed, the width obtained with raw data and average subtraction is similar at threshold, and higher for raw data at higher levels. The width obtained in the early phase of responses and with combined processing is similar at threshold, and is higher for the early phase of response at higher stimulation levels. The average subtraction thus induces a decrease in width of activation at high stimulation levels, but not at threshold.

The spike count, normalized for each rat to the highest spike count measured in the raw data (Figure 3.32C), also shows an increase with stimulation level (mult.lin.reg,  $N=7$ ,  $p < 0.05$ ). The increase in spike count is more linear than the increase of width and does not seem to reach a plateau in the tested range of levels.

If the spikes in the early and late time window come from different neuronal populations, it is interesting to look at the ratio of all generated spikes that are in the early phase of responses and its variation with stimulation level. It can be an indicator of different behaviors of activation of the different populations of neurons. Here, the fraction of early spikes is significantly



### 3.7. Effect of stimulation level

larger at medial locations at high stimulation levels (significance is reached at 1.5 V above threshold and higher, mult.lin.reg,  $N=7$ ,  $p < 0.05$ ). No effect of the stimulation level is however identified (Figure 3.32D).

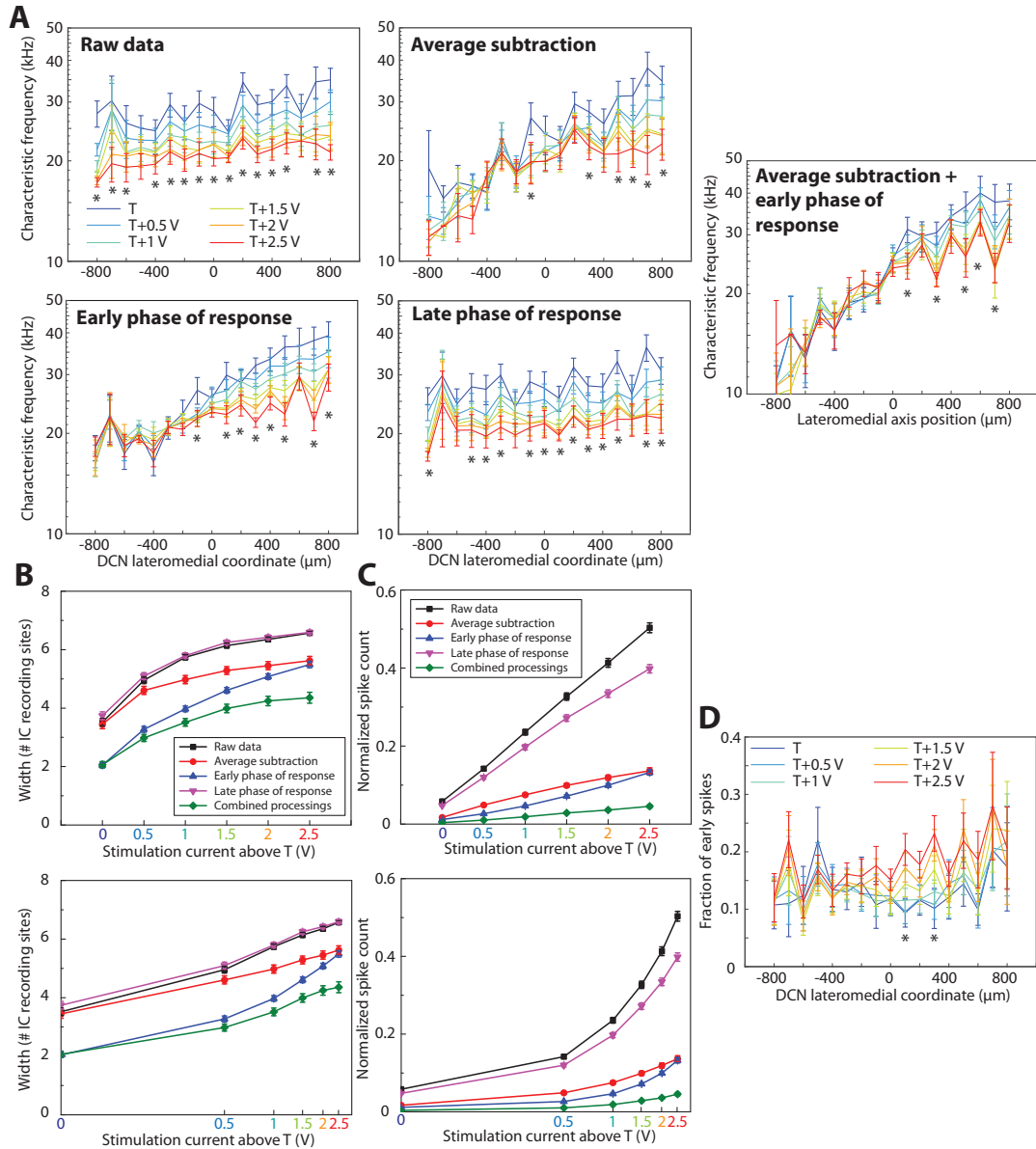


Figure 3.32: A) Characteristic frequencies obtained following stimulation at different lateromedial positions with increasing stimulation current (from blue to red), after the different processing strategies. B-C) Effect of increasing stimulation level following a linear (top) or logarithmic (bottom) scale on the width of IC activity (B) and the normalized spike count (C), after the different processing strategies. D) Fraction of spikes in the early phase of responses following stimulation at different lateromedial positions with increasing stimulation level. Statistically significant differences between levels are indicated with a star.

### 3.7.3 Synthesis

The analysis of effect of stimulation level on the IC response map characteristic frequencies shows a general decrease in CFs at higher voltages, together with an increase in width and spike count. The increased volume of activation following stimulation with higher voltage could help explain the obtained results. The higher widths can be explained by the greater lateral extent of stimulation. The decrease in CF could be explained by the increased depth of stimulation if the deeper layers correspond to neurons with lower CFs. A similar change in CF with stimulation level in ABI patients might lead to altered pitch perception when the stimulation level is changed, and an increased loudness would be combined to a change of pitch in amplitude modulation strategies. This might help explain the difficulty in pitch ranking of the different electrodes experienced by some ABI patients<sup>[13,112]</sup>.

As described earlier, the decrease in CF at increasing stimulation levels does not show the same behavior in the tonotopically-organized activity (average subtraction and early phase of responses). Particularly, CFs don't decrease at lateral stimulation sites, even if the width of activation and spike count increase. This could be explained by the fact that the neurons generating the tonotopically-organized activity are forming a thin layer. In that case, increasing the stimulation level would generate an increase in width and spike count due to the increased lateral extent of stimulation, but no decrease in CF since no tonotopically-organized neurons with lower CFs would be present at deeper locations.

## 3.8 Stimulation pairs orientations and interelectrode distances

During bipolar electrical stimulation, the current is passed between two electrodes of small (and usually similar) area in contact with the tissue. The voltage field generated in the tissue depends on the distance between the two electrodes and on the orientation of the bipole. Additionally, in the case of surface stimulation of an anisotropic tissue containing fibers with a specific orientation, the shape of the volume of activation is influenced by the anisotropy<sup>[126]</sup>. The orientation of the dipole can thus potentially have an effect on the activation properties of these fibers.

In the stimulation of the auditory brainstem, it is interesting to investigate whether the distance between the two stimulation electrodes and the orientation of the pair compared to the lateromedial axis have an influence on the recorded IC parameters, both in terms of tonotopic organisation and selectivity. Two specific arrays are designed for this purpose, one to study the effect of stimulation with very close pairs (200  $\mu\text{m}$  center-to-center distance, described in section 3.4.1), and the second to have a regular coverage of the whole surface of the DCN with a hexagonal configuration to study the independent effects of orientation and distance, at all stimulation pair positions on the surface of the DCN (described in section 3.4.2).

## 3.8. Stimulation pairs orientations and interelectrode distances

---

### 3.8.1 14-electrode array with 200 $\mu\text{m}$ spaced pairs

The first tested electrode array consists of 14 electrode sites arranged in 7 pairs of electrodes covering the surface of the DCN (Figure 3.33A). Pairs with interelectrode distances between 200 and 800  $\mu\text{m}$  and various orientations are tested. In order to analyze the effect of distance and orientation, the results from all stimulation pairs are separated into 12 groups, each with a specific distance and orientation (shown in different colors on the plot). As mentioned earlier, due to the correlation between distance and orientation in this design, the main interest is to compare the group with 200  $\mu\text{m}$  distance to the other groups. Data with 200  $\mu\text{m}$  distance will be referred to as 'close pairs' in the following analyses of this section.

The percentage of runs with significant activity for each group is important to consider in this context, to assess if stimulation pairs with the smallest tested interelectrode distance can still efficiently stimulate the neurons that generate activity in the IC. In raw data, the percentage of significant maps generated with close pairs is not smaller than any other groups, and is even significantly larger than the pairs with 800  $\mu\text{m}$  distance and  $0^\circ$  orientation (Figure 3.33C, mult.lin.reg,  $N=3$ ,  $p < 0.05$ ). After average subtraction, close pairs generate activity in significantly less runs than pairs with a distance of 412  $\mu\text{m}$  and an orientation of  $-14^\circ$  (mult.lin.reg,  $N=3$ ,  $p < 0.05$ ), but no other groups ( $p > 0.05$ ). In the early time window, no significant differences between close pairs and other groups is obtained (mult.lin.reg,  $N=3$ ,  $p > 0.05$  in all cases). After combined analysis, close pairs generate activity in significantly less runs than pairs with a distance of 412  $\mu\text{m}$  and an orientation of  $-14^\circ$  (mult.lin.reg,  $N=3$ ,  $p < 0.05$ ), but no other groups (mult.lin.reg,  $N=3$ ,  $p > 0.05$ ). The percentage of responses generated by close pairs is thus not significantly lower than all other groups in all processings, suggesting that the neurons generating responses in the IC are stimulated as efficiently as with larger interelectrode distance pairs.

### Tonotopic organisation

Figure 3.33B shows the lateromedial variations of characteristic frequency (CF) following the different types of processing presented in the previous sections. Averages of the  $N=3$  datasets and standard errors are plotted, as well as the linear regression line for each group. Multiple regression analysis is performed for each group to identify significant correlations of CFs (or other parameters) with lateromedial or rostrocaudal coordinates. All pairs of groups are also compared with multiple linear regression, considering the effect of the factors (lateromedial and rostrocaudal positions, and group) and the interactions between factors. In the raw data, no significant correlation between the lateromedial position and the CF are identified in any groups ( $p > 0.05$  in all cases). In the comparison between groups, the CFs obtained with close pairs show no significant differences with any other group ( $p > 0.05$  in all cases). In the average subtraction and the early phase of response, although the lateromedial effect of CF is clear in most groups, the correlation between CF and lateromedial position is significant only in two groups, the group with a distance of 412  $\mu\text{m}$  and an orientation of  $14^\circ$  and the group with a

### Chapter 3. New Generation Auditory Brainstem Implant (ABI)

distance of 500  $\mu\text{m}$  and an orientation of  $-36^\circ$  ( $p < 0.05$  in both cases).

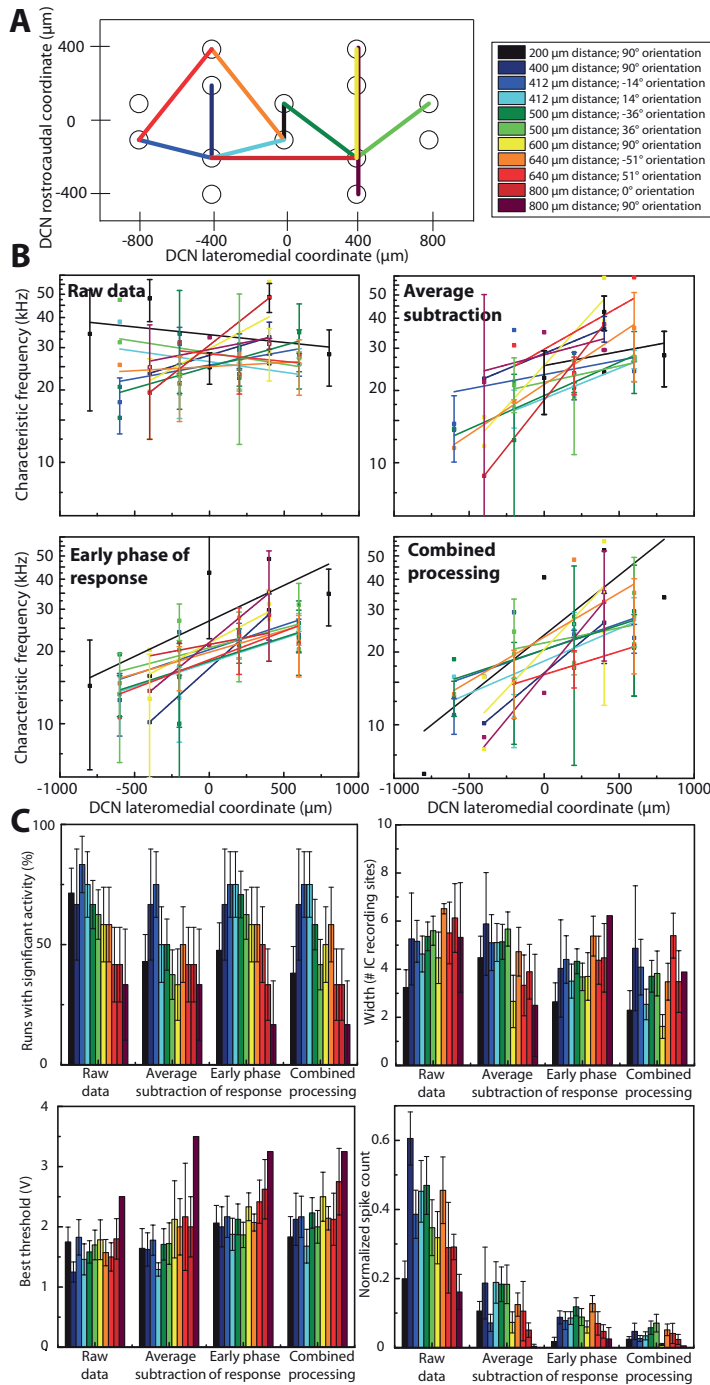


Figure 3.33: A) Illustration of the different groups considered for the analysis, each with a specific interelectrode distance and orientation of the pair. B) Variations of characteristic frequency (CF) with lateromedial position of stimulation for all processing types. C) Effect of the Angle/Distance groups on the percentage of runs with significant activity, the width of activity in the IC, the best threshold and the normalized spike count, for each processing type.

### 3.8. Stimulation pairs orientations and interelectrode distances

---

The lack of significance in other groups ( $p > 0.05$ ) is likely due to the variability of the data and the low number of datasets ( $N=3$ ). The access to tonotopy by close pairs is not significantly different than any other groups ( $p > 0.05$ ). In the early phase of response, the CFs obtained with close pairs are significantly higher than most other groups. This difference is significant with the group with  $412 \mu\text{m}$  distance and  $14^\circ$  orientation, and the group with  $500 \mu\text{m}$  distance and  $-36^\circ$  orientation ( $p < 0.05$  in both cases). After combined processing, no significant latero-medial effect of CF is identified ( $p > 0.05$  in all cases). The CFs obtained with close pairs are not significantly different than other groups ( $p > 0.05$  in all cases).

Overall, these results mean that the access to the tonotopic organisation of the IC does not seem to be better with the smallest interelectrode distance ( $200 \mu\text{m}$ ) compared to the other groups. In the early time window, the average CF obtained with close pairs is on average higher than with pairs with larger interelectrode distances, indicating a potentially important difference in DCN neurons activation by these close pairs that will be discussed in following sections.

#### Intensity parameters

In the raw activity, the width of activation is smaller for close pairs than for two other groups of data, the group with a distance of  $500 \mu\text{m}$  and an orientation of  $-36^\circ$ , and the group with a distance of  $640 \mu\text{m}$  and an orientation of  $-51^\circ$  ( $p < 0.05$  in both cases). In the data after average subtraction and in the early phase of responses, no significant differences in widths are obtained in the groups comparisons ( $p > 0.05$  in all cases). In the combined analysis, the close pairs induce a significantly lower width than the group with a distance of  $640 \mu\text{m}$  and an orientation of  $51^\circ$  ( $p < 0.05$ ), but not the other groups.

No significant differences between close pairs and other groups are obtained on the best threshold of activation, in any of the processing types ( $p > 0.05$  in all cases). The larger values of threshold observed with the group with a distance of  $800 \mu\text{m}$  and an orientation of  $90^\circ$  are obtained with only one datapoint. This is due to the low percentage of significant responses of this group and the relatively low total number of datasets ( $N=3$ ). They can therefore not be considered in the analysis.

In raw data and early phase of responses, normalized spike counts are smaller for close pairs than for most groups with distances between  $400$  and  $640 \mu\text{m}$  ( $p < 0.05$ ). At higher distances, the normalized spike rate is not significantly different from close pairs ( $p > 0.05$  in all cases). In the data after average subtraction or after combined analysis, no significant differences between groups is present ( $p > 0.05$  in all cases).

### Synthesis

The effect on all parameters obtained with 200  $\mu\text{m}$  distance pairs are consistent with the fact that the volume of activation is smaller than with larger interelectrode distances. Particularly in the early phase of responses, a tonotopic organisation is observed in the responses obtained with 200  $\mu\text{m}$  spaced pairs. The width of activation and spike count are also smaller with 200  $\mu\text{m}$  spaced pairs than with most responses obtained with larger distances. This is not associated to an increase in threshold, showing that the efficiency of stimulation is not affected.

The higher average CF in the early time window can be related to the higher CFs obtained on average at lower stimulation levels in section 2.7 (effect of stimulation level), suggesting that the deeper layer have lower CFs than shallower layers. By using a smaller current level (thus a more spatially specific stimulation), the depth of activated neurons is smaller and the low CFs of deeper layers are not reached. These results confirm that the spatial selectivity might be higher with the smallest interelectrode distances, without however improving the tonotopic organization of responses.

### 3.8.2 20-electrode array with hexagonal configuration of electrodes

The second tested electrode array consists of 20 electrode sites arranged in a hexagonal configuration, covering a slightly larger surface than the 14-electrode array (1.9 mm x 1.1 mm vs 1.7 mm x 0.9 mm). The hexagonal arrangement of electrodes is similar to the arrangement of electrode sites used in the clinical ABIs (with one extra line) and allows an independent study of orientation and distance of the electrode pair, as the electrode sites are equidistant in all three orientations. The distance between two neighbouring electrodes is 400  $\mu\text{m}$ , and the three orientations are  $-60^\circ$ ,  $0^\circ$  and  $60^\circ$  (Figure 3.34).

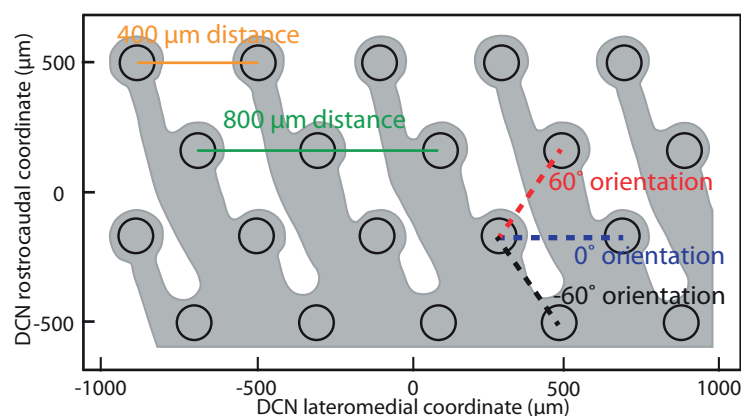


Figure 3.34: Schematic of the stimulation array showing the inter-electrode distance (400 and 800  $\mu\text{m}$ ), and the three orientations ( $-60^\circ$ ,  $0^\circ$  and  $60^\circ$ ), with respect to the lateromedial (horizontal) axis.

### 3.8. Stimulation pairs orientations and interelectrode distances

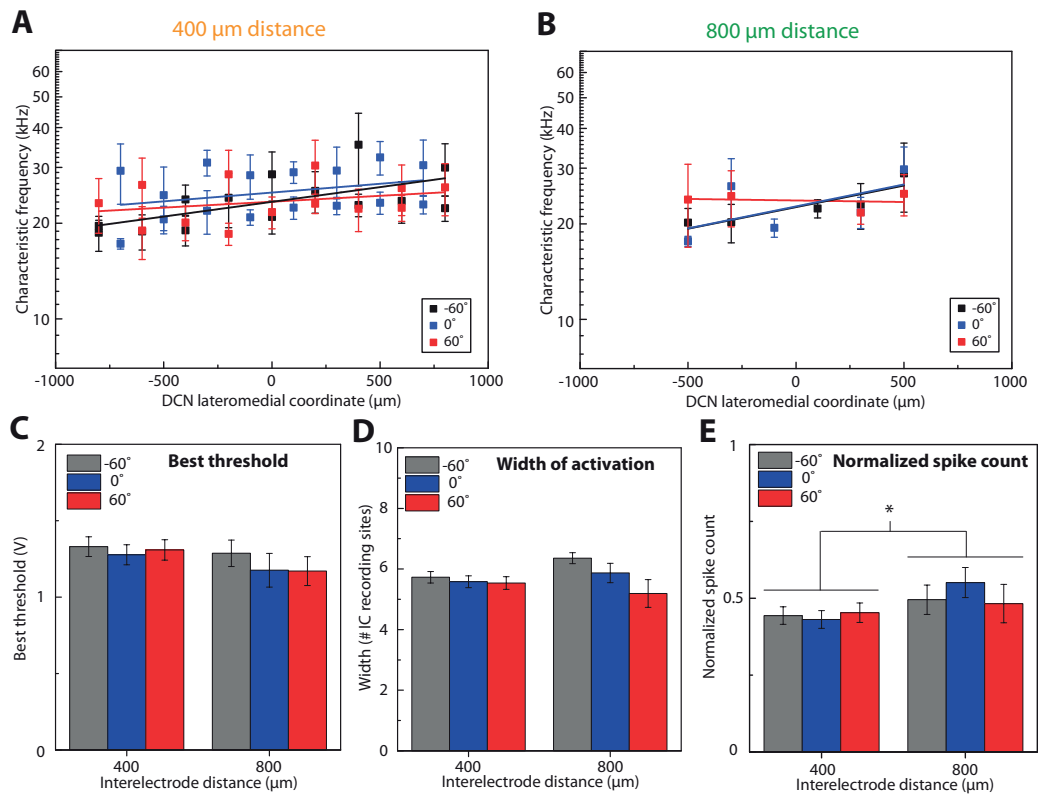


Figure 3.35: A, B) Comparison of tonotopic gradient for pairs with the three orientations (-60, 0 and 60 degrees), for 400  $\mu\text{m}$  (A) and 800  $\mu\text{m}$  (B) distance, for the raw data. C, D, E) Effect of distance and orientation of the stimulation pair on measured best threshold (C), width of activation (D) and normalized spike count (E).

#### Raw data

Analysis of distance and orientation effects on raw data (Fig. 3.35) shows that the only group with significant correlation between CF and lateromedial position is the group with 400  $\mu\text{m}$  distance and negative orientation (mult.lin.reg,  $N=7$ ,  $p < 0.05$  for the lateromedial position factor). Other groups, with a distance of 400  $\mu\text{m}$  and an orientation of 0° or 60°, and with a distance of 800  $\mu\text{m}$  and all three orientations, do not show any significant correlation between CF and lateromedial position ( $p > 0.05$  in all cases). No significant differences between groups are obtained (mult.lin.reg,  $N=7$ ,  $p > 0.05$  in all cases). In the considered intensity parameters (best threshold, width and spike count), the only significant effect is a larger spike count following stimulation with 800  $\mu\text{m}$  distance pairs compared to 400  $\mu\text{m}$  distance pairs (mult.lin.reg,  $N=7$ ,  $p < 0.05$ ; Fig. 3.35E).

Combined processing

After combined processing, when only the data obtained with the larger inter-electrode distance (800  $\mu\text{m}$ ) are considered, fewer rats (4/7 vs. 6/7 with 400  $\mu\text{m}$  distance) show a significant correlation between CF and lateromedial position (mult.lin.reg,  $p < 0.05$  for these 4 rats). The range of CFs accessed is also smaller (15 to 36.1 kHz, 1.27 octaves in Fig. 3.36B versus 9 to 52.3 kHz, 2.54 octaves in Fig. 3.36A). At 800  $\mu\text{m}$  distance, the range of CFs is larger at a  $-60^\circ$  orientation (15 to 36.1 kHz, 1.27 octaves) than at the two other orientations,  $0^\circ$  (16 to 28.3 kHz, 0.82 octaves) and  $60^\circ$  (19.7 to 34.2 kHz, 0.8 octaves). At this distance, the correlation between CF and lateromedial position is significant for  $0^\circ$  and  $-60^\circ$  orientation (mult.lin.reg,  $N=7$ ,  $p < 0.05$ ), but not for  $60^\circ$  orientation (mult.lin.reg,  $N=7$ ,  $p > 0.05$ ).

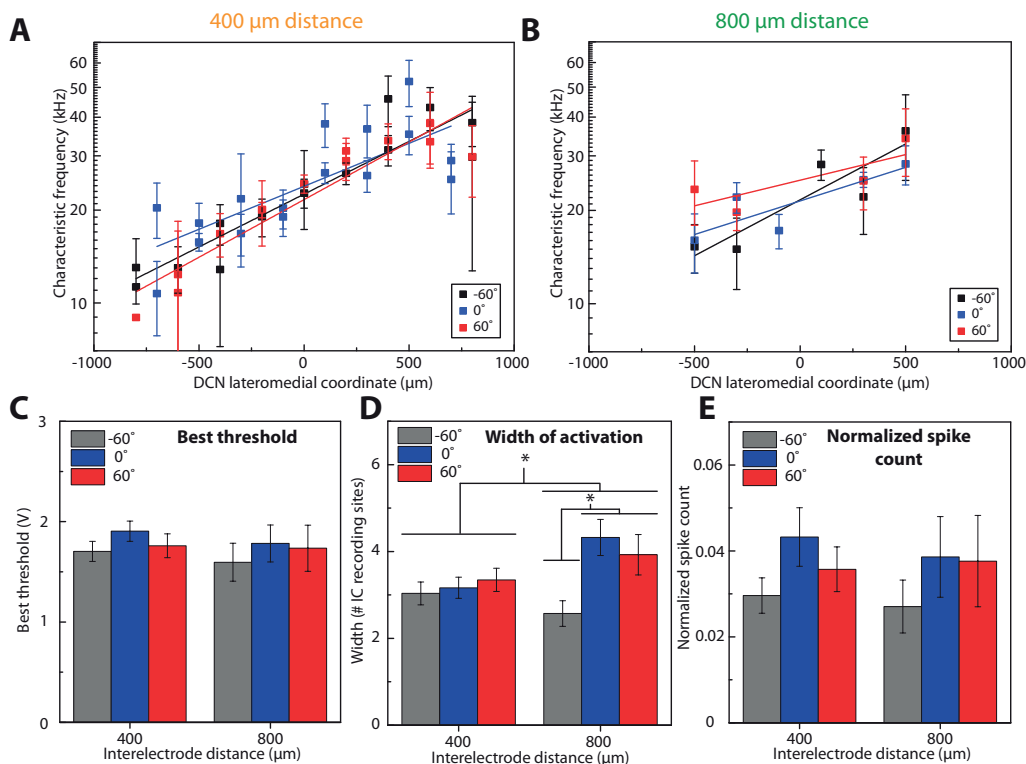


Figure 3.36: A, B) Comparison of tonotopic gradient for pairs with the three orientations, for 400  $\mu\text{m}$  (A) and 800  $\mu\text{m}$  (B) distance, for the early activity after average subtraction. C,D,E) Effect of distance and orientation of the stimulation pair on measured best threshold (C), width of activation (D) and normalized spike count (E). Significant differences ( $p$ -value  $< 0.05$ ) are indicated with a star.

Larger inter-electrode distance also broadens the width of activation, for all orientations combined (One-way Anova,  $N=7$ ,  $p < 0.05$ ). For a 400  $\mu\text{m}$  inter-electrode distance, the width is on average 3.17 recording sites in IC, whereas for 800  $\mu\text{m}$  the width is on average 3.6 recording sites (Fig. 3.36D). Again, the only effect of electrode pair orientation is for 800  $\mu\text{m}$  distance, and



### 3.8. Stimulation pairs orientations and interelectrode distances

---

the pairs with a  $-60^\circ$  orientation are different (they generate a narrower width than the other orientations, One-way Anova,  $N=7$ ,  $p<0.05$ ). This orientation also shows the best tonotopic organisation at that distance. It is close to orthogonal to the CF shift following combined processing identified in previous sections ( $12^\circ$  orientation, angle of  $72^\circ$  between the two).

#### Synthesis

These analyses highlight several properties of the results obtained with an interelectrode distance of  $800\ \mu\text{m}$  compared to  $400\ \mu\text{m}$ . First,  $800\ \mu\text{m}$  spaced pairs generate higher spike counts in raw data. Then, in combined processing, they lead to higher widths and a lower range of CFs. At this distance, the orientation also seems more critical and generates lower widths and a better tonotopic organisation when it is close to orthogonal to the tonotopic axis. No significant changes in normalized spike count are obtained between the different distance and orientation conditions, indicating a similar intensity of activation in the IC. While the 'loudness level' cannot be measured as such in animals, the normalized spike rate can be used to estimate it.

These results are consistent with a higher volume of activation generated by the  $800\ \mu\text{m}$  distance data. Additionally, when the two electrode sites of a pair are located at different locations along the tonotopic axis (i.e. the orientation of the pair is close to the orientation of the tonotopic axis), it is likely that there is a volume of activation below each stimulation site that correspond to different CFs, thus generating higher width in the IC and poorer tonotopic organisation.

Following these analyses, it can be concluded that smaller distances are preferable in order to generate more spatial selectivity of stimulation, with similar loudness levels. A limitation in density is however likely to come from the limitation in the total number of electrode sites covering the surface of the CN. In order to maximize the tonotopic organisation of responses and minimize the width of activation in the case of larger interelectrode distances, it might also be important to use an orientation of the electrode pair close to orthogonal to the tonotopic axis.

### 3.9 Comparison between monopolar and bipolar stimulation

#### 3.9.1 Effect on tonotopic organisation of responses

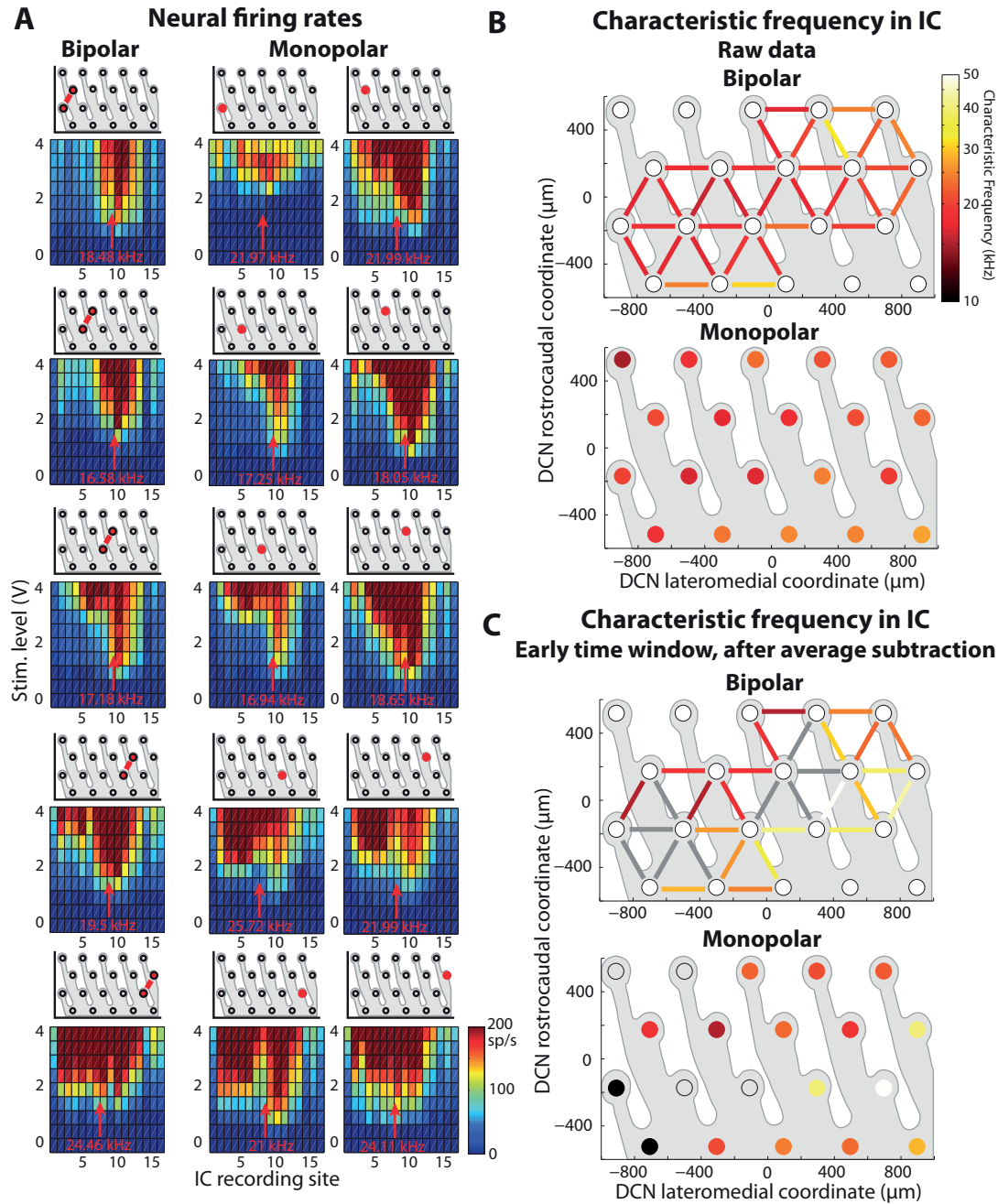


Figure 3.37: A) IC response maps (raw data) to bipolar electrical stimulation with five different bipolar pairs along the lateromedial axis (left column), and in response to monopolar stimulation with the corresponding individual electrodes (middle and right columns) in an individual rat (11). B) CF matrices (raw data) for bipolar stimulation (top) or monopolar stimulation (bottom). C) CF matrices (after combined processing) for bipolar stimulation (top) or monopolar stimulation (bottom).

### 3.9. Comparison between monopolar and bipolar stimulation

In this section, results following stimulation with the 20-electrode array (section 3.4.2) are presented. Response patterns from monopolar stimulation do not differ greatly from those described for bipolar stimulation. Figure 3.37A shows raw IC response maps following bipolar stimulation with five different pairs vs. monopolar stimulation with the 10 corresponding stimulation sites. Qualitatively similar spatial variations are observed both in raw data (Fig. 3.37B) and after combined processing (Fig. 3.37C).

Results show no significant differences in the access to tonotopy between monopolar and bipolar data (multiple linear regression,  $N=4$ ,  $p > 0.05$  both for the first order stimulation configuration effect and for the interaction stimulation configuration / position), both in the raw data and after combined processing (Fig. 3.38A-B).

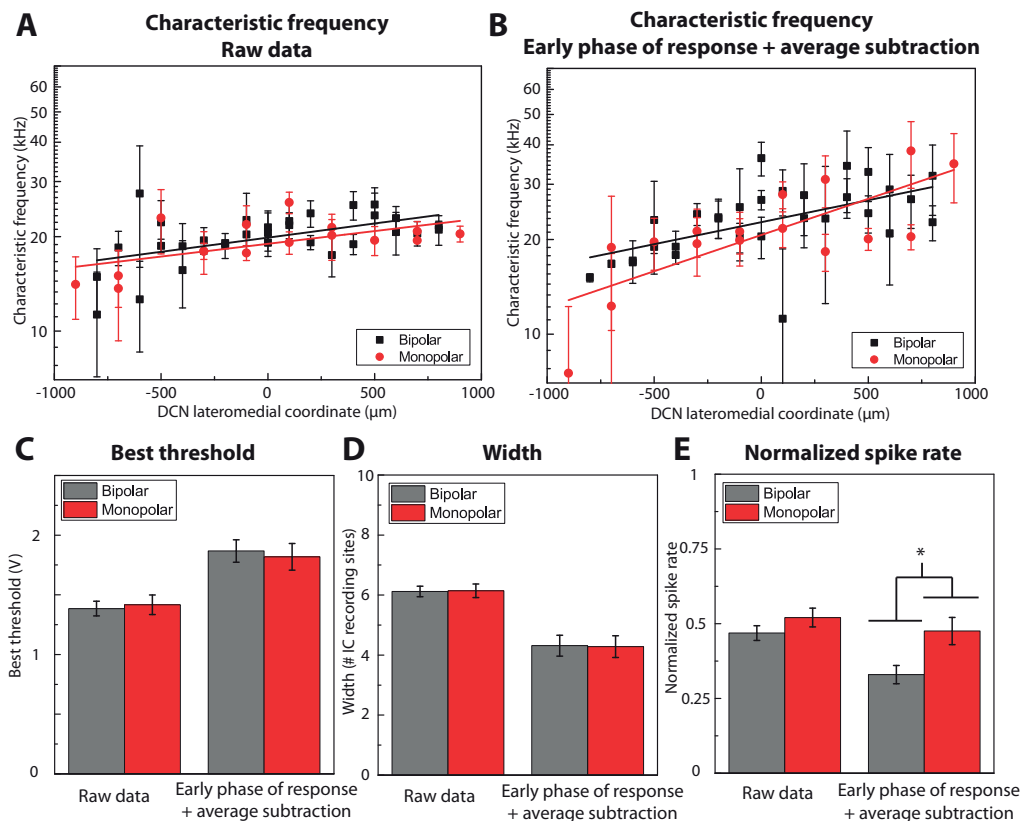


Figure 3.38: A) Correlation between CFs of raw IC response maps and their lateromedial position for monopolar and bipolar stimulation. B) Correlation between CFs after combined processing and their lateromedial position, for monopolar and bipolar stimulation. C, D, E) Threshold (C), width of activation (D) and normalized generated spike rate (E) for monopolar and bipolar stimulation, for raw data and after combined processing.

### 3.9.2 Effect on intensity parameters

After combined processing, evoked spike rates are significantly higher in monopolar stimulation than in bipolar stimulation (Fig 3.38; One-way Anova, N=4,  $p < 0.05$ ). This effect is also observed in the raw data but does not reach significance (One-way Anova, N=4,  $p > 0.05$ ). No significant difference in threshold or width of activation is found between monopolar and bipolar stimulation, both before and after processing (Fig 3.38; One-way Anova, N=4,  $p > 0.05$ ).

### 3.9.3 Synthesis

The main conclusion for this study of comparison between monopolar and bipolar stimulation is that the access to the tonotopy does not significantly differ, but that the larger spike rate obtained in monopolar than in bipolar stimulation suggests that the volume of activation following bipolar stimulation might be smaller. Even if this does not result in an increased frequency selectivity in the IC, it can potentially be used on the edge of the CN to better shape the volume of activation and thus minimize side effects due to off-target stimulation. This will be further discussed in the discussion of this chapter.

## 3.10 Using alternative stimulation pulse waveforms

### 3.10.1 Range of tested waveforms

The goal of this section is to investigate the effect of different pulse waveforms of stimulation on the properties of the IC response maps. The effect of the polarity of stimulation (cathodic-anodic or anodic-cathodic) with a symmetric biphasic waveform and of the duration of the phases are investigated. The effect of asymmetry between the two phases (with charge-balanced pulses) on the properties of activation is also tested. Lastly, a waveform initially designed to temporarily inactivate the neurons closest to the electrodes while activating neurons at larger distances is tested, in an attempt to bypass the neuronal layer at the surface of the DCN and directly stimulate the pyramidal neurons present in the second layer.

In order to test these different elements, eight waveforms are used to stimulate five electrode sites of the 20-electrode array (section 3.4.2) located at different positions along the lateromedial axis (at a rostrocaudal coordinate of  $173 \mu\text{m}$ ), in a monopolar configuration (Figure 3.39, left):

- A: biphasic symmetric, 0.2ms/phase, cathodic-anodic
- B: biphasic symmetric, 0.2ms/phase, anodic-cathodic
- C: biphasic symmetric, 0.1ms/phase, cathodic-anodic
- D: biphasic symmetric, 0.1ms/phase, anodic-cathodic
- E: biphasic asymmetric, 0.4ms/0.1ms, charge balanced, cathodic-anodic
- F: biphasic asymmetric, 0.4ms/0.1ms, charge balanced, anodic-cathodic

### 3.10. Using alternative stimulation pulse waveforms

G: triphasic asymmetric, 0.4ms/0.1ms/0.2ms, charge balanced, cathodic pre-pulse below threshold, cathodic-anodic

H: triphasic asymmetric, 0.4ms/0.1ms/0.2ms, charge balanced, anodic pre-pulse below threshold, anodic-cathodic

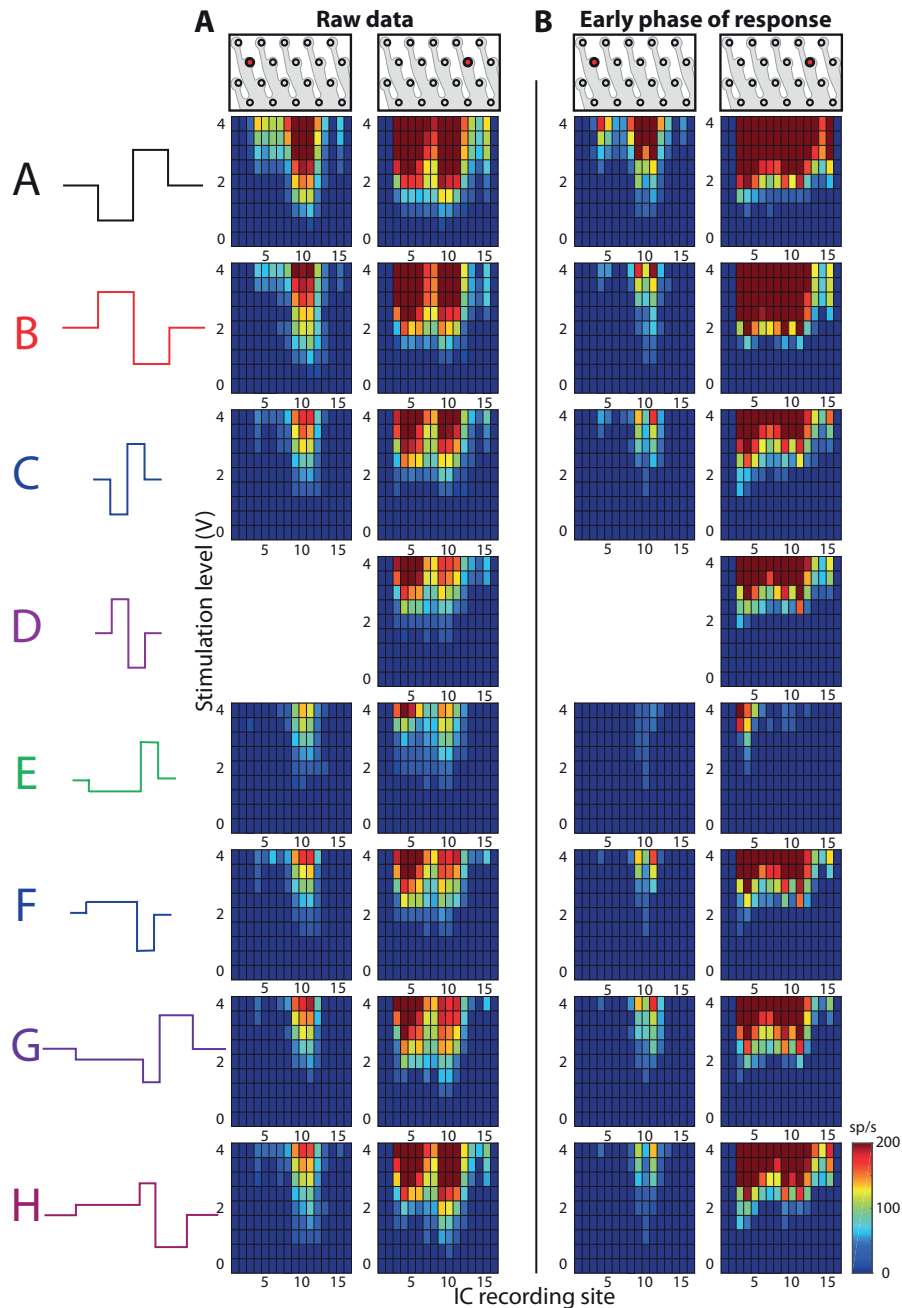


Figure 3.39: Left: Illustration of the 8 tested waveforms. A: Raw IC response maps recorded from the IC following stimulation with each waveform at two different stimulation sites. B: Early phases of the IC response maps shown in A.

The first effect of interest here is the tonotopic organisation of response and the frequency selectivity measured in the IC. The goal is to investigate whether a specific waveform allows a better access to different frequencies and can bring better tonotopic cues than others. The effect on the stimulation threshold and more generally the intensity of activation resulting from stimulation with the different waveforms can be linked to the efficiency of stimulation. This is important to consider in the context of power consumption for implants, as well as for the chronic safety of stimulation.

### 3.10.2 IC response maps characterization

Figure 3.39 shows IC response maps following stimulation with the eight different waveforms, with two electrode sites varying in their lateromedial position. Average spike rates over the 30 ms time window after stimulation (containing all generated spikes) and over the early phase of responses as in the previous sections are displayed.

The waveform has a qualitative effect on the IC response maps, in their intensity of activation but also in some cases on their width of activation and location of activity along the IC recording array. As seen in the datasets presented in earlier sections, there is also here a large variability between datasets, and extracting relevant effect of different waveforms is challenging. A similar strategy is then used, with separation between early and late phases of responses, and subtraction of the average activity to highlight local effects. Effects of each of the waveforms on the different components of responses will be presented in the following sections.

### 3.10.3 Effect of polarity on symmetric pulses

First, we will consider the effect of polarity on a 0.2 ms/phase pulse. Waveforms of both polarities (A and B) show significant correlation between characteristic frequency and lateromedial position of stimulation in the early phase of activity, as well as in the combined processing (Fig 3.40A, mult.lin.reg,  $N=7$ ,  $p < 0.05$ , significant lateromedial variations indicated with a star). No significant difference in CF variation is obtained between the two polarities in any of the processing types (mult.lin.reg,  $N=7$ ,  $p > 0.05$ ).

The width of activation varies significantly with lateromedial position in raw data, average subtraction data and early time window data for A and B, and in combined processing for B, showing lower widths at lateral locations (mult.lin.reg,  $N=7$ ,  $p < 0.05$ ). No significant difference between the two polarities are obtained (mult.lin.reg,  $N=7$ ,  $p > 0.05$ ; Fig 3.40B). For the other parameters, the average values obtained by stimulating all locations on the DCN are considered for the comparison (Fig 3.41). No significant differences between the two polarities are obtained in the threshold, in the normalized spike rate of in the width of activation (One-way Anova,  $N=7$ ,  $p > 0.05$ ).

### 3.10. Using alternative stimulation pulse waveforms

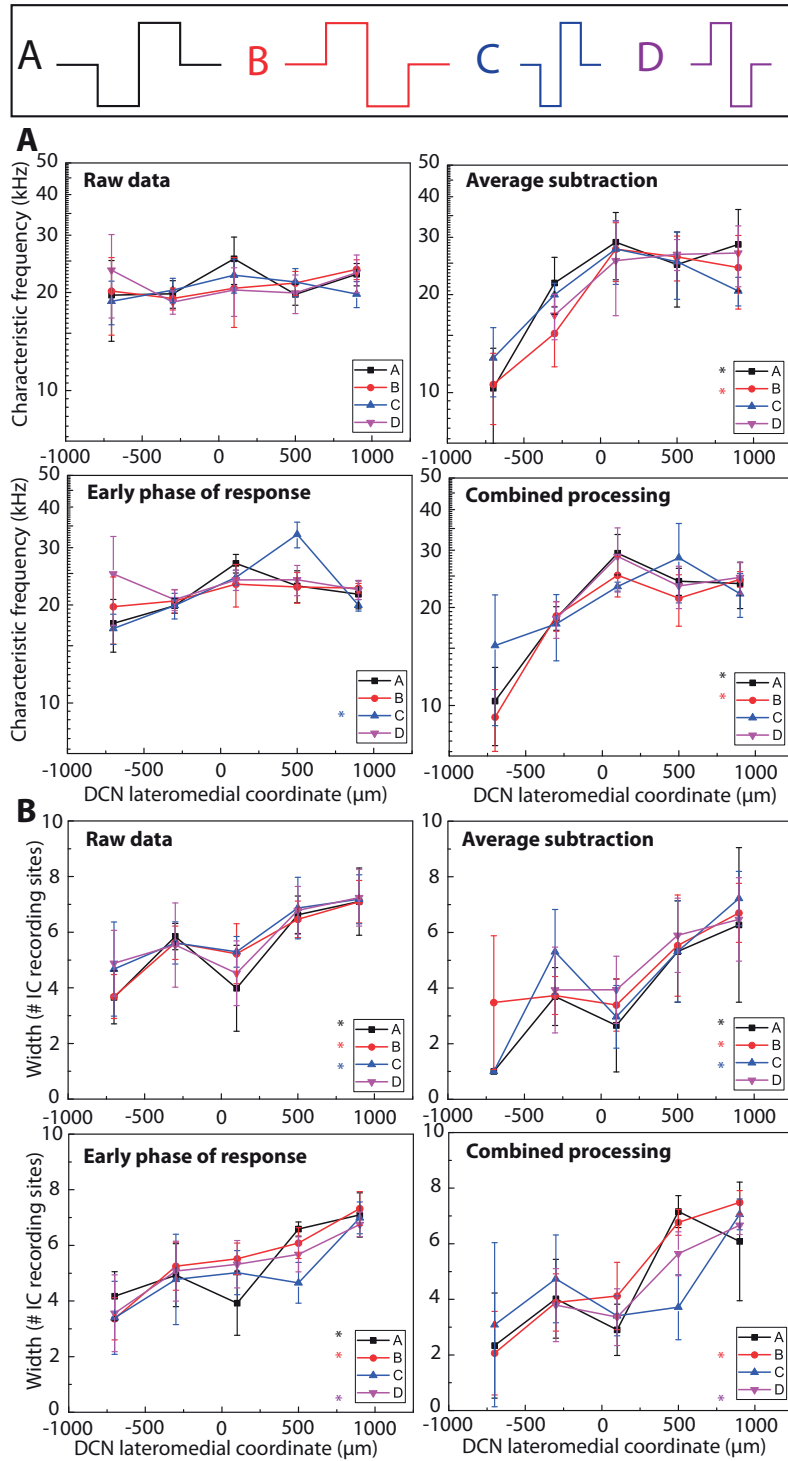


Figure 3.40: A) Characteristic frequencies and B) widths of activation at different lateromedial positions for the four tested symmetrical waveforms, measured on raw data, after average subtraction, on the early phase of responses and following combined processing.

### Chapter 3. New Generation Auditory Brainstem Implant (ABI)

Considering the effect of polarity on shorter pulses (0.1 ms/phase) leads to slightly different results. The cathodic/anodic waveform (C) shows a significant correlation between CF and lateromedial position of stimulation in the early time window (mult.lin.reg,  $N=7$ ,  $p < 0.05$ ), but not the opposite waveform (D) (mult.lin.reg,  $N=7$ ,  $p > 0.05$ ; Fig 3.40A). Both polarities generate lower width of activity when stimulating from lateral positions compared to medial positions (mult.lin.reg,  $N=7$ ,  $p < 0.05$  in both cases; Fig 3.40B).

Direct comparison of the two polarities shows that the cathodic-anodic waveform generates lower thresholds than the anodic-cathodic waveform in the raw data and the early phase of responses (One-way Anova,  $N=7$ ,  $p < 0.05$  in both cases), and is thus more efficient in generating activity in the IC (Fig 3.41C-D). No other parameters show significant differences between the two polarities (One-way Anova,  $N=7$ ,  $p > 0.05$  in all cases) with this shorter pulse duration (0.1 ms/phase).

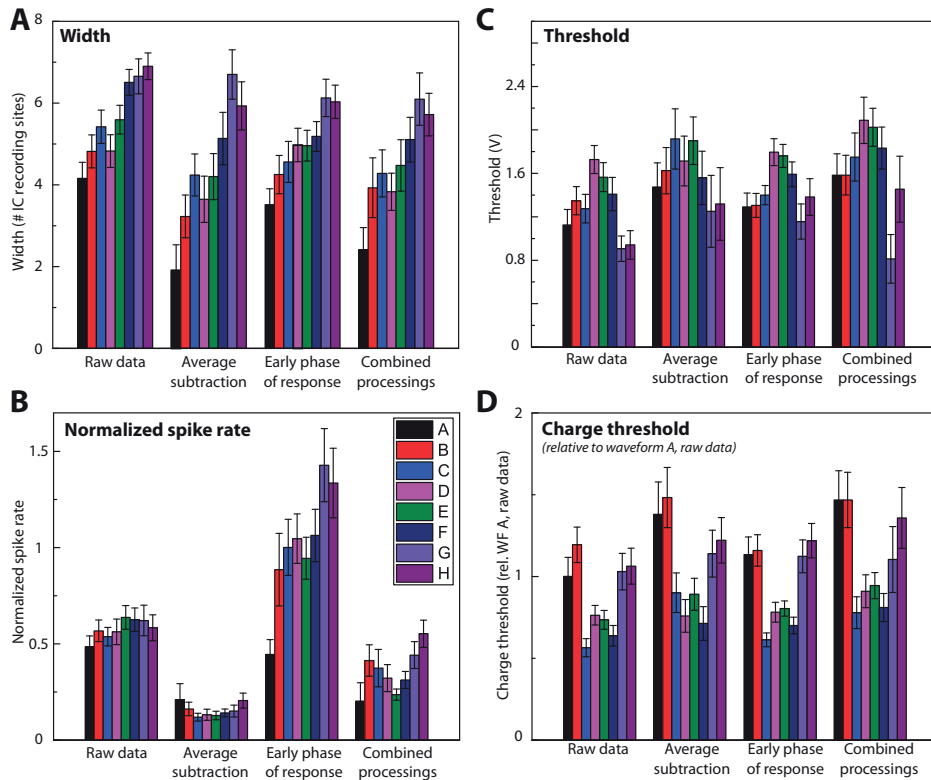


Figure 3.41: Effect of waveform on A) width of activity in the IC, B) normalized spike rate, C) current threshold and D) charge threshold, for the different processing types.

#### 3.10.4 Effect of phase duration on symmetric pulses

The effect of the phase duration on the different analyzed parameters can be investigated by direct comparison of waveforms A and C (cathodic-anodic, 0.2 and 0.1 ms/phase) and B and



### 3.10. Using alternative stimulation pulse waveforms

---

D (anodic-cathodic, 0.2 and 0.1 ms/phase). No effect of phase duration is obtained on the correlation between CF or width and the location of stimulation electrode (mult.lin.reg, N=7,  $p > 0.05$  in all cases), showing a similar access to the tonotopy of the DCN by waveforms of different phase durations.

The difference between threshold stimulation level and associated charge in the analysis of phase duration effect is important to consider (Fig 3.41C-D). Larger thresholds are obtained at 0.1 ms/phase than at 0.2 ms/phase for both polarities, although the difference is significant only for the anodic-cathodic polarity (One-way Anova, N=7,  $p < 0.05$ ). However, a longer phase duration lead to a higher charge per phase for the same stimulation level. The charge threshold is significantly smaller at 0.1 ms/phase than at 0.2 ms/phase for both polarities (One-way Anova, N=7,  $p < 0.05$  in both cases). This behavior is well known, and characterized by the strength-duration and phase-duration curves, describing the relationships between threshold current/charge and pulse duration<sup>[134]</sup>. As pulse duration is reduced, the voltage threshold increases but the charge threshold decreases, a behavior that depends on the time constant of the stimulated neuronal elements. Test with a greater range of pulse durations would be necessary to fully characterize the system and measure its time constant.

In these data, considering that all other response map parameters do not show significant effects of phase duration, shorter phase durations should then be privileged because they provide efficient stimulation at much lower charge per phase, with only marginal increase in stimulation level. Since the damage was shown to primarily depend on the current density and the charge per phase, the range between stimulation and damage threshold can thus be increased by using small phase durations.

#### 3.10.5 Asymmetric stimulation pulses

In the asymmetric pulses, the effective stimulation phase has a duration of 0.1 ms/phase, similar to the symmetric pulses with short duration (waveforms C and D) presented in the previous section. They are thus directly compared to investigate the effect of asymmetry on pulses with similar charge per phase.

The cathodic-anodic asymmetric waveform (E) shows a significant correlation between lateromedial position and CF in the early phase of responses and after combined processing (mult.lin.reg, N=7,  $p < 0.05$  in both cases). In the other polarity (F), these correlations don't reach significance (mult.lin.reg, N=7,  $p > 0.05$  in all cases). Direct comparison of waveforms C, D, E and F shows that the tonotopic organisation of responses with waveform E is significantly different compared to waveforms D and F, with a larger range of CFs and a larger slope (mult.lin.reg, N=7,  $p < 0.05$ ). Indeed, the results of multiple linear regression analysis show a significant interaction between the waveform and the lateromedial position of stimulation, in the early phase of responses for E vs F and E vs D, and after combined processing for E vs F

### Chapter 3. New Generation Auditory Brainstem Implant (ABI)

Waveform E thus shows better tonotopic organisation than the other waveforms, both in the early phase of responses and after combined processing (Fig 3.42A).

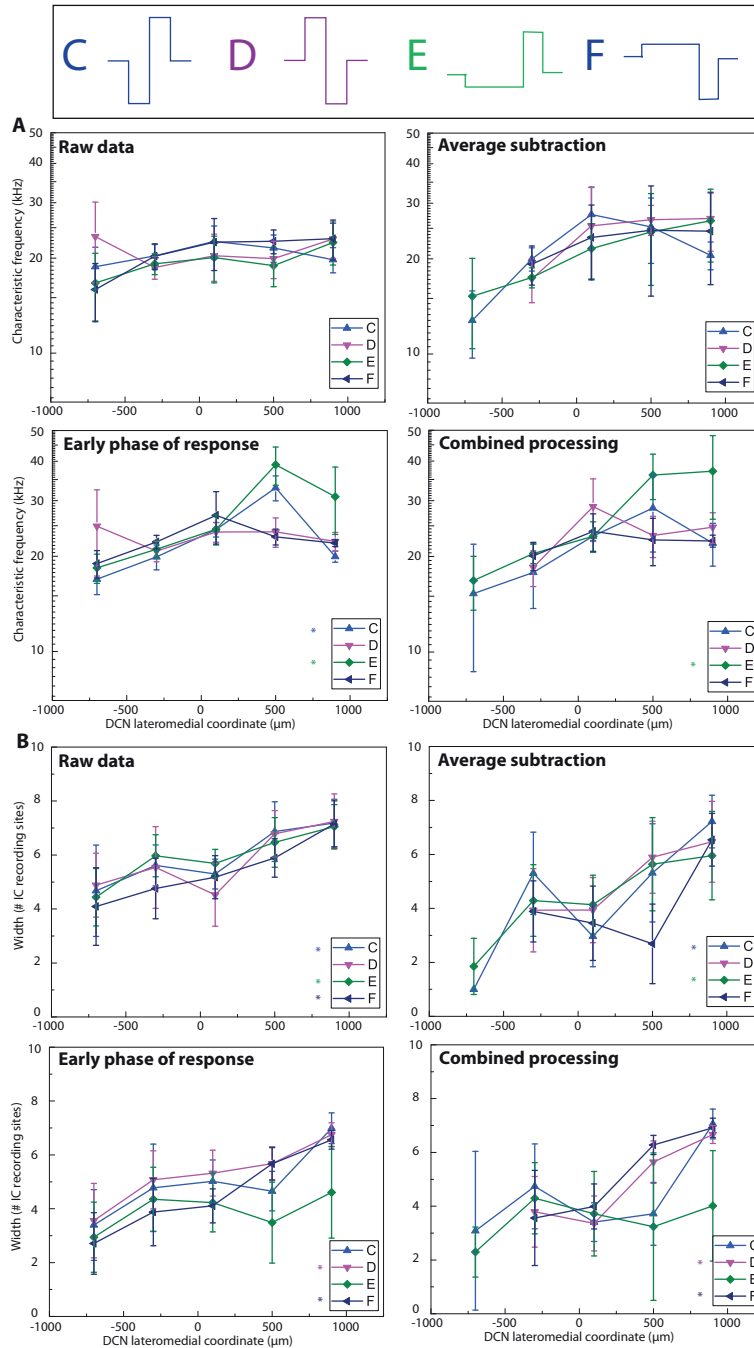


Figure 3.42: A) Characteristic frequencies and B) widths of activation at different lateromedial positions for waveforms C, D, E and F measured on raw data, after average subtraction, on the early phase of responses and after combined processing.

### 3.10. Using alternative stimulation pulse waveforms

Waveform E also shows a lower width than C, D and F in the early phase of responses and after combined processing at medial locations (Fig 3.42B). This difference does however not reach significance (mult.lin.reg,  $N=7$ ,  $p > 0.05$ ).

Because of the similar charge per phase of the different pulses considered in this analysis, considering the current or charge thresholds is equivalent. The threshold of waveforms D and E are significantly higher than C in the early time window (One-way Anova,  $N=7$ ,  $p < 0.05$ , Fig 3.41C-D). Direct comparison of spikes generated by the different waveforms shows that in the early phase of responses, the spike rate generated by waveform E is significantly lower than waveform C (One-way Anova,  $N=7$ ,  $p < 0.05$ ; Fig 3.41B).

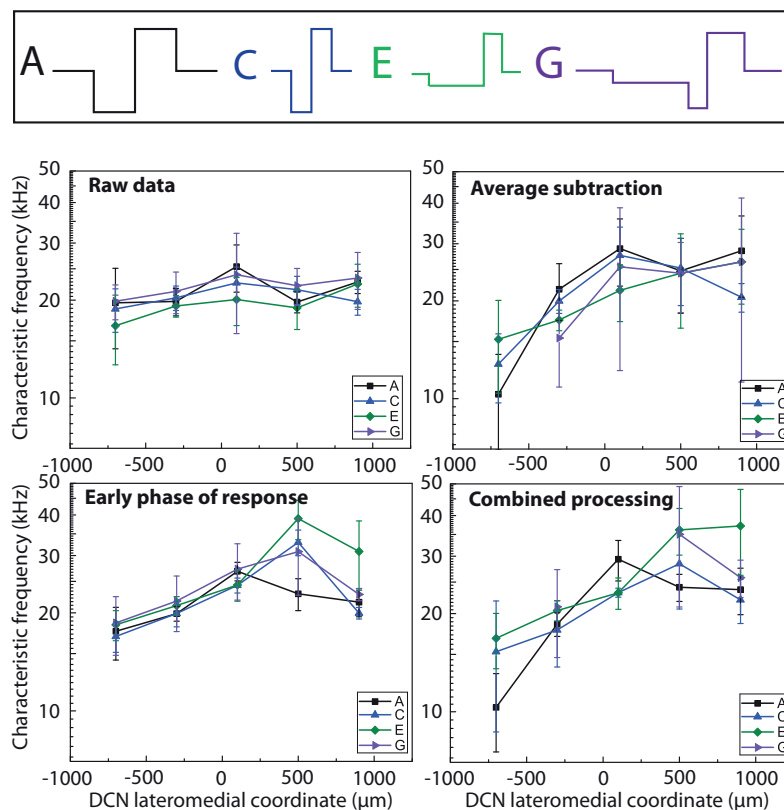


Figure 3.43: Characteristic frequencies at different lateromedial positions for the four tested cathodic-first waveforms measured on raw data, after average subtraction, on the early phase of responses and following combined processing.

These analyses show that the asymmetric waveform with anodic stimulation phase (E) generates the best tonotopic organisation of responses in the early phase of responses, with however a higher threshold than the symmetric waveform with similar polarity, and lower spike rates. This waveform might thus be more selective for tonotopically organized neurons, or for neuronal bodies over fibers of passage, and at the expense of a weaker activity might

generated a better tonotopic organization in the responses.

### 3.10.6 Triphasic stimulation pulse

Direct comparison of waveforms A and G are performed since they have similar polarities, and the effect of adding a subthreshold prepulse (waveform G) can be investigated (Fig 3.41 and 3.43). Results show that waveform A generates higher thresholds than waveform G after combined processing (One-way Anova,  $N=7$ ,  $p < 0.05$ ). Otherwise, no differences between these two waveforms are obtained.

### 3.10.7 Synthesis

The conclusions of this study of the effect of the stimulation waveform on IC response parameters can be articulated in three different points:

- While the polarity has little effect on the 0.2 ms/phase symmetric waveform, it is shown to have an influence on 0.1 ms/phase symmetric waveforms. In this case, the anodic-cathodic waveform generates higher thresholds of activation than the cathodic-anodic waveform.
- The threshold mainly depends on the stimulation level rather than the charge per phase, in the two phase durations tested here (0.1 and 0.2 ms/phase). Short pulses (0.1 ms/phase) are thus advantageous in terms of safety, as a lower charge per phase is necessary to generate activity.
- The analysis of asymmetric waveforms shows that the access to tonotopy in the early phase of response is best with waveform E (long cathodic – short anodic phases). The difference is significant compared to the asymmetric waveform of opposite polarity, as well as the symmetric waveforms of both polarities, with 0.1 or 0.2 ms/phase. The spike rate generated by waveform E is significantly smaller than cathodic/anodic symmetrical waveforms of 0.1 and 0.2 ms/phase and anodic/cathodic symmetrical waveform of 0.2 ms/phase.

Several directions are proposed here, following this waveform study. First, reducing the phase duration seems to lead to lower charge thresholds, which allows safer and more energy-efficient stimulation, as was suggested in<sup>[91]</sup>.

Introducing an asymmetry in the pulses might lead to stimulation with a better tonotopic organisation. The asymmetric waveforms were tested here with the hypothesis that the long cathodic / short anodic waveform would preferentially stimulate neuronal bodies over fibers of passage, as was shown in a simulation study<sup>[124]</sup>. It is difficult to say whether this is what we achieved here, but the better tonotopic organisation of responses suggests that this waveform

type could indeed be efficient in preferentially targeting tonotopically-organised neurons.

A complete characterization of the threshold dependence on the polarity of the stimulation phase would be also relevant, as psychophysical studies in ABI patients suggested that the anodic phase is more efficient than the cathodic phase<sup>[32]</sup>.

This preliminary study of different waveforms of stimulation in a rat model thus highlights the large dependence of the efficiency of stimulation and tonotopic organization of responses on the stimulation waveform.

## 3.11 Discussion

This chapter presents a mapping of the DCN surface with electrical stimulation characterized by ABR far-field responses and direct multiunit recordings from the IC, with an emphasis on the access to frequency-tuned neurons resulting in the extraction of a frequency-specific component in IC recordings.

### 3.11.1 Electrodes configuration effect on the tonotopic organisation of responses

#### Inter-electrode distance

Based on the isolated tonotopically organised responses, we propose guidelines for optimization of the tonotopy and selectivity of stimulation. First, our results yield a more extensive tonotopic pattern for response for small vs. large distances between electrodes of a bipolar pair. In addition, the width of activation in the IC increased with this distance, indicating lower frequency selectivity at large distances, for equal loudness levels.

The widest spacing used in our experiments (800  $\mu\text{m}$ ) is smaller than that found in the clinical ABI electrode array (about 1 mm). Based on our data, we suggest that reducing inter-electrodes distance would benefit spatial selectivity and may lead to the reduction of extra-auditory side effects using bipolar stimulation.

In the studies performed here, inter-electrode distances of 200  $\mu\text{m}$  showed similar stimulation efficiency than higher distances. We do not know if the efficiency of stimulation would be smaller if the inter-electrode was further decreased, but the next limit to consider is the electrode site diameter, that must be large enough to have safe current and charge density levels. Additionally, the density of electrode sites might be limited by the total number of stimulation sites. For these reasons, we do not foresee that further reducing the interelectrode distance could be beneficial in the development of a new ABI array.

### Orientation of the electrode pair

At larger interelectrode distances, we showed that the orientation of the pair should be close to orthogonal to the tonotopic axis in order to optimize the tonotopic organisation of stimulation. Optimizing the orientation of the pair thus seems to allow a shaping of the current field within the CN. Besides the optimization of the tonotopic organisation of responses, the possibility to shape the activation volume could be used to reduce extra-auditory side-effects by using bipolar stimulation with specific orientations, particularly on the edges of the CN.

### Bipolar and monopolar stimulation

Although present results indicate that bipolar electrode configuration alone does not result in narrower receptive fields than monopolar configuration, spike rates following monopolar stimulation are on average higher than following bipolar stimulation, indicating a larger volume of activation with monopolar stimulation. Contrary to studies comparing monopolar and bipolar stimulation in the cochlea<sup>[5,22,135,190,219]</sup>, the threshold obtained with bipolar stimulation is not higher than with monopolar stimulation.

In the human ABI, bipolar stimulation is used intra-operatively to assist the positioning of the ABI array, but monopolar stimulation is used to conserve battery life for normal everyday use<sup>[75]</sup>. In a situation where the density of electrodes is increased, it would be highly relevant to study whether the larger number of possibilities and orientations with bipolar stimulation can lead to an improvement of audiological results, and if these advantages are sufficient to counteract the drawback of higher power requirements of bipolar stimulation.

Monopolar and bipolar stimulation configurations are not the only possible options. Tripolar or multipolar stimulation configurations have been shown to allow greater current steering and spatial selectivity of stimulation. However, these modes of stimulation were typically associated to higher threshold than monopolar and bipolar stimulation and thus to require even more power<sup>[22]</sup>. A tradeoff has to be found between current focusing and power consumption in this case. Tripolar and multipolar stimulation also require more complex current sources and stimulation protocols than the clinically-used monopolar and bipolar modes of stimulation.

### Pulse waveforms

The waveform study presented here is an attempt at improving the monopolar stimulation. As shown in the corresponding section, using shorter pulses and introducing an asymmetry in the pulse might be beneficial in terms of chronic safety of stimulation and of power efficiency and functionality. An important point to consider here is that all tests were performed at low frequencies (28 Hz), in order to be able to measure eABRs and IC response maps following each stimulation pulse. However, clinically-used speech processors use much higher stimulation

pulse rates (250-300 Hz for the SPEAK processing strategy used in the Cochlear ABI device, and 600-1800 Hz for the CIS strategy used in the Med-El ABI device<sup>[113]</sup>) and ABI patients show a frequency-dependence in the stimulation thresholds<sup>[32]</sup>. It would then be highly relevant to test whether the effects identified in this study would be conserved at higher stimulation pulse rates.

In the frame of this study, only a small range of parameters and waveforms were tested, which can thus be considered as preliminary in this respect. It is used to investigate potential directions that seem promising to follow in order to optimize the waveform of stimulation for the ABI. The logic continuation of this study would be articulated in two phases. First, further exploring the waveforms that are tested here, by doing a complete study of pulse duration on symmetric and asymmetric pulses, testing different ratios of asymmetry or testing other parameters for the triphasic pulse could validate the results obtained here and lead to a better understanding of the selectivity of each waveform. In this study, the tested locations were all along the same lateromedial axis. Performing a complete location study including several rostrocaudal locations with these waveforms might also give more insight into the stimulation of the different neuronal populations. Then, it would also be interesting to expand this study by adding interpulse intervals, or waveforms with passive discharge in the second phase. Testing the effect of using asymmetric waveforms in a bipolar stimulation mode is also promising, as it might concentrate the volume of activation below one of the stimulation sites, whereas symmetrical waveforms induce close-to-symmetrical volumes of activation below both stimulation sites<sup>[32]</sup>.

#### 3.11.2 Neurophysiology

##### Variability

We found a high intersubject variability of IC response map patterns in response to electrical stimulation. Histology confirmed reliability of placement on the DCN, so large differences in array placement do not appear to cause this variability, although some edge electrodes were beyond the edges of the DCN. Variable position of the IC recording probe with respect to the various neuronal populations described in the IC might also influence the recordings<sup>[117]</sup>. A potential effect of anesthesia might influence DCN neurons excitability and IC neuron responsiveness<sup>[96,121]</sup>. A combination of all these factors and possible intrinsic differences between the rats could help explain the observed variability.

##### Effect of processing

We investigated the effect of subtracting the overall spike rates because they might be generated by wide frequency tuned neuronal populations and mask location-specific activity generated by narrow frequency-tuned neuronal populations. Despite the large variability obtained in the general pattern of activation of the IC response maps, tonotopic organization

### Chapter 3. New Generation Auditory Brainstem Implant (ABI)

---

became clearer after subtracting the overall activity and using the early responses. Moreover, this residual neural activity reveals a tonotopic pattern with a larger range of CFs and higher tuning of responses (as indicated by the diminished widths of IC response maps).

We investigated the arrival timing of spikes because they might reveal mechanisms for neural activity masking. We found a dichotomy in spike times that we called early latency and late latency spikes. Early latency spikes appeared to be more tonotopic auditory responses than late latency spikes. It is important to note, however, that this mechanism of extracting tonotopic cues appears to be independent of subtraction of common evoked activity, and that there are multiple mechanisms for neural activity masking in the auditory brainstem stimulation. The several phases of activity in the PST histogram in response to electrical stimulation could be explained by: 1) a fast-conducting, direct pathway from the CN to the IC, and 2) a longer-latency pathway either consisting of slower-conducting axons or the presence of one or more synapses. The limit between early and late activity is clear in most runs at a latency of about 7 ms, although this latency differs from run to run and a small overlap may be present.

#### Origin of early activity

We suggest that at least part of the early activity is generated by DCN pyramidal neurons, which are immediately beneath the electrode array and have large axons that project directly to the IC with a tonotopic organization<sup>[3,178]</sup>. The lateromedial tonotopic organisation of responses observed in the early time window (before and after subtraction of average activity) supports this hypothesis, as the tonotopic organisation of the pyramidal neurons follows a dorsomedial-to-ventrolateral axis. Another population of neurons that might contribute to the early activity is the T-stellate cells located in the VCN, which correspond to the type I multipolar cells in the human. They are narrowly tuned to sound frequency and have a 'chopper' pattern of response, a succession of short bursts of spikes, with direct projections to the IC.

#### Origin of late activity

The origin of the late activity may be one or more of the other elements within the DCN (polysynaptic activity involving the parallel fibers), the VCN (polysynaptic activity starting in the spherical and globular bushy cells, T stellate cells) or polysynaptic pathways in the IC. Parallel fibers are located at the surface of the DCN and have excitatory input to the pyramidal neurons in the second layer of the DCN. They are not tonotopically organized and would activate pyramidal neurons across the tonotopic axis of the DCN. In addition, the presence of at least one synapse would induce later activity in the IC than a direct pathway.

The spherical and globular bushy cells are located in the AVCN and project via the ventral acoustic stria to the superior olive (SO) and the lateral lemniscus (LL), where they form



synapses with third order neurons which then project to the IC. In that case also, the presence of a synapse would lead to later activity in the IC than a direct pathway. Finally, pyramidal cells with 'pauser' type of responses generate a sharp early burst of spikes followed by a longer-lasting activity a few milliseconds later<sup>[216]</sup>, which might also contribute to the late phase of responses.

Like the DCN, the AVCN and PVCN also have their own tonotopic organisation, following a dorsomedial-ventrolateral axis. The medial region of the AVCN is located rostrally to the DCN in the rat, according to the 3D reconstruction shown in figure 3.6A. One hypothesis is that stimulation of rostral sites of the DCN might stimulate high-frequency regions of the AVCN if the current spreads. This hypothesis is supported by the larger CFs obtained when stimulating at rostral sites in the late phase of activity. The high-frequency late activity would then be at least partly generated by one or several AVCN cell types mentioned in the previous paragraph.

Analysis of the time centroid of the late activity shows a large dependence on the IC recording site, but only a small dependence on the lateromedial position of stimulation. This is one more clue that the late activity is not lateromedial location-specific. The timing dependence on the IC recording site is more difficult to explain. Low CF fibers appear to generate later activity than high CF fibers, which might be a reflection of the lower intensity of activation of low CF fibers. This could be because the surgical approach and the array position do not seem to allow stimulation of DCN low CF regions, located too laterally and ventrally.

Finally, a possible contribution to the late activity could be explained by the intact auditory nerve of the animal model used in these experiments. Efferent activation of the auditory neurons might be generated, which could generate a conduction of the impulses to distant areas of the CN, thus blurring the tonotopy. The animal model of the ABI could thus be improved by deafening.

#### **Access to the rat hearing range**

Our results suggest a portion of the auditory tonotopic axis is not accessible, even after extraction of the tonotopically-organized spikes. The audible range of frequencies in rats (0.25-80 kHz) is wider than the one we tested (1 - 45 kHz). The latter corresponds to the range of high sensitivity<sup>[86]</sup>. In our experiments, even with the largest CF range obtained, the lowest evoked CF is about 8 kHz, implying the lower frequency range (1 – 8 kHz) could not be accessed. While the flexible ABI conforms well to the surface of the DCN, the lower frequency region of the DCN may be more ventrally located<sup>[174]</sup> and therefore not accessible with our surgical approach.

As mentioned in the introduction, penetrating auditory brainstem implants (PABI) were developed in an attempt to have a better access to the tonotopic organization of the VCN, but did not result in an improvement of audiologic outcomes compared to surface ABIs<sup>[149]</sup>.

### **Chapter 3. New Generation Auditory Brainstem Implant (ABI)**

---

Following in-depth analysis of anatomical properties of the human cochlear nucleus complex, Rosahl et al. proposed a combined surface/penetrating ABI array, with surface electrodes on the inferior half and penetrating electrodes in the superior half<sup>[167]</sup>. However, the main limitation of PABI strategies is the difficulty of placement in the VCN, due to anatomical variability and possible distortions due to tumours. The possibility to intraoperatively tune the placement of surface ABIs remains a critical advantage.

The complex tonotopy of the cochlear nucleus lead to the development of auditory implants targeting other auditory structures. The auditory midbrain implant (AMI), targeting the central nucleus of the inferior colliculus was then developed. Despite the bypass of more auditory processing, it is thought that the clearer tonotopic organization of the inferior colliculus, as well as the absence of tumour-induced damage, might be advantageous<sup>[180]</sup>. An AMI clinical trial between 2006 and 2008 with a multisite single-shank penetrating array showed similar levels of speech hearing outcomes with the AMI compared to the surface ABI. The main challenge was the correct implantation of the electrode array into the central nucleus of the inferior colliculus, with only one of the five implanted devices reaching the targeted implantation location. Limited temporal integration properties were also obtained<sup>[105]</sup>. Further developments with a double shank array and a new surgical approach suggest that better hearing outcomes might be obtained with this improved AMI<sup>[106]</sup>.

The auditory thalamus is also considered as a target for an auditory implant, and showed low thresholds and high dynamic ranges in a feasibility study<sup>[11]</sup>. Each of the studies targeting the central auditory nuclei add to the understanding of the artificial stimulation of the auditory system and the role of the different structures and might thus help achieving high levels of speech understanding for patients who are not candidates for cochlear implants.

#### **3.11.3 eABRs vs IC**

##### **eABRs and audiologic outcomes in clinical ABIs**

Electrically-generated auditory brainstem response (ABR) measurements are used during ABI implantation surgery to assess the placement of the ABI array. However, the presence of useful auditory sensations for a given stimulation site was not shown to directly correspond to the presence of an ABR during intraoperative testing. However, more thorough analysis of intraoperative eABRs suggested that the presence of one particular peak was highly correlated to useful auditory sensations<sup>[75]</sup>.

##### **Link between IC recordings and eABRs**

In these results, no correlation between the presence of significant activity in the IC and detectable eABRs was found. When comparing the location-dependence of the parameters extracted from both signals however, some interesting information can be extracted. In par-

ticular, important rostrocaudal effects were identified on both signals. A higher amplitude and a higher number of peaks were identified in the eABRs at rostral locations. In the late phase of responses in the IC, the characteristic frequency (CF) was shown to be higher at rostral locations, close to the AVCN region corresponding to high CFs. These two effects could be linked and suggest stronger activation of VCN neurons at rostral locations. Bushy cells in the VCN are thought to be the neural correlates generating auditory brainstem responses because of their polysynaptic projections to the IC, which generate sequential activation of the superior olive (SO) and the lateral lemniscus (LL), before reaching the IC, thus generating the different peaks of the ABRs<sup>[130]</sup>.

Activation of CN neurons that have direct projections to the IC might be linked to eABRs with a smaller number of peaks, as the activated pathway does not imply sequential activation of several auditory nuclei. Particularly, stimulation of the pyramidal neurons, hypothesized to be the main source of tonotopically-organised activity in our recordings, might not be linked to eABRs with multiple peaks, as the projections of the pyramidal neurons to the IC are direct. This also means that the interpretation of the neural correlates of each peak is unclear, since the peak that corresponds to the IC activity in the polysynaptic VCN-IC pathway might not have the same latency as in the direct pathway. Both pathways can be simultaneously activated, further increasing the complexity of the generated eABRs.

Another information that can be extracted from the comparison between eABR and IC results is the low lateromedial variation in thresholds in both cases. This might be linked to a good contact of the array with the DCN surface due to the conformability of the array. Such a close contact resulting in uniform thresholds across the array might be beneficial in a clinical context for minimization of electrode-to-neurons distance and thus of current thresholds, which might result in decreased side-effects.

#### 3.11.4 Potential for translation of results for clinical use

Processing to reveal tonotopic cues may have implication for comprehending frequency cues in ABI patients. However, there are important distinctions in extending these results. Our results were obtained with animals without hearing impairment, and it is clear that impairment changes the anatomy and function of the CN<sup>[175,177]</sup>. Secondly, it is not clear that the human brain processes the spike responses to electrical stimuli in a way similar to that shown here to increase the tonotopic pattern. Future prostheses should consider whether targeting specific neurons might provide unmasked frequency cues, and thus more independent channels of information.

Caution must be taken when translating results from rodents to humans, because of the significant differences between these two species. First, rat and human CN have huge differences in size. The rat CN is about 1/16 the size of the human<sup>[167]</sup>. There are also distinct cytoarchitectonic differences. The stratified structure of the human DCN is different than in

### Chapter 3. New Generation Auditory Brainstem Implant (ABI)

---

animals, and the human may lack the numerous granule cells found in most animals<sup>[17,139]</sup>. Neurons that might correspond to the rat pyramidal neurons were identified in the human, but they lack the radial organisation present in most mammals.

In addition to the neurophysiological differences between species, the placement of the ABI array might not be similar in the rat and in humans. The possible anatomical targets of the ABI in humans are the DCN surface and part of the PVCN surface, located on the floor of the lateral recess of the 4th ventricle. It is thought that the DCN is the main target, as it is much larger than the PVCN, and because the PVCN shows some variations in depth<sup>[201]</sup>. However, some evidence shows that there are considerable differences in placement across patients<sup>[18]</sup> as well as anatomical differences<sup>[167]</sup> that make the precise target of the ABI unclear and variable.

Despite these limitations, it seems highly relevant to test whether some of the effects identified in this study, like the importance of orientation of the electrode pair during bipolar stimulation, could be replicated with ABI patients. Particularly, the potential reduction of side-effects due to current steering could have direct implications on the programming of ABI devices, and could help justify further improvements of the ABI array and protocol. This study is thus a step in the direction of improving spatial selectivity of stimulation in ABI to reduce non-auditory side-effects, improve spectral resolution and ultimately speech hearing outcomes. In the general discussion of this thesis, steps towards a clinical validation of the effects highlighted in this chapter will be proposed, as well as a new ABI array design with a higher density of stimulation sites.

### Contributions

Surgeries for the animal experiments performed in the chapter were performed by A.E. Hight in the ABI lab, Eaton-Peabody Laboratories, at the Massachusetts Eye and Ear Infirmary (MEEI), building upon a surgical protocol developed by D.J. Lee and R.U. Verma. Current sources were designed and built by E. Foss. Recording and data acquisition setup was developed by K. Hancock and A.E. Hight. Calculation of the maximal polyimide thickness to achieve bending of a polyimide film around a cylinder was performed by N. Vachicouras. A.E. Hight participated in the design of the experimental protocol and to the data analysis, and him and M.C. Brown contributed to the interpretation of the data. Post-experiment histology was performed by M.C. Brown and S. Narasimhan.

## 4 Optogenetic stimulation of the spinal cord

### Abstract

In the past 10 years, optogenetics has become a technique of critical importance in neuroscience. It enables an in-depth analysis of the function of neuronal subtypes within complex neural networks because of its cell-type selectivity. Additionally, optical stimulation can provide significant advantages over electrical stimulation, including the absence of current spread and of a stimulation artefact. In the context of spinal cord damage and repair, the development of devices enabling chronic light delivery to the spinal cord is essential to provide a way of stimulating key elements of the locomotor neural circuitry. The effect of optical stimulation of specific types of neurons on the recovery can be studied, potentially leading to an optimization of the stimulation protocol during recovery. The spinal cord is a mechanically challenging environment, and the device must have a small size and not damage the spinal cord upon important movements of the animal.

In this chapter, we present an LED-based stimulation array that enables optical illumination of the spinal cord over several weeks, without inducing functional damage to the spinal cord. In a proof-of-concept *in vivo* study, we show that the light irradiance is high enough to reliably generate EMGs in both legs of the animals, in the tibialis anterior (TA) and the vastus lateralis (VL) muscles. The difference between the stimulation with single LEDs and pairs of LEDs in series is investigated, as well as the effect of the different parameters of the stimulation pulses (pulse duration and pulse rate). Directions for further improvements of the device functionality and safety are proposed. The presented device brings a lot of possibilities to dissect neural circuits, understand the role of each neuronal type and possibly optimize recovery following injuries, in fields much wider than spinal cord research.

### 4.1 Introduction

#### 4.1.1 Optogenetics in the context of spinal cord damage and repair

Spinal cord injuries lead in half cases to chronic paralysis, due of the low ability of the central nervous system to repair itself<sup>[198]</sup>. However, strategies that take advantage of the activity-dependent plasticity of remaining neural circuits can be developed to partially restore the lost function<sup>[23]</sup>. Particularly, an electrochemical neuroprosthesis was developed and showed, after specific active training, restoration of full weight-bearing locomotion in rats with a spinal cord injury. This neuroprosthesis combines chemical and electrical stimulation to reactivate dormant circuits<sup>[198]</sup>.

Electrode location and configuration are critical to stimulate specific sections of the spinal cord to activate preferentially flexor or extensor muscles. A spatiotemporal neuromodulation protocol combining spatially specific stimulation at selected locations with temporally specific patterns of stimulation depending on the stage in the gait cycle was shown to improve motor control and gait rehabilitation<sup>[206]</sup>, confirming the critical importance of spatially distributed stimulation sites.

The mechanisms by which electrical stimulation of the spinal cord activate motor circuits have been investigated by simulation and experimental studies. The main hypothesis is that the stimulation primarily recruits the myelinated afferent fibers of the dorsal roots, corresponding to proprioceptive feedback circuits<sup>[206]</sup>. These circuits then activate spinal circuits, enabling sensory feedback to be a source of motor control<sup>[31]</sup>. It is thought that electrical stimulation current poorly penetrates the spinal cord but rather spreads in the cerebrospinal fluid, thus stimulating myelinated fibers and not axons within the gray matter. Motor axons stimulation at the exit of the spinal cord are also recruited, but at higher thresholds than sensory axons, and only at some caudal locations<sup>[31]</sup>. The effect of selectively targeting different spinal structures (motor axons and spinal cord interneurons) on the gait and rehabilitation parameters is thus still unclear and hard to investigate with electrical stimulation.

Optogenetics is a tool that allows cell-type specific stimulation of neural tissue by first transfecting the gene coding for a light-sensitive ion channel (usually Type 2 channelrhodopsin, ChR2) into target neurons under the control of a specific promoter, and then activating them with light of a specific wavelength (473 nm for ChR2). Provided that cell-type specific promoters can be isolated and used for the targeting of motor and sensory fibers or interneurons of the spinal cord, the effect of individually activating the different parts of the spinal cord circuits can be investigated. Additionally, light does not spread as current does, and only neurons in the beam of light will be activated. Developing an optogenetic stimulation platform for the spinal cord would then allow to dissect the role of each cell type in recovery, and possibly to optimize this recovery thanks to specifically tailored protocols.

### 4.1.2 Challenges associated to chronic optogenetic stimulation of the spinal cord

In order to do optogenetic studies of the spinal cord, the light delivery device must allow for stable chronic stimulation for two main reasons. First, the study of locomotor tasks in vivo require awake recordings. Then, one of the main scientific questions is whether optogenetic stimulation can improve recovery and/or walking patterns following spinal cord injury, over the course of weeks to months. A light delivery device that is stable chronically is thus required.

Although laser-coupled optical fibers are widely used for optogenetic studies, they are poorly suited for chronic experiments. In the absence of an implantable light source, the device will remain tethered. Additionally, the spinal cord is a mechanically challenging environment. The small available space for implantation, the presence of soft spinal cord tissue (100-1,500 kPa) and the large natural movements of the spinal cord (up to 30% of dynamic strain) prevent the safe chronic use of stiff implants that induce spinal cord damages leading to walking impairments<sup>[136]</sup>.

Using an LED-based implant can overcome these challenges, and has the additional advantage of having a large design flexibility and the possibility to have a spatial distribution of LEDs. This can enable for instance a design with LEDs located on both sides of the spinal cord. The lateral selectivity of stimulation can be studied, as well as the effect of simultaneous bilateral stimulation. An LED-based device implanted epidurally also enables surface stimulation of the spinal cord, as opposed to the laser-coupled optical fiber approach, usually used with fibers penetrating the neural tissue<sup>[28]</sup>.

The size and mechanical properties of the implant are critical. The device integrating the LEDs and their encapsulation must be thin and conformable enough to be slid below the vertebrae during surgery. The spinal cord must also not be compressed and damaged, even upon important movements of the animal. Thermal safety must also be considered, as the LEDs generate heat when powered, and can induce chronic damage to the tissue. In the second chapter of this thesis, a parameter space for thermally safe stimulation of neural tissue was defined and will be used as a guide in this study.

### 4.1.3 Goals of the study

- Obtain a proof of principle of optical stimulation of the spinal cord in a mouse model for chronic experiments, in order to validate a technology that can potentially be used to dissect neuronal circuitry in the spinal cord and to better understand the mechanisms of recovery following spinal cord damage.
- Assess the location selectivity of spinal cord stimulation with EMG recordings in a device integrating 4 LED.
- Study the EMG recruitment curves and the effects of stimulation parameters - pulse

## Chapter 4. Optogenetic stimulation of the spinal cord

duration and pulse rate - on the evoked responses.

- Analyse the chronic variation of threshold and other EMG response properties
- Investigate the chronic thermal and mechanical safety of the device with histological analysis of the tissue and detection of any impairment of normal walking due to the device.

### 4.2 Optoelectronic device for spinal cord stimulation

#### 4.2.1 Device with 4 LEDs for lateral spinal cord stimulation

The device developed for chronic stimulation of the spinal cord is integrating two LEDs for the stimulation of the left side and two for the stimulation of the right side of the spinal cord (Figure 4.1A), following the process flow for optoelectronic devices presented in the first chapter of this thesis .

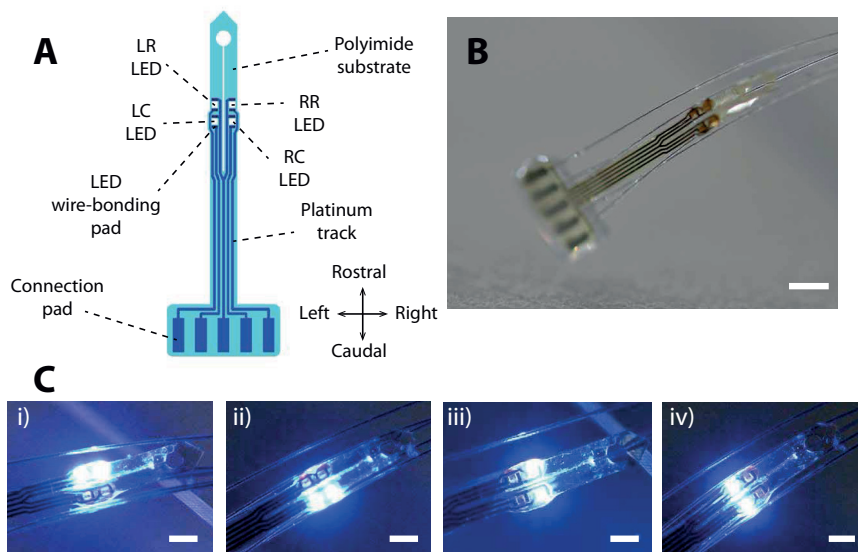


Figure 4.1: A) Design of the spinal cord optical stimulation device, showing the labelling of the LEDs according to their position: left rostral (LR), left caudal (LC), right rostral (RR) and right caudal (RC). B) Photograph of the finished device (scale bar: 2 mm). C) Illustration of the four possibilities to power two LEDs in series to stimulate the right (i) or left (ii) side of the spinal cord, or bilaterally on a more rostral (iii) or caudal (iv) locations.(scale bars: 1 mm)

The four LEDs are labeled according to their position, on the right (R), left (L), and on the rostral (R) or caudal (C) side of the implant (according the anatomical orientations after



## 4.2. Optoelectronic device for spinal cord stimulation

---

implantation). Following this notation, the four LEDs are then labeled RR, RC, LR and LC. The shape of the substrate is designed for epidural implantation of the device below the mice vertebrae. In order to maximize the lateral positioning of the LEDs and facilitate the implantation of the device, a slit in the substrate along the midline of the device is designed. The center-to-center distance between two LEDs is 750  $\mu\text{m}$  in both directions. Due to the design of the connections, LEDs can be powered individually or by pairs (Figure 4.1C). The two LEDs on each side of the spinal cord can be powered in series, in order to maximize the light power delivered on one side and to study the lateral selectivity of stimulation. Alternatively, the two LEDs located at the same level in the spinal cord can be powered in series, in order to test the effect of simultaneous bilateral stimulation.

### 4.2.2 Experimental model

The experimental models are transgenic mice expressing channelrhodopsin (ChR2) under the control of the Thy1 promoter, widely expressed in projection neurons. This model is known to have a low threshold to optical stimulation, due to the robust expression of the ChR2<sup>[215]</sup>.

In order to record motor activity generated by optical stimulation of the spinal cord, EMG recording electrodes are implanted in two different muscles of each leg. These muscles are the vastus lateralis (VL), a knee extensor muscle, and the tibialis anterior (TA), a ankle flexor muscle, in the right (R) and the left (L) leg. The four EMG channels are thus labeled RTA, RVL, LTA and LVL in the following sections.

### 4.2.3 Characterization of device placement

During implantation surgery, the mice are anesthetized with isoflurane and three different laminectomies are performed, at the levels T12-T13, T13-L1 and L2-L3. The implant is then passed through the third laminectomy and slid below the vertebrae, until the four LEDs are placed against the spinal cord at the spinal level L3. The connector is then secured in place with sutures, and the percutaneous amphenol connector (Omnetics) is secured on the skull of the animal with dental cement.

A microCT scan confirming the placement of the implant is shown on figure 4.2. On this image, we can see the four LEDs below the vertebrae, as well as the platinum tracks and the connector. Although the connector slightly slid on the left, the active part of the device is located along the midline. Figure 4.2C shows a rostral view of the spinal canal, with the LEDs located dorsally against the spinal cord (not visible here).

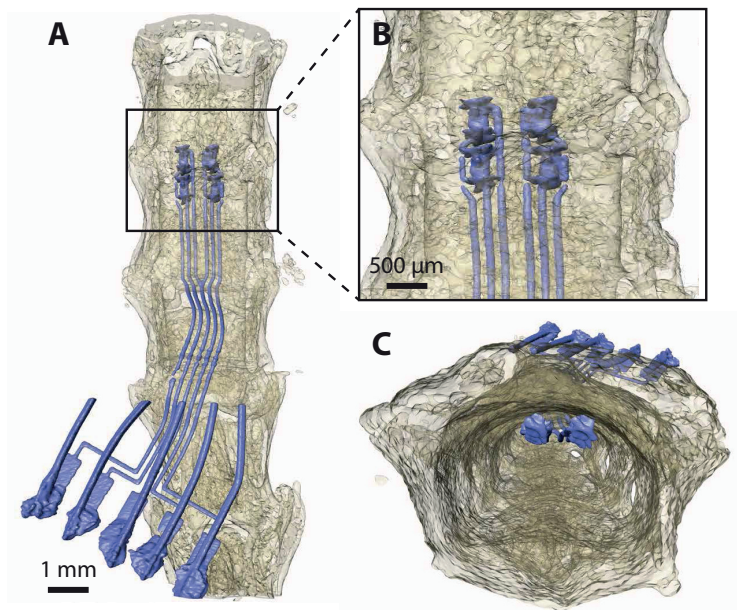


Figure 4.2: MicroCT images confirming the device position, with the active part located below the vertebrae, along the midline.

### 4.3 Functional validation

#### 4.3.1 Experimental setup and stimulation protocol

The LEDs are powered by a custom-built current source. EMG signals are recorded using a RZ5 processing unit (Tucker-Davis Technologies, sampling frequency 12 kHz), for the 4 EMG channels simultaneously. Signals are pre-amplified and pre-filtered (10-2,000 Hz bandpass) by an AM-amplifier. Responses following 10 to 20 pulses are obtained for each condition and the signals are analysed offline with programs written in MATLAB.

These experiments present the results obtained on two mice. The first mouse provides a proof of principle for chronic optical stimulation, with optical pulses of 5 ms duration, at a pulse rate of 1 Hz. Recordings are obtained at day 8, 24, 44 and 57 after surgery. The second mouse is used for a more systematic testing of the threshold and the effect of pulse duration (5 - 20 ms) and pulse rate (1 - 20 Hz) on the responses. Recordings are obtained on day 7, 14, 21, 28 and 35 after surgery.

#### 4.3.2 Raw EMG responses

Strong and consistent EMG recordings following optical stimulation of the spinal cord are obtained (Figure 4.3). In the examples displayed on figure 4.3A, EMGs recorded in four

muscles (RTA, RVL, LTA and LVL) are shown following stimulation with two pairs of LEDs at different current levels, on the right side (RR + RC) and the left side (LR + LC) of the spinal cord. These awake recordings are obtained 7 days after device implantation.

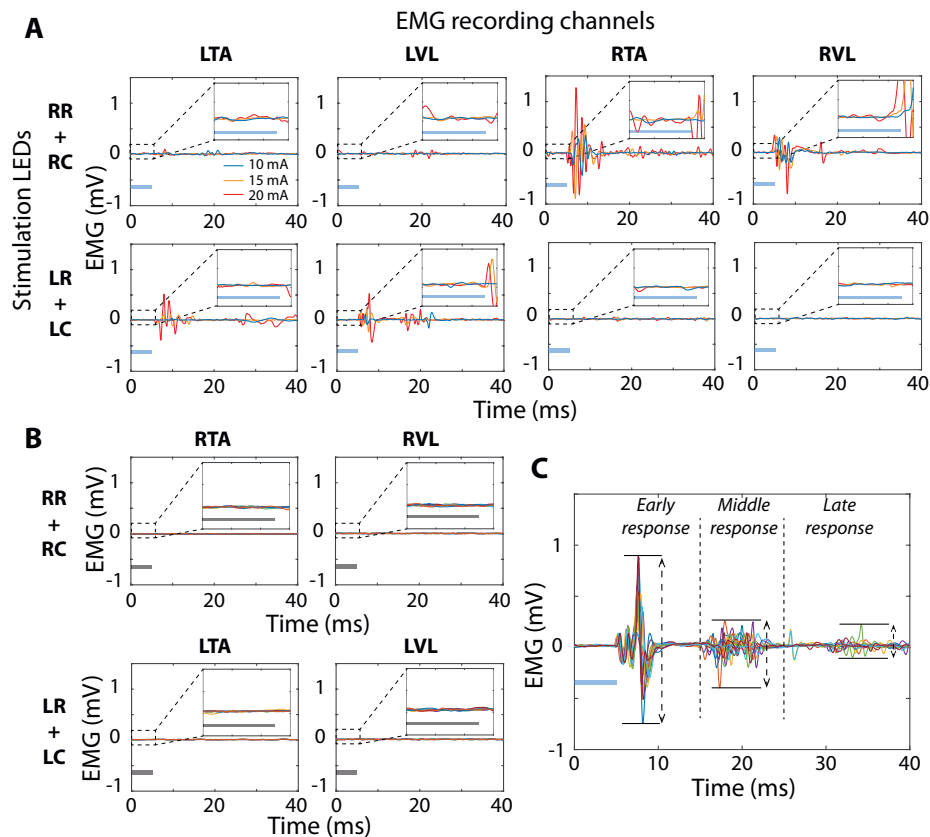


Figure 4.3: A) EMG recordings from four different muscles (LTA, LVL, RTA, RVL) following stimulation with the pair of LEDs on the right side (RR: Right Rostral; RC: Right Caudal) and the left side (LR: Left Rostral; LC: Left Caudal) of the spinal cord, for three different currents powering the LEDs. The insets display enlarged versions of the 5 ms stimulation pulse, showing the absence of stimulation artefact. B) EMG recordings following stimulation with LEDs with reversed connections, confirming the absence of current leak in the device. C) EMG recording illustrating the extraction of peak-to-peak amplitudes of the three phases of responses, the early response (ER), middle response (MR) and late response (LR).

The first observation is the lateral selectivity of activity in the displayed recordings (Figure 4.3A). Indeed, the pair of LEDs located on the right generates activation in the muscles of the right leg (RTA and RVL), and the pair of LEDs on the left generates activation in the muscles of the left leg (LTA and LVL). The lateral selectivity shows some variations, as described in the following sections.

It is necessary here to provide evidence that the activity is not the result of an electrical

## Chapter 4. Optogenetic stimulation of the spinal cord

---

leak in the device. First, electrical stimulation is associated to a stimulation artefact after the pulse. Here, the pulse duration is 5 ms, and it is likely that a separate artefact would be generated by the beginning and the end of the pulse. An artefact following the end of the pulse would be masked by the generated EMG, so impossible to detect. However, an artefact following the beginning of the pulse would likely be visible before the onset of the EMG. The insets of figure 4.3A show enlarged versions of the first 6 ms following stimulus onset. Small variations in the signals are observed, but they are not consistent between the different stimulation current levels. It is then concluded that they are not stimulation artefacts, and are rather generated by random movements of the animal.

The second control that is performed in order to check that the stimulation is not the result of an electrical leak in the device is to reverse the connection of the LEDs (+/-). As a result, the LEDs block the current and do not generate any light. If there was a leak in the device, a path for the current would be present and electrical stimulation of the spinal cord could be induced. Figure 4.3B shows examples of two pairs of LEDs with reversed connections, with the stimulation parameters being otherwise the same as the example shown in panel A. No activity or stimulation artefact can be observed in these runs. It is then concluded that the observed activity is not the result of an electrical leak in the insulation of the device, but is rather generated by optical stimulation.

### 4.3.3 EMG parameters characterization

To perform quantitative analysis of the recorded EMGs, several parameters are extracted from all four channels. First, the root mean square (RMS) of the generated signal is measured. This represents the energy of the signal and provides a characterization of the intensity of activity in each muscle. Then, as illustrated in figure 4.3C, the EMG activity was identified to occur in one or several of three different phases, with limits at about 15 and 25 ms after stimulus onset. The maximal peak-to-peak amplitude of the signal during the early, middle and late responses (ER, MR and LR) are extracted following each individual pulse. For each response parameter  $R$ , the lateral selectivity  $L$  is measured in each muscle as  $L = \frac{R_{ipsilateral}}{R_{ipsilateral} + R_{contralateral}}$ , with  $R_{ipsilateral}$  and  $R_{contralateral}$ , values of the response parameter respectively in the ipsilateral and contralateral muscle with respect to the stimulation. Values vary between 0 and 1, from purely contralateral (0) to purely ipsilateral response (1).

The effect of stimulation with pulsed LEDs powered with different current levels on the four parameters extracted from the generated EMGs are displayed on figure 4.4. These data are obtained from the second mouse, 7 days after implantation, with a pulse duration of 5 ms and a pulse rate of 1 Hz. In the first column, the data following stimulation with the left pair of LEDs (LR + LC) is presented. Columns 2 and 3 show the data generated by stimulation of the two single LEDs (LC and LR).

Stimulation with the pair of LEDs generates stronger activity with lower thresholds than single LEDs, an effect visible in all four analysed parameters. The pair consists of two LEDs connected in series and located  $750\ \mu\text{m}$  apart (center-to-center), which corresponds to about  $500\ \mu\text{m}$  spacing, along the same side of the spinal cord. A larger response by the pair of LEDs can be explained by the higher total power brought to the tissue. The relatively low distance between the two LEDs indicates that a partial overlap of the light is very likely, especially because of the non-directionality of the LED light.

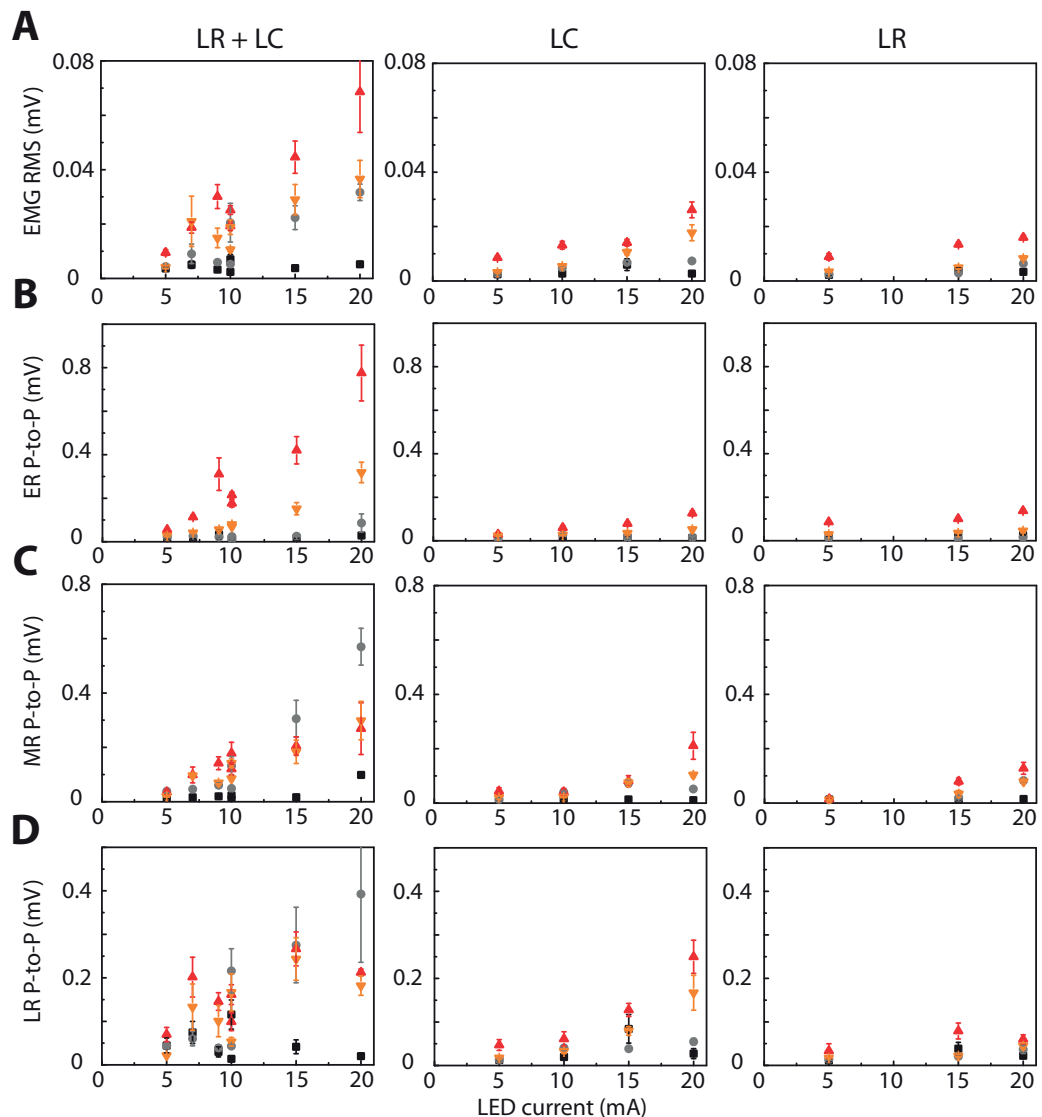


Figure 4.4: A) EMG RMS and peak-to-peak amplitude of B) the early phase (ER), C) the middle phase (MR) and D) the late phase (LR) of responses following stimulation at different current levels of the left pair of LEDs and of the two individual LEDs.

## Chapter 4. Optogenetic stimulation of the spinal cord

The thresholds were visually determined during experiments, for each of the two lateral pairs of LEDs, as the lowest current level generating a visible and repeatable movement of the leg. In the example shown on figure 4.4, the visually determined threshold was 6 mA for the pair LR + LC. It visually corresponds to the increase in peak-to-peak amplitude of at least one of the three phases of activity. For the LEDs LR + LC, EMG parameters from all four EMG channels show significant increase of activity at threshold compared to below threshold (mult.lin.reg, N=10 repetitions,  $p < 0.05$ ).

For each of the two considered muscles (TA and VL), the lateral selectivity (or fraction of ipsilateral activity) following stimulation on each side of the spinal cord is measured. A value of lateral selectivity higher than 0.5 thus indicates that the ipsilateral activity is stronger than the contralateral activity. In the amplitude of the early response, ipsilateral muscles show stronger responses than contralateral muscles (Fig. 4.5), showing the lateral selectivity of stimulation, as indicated by a lateral selectivity higher than 0.5. This selectivity means that LEDs located on one side of the spinal cord preferentially stimulate the leg muscles on the same side. For both leg muscles and both sides of stimulation, the lateral selectivity decreases in most cases at later phases of response. The peak-to-peak amplitude of the late response shows in some cases contralateral muscles having stronger responses than ipsilateral muscles, as indicated by a measure of lateral selectivity lower than 0.5. It shows that contralateral responses preferentially occur later in the responses, which can be due to left-right circuit communication in the spinal cord.

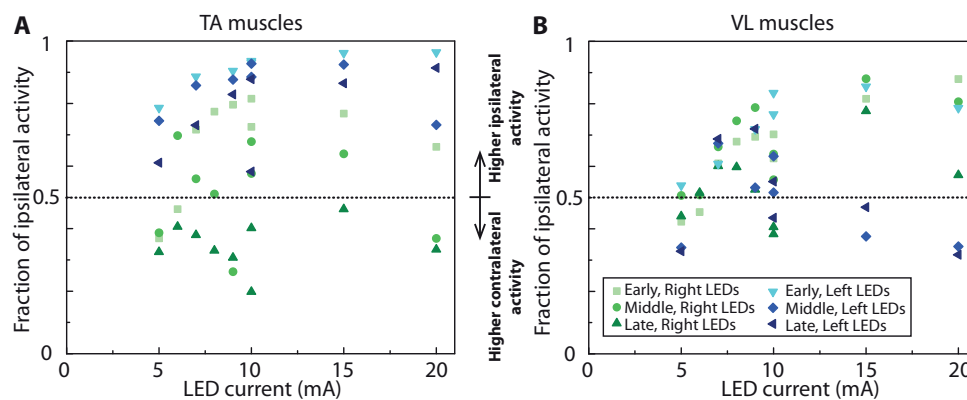


Figure 4.5: Fraction of ipsilateral activation for the early, middle and late phases of response in A) the tibialis anterior (TA) and B) the vastus lateralis (VL) muscles

### 4.3.4 Parametric study

The effect of varying the pulse duration and pulse rate are investigated in this section. Since there can be variations in the current threshold used to power single or pairs of LEDs that generate EMGs, both parametric studies are performed at a current of 5 mA above threshold, visually determined with a pulse duration of 5 ms and a pulse rate of 1 Hz. These parameters

were chosen because they generate stable EMGs, on which the effect of varying stimulation parameters can be studied. Pulse duration and pulse rate experiments are performed on mouse 2 at days 7, 14, 21, 28 and 35 after surgery.

**Pulse duration**

Figure 4.6A presents the peak-to-peak amplitude of the early, middle and late responses following stimulation with the two pairs of LEDs RR + RC and LR + LC, at day 7 after surgery. Pulse durations of 5, 10 and 20 ms are tested. Stimulation of the right pair of LEDs shows a significant correlation between the pulse duration and the amplitude of the late response in both right leg muscles (mult.lin.reg, N=10 repetitions,  $p < 0.05$  in both cases). The other parameters, including the parameters of the EMG channels in the left leg, do not show a significant correlation with pulse duration (mult.lin.reg, N=10 repetitions,  $p > 0.05$  in all cases).

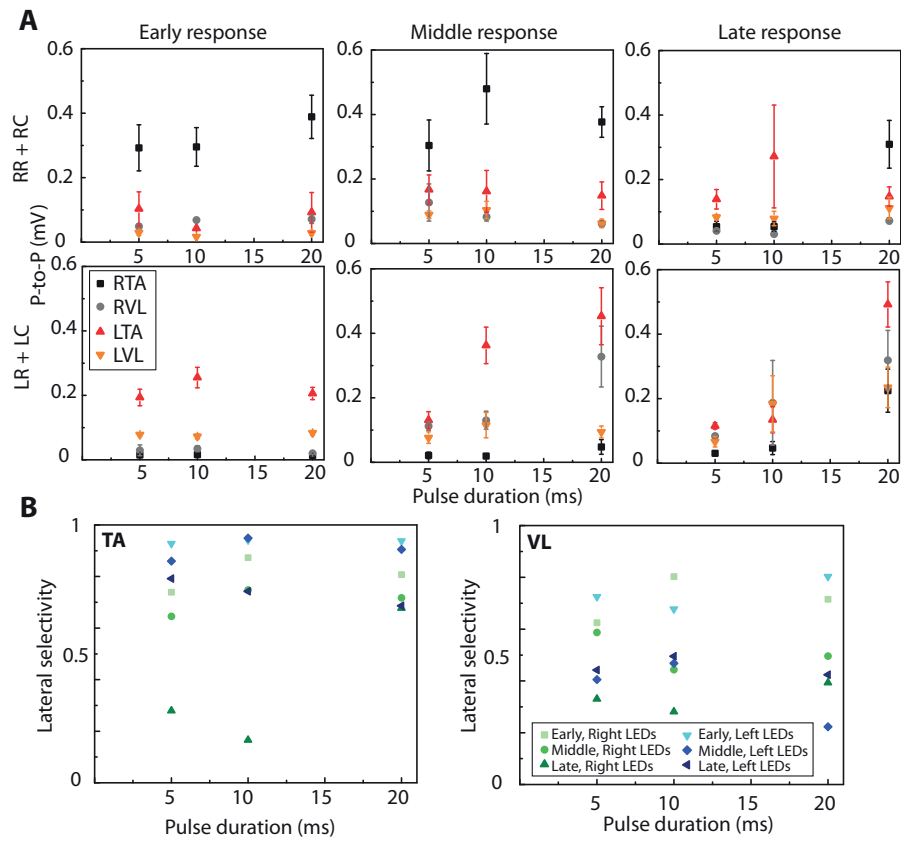


Figure 4.6: A) Stimulation pulse duration effect on the EMG peak-to-peak amplitude of the early, middle and late responses, for the pairs of LEDs stimulating the right (RR + RC) and left (LR + LC) sides of the spinal cord. B) Stimulation pulse duration effect on the lateral selectivity of activation in the tibialis anterior (TA) and vastus lateralis (VL) muscles.

Following stimulation with the left pair of LEDs, all LTA parameters show a significant correla-

## Chapter 4. Optogenetic stimulation of the spinal cord

---

tion with the pulse duration (mult.lin.reg, N=10 repetitions,  $p < 0.05$  for all LTA parameters). Unlike the stimulation on the right side, some contralateral EMG parameters also increase with pulse duration: The amplitude of the early and late responses in the RTA muscle, and the amplitude of the middle and late responses in the RLV muscle (mult.lin.reg, N=10 repetitions,  $p < 0.05$  in both cases).

The lateral selectivity of stimulation (Figure 4.6B) shows a different behavior for the two considered muscles, the tibialis anterior (TA) and the vastus lateralis (VL). While the lateral selectivity in the TA increases with pulse duration until reaching values higher than 0.7 for all parameters, no trends can be identified in the lateral selectivity of the VL muscle. We can then conclude from this study that increasing the pulse duration generates an increase in the intensity of generated EMGs, mainly on the same side as the stimulation. The lateral selectivity of stimulation increases with pulse duration in the TA muscle.

### Pulse rate

Figure 4.7A shows the variations in the EMG parameters following stimulation at 1, 2, 10 and 20 Hz with the right pair of LEDs, and 1, 2, 5, 10 and 20 Hz with the left pair of LEDs on day 14 after surgery.

Stimulation with the right pair of LEDs (RR + RC) shows a significant negative correlation between the pulse rate and the amplitude of the early and middle responses in the right EMG channels (mult.lin.reg, N=10 repetitions,  $p < 0.05$  in both cases). The correlation is also significant in the LTA muscle for the amplitude of the middle and late responses (mult.lin.reg, N=10 repetitions,  $p < 0.05$  in both cases). Following stimulation with the left pair of LEDs (LR + LC), the only parameter that shows a significant variation with pulse rate is the peak-to-peak amplitude of the middle response for the left EMG channels (mult.lin.reg, N=10 repetitions,  $p < 0.05$ ). The lateral selectivity seems to decrease with pulse rate in the VL muscles, and shows no identifiable trend in the TA muscle (Figure 4.7B).

These results indicate that increasing the pulse rate generates a strong decrease in the EMG intensity parameters, primarily on the ipsilateral side. In fact, ChR2 decreases in synchronicity of spikes as the frequency of stimulation is increased<sup>[20,76]</sup>. However, ChR2 was shown to follow pulse rates up to about 40 Hz<sup>[20,70]</sup>. Since all frequencies were tested with the same light intensity in our experiments, it is possible that increased pulse rates simply lead to increased thresholds.

This behavior could be explained by the relatively slow kinetics of the ChR2 that shows an off time constant  $\tau_{off}$  of about 10 ms and a slow recovery following inactivation (50% recovery after about 5 sec)<sup>[70,108]</sup>. If the recovery following inactivation is not complete when the next light pulse is generated, the following neuronal activation will be less synchronized and thus the potential generated EMG will be of reduced amplitude. This effect can be expected to hap-



pen at all tested frequencies, but is much more important as the frequency increases. Other opsin constructs, like Chronos<sup>[76]</sup>, ReaChR<sup>[107]</sup> or ChR2 mutants (ET/TC)<sup>[20]</sup> could potentially overcome this problem because of their faster kinetics.

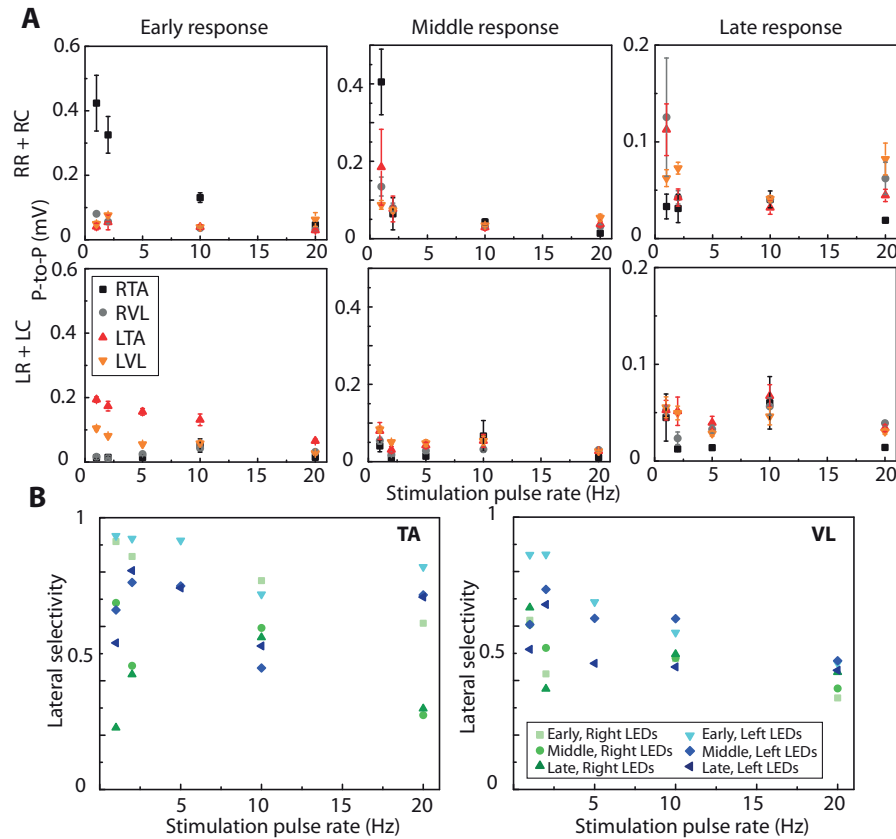


Figure 4.7: A) Stimulation pulse rate effect on the EMG peak-to-peak amplitude of the early, middle and late phase of responses, for the pairs of LEDs stimulating the right (RR + RC) and left (LR + LC) sides of the spinal cord. B) Stimulation pulse rate effect on the lateral selectivity of activation in the tibialis anterior (TA) and vastus lateralis (VL) muscles.

## 4.4 Chronic stability and safety

### 4.4.1 EMG parameters chronic variations

During each experiment on the second tested mouse, the current threshold generating a visible and repeatable movement of the leg is visually determined for each of the two lateral pairs of LEDs. The threshold variations over time during the five weeks of testing are displayed on figure 4.8A. The general trend that can be observed is a decrease in threshold between the first and the second weeks after implantation ( $-3$  mA for both pairs), followed by a stabilization with variations of  $\pm 1$  mA between each of the following tests. This behavior can be explained by residual blood that might still be present at day 7, absorbing part of the light. This blood

## Chapter 4. Optogenetic stimulation of the spinal cord

would then be cleared between day 7 and 14 as the healing progresses, resulting in a decrease in threshold, followed by a stabilization in the following weeks.

Figure 4.8B displays an overlay of EMGs obtained with the right pair of LEDs (RR + RC) at each tested post-implantation day. Although there are some variations in amplitude, the latencies of the responses do not change over time. For instance, RTA recording shows an early and middle response in all cases.

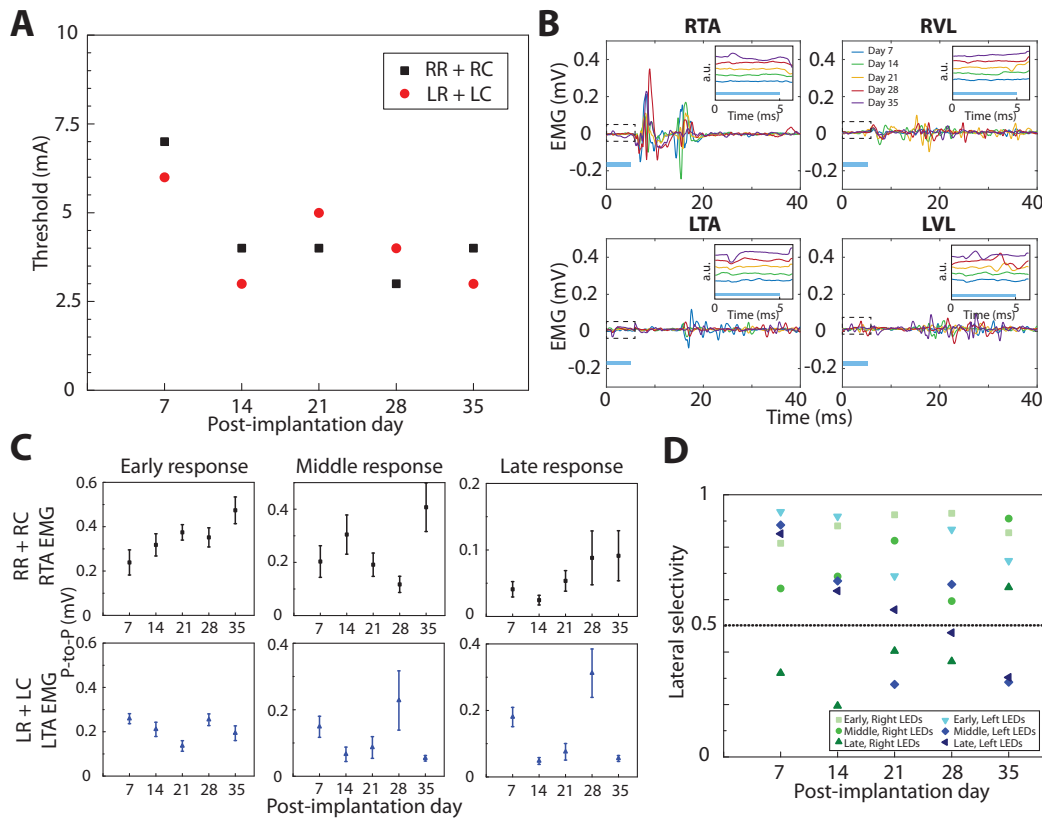


Figure 4.8: Chronic variations of EMG parameters. A) Visually determined threshold obtained for the two lateral pairs of LEDs over time. B) EMGs obtained with the right pair of LEDs (RR + RC) at each post-implantation day. Insets: Zoom in the first 6 ms following stimulation onset, showing a stimulation artefact increasing over time in some cases. C) Chronic variations of the EMG peak-to-peak amplitude of the early, middle and late responses in the ipsilateral TA muscle, for the pairs of LEDs stimulating the right (RR + RC) and left (LR + LC) sides of the spinal cord (pulse rate: 1Hz, pulse duration: 5 ms, current level: 5 mA above visually-determined threshold). D) Lateral selectivity of TA muscle activation over time, for the early, middle and late responses, for the right and left pairs of LEDs.

In some cases, a stimulation artefact appears over time, visible here in the LTA recording. Several clues indicate that the responses are not generated by parasitic electrical stimulation.

First, this artefact is not present in all runs and recordings and is not necessarily linked to the presence of an EMG in the recordings. Then, the response does not qualitatively change over time, which would likely be the case if the stimulation mode was going from optical to electrical. For instance, electrically-generated EMGs could follow pulse trains at higher frequency (40 Hz)<sup>[31]</sup>, which is not the case here in any of the tests, even at day 28 and 35, although it could be due to an increase in threshold. Additionally, tests with opposite polarity of current were performed each week in all LEDs, and none of them show any artefact or EMG responses, confirming the absence of leak in the device. Examination of the devices after sacrificing the animals showed significant damage on some wires of the stimulation and the recording devices at the level of the headplug. This damage typically appears over time, and could explain the presence of a stimulation artefact in the recordings. These clues then strongly suggest that the appearance over time of a stimulation artefact is not due to a damage in the device encapsulation at the level of the LED active sites, but rather to a damage in the insulation of the wire at the level of the headplug.

Analysis of the parameters extracted from the generated EMGs show no consistent change over time. The current level used to power the LEDs at each time point and for each pair of LEDs in this figure is 5 mA above visually determined threshold, to compensate for chronic threshold variations (Figure 4.8C). The lateral selectivity of the activity recorded in the TA muscle over time (Figure 4.8D) also shows no identifiable general trend, although the higher lateral selectivity of early response compared to late responses seems to be conserved at each time point.

These analyses mean that first, we are able to generate and record EMGs over time, up to 35 days in mouse 2 (and up to 57 days in mouse 1, not displayed here). Since the presented analyses focus on data obtained in one mouse, only general trends can be observed. A higher number of mice is necessary in order to show and explain specific variations over time.

#### 4.4.2 Integrity of the walking functionality

In order to investigate the integrity of the walking functionality, recordings of mice walking on a horizontal ladder with random distances between each rung are obtained. Functional damages of the spinal cord can be detected by an increase of the 'slip' and 'miss' steps, when the foot is not placed at the right position and slides from, or misses the rung. The random distances between the rungs make the task challenging, thus highlighting potential walking impairments due to spinal cord damages.

The test was performed on two different mice, before implantation and on day 35 after implantation. The total percentage of 'hit' was measured before and after implantation. Results show very similar percentages of 'hit' in the two conditions, suggesting that no impairment of functionality due to the presence of the device or the stimulation is generated.

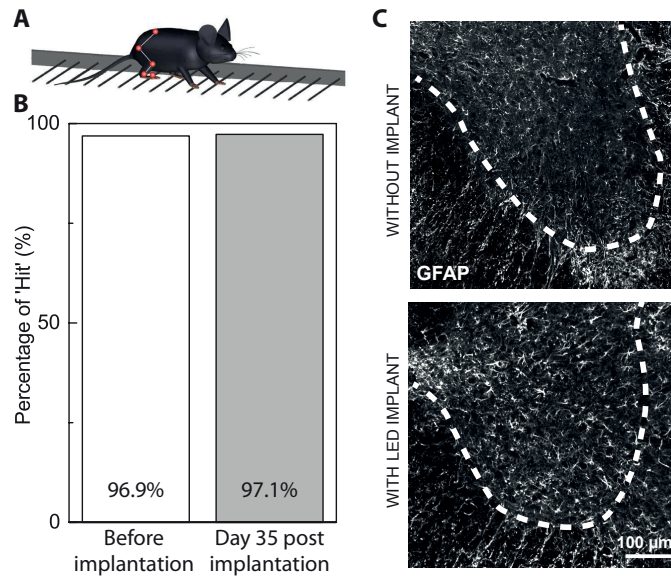


Figure 4.9: A) Illustration of the ladder test. B) Percentage of 'Hit' steps before and after device implantation. C) Coronal sections of the right side of the spinal cord at the level L2, with and without LED implant, with labeling of glial fibrillary acidic protein (GFAP), a marker of inflammation shown in white. The dotted line is the separation between white and grey matter in the spinal cord.

### 4.4.3 Histological analysis

Histological analysis of the explanted tissue with highlighted GFAP, a marker for astrocytes associated with tissue inflammation is shown on figure 4.9C. More astrocytes seem to be present on the spinal cord with LED implant, suggesting that some inflammation is generated by the implant. Quantitative analysis of different markers of inflammation would be necessary to fully characterize the extent of this inflammation.

## 4.5 Discussion

### 4.5.1 Optical power and thermal heating

The presented results provide a proof of principle of optogenetic stimulation of the spinal cord with a device integrating an array of LEDs. The power generated by these LEDs was shown to be sufficient to generate EMG responses in the leg muscles following unilateral spinal cord stimulation, both in the ipsilateral and contralateral leg muscles.

The threshold for both pairs of LEDs after stabilization (about two weeks) is 3-5 mA. Measurements of LEDs power in the first chapter of this thesis at a current of 5 mA showed optical power of about 2.5 mW per LED, so about 5 mW per pair of LEDs, and a voltage bias for a

pair of LEDs of about 7 V. The surface of light generation for each LED is about  $190 \times 230 \mu\text{m}^2$ , so a power of 5 mW corresponds to a power density of about  $57.2 \text{ mW}/\text{mm}^2$ . At the single cell level, the necessary power density to generate channelrhodopsin activation is about  $1 \text{ mW}/\text{mm}^2$ <sup>[215]</sup>. Considering that the light of these LEDs is not completely directional, the power density at the tissue level is lower than at the surface of the LED. Additionally, the neurons or the projections expressing ChR2 are not necessarily at the surface of the spinal cord. Due to absorption and scattering in the tissue, the power decreases exponentially with depth. These two elements can thus explain the discrepancy between the ChR2 activation threshold and the visually determined threshold for leg movement.

Chronic increases of temperature as low as  $1^\circ\text{C}$  have been shown to induce differences in the neurophysiological properties of neurons, and the official regulations prevent a chronic increase of temperature larger than  $2^\circ\text{C}$ <sup>[51,119]</sup>. As seen in chapter 2 of this thesis, the chronic increase in temperature mainly depends on the duty cycle and the current. A model of thermal heating was developed based on measurements in air at the surface of the device, in order to predict the average increase at the surface of the tissue for each condition. The standard parameters of pulse rate and pulse duration used in these experiments (1 Hz and 5 ms) correspond to a duty cycle of 0.5%, at which chronic increases in temperature are below  $1^\circ\text{C}$  at 20 mA, the highest tested current level.

For the pulse rate studies, a maximal duty cycle of 10% at a pulse rate of 20 Hz and a pulse duration of 5 ms was used. At that duty cycle, the current generating an average temperature increase of  $1^\circ\text{C}$  is about 2.6 mA, well below the current levels between 8 and 12 mA used here. The highest pulse rate used in this study is thus not safe for chronic stimulation. For a pulse duration of 5 ms and a stimulation current of 5 mA (close to the threshold value after stabilization), the pulse rate generating an average increase in temperature at the surface of the tissue of  $1^\circ\text{C}$  is 10 Hz. The pulse rate thus needs to be lower than this value to achieve chronic thermal safety at threshold.

The pulse duration studies performed suggest that longer pulse durations might generate stronger EMGs than shorter pulse durations, perhaps because more fibers are recruited. The three pulse durations tested (5, 10 and 20 ms) correspond, at 1 Hz, to duty cycles of 0.5, 1 and 2%. At a duty cycle of 2%, an average temperature increase of  $1^\circ\text{C}$  is generated by a current of about 10 mA, slightly below the maximal current of 12 mA used in these experiments. This pulse duration might then be too long in terms of chronic thermal safety, and shorter pulse durations should be favoured. The optimal pulse duration then has to be determined as a tradeoff between efficiency and thermal heating.

### 4.5.2 Device

In the two mice, all 4 LEDs were still functional on the last tested day, respectively on day 57 and 35 post implantation. It is thus not the limiting factor for chronic experiments, the wear

## Chapter 4. Optogenetic stimulation of the spinal cord

---

of the cables at the level of the headplug inducing failure of the EMGs before a failure of the LEDs. In order to increase the total implantation time and the quality of recordings, it is then important to use a setup that allows an improved chronic stability of the EMGs.

The absence of functional damage to the spinal cord validates the possibility to use this device in our experiments. Despite the fact that the LEDs are rigid, and that the wires connecting the LEDs to the neighbouring pads increase the total thickness of the device, the PDMS encapsulation allows to have a soft surface of contact that prevents any functional damage of the spinal cord upon natural movements of the animal, for several weeks of implantation.

However, the presence of markers of inflammation on the surface of the spinal cord suggests that the device could be improved in order to provide a better interface with the spinal cord with minimal inflammation. For instance, using an alternative technique than wire-bonding to connect the LEDs, like eutectic bonding, would lead to thinner devices, that are thus less invasive and safer for the spinal cord. Developing a completely soft interface could also further decrease the mechanical mismatch with the spinal cord tissue. Indeed, even if thinner LEDs are used compared to the LEDs used in this project (50  $\mu\text{m}$ ), the soft-to-hard transition remain a mechanical challenge in the long term function of the device, especially under mechanical constraints. Flexible LEDs are under development<sup>[39,80,102,189]</sup> and might be a potential future solution for soft optoelectronic interfaces.

Decreasing the average heating in the tissue could lead to thermally safe stimulation at higher illumination levels. One of the ways to achieve this could be to use a thermally-conductive epoxy at the back of the LEDs in order to act as a heat sink. The device could also be improved by optimizing the light extraction. This could be achieved by adding a micromirror on the backside of the LEDs<sup>[21]</sup>. Although the device would be thicker, the total light brought to the tissue at a certain current level could be increased. This could then potentially lower the tissue heating for the same functionality.

### 4.5.3 Potential applications

We provided a proof of principle of chronic optogenetic stimulation of the spinal cord in a mouse model with broad ChR2 expression in projection neurons. We presented a platform that is transferrable to specific applications, such as selective targeting of motor fibers, or specific interneurons of the spinal cord, among others. For each of these neuronal subtypes, the precise role in the spinal cord processing and motor control can be studied, as well as their potential role in the recovery mechanism.

The effect of stimulation location can be investigated by directly targeting neurons in the spinal cord as opposed to fibers on the side of the spinal cord. Indeed, the main hypothesis for electrical stimulation is that it stimulates the fibers on the sides of the spinal cord, at the level of the DRGs. As optical stimulation targets the neurons that are located directly in the

beam of light, a greater control on the location of stimulation can be achieved. Some further understanding of the mechanisms of recovery could be obtained by comparing different locations and modes of stimulation. The developed device thus has a great potential as a spinal cord stimulation research platform to better understand the role of each neuronal type in the processing and potentially also in the recovery mechanisms following a spinal cord injury.

### **Contributions**

Surgeries for animal experiments presented in this chapter were performed in the laboratory of Prof. G. Courtine at EPFL, by L. Asboth, N. Pavlova and P. Shkorbatova. MicroCT images were obtained by J. Gandar. Histology was performed by L. Asboth. Part of the stimulation setup was optimized by M. Jobin.





# 5 Discussion

## 5.1 Selectivity of stimulation

One of the main goals of this thesis is to define technological routes to improve selectivity of surface stimulation of nervous tissue. Beyond auditory brainstem or spinal cord stimulation, the main contributions can thus be related to the spatial, structural and cell-type selectivity of neuronal stimulation and used for other surface nervous system stimulation applications.

### *Spatial selectivity*

- Using microfabrication strategies to decrease the area of stimulation sites and increase their density enables a greater tailoring of the stimulation configuration (bipolar or monopolar, various inter-electrode distances and orientations), which in turn may increase the possibilities of current steering. In bipolar stimulation, interelectrode distance and electrode pair orientation can be tuned to obtain higher frequency selectivity at similar loudness levels. Safety of stimulation and minimal power consumption can be provided by an electrode coating increasing the charge injection capacity and decreasing the impedance of the electrode sites.
- The conformability of the array enables a close contact with the target tissue, resulting in most cases in uniform minimal thresholds over the surface. Decrease of the current levels might then lead to a minimization of current spread.
- The use of optical stimulation did not lead to an improved spatial selectivity of stimulation as such, because of the relatively large LEDs and their absence of directionality, but using optogenetics can nevertheless avoid the problem of current spread in the tissue, thus effectively also contributing to an increased spatial selectivity of stimulation of neural tissue.

### *Structural selectivity*

An asymmetric waveform (long cathodic, short anodic) was shown in simulation studies to

preferentially activate neuron somata over fibers of passage. With this particular waveform, we obtained better tonotopic organisation and lower width of activation than with other waveforms. Results need to be confirmed and tested in different contexts, but this suggests that asymmetric waveforms in monopolar or bipolar configurations could be also used in other applications to achieve structural selectivity with preferential stimulation of neuronal somata.

### *Cell-type selectivity*

- In this thesis a technological platform that enables chronic optical stimulation of selected cell-types in mice is presented, with a proof of concept of spinal cord optogenetic stimulation. Because of the advantages of the microfabrication process allowing for a large flexibility in design, many other systems can be targeted, like the surface of the cortex, the peripheral nerves or the surface of the brainstem.
- Although no true cell-type selectivity can be achieved with electrical stimulation, an optimization of the stimulation protocol leading to optimal levels of spatial and structural selectivity can result in cell-type specific stimulation, depending on the structure and organization of the target tissue.

## 5.2 Strategies towards an improvement of ABI outcomes

This section proposes potential routes to improve the surface auditory brainstem implant, and presents an 'ideal' ABI array. Hypotheses on the mechanical and geometrical properties of the electrode array as well as on the stimulation protocol are based on the studies presented in this thesis and on previous studies and clinical reports of ABIs.

### 5.2.1 Substrate

First, increasing the conformability of the array compared to current clinical ABI arrays might be one of the keys to decreasing the distance to target neurons and obtaining uniform and minimal current thresholds over the whole surface of an array. This can be achieved by using thin-film technologies based on flexible substrates and mesh-like structures, as presented in this thesis. The use of softer substrates, such as elastomers, is dependent on the minimal feature size of the metallization achievable compared to the size requirements for a human ABI. This might be possible since the available surface of the human CN (about 3-by-8 mm<sup>2</sup>) is much larger than the rat DCN surface (1-by-2 mm<sup>2</sup>) accessible in the experimental setup presented in chapter 3, and because of potential technological improvements allowing for elastomer-based electrode arrays with feature sizes smaller than 100 μm.

Designing a soft ABI would however induce important implantation challenges. During implantation, the electrode array is slid between the brainstem and the cerebellum<sup>[180]</sup>, so

## 5.2. Strategies towards an improvement of ABI outcomes

---

using a soft array would induce a buckling of the substrate<sup>[81,100]</sup>. A solution to this challenge would be to temporarily stiffen the back of the array. This can be achieved for instance with stiff bioresorbable coatings based on silk<sup>[88,210]</sup> or polymers<sup>[55,196]</sup>, or with mechanically adaptable materials<sup>[204]</sup>. An important point is the kinetics of the changes in mechanical properties. Indeed, after initial placement of the ABI array during implantation surgery, the possibility to evoke auditory brainstem responses (ABR) from different pairs of the array is assessed, in order to detect any misplacement and to correct it. Several changes in placement and ABR measurements might then be performed, a time during which the ABI must remain stiff.

Designing an array with a soft substrate with engineered temporary stiffness might then optimally combine conformability and ease of insertion for a new ABI. A new design (Figure 5.1) with an 8  $\mu\text{m}$  thick polyimide layer integrating platinum tracks and electrode sites is proposed here, similar to what is presented in this thesis. In order to improve the conformability of the substrate around the curved human brainstem, the substrate is only slightly larger (about 25  $\mu\text{m}$ ) than the tracks and the electrode sites. Bioresorbable silk coatings are very promising for temporary stiffening of the back of the device, as the dissolution time (usually of a few min) is dependent on the silk thickness, and can be increased to about 1 hr with an ethanol treatment prior to implantation<sup>[88]</sup>.

### 5.2.2 Electrode sites diameter

In terms of geometrical properties of the implant, we propose several changes. First, the total footprint of the electrode pad in the clinical device is about 3.5-by-8  $\text{mm}^2$  (Cochlear) and 3-by-5.5  $\text{mm}^2$  (Med-El). However, the actual footprint covered by the electrode sites is smaller than this, about 2.3-by-7.8  $\text{mm}^2$  (Cochlear) and 2.3-by-4.7  $\text{mm}^2$  (Med-El). Making the total footprint of the electrode array larger than the target CN surface, with the actual footprint covered with electrode sites of about 3-by-8  $\text{mm}^2$  would increase the potential number of useful stimulation sites on the CN surface.

As mentioned in this thesis, an increase of the density of electrode sites would increase the number of possibilities to shape the current field, potentially improving the spectral resolution of ABIs. Currently, the ABI array contains 15-21 electrode sites with diameters between 550 and 700  $\mu\text{m}$ , and center-to-center distances of about 1 mm. The minimal diameter must be carefully considered, in terms of current and charge thresholds, current density and charge injection capacity of the electrode material. Audiological measures in ABI patients show thresholds between 10 and 200  $\text{nC}/\text{phase}$ <sup>[186]</sup>. These threshold values, obtained with pulses of 300  $\mu\text{s}$  duration and electrode diameters of 700  $\mu\text{m}$ , correspond to charge densities of about 2.6 to 52  $\mu\text{C}/\text{cm}^2$ . The dynamic range was usually between 10 and 20 dB. The highest measured value for the maximal comfortable loudness level across all tested patients was 1 mA. This current value is then used in the following calculations as the maximal current level to achieve, although it may vary substantially with pulse duration and electrode diameter.

Tissue damage due to chronic overstimulation was shown to depend on the charge density and charge per phase for macroelectrodes (area  $> 0.001 \text{ cm}^2$ , corresponding to a diameter  $> 356 \mu\text{m}$  for circular electrodes)<sup>[44]</sup>, according to the formula:  $\log\left(\frac{Q}{A}\right) = k - \log(Q)$ , with  $Q$ : charge per phase,  $A$ : electrode geometrical area and  $k$ : a factor varying between 1.5 and 2 depending on the experimental conditions<sup>[122,134,185]</sup>. Using a conservative value of  $k=1.5$ , a pulse duration (used in most experiments of this thesis) of 0.2 ms/phase and a maximal current of 1 mA, the electrode diameter allowing for safe stimulation is about 400  $\mu\text{m}$ . This value is thus the selected diameter for the proposed ABI design, and represents a substantial decrease compared to the clinical ABI electrode diameters of 550  $\mu\text{m}$  (Med-El) or 700  $\mu\text{m}$  (Cochlear).

### 5.2.3 Density of electrode sites

In the clinical implants, the center-to-center distance is about 1.1 mm (Cochlear) and 1.05 mm (Med-El), corresponding to gaps between electrodes of respectively 400  $\mu\text{m}$  and 500  $\mu\text{m}$ . With the electrode diameter tested here (400  $\mu\text{m}$ ), a tradeoff must be found between increasing the density of electrodes and limiting their number. We propose here a design that limits the number of electrode sites to 42, with center-to-center distances of 800  $\mu\text{m}$ , which corresponds to a decrease in distance of about 27% for twice as many channels compared to the 21-channels ABI.

An insight into the field of retinal prostheses where the spatial resolution and the number of channels are crucial for the visual acuity shows that such a high number of channels is feasible for a clinical implant. Indeed, the Argus II retinal implant system integrates an electrode array with 60 stimulation sites<sup>[116]</sup>. However, important challenges associated to the strong increase in number of channels are envisioned here. First, the size of the lead connecting the internal processing system to the array must contain the tracks for the 42 channels. We envision, with the polyimide/platinum microfabrication technology, that the width of the tracks can be as small as 50  $\mu\text{m}$ , with a similar gap between two tracks. This would result in a total width of the lead of about 4.2 mm, for a thickness of a few micrometers. In the clinical ABIs, the diameter of the lead is about 1.2 mm (Cochlear) and 1.3 mm (Med-El). A comparison of the sections of the lead shows that this should not be an important challenge: In the clinical implant, the section is 1.13 to 1.32  $\text{mm}^2$ , while on the proposed design, even with an overestimated substrate thickness of 100  $\mu\text{m}$ , the section would be 0.42  $\text{mm}^2$ .

The second challenge associated to increasing the number of channels is the extra time required in the programming sessions in order to test all the possible stimulation sites and configurations. Here, a protocol could be developed where, after initial test of all stimulation sites, only the stimulation sites showing the best perceptual performances can be included for further testing and programming of the device. A more automated fitting process for the

implant could also potentially reduce the time of tests<sup>[112]</sup>.

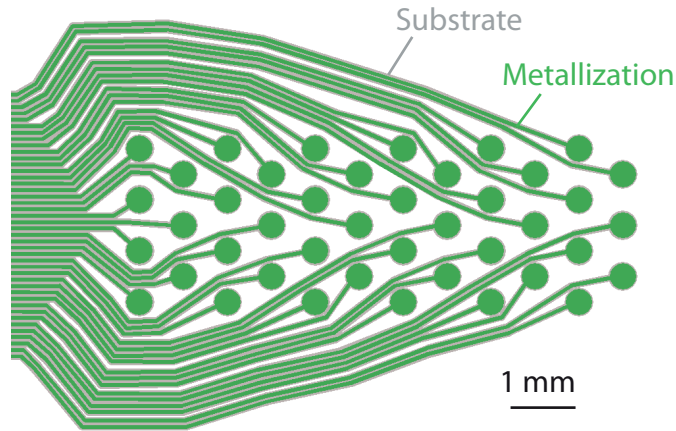


Figure 5.1: Proposed clinical ABI design

### 5.2.4 Stimulation electrode material

The charge density corresponding to a current level of 1 mA with a pulse duration of 0.2 ms and an electrode diameter of  $400\ \mu\text{m}$  is  $0.16\ \text{mC}/\text{cm}^2$ , which is thus considered as the necessary charge injection capacity of the stimulation material. As mentioned in chapter 2 of this thesis, the charge injection capacity also depends on the pulse rate and the exact in vivo conditions. Platinum and platinum/iridium have a charge injection capacity of about  $0.05\text{-}0.15\ \text{mC}/\text{cm}^2$ , depending on the electrode area and geometry<sup>[44,168]</sup>. The charge injection capacity thus needs to be improved.

Additionally, decreasing the electrode diameter compared to the clinical ABI electrodes will lead to an increase in impedance modulus, which is not favourable for power consumption of the implant. Here, we also propose to test bipolar stimulation configurations, leading to more power consumption than monopolar stimulation. Decreasing the impedance modulus of the electrode through a modification of the electrode surface might thus decrease the power requirements, compensating for the smaller diameters and bipolar configurations.

The Argus II retinal prosthesis system uses an array of stimulation electrodes of  $200\ \mu\text{m}$  diameter<sup>[116]</sup>. In order to increase the surface area of the electrode sites, they use a specifically tailored electroplated platinum ('Platinum grey', patent US 6974533 B2). Standard electroplated platinum (platinum black) results in an increase of surface area of about 200 times, with however a weak structure of the coating and a low stability over time. Due to the different electroplating protocol including a slower rate, the stability of the platinum grey is greater than that of platinum black, with a fractal design leading to an increase of the electrode surface area of about 5 times associated to a decrease in impedance modulus and increase in charge injection capacity. Platinum grey is thus an example of successful coating used for neural

stimulation electrode.

The coating presented in this thesis, electropolymerized PEDOT:PSS, induces a decrease in impedance modulus of more than one order of magnitude and an increase in CIC to about  $1.6 \text{ mC/cm}^2$  for a  $0.6 \mu\text{m}$  thick coating. These properties are thus ideal for a clinical implant. In fact, clinical tests of a recording array with PEDOT:PSS coatings on the electrode sites were performed intraoperatively and showed the possibility to record single spikes from the surface of the cortex due to the efficient interface provided by the coating<sup>[87]</sup>. However, PEDOT:PSS coatings were shown to have low stability over time, with loss of electrochemical properties and delamination upon long-term stimulation<sup>[61]</sup>. Stabilizing the structure might be an efficient way to increase the electrochemical stability of conducting polymers, as the main hypotheses of failure mechanisms are the stress in the film or volume changes due to ion transport<sup>[10]</sup>. Composites of conducting polymers with other polymers<sup>[85]</sup> or carbon nanotubes (CNT)<sup>[10,115]</sup> might be a way to improve chronic stability of the coatings, and seem promising to reach the level of stability necessary for a chronic implantation of many years.

### 5.2.5 Stimulation protocol

In terms of stimulation parameters, clinical stimulators can generate symmetric biphasic pulses with interphase intervals, with different pulse durations and pulse rates. However, their flexibility is still limited, and the use of other pulse shapes, like asymmetric pulses, is not possible. Here, we suggest that enabling a greater flexibility in the design of the stimulation protocol might be beneficial.

First, the different types of stimulation protocols investigated in this thesis (monopolar/bipolar, various interelectrode distances and orientations, various pulse waveforms) were shown to influence the neuronal recruitment properties and to potentially enable a tuning of the spatial or structural selectivity of stimulation. Although rat and human CNs show distinct differences<sup>[17]</sup>, they contain in both cases a multitude of neuronal types, playing different roles in the processing of speech. In our rat experiments, varying the stimulation protocol was shown to affect the responses both in their frequency tuning properties, but also in their general intensities (threshold and spike rate). Knowing that these waveforms could be further optimized and were sampled in a great amount of potential waveforms, the total variations in response properties due to the stimulation protocol might be very large.

Moreover, large subject variations were identified in clinical ABIs<sup>[13,18,167,180]</sup>. They might be due to the different conditions of the CN (affected or not by tumours), to differences in placement, in surgery, in the device itself, or even to intrinsic neurophysiological differences. Although the cause of the variability might not be the same, we also observed an important subject-to-subject variability in our rat experiments. A stimulation protocol optimized for one patient might thus not be as efficient for another patient, and individual adaptability seems of high importance. There might also be differences between subjects and between different

## 5.2. Strategies towards an improvement of ABI outcomes

---

stimulation electrodes within a single subject in the resolution of spectral and temporal information. Thus, some electrodes might be better suited for transmission of spectral information, and some others of temporal information<sup>[127]</sup>. Adapting stimulation protocols to the spectral and temporal properties of stimulation of each electrode site might then also lead to better speech understanding.

Although there are uncertainties in the applicability of the obtained results in humans, enabling a greater flexibility in the stimulation protocol, as well as personalized tuning of the stimulation parameters over time might be of high importance on the path to improved hearing outcomes of ABI patients. This illustrates that the physical array is not the only possible aspect of technical improvement of the ABI. A modification of the stimulator enabling more programming flexibility also seems of critical importance to bring true changes in the outcomes of ABI users.

### 5.2.6 Clinical validation

In light of the differences between the auditory systems of the rat experimental model and humans, it seems highly important, in order to justify the implementation of proposed changes, to study the effect of different electrodes configuration with the existing clinical device. In particular, a systematic test of bipolar configurations with small interelectrode distances on the pitch ranking of electrodes compared to larger interelectrode distances might determine whether this part of our results is transferrable. The bipolar stimulation used clinically during intraoperative testing is usually performed with large interelectrode distances, in order to test the eABR elicited by stimulation at the edges of the array<sup>[75]</sup>, and is not used for pitch ranking. Additionally, testing whether using different orientations of electrode pairs has an effect on the pitch ranking has not been done, to our knowledge, and might also have similar results than in our animal study.

Several audiological studies have been performed on the effect of pulse rate, pulse duration, polarity and number of stimulation sites<sup>[13,32,105,127,184]</sup>. For instance, the threshold to electrical stimulation was shown to decrease as the pulse rate was increased, up to about 200 to 300 Hz where it reached a plateau. These studies are limited to the range of stimulation parameters allowed by the clinical stimulators. If changes in the array or stimulator can be implemented, the proposed tests would include the effect of stimulation configuration, location, waveform and pulse parameters (pulse rate, pulse train duration) on:

- the threshold for acoustic perception,
- the presence or absence of extra-auditory side-effects,
- the pitch ranking, particularly the redundancy of different sites for the same frequency, and the resolution on the frequency axis (that might be represented by a 'tone-like' or a 'click-like' perception),

- the transmission of temporal informations of speech (vowel durations, consonants),
- the speech hearing outcomes and their improvement over time until reaching stable performances.

The challenge to consider here is the large increase in parametric space, and the resulting complexity of the tests. Solutions to narrow the parametric space to 'potentially good' configuration would have to be found, including a partial automatization of tests, in order to limit the time of fitting for each patient. In a research context, finding a few patients that agree to undergo substantial testing of the different potential stimulation protocols might be feasible, but clear and fast protocols should be found for general implementation in the clinics. The big challenge will thus be to implement this while keeping as much flexibility and personalization as possible.

### 5.3 Clinical translation of optogenetics

Many potential applications of optogenetics in a research context were mentioned in this thesis, and the list is not exhaustive. This technique clearly has a bright future for elucidating neural circuits, not only in spinal cord research or neuroprosthetic research, but in the whole neuroscience field. As a result, several clinical applications are emerging, and could have a great impact on treatment of many neurological conditions. However, there are still challenges to overcome in order to foresee a clinical translation of optogenetics-based therapies.

While the channelrhodopsin protein does not seem to disturb the normal function of the neurons in the absence of light stimulation<sup>[50]</sup>, the transfection of the gene in the target cells in a safe and controlled way is the first challenge to overcome. One possibility is viral delivery of genes, a technique that has been developed and tested for several years for gene therapy. There are some ongoing clinical trials for the treatment of Parkinson's disease<sup>[207]</sup> and retina degenerative diseases<sup>[41]</sup> that might pave the way for viral transfection of opsin genes for optogenetic applications. Another strategy that is being considered is the transplantation of cells containing the ChR2 gene at the site of light delivery. The main challenge with this strategy is the proper integration of the transplanted cells into the neuronal circuitry<sup>[207]</sup>. Promising studies in diabetic mice show the possibility to better regulate glucose levels following transplantation of opsin-containing cells in the pancreas and light illumination<sup>[40]</sup>.

Targeting the retina for diseases such as retinitis pigmentosa is one of the applications most likely to lead to clinically-approved optogenetic therapy in the near future<sup>[25,79]</sup>. Indeed, the eye is quite 'isolated' from an immunological point of view, and removing it in case of problems would not induce further damage to an already blind individual. The safety consideration is thus less of a problem compared to the targeting of other more central systems, such as the brainstem, deep brain nuclei or the spinal cord. In fact, a clinical trial for optogenetic treatment of retinitis pigmentosa has recently started<sup>[163]</sup>.



The next challenge is in terms of light delivery. The requirements for devices themselves were discussed in the fourth chapter of this thesis, but other aspects associated to light delivery should also be considered, like the temperature increase in the tissue due to illumination with high light intensities<sup>[9,194]</sup>. Thermal measurements at the surface of the tissue showed significant heating due to light illumination. This parameter must be considered, for instance by changing the wavelength of light, as red light was shown to induce less heating than blue light.

Clinical translation of optogenetics has started with the application on the retina, which will hopefully pave the way for the clinical trials and approval of therapies for other nervous system dysfunctions.

#### 5.4 Clinical translation of microfabricated implants

Microfabrication technologies have several features that make them very advantageous for neuroprostheses, including a great flexibility in design with rapid prototyping, batch fabrication and the possibility to design conformable arrays with small feature sizes ( $<100\ \mu\text{m}$ ). Further decreasing the mechanical mismatch between the microfabricated thin-film implants and the target tissue to optimize the conformability, functionality and integration is the subject of promising research for many applications<sup>[81,100,136]</sup>.

However, further development is necessary to make thin-film microfabricated arrays implantable and functional for several years for stimulation and/or recording, as is required for many neuroprostheses. While the thick silicone rubber encapsulation of clinical implants might provide a sufficient hermeticity over several years<sup>[199]</sup>, the hermeticity of miniaturized devices is an important challenge, because layers of elastomers or flexible polymers of a few  $\mu\text{m}$  thickness are not completely impermeable over time, affecting the integrity of the implants<sup>[33]</sup>. This is due to the gap between the polymeric chains, allowing diffusion of small molecules such as water through the layer. Some solutions for the hermetic sealing of miniaturized implantable components, such as implantable pulse generators (IPGs) are envisioned, based for instance on a stacking of layers of Parylene-C and  $\text{SiO}_2$ <sup>[77]</sup>. However, the integration with soft conformable devices is still a great challenge, and solutions for long-term implantable thin film implants will have to be developed.

The corrosion of the metals, particularly with small electrode sites, is also a challenge to consider. The corrosion of platinum<sup>[217]</sup> can lead to damaging reaction by-products and failure of the implant over time. Use of non-metallic coatings, such as conducting polymers or other coatings<sup>[44]</sup> can, in addition to improving the charge transduction, protect the underlying metallic layer and thus prevent corrosion. The use of conducting polymer coatings thus seem also promising in this respect, provided that their long-term stability can be improved.

Finding long-term solutions to these challenges will enable the clinical translation of many thin-film microfabricated devices, with the potential to improve the outcomes of neuroprosthetic devices. Some thin-film devices, such as soft microelectrocorticography (micro-ECOG) for the localization of the source of epilepsy, have much shorter term requirements (days to weeks) and might reach the clinics much faster, with already acute tests that can be performed<sup>[87]</sup>.

### 5.5 Outlook: towards closed-loop sensory neuroprostheses

A critical point highlighted in this thesis is the necessity to consider the neuronal structure of the system to be stimulated, in order to tailor the stimulation selectivity and reach the targeted function. Additionally, there might be important differences between subjects in terms of responses to the electrical/optical stimulation, injury location and type, location of the implant or neurophysiological properties that can explain potential differences in outcomes of neuroprosthetic devices. A greater flexibility in the stimulation protocol might help compensating for inter-individual differences. In this context, closed-loop control strategies of the stimulation might be considered, in order to personalize and dynamically adapt stimulation in such neuroprostheses.

Closed-loop strategies for the control of neuroprostheses are based on the combination of stimulation and recording capabilities. The stimulation-evoked activity is recorded and used as a feedback in the control of the stimulation. Many different control algorithm can be used for real-time adaptation of the stimulation protocol based on recorded feedback, as detailed in<sup>[209]</sup>.

Closed-loop strategies were first considered in the control of upper-arm prostheses, as the lack of sensory feedback was hypothesized to be a reason for poor performance<sup>[38]</sup>. Closed-loop motor neuroprostheses show improved performance compared to open-loop neuroprostheses, facilitating subject learning and optimally taking advantage of neuroplasticity to optimize performances<sup>[147]</sup>. A bidirectional hand neuroprosthesis enabling real-time sensory feedback also showed an improvement in efficacy of hand prostheses<sup>[160]</sup>. In deep brain stimulation, closed-loop control systems showed better identification of pathological neural patterns and subsequently more efficient amelioration of Parkinson's disease symptoms in a primate model<sup>[169]</sup>. Closed-loop control was also shown to be possible with optogenetics, opening the door to many new developments in neurological research<sup>[64]</sup>.

While many papers describe the implementation of closed-loop control systems in motor neuroprostheses, very few are targeted towards sensory neuroprostheses. Yet, they are also potentially useful, since most of the protocols of stimulation in auditory and visual implants are based on fixed algorithms decoding the environmental stimulus (sound/image), selecting

## 5.5. Outlook: towards closed-loop sensory neuroprostheses

the electrode sites and sending the stimulation with a pre-defined protocol. Some elements of this protocol, including the stimulation level and the selection of stimulation electrode sites, can be adapted based on behavioral feedback or evoked potential recordings during a selected number of fitting sessions in the months following implantation. However, it is known that neural plasticity plays an important role in the adaptation to artificial stimulation<sup>[47,131,154]</sup>, and an adaptation of the stimulation protocol based on real-time recordings of the sensory system might lead to an optimization of performances.

In the auditory system, closed-loop strategies are being investigated for cochlear implants<sup>[128]</sup> (Fig. 5.2A). The potential use of several evoked potentials from the peripheral and central auditory systems and of extracochlear electrodes are being tested. These recordings can provide feedback on the threshold and comfort levels, the bilateral loudness balance or even in some cases speech perception. It can potentially provide great advantages in the fitting of the implant, particularly in infants, where the behavioral feedback is very limited.

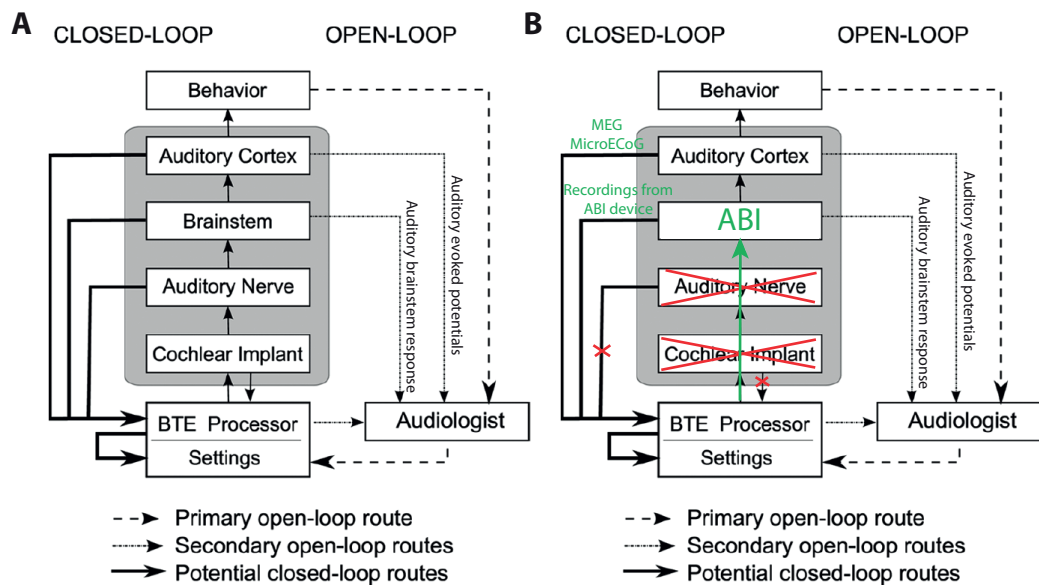


Figure 5.2: A) Schematic of open-loop and closed-loop cochlear implant control system, and B) its modifications for ABIs (Adapted from<sup>[128]</sup>). BTE=behind the ear

Developing a closed-loop ABI might provide several advantages. First, one of the challenges associated with increasing the number of electrodes and the flexibility of stimulation protocol is the resulting increased complexity of implant fitting and associated time. A closed-loop system could automatically optimize the parameters to what can achieve the best speech hearing outcomes. Second, it is difficult to assess behaviorally the optimal frequency selectivity that is possible to achieve, and which protocol can generate it. Developing a closed-loop

system with information on the frequency selectivity might provide a way to optimally replicate complex patterns of sound. This is shown in a paper exploring the potential of using reinforcement-based learning for closed-loop auditory implants using CN microstimulation and IC recordings<sup>[101]</sup>. The authors showed that stimulation patterns in the CN optimally replicating frequency-specific acoustic stimulation could be learned over 20 minutes of testing, without any user input.

While auditory evoked potentials can be used to obtain information on the threshold of stimulation, they cannot provide information on the frequency content of stimulation. Using implanted recording microelectrodes in the IC<sup>[101]</sup> for this purpose is too invasive to be implemented in human patients. The potential recordings for a closed-loop ABI system are presented on figure 5.2B. One potential solution is the recording of activity generated from ABI electrode sites that are not used for stimulation. It should be investigated whether these recordings can be relevant as a feedback for the ABI fitting protocol. Alternatively, recordings from the auditory cortex could be used to obtain information on the tonotopic selectivity of stimulation, as the tonotopic organization of the auditory cortices, although very complex, has been well characterized<sup>[176]</sup>. This could potentially be done with a soft, high-density micro-ECoG array implanted at the surface of the auditory cortex. However, implanting an additional electrode array at the surface of the cortex is invasive, and thus difficult to justify without evidence of a clear improvement in speech hearing outcomes with such a system. A non-invasive alternative with high spatial (2-3 mm) and temporal (1 ms) resolution is magnetoencephalography (MEG), but it requires complex instrumentation and cannot be portable<sup>[73]</sup>. It could however be used for research, to investigate the potential benefits of a closed-loop system for ABIs, initially for a few number of fitting sessions.

Achieving closed-loop sensory neuroprostheses might lead to a new, higher-level type of selectivity. Instead of aiming for optimal spatial, structural or cell-type selectivity at the neuronal level, we could achieve 'systems' selectivity, with limited a priori on what would be the optimal way to stimulate the system. This selectivity would be based on the functional clinical outcomes and would optimally take advantage of neuroplasticity, with a continuous, dynamic and personalized adaptation of the stimulation protocol. It might be through such strategies that a leap in the clinical outcomes of sensory neuroprostheses will be achieved.

## Bibliography

- [1] T V F Abaya, S Blair, P Tathireddy, L Rieth, and F Solzbacher. A 3D glass optrode array for optical neural stimulation. *Biomedical Optics Express*, 3(12):3087, 2012.
- [2] C Adams, K Mathieson, D Gunning, W Cunningham, M Rahman, J D Morrison, and M L Prydderch. Development of flexible arrays for in vivo neuronal recording and stimulation. *Nuclear Instruments & Methods in Physics Research Section a-Accelerators Spectrometers Detectors and Associated Equipment*, 546(1-2):154–159, 2005.
- [3] Joe.C Adams. Ascending projections to the inferior colliculus. *J Comp Neurol*, 183(3):519–538, 1979.
- [4] Saif I. Al-Juboori, Anna Dondzillo, Elizabeth a. Stubblefield, Gidon Felsen, Tim C. Lei, and Achim Klug. Light Scattering Properties Vary across Different Regions of the Adult Mouse Brain. *PLoS ONE*, 8(7):1–9, 2013.
- [5] B. J. Allitt, a. R. Harris, S. J. Morgan, G. M. Clark, and a. G. Paolini. Thin-film micro-electrode stimulation of the cochlea in rats exposed to aminoglycoside induced hearing loss. *Hearing Research*, 331:13–26, 2016.
- [6] Pino Alonso, Daniel Cuadras, Loes Gabriels, Damiaan Denys, Wayne Goodman, Ben D. Greenberg, Fiacro Jimenez-Ponce, Jens Kuhn, Doris Lenartz, Luc Mallet, Bart Nuttin, Eva Real, Cinto Segalas, Rick Schuurman, Sophie Tezenas Du Montcel, and Jose M. Menchon. Deep brain stimulation for obsessive-compulsive disorder: A meta-analysis of treatment outcome and predictors of response. *PLoS ONE*, 10(January 2014):1–17, 2015.
- [7] Juan Carlos Alvarado, Verónica Fuentes-Santamaría, Tania Jareño Flores, José Luis Blanco, and José M. Juiz. Normal variations in the morphology of auditory brainstem response (ABR) waveforms: A study in wistar rats. *Neuroscience Research*, 73:302–311, 2012.
- [8] Polina Anikeeva, Aaron S Andalman, Ilana Witten, Melissa Warden, Inbal Goshen, Logan Grosenick, Lisa a Gunaydin, Loren M Frank, and Karl Deisseroth. Optetrode: a multi-channel readout for optogenetic control in freely moving mice. *Nature neuroscience*, 15(1):163–170, 2012.

## Bibliography

---

- [9] Gonzalo Arias-Gil, Frank Walter Ohl, Kentaroh Takagaki, and Michael Thomas Lippert. Measurement, modeling, and prediction of temperature rise due to optogenetic brain stimulation. *Neurophotonics*, 3(4):045007, 2016.
- [10] M Asplund, T Nyberg, and O Inganas. Electroactive polymers for neural interfaces. *Polymer Chemistry*, 1(9):1374–1391, 2010.
- [11] Craig a Atencio, Jonathan Y Shih, Christoph E Schreiner, and Steven W Cheung. Primary auditory cortical responses to electrical stimulation of the thalamus. *Journal of neurophysiology*, 111:1077–87, 2014.
- [12] Suleman Ayub, Falk Barz, Oliver Paul, Senior Member Ieee, Patrick Ruther, and Member Ieee. Heterogeneous 3D Optrode with Variable Spatial Resolution for Optogenetic Stimulation and Electrophysiological Recording. pages 1762–1765, 2016.
- [13] M. Azadpour and C.M. McKay. Processing of speech temporal and spectral information by users of auditory brainstem implants and cochlear implants. *Ear and hearing*, 35(5):e192–e203, 2014.
- [14] Dong-Hyun Baek, Jeyeon Lee, Hang Jin Byeon, Hoseok Choi, In Young Kim, Kyoung-Min Lee, James Jungho Pak, Dong Pyo Jang, and Sang-Hoon Lee. A thin film polyimide mesh microelectrode for chronic epidural electrocorticography recording with enhanced contactability. *Journal of neural engineering*, 11:046023, 2014.
- [15] E V Bagshaw and M H Evans. Measurement of current spread from microelectrodes when stimulating within the nervous system. *Experimental brain research. Experimentelle Hirnforschung. Experimentation cerebrale*, 25:391–400, 1976.
- [16] J S Baizer, S Manohar, N A Paolone, N Weinstock, and R J Salvi. Understanding tinnitus: The dorsal cochlear nucleus, organization and plasticity. *Brain Research*, 1485:40–53, 2012.
- [17] Joan S. Baizer, Keit Men Wong, Nicholas a. Paolone, Nadav Weinstock, Richard J. Salvi, Senthilvelan Manohar, Sandra F. Witelson, James F. Baker, Chet C. Sherwood, and Patrick R. Hof. Lamina and neurochemical organization of the dorsal cochlear nucleus of the human, monkey, cat, and rodents. *Anatomical Record*, 297(August 2013):1865–1884, 2014.
- [18] Samuel Barber, Elliott D. Kozin, M Cunnane, S. Puram, P. Shah, M. Smith, A. Remenschneider, B. Herrmann, M Christian Brown, and Daniel J Lee. Position of Auditory Brainstem Implant Electrode Array Correlates with Audiometric Outcomes. In *Assoc Res Otolaryngol*, 2016.
- [19] John Martin Barrett, Rolando Berlinguer-Palmini, and Patrick Degenaar. Optogenetic approaches to retinal prosthesis. *Visual neuroscience*, 31(2014):345–54, 2014.

- 
- [20] André Berndt, Philipp Schoenenberger, Joanna Mattis, Kay M Tye, Karl Deisseroth, Peter Hegemann, and Thomas G Oertner. High-efficiency channelrhodopsins for fast neuronal stimulation at low light levels. *Proceedings of the National Academy of Sciences of the United States of America*, 108:7595–600, 2011.
- [21] Xiaopeng Bi, Tian Xie, Bin Fan, Wasif Khan, Yue Guo, and Wen Li. A Flexible , Micro-Lens-Coupled LED Stimulator for Optical Neuromodulation. *IEEE Transactions on Biomedical Circuits and Systems*, pages 1–7, 2016.
- [22] Ben H. Bonham and Leonid M. Litvak. Current focusing and steering: Modeling, physiology, and psychophysics. *Hearing Research*, 242:141–153, 2008.
- [23] D. Borton, S. Micera, J. D. R. Millan, and G. Courtine. Personalized Neuroprosthetics. *Science Translational Medicine*, 5(210):210rv2–210rv2, 2013.
- [24] Jane Bradbury. Molecular insights into human brain evolution. *PLoS Biology*, 3(3):0367–0370, 2005.
- [25] V Busskamp, S Picaud, J a Sahel, and B Roska. Optogenetic therapy for retinitis pigmentosa. *Gene Therapy*, 19(2):169–175, 2012.
- [26] Dengke Cai, Andreas Neyer, R??diger Kuckuk, and H. Michael Heise. Raman, mid-infrared, near-infrared and ultraviolet-visible spectroscopy of PDMS silicone rubber for characterization of polymer optical waveguide materials. *Journal of Molecular Structure*, 976(1-3):274–281, 2010.
- [27] Luke Campagnola, Hong Wang, and Mark J Zylka. Fiber-coupled light-emitting diode for localized photostimulation of neurons expressing channelrhodopsin-2. *Journal of neuroscience methods*, 169(1):27–33, 2008.
- [28] Andres Canales, Xiaoting Jia, Ulrich P Froriep, Ryan a Koppes, Christina M Tringides, Jennifer Selvidge, Chi Lu, Chong Hou, Lei Wei, Yoel Fink, and Polina Anikeeva. Multifunctional fibers for simultaneous optical, electrical and chemical interrogation of neural circuits in vivo. *Nature Biotechnology*, 33(3):277–284, 2015.
- [29] N B Cant and C G Benson. Parallel auditory pathways: projection patterns of the different neuronal populations in the dorsal and ventral cochlear nuclei. *Brain Research Bulletin*, 60(5-6):457–474, 2003.
- [30] M. Capogrosso, T. Milekovic, D. Borton, F. Wagner, E. Martin Moraud, J.-B. Mignardot, N. Buse, J. Gandar, Q. Barraud, D. Xing, E. Rey, S. Duis, Y. Jianzhong, W. K. D. Ko. Q. Li, P. Detemple, T. Denison, S. Micera, E. Bezard, J. Bloch, and G. Courtine. A brain-spinal interface alleviating gait deficits after spinal cord injury in primates. *Nature*, In Press(7628):284–288, 2016.

## Bibliography

---

- [31] Marco Capogrosso, Nikolaus Wenger, Stanisa Raspopovic, Pavel Musienko, Janine Beaulac, Lorenzo Bassi Luciani, Grégoire Courtine, and Silvestro Micera. A Computational Model for Epidural Electrical Stimulation of Spinal Sensorimotor Circuits. *The Journal of Neuroscience*, 33(49):19326–19340, 2013.
- [32] Robert P Carlyon, John M Deeks, and Colette M McKay. Effect of Pulse Rate and Polarity on the Sensitivity of Auditory Brainstem and Cochlear Implant Users to Electrical Stimulation. *Journal of the Association for Research in Otolaryngology: JARO*, 16:653–68, 2015.
- [33] Moo Sung Chae, Zhi Yang, and Wentai Liu. *Implantable Neural Prostheses 2*. 2010.
- [34] H. Chandler Elliott. Cross-sectional diameters and areas of the human spinal cord. *The Anatomical Record*, 93(3):287–293, 1945.
- [35] Y Y Chen, H Y Lai, S H Lin, C W Cho, W H Chao, C H Liao, S Tsang, Y F Chen, and S Y Lin. Design and fabrication of a polyimide-based microelectrode array: Application in neural recording and repeatable electrolytic lesion in rat brain. *Journal of Neuroscience Methods*, 182(1):6–16, 2009.
- [36] Shaokoon Cheng, Elizabeth C. Clarke, and Lynne E. Bilston. Rheological properties of the tissues of the central nervous system: A review. *Medical Engineering and Physics*, 30:1318–1337, 2008.
- [37] J A Chikar, J L Hendricks, S M Richardson-Burns, Y Raphael, B E Pflugst, and D C Martin. The use of a dual PEDOT and RGD-functionalized alginate hydrogel coating to provide sustained drug delivery and improved cochlear implant function. *Biomaterials*, 33(7):1982–1990, 2012.
- [38] Dudley S. Childress. Closed-loop control in prosthetic systems: Historical perspective. *Annals of Biomedical Engineering*, 8:293–303, 1980.
- [39] Jun Hee Choi, Eun Hyung Cho, Yun Sung Lee, Mun Bo Shim, Ho Young Ahn, Chan Wook Baik, Eun Hong Lee, Kihong Kim, Tae Ho Kim, Sangwon Kim, Kyung Sang Cho, Jongseung Yoon, Miyoung Kim, and Sungwoo Hwang. Fully flexible gan light-emitting diodes through nanovoid-mediated transfer. *Advanced Optical Materials*, 2:267–274, 2014.
- [40] Brian Y Chow, Edward S Boyden, E. S. Boyden, F Zhang, E. Bamberg, G. Nagel, K. Deisseroth, X. Han, E. S. Boyden, F Zhang, L.-P. Wang, M. Brauner, J. F. Liewald, K. Kay, N. Watzke, P. G. Wood, E. Bamberg, G. Nagel, a. Gottschalk, K. Deisseroth, B. Y. Chow, X. Han, a. S. Dobry, X. Qian, a. S. Chuong, M. Li, M. a. Henninger, G. M. Belfort, Y. Lin, P. E. Monahan, E. S. Boyden, Y. I. Wu, D. Frey, O. I. Lungu, a. Jaehrig, I. Schlichting, B. Kuhlman, K. M. Hahn, H. Ye, M. Daoud-El Baba, R. W. Peng, M. Fussenegger, T. Yamashita, a. Terakita, Y. Shichida, X. Li, D. V. Gutierrez, M. G. Hanson, J. Han, M. D. Mark, H. Chiel, P. Hegemann, L. T. Landmesser, S. Herlitze, M. Yazawa, a. M. Sadaghiani, B. Hsueh, R. E. Dolmetsch, M. J. Kennedy, R. M. Hughes, L. a. Peteya, J. W. Schwartz,



- M. D. Ehlers, C. L. Tucker, E. S. Boyden, J. G. Bernstein, P. a. Garrity, E. S. Boyden, C. T. Wentz, J. G. Bernstein, P. Monahan, a. Guerra, a. Rodriguez, E. S. Boyden, B. Y. Chow, E. S. Boyden, X. Wang, X. Chen, Y. Yang, a. N. Zorzos, J. Scholvin, E. S. Boyden, C. G. Fonstad, V. Gradinaru, M. Mogri, K. R. Thompson, J. M. Henderson, K. Deisseroth, R. C. Wykes, J. H. Heeroma, L. Mantoan, K. Zheng, D. C. MacDonald, K. Deisseroth, K. S. Hashemi, M. C. Walker, S. Schorge, D. M. Kullmann, M. Desai, I. Kahn, U. Knoblich, J. Bernstein, H. Atallah, a. Yang, N. Kopell, R. L. Buckner, a. M. Graybiel, C. I. Moore, E. S. Boyden, S. B. Kodandaramaiah, G. T. Franzesi, B. Y. Chow, E. S. Boyden, C. R. Forest, M. Heiman, a. Schaefer, S. Gong, J. D. Peterson, M. Day, K. E. Ramsey, M. Suárez-Fariñas, C. Schwarz, D. a. Stephan, D. J. Surmeier, P. Greengard, N. Heintz, W. J. Alilain, X. Li, K. P. Horn, R. Dhingra, T. E. Dick, S. Herlitze, J. Silver, J. C. Williams, T. Denison, M. Cavazzana-Calvo, E. Payen, O. Negre, G. Wang, K. Hehir, F. Fusil, J. Down, M. Denaro, T. Brady, K. Westerman, R. Cavallesco, B. Gillet-Legrand, L. Caccavelli, R. Sgarra, L. Maouche-Chrétien, F. Bernaudin, R. Girot, R. Dorazio, G. J. Mulder, a. Polack, a. Bank, J. Soulier, J. Larghero, N. Kabbara, B. Dalle, B. Gourmel, G. Socie, S. Chrétien, N. Cartier, P. Aubourg, a. Fischer, K. Cornetta, F. Galacteros, Y. Beuzard, E. Gluckman, F. Bushman, S. Hacein-Bey-Abina, P. Leboulch, a. Gerits, R. Farivar, B. R. Rosen, L. L. Wald, E. S. Boyden, W. Vanduffel, B. Lin, a. Koizumi, N. Tanaka, S. Panda, R. H. Masland, V. Busskamp, B. Roska, S. a. Stanley, J. E. Gagner, S. Damanpour, M. Yoshida, J. S. Dordick, and J. M. Friedman. Optogenetics and translational medicine. *Science translational medicine*, 5:177ps5, 2013.
- [41] J.D. Chulay. Retinal gene therapy advancing into clinical reality. *Ophthalmology Times*, 2015.
- [42] B.M. Clopton, J.A. Winfield, and F.J. Flammino. Tonotopic organisation: Review and analysis. *Brain Research*, 76:1–20, 1974.
- [43] S F Cogan. In vivo and in vitro differences in the charge-injection and electrochemical properties of iridium oxide electrodes. *2006 28th Annual International Conference of the IEEE Engineering in Medicine and Biology Society, Vols 1-15*, pages 6388–6391, 2006.
- [44] S F Cogan. Neural stimulation and recording electrodes. *Annual Review of Biomedical Engineering*, 10:275–309, 2008.
- [45] V Colletti, R V Shannon, M Carner, S Veronese, and L Colletti. Progress in restoration of hearing with the auditory brainstem implant. *Prog Brain Res*, 175:333–345, 2009.
- [46] Vittorio Colletti and Robert V Shannon. Open set speech perception with auditory brainstem implant? *The Laryngoscope*, 115:1974–8, 2005.
- [47] Olivier Collignon, François Champoux, Patrice Voss, and Franco Lepore. *Sensory rehabilitation in the plastic brain*, volume 191. 2011.
- [48] Cochlear corporation. [www.cochlear.com](http://www.cochlear.com).

## Bibliography

---

- [49] X Y Cui and D C Martin. Electrochemical deposition and characterization of poly(3,4-ethylenedioxythiophene) on neural microelectrode arrays. *Sensors and Actuators B-Chemical*, 89(1-2):92–102, 2003.
- [50] Karl Deisseroth. Optogenetics. *Nature Methods*, 8(1):26–29, 2011.
- [51] Maged M Elwassif, Qingjun Kong, Maribel Vazquez, and Marom Bikson. Bio-heat transfer model of deep brain stimulation-induced temperature changes. *Journal of neural engineering*, 3(4):306–315, 2006.
- [52] M. a. Escabí, N. C. Higgins, a. M. Galaburda, G. D. Rosen, and H. L. Read. Early cortical damage in rat somatosensory cortex alters acoustic feature representation in primary auditory cortex. *Neuroscience*, 150:970–983, 2007.
- [53] Jonathan a Fan, Woon-Hong Yeo, Yewang Su, Yoshiaki Hattori, Woosik Lee, Sung-Young Jung, Yihui Zhang, Zhuangjian Liu, Huanyu Cheng, Leo Falgout, Mike Bajema, Todd Coleman, Dan Gregoire, Ryan J Larsen, Yonggang Huang, and John a Rogers. Fractal design concepts for stretchable electronics. *Nature communications*, 5:3266, 2014.
- [54] J J FitzGerald, N Lago, S Benmerah, J Serra, C P Watling, R E Cameron, E Tarte, S P Lacour, S B McMahon, and J W Fawcett. A regenerative microchannel neural interface for recording from and stimulating peripheral axons in vivo (vol 9, 016010, 2012). *Journal of Neural Engineering*, 9(2), 2012.
- [55] C P Foley, N Nishimura, K B Neeves, C B Schaffer, and W L Olbricht. Flexible microfluidic devices supported by biodegradable insertion scaffolds for convection-enhanced neural drug delivery. *Biomedical Microdevices*, 11(4):915–924, 2009.
- [56] L M Friesen, R V Shannon, D Baskent, and X Wang. Speech recognition in noise as a function of the number of spectral channels: comparison of acoustic hearing and cochlear implants. *The Journal of the Acoustical Society of America*, 110(2):1150–1163, 2001.
- [57] Shefin S George, Andrew K Wise, James B Fallon, and Robert K Shepherd. Evaluation of focused multipolar stimulation for cochlear implants in long-term deafened cats. *Journal of neural engineering*, 12:036003, 2015.
- [58] Sabrina M. Gippert, Christina Switala, Bettina H. Bewernick, Sarah Kayser, Alena Bräuer, Volker a. Coenen, and Thomas E. Schlaepfer. Deep brain stimulation for bipolar disorder—review and outlook. *CNS Spectrums*, (February):1–4, 2016.
- [59] Christian Goßler, Colin Bierbrauer, Rüdiger Moser, Michael Kunzer, Katarzyna Holc, Wilfried Pletschen, Klaus Köhler, Joachim Wagner, Michael Schwaerzle, Patrick Ruther, Oliver Paul, Jakob Neef, Daniel Keppeler, Gerhard Hoch, Tobias Moser, and Ulrich T Schwarz. GaN-based micro-LED arrays on flexible substrates for optical cochlear implants. *Journal of Physics D: Applied Physics*, 47:205401, 2014.

- 
- [60] Viviana Gradinaru, Murtaza Mogri, Kimberly R Thompson, Jaimie M Henderson, and Karl Deisseroth. Optical deconstruction of parkinsonian neural circuitry. *Science (New York, N.Y.)*, 324(April):354–9, 2009.
- [61] R A Green, P B Matteucci, R T Hassarati, B Giraud, C W Dodds, S Chen, P J Byrnes-Preston, G J Suaning, L A Poole-Warren, and N H Lovell. Performance of conducting polymer electrodes for stimulating neuroprosthetics. *J Neural Eng*, 10(1):16009, 2013.
- [62] Kenneth P. Greenberg, Aaron Pham, and Frank S. Werblin. Differential Targeting of Optical Neuromodulators to Ganglion Cell Soma and Dendrites Allows Dynamic Control of Center-Surround Antagonism. *Neuron*, 69(4):713–720, 2011.
- [63] Warren M. Grill and J. Thomas Mortimer. Inversion of the current-distance relationship by transient depolarization. *IEEE Transactions on Biomedical Engineering*, 44(1):1–9, 1997.
- [64] Logan Grosenick, James H. Marshel, and Karl Deisseroth. Closed-loop and activity-guided optogenetic control. *Neuron*, 86(1):106–139, 2015.
- [65] Nir Grossman, Vincent Poher, Matthew S Grubb, Gordon T Kennedy, Konstantin Nikolic, Brian McGovern, Rolando Berlinguer Palmi, Zheng Gong, Emmanuel M Drakakis, Mark a a Neil, Martin D Dawson, Juan Burrone, and Patrick Degenaar. Multi-site optical excitation using ChR2 and micro-LED array. *Journal of neural engineering*, 7(1):16004, 2010.
- [66] Benedikt Grothe, Michael Pecka, and David Mcalpine. Mechanisms of Sound Localization in Mammals. *Physiol. Rev.*, 90:983–1012, 2010.
- [67] Duncan a. Groves and Verity J. Brown. Vagal nerve stimulation: A review of its applications and potential mechanisms that mediate its clinical effects. *Neuroscience and Biobehavioral Reviews*, 29(June 2004):493–500, 2005.
- [68] Amelie A. Guex, Nicolas Vachicouras, Ariel Edward Hight, M Christian Brown, Daniel J Lee, and Stephanie P. Lacour. Conducting polymer electrodes for auditory brainstem implants. *J. Mater. Chem. B*, 3:5021–5027, 2015.
- [69] Nathalie K. Guimard, Natalia Gomez, and Christine E. Schmidt. Conducting polymers in biomedical engineering. *Progress in Polymer Science*, 32:876–921, 2007.
- [70] Lisa a Gunaydin, Ofer Yizhar, André Berndt, Vikaas S Sohal, Karl Deisseroth, and Peter Hegemann. Ultrafast optogenetic control. *Nature neuroscience*, 13(3):387–392, 2010.
- [71] L A Guo, K W Meacham, S Hochman, and S P DeWeerth. A PDMS-Based Conical-Well Microelectrode Array for Surface Stimulation and Recording of Neural Tissues. *Ieee Transactions on Biomedical Engineering*, 57(10):2485–2494, 2010.
- [72] Robert D. Hall. Estimation of surviving spiral ganglion cells in the deaf rat using the electrically evoked auditory brainstem response. *Hearing Research*, 45:123–136, 1990.

## Bibliography

---

- [73] Matti Hämäläinen, Riitta Hari, Risto J. Ilmoniemi, Jukka Knuutila, and Olli V. Lounasmaa. Magnetoencephalography theory, instrumentation, and applications to noninvasive studies of the working human brain. *Reviews of Modern Physics*, 65:413–497, 1993.
- [74] D.E. Harrison, D.D. Cailliet, S.J. Troyanovich, and S.O. Harrison. A review of biomechanics of the central nervous system - Part II: Spinal cord strains from postural loads. *Journal of manipulative and physiological therapeutics*, 22(5):322–332, 1999.
- [75] Barbara S Herrmann, M Christian Brown, Donald K Eddington, Kenneth E Hancock, and Daniel J Lee. Auditory brainstem implant: electrophysiologic responses and subject perception. *Ear and hearing*, 36:368–376, 2015.
- [76] Ariel Edward Hight, Elliott D. Kozin, Keith Darrow, Ashton Lehmann, Edward Boyden, M. Christian Brown, and Daniel J. Lee. Superior temporal resolution of Chronos versus channelrhodopsin-2 in an optogenetic model of the auditory brainstem implant. *Hearing Research*, 322:235–241, 2015.
- [77] Andreas Hogg, Stefanie Uhl, François Feuvrier, Yann Girardet, Benjamin Graf, Thierry Aellen, Herbert Keppner, Yanik Tardy, and Jürgen Burger. Protective multilayer packaging for long-term implantable medical devices. *Surface and Coatings Technology*, 255:124–129, 2014.
- [78] B A Hollenberg, C D Richards, R Richards, D F Bahr, and D M Rector. A MEMS fabricated flexible electrode array for recording surface field potentials. *J Neurosci Methods*, 153(1):147–153, 2006.
- [79] S. G. Jacobson, a. Sumaroka, X. Luo, and a. V. Cideciyan. Retinal optogenetic therapies: Clinical criteria for candidacy. *Clinical Genetics*, 84:175–182, 2013.
- [80] Chang Kyu Jeong, Kwi-II Park, Jung Hwan Son, Geon-Tae Hwang, Seung Hyun Lee, Dae Yong Park, Han Eol Lee, Hwan Keon Lee, Myunghwan Byun, and Keon Jae Lee. Self-powered fully-flexible light-emitting system enabled by flexible energy harvester. *Energy Environ. Sci.*, 7:4035–4043, 2014.
- [81] Jae Woong Jeong, Gunchul Shin, Sung Il Park, Ki Jun Yu, Lizhi Xu, and John a. Rogers. Soft materials in neuroengineering for hard problems in neuroscience. *Neuron*, 86(1):175–186, 2015.
- [82] S. Jezernik, M. Craggs, W.M. Grill, G. Creasey, and N.J.M. Rijkhoff. Electrical stimulation for the treatment of bladder dysfunction: Current status and future possibilities. *Neurological research*, 24(5):413–430, 2013.
- [83] K. Kampasi, J. Seymour, K. Na, K. D. Wise, and E. Yoon. Fiberless multicolor optoelectrodes using Injection Laser Diodes and Gradient-index lens coupled optical waveguides. *2015 Transducers - 2015 18th International Conference on Solid-State Sensors, Actuators and Microsystems, TRANSDUCERS 2015*, pages 273–276, 2015.

- [84] E.R. Kandel, J.H. Schwartz, and T.M Jessell. *Principles of neural science*. 4th edition, 2000.
- [85] Gagan Kaur, Raju Adhikari, Peter Cass, Mark Bown, and Pathiraja Gunatillake. Electrically conductive polymers and composites for biomedical applications. *RSC Adv.*, 5:37553–37567, 2015.
- [86] J B Kelly and B Masterton. Auditory sensitivity of the albino rat. *Journal of comparative and physiological psychology*, 91(4):930–936, 1977.
- [87] D Khodagholy, J N Gelinas, T Thesen, W Doyle, O Devinsky, G G Malliaras, and G Buzsaki. NeuroGrid: recording action potentials from the surface of the brain. *Nat Neurosci*, 18(December):310–315, 2015.
- [88] D H Kim, J Viventi, J J Amsden, J L Xiao, L Vigeland, Y S Kim, J A Blanco, B Panilaitis, E S Frechette, D Contreras, D L Kaplan, F G Omenetto, Y G Huang, K C Hwang, M R Zakin, B Litt, and J A Rogers. Dissolvable films of silk fibroin for ultrathin conformal bio-integrated electronics. *Nature Materials*, 9(6):511–517, 2010.
- [89] Dong-Hwan Kim, James a Wiler, David J Anderson, Daryl R Kipke, and David C Martin. Conducting polymers on hydrogel-coated neural electrode provide sensitive neural recordings in auditory cortex. *Acta biomaterialia*, 6(1):57–62, January 2010.
- [90] T.-i. Kim, J G McCall, Y H Jung, X Huang, E R Siuda, Y Li, J Song, Y M Song, H A Pao, R.-H. Kim, C Lu, S D Lee, I.-S. Song, G Shin, R Al-Hasani, S Kim, M P Tan, Y Huang, F G Omenetto, J A Rogers, and M R Bruchas. Injectable, Cellular-Scale Optoelectronics with Applications for Wireless Optogenetics. *Science*, 340(6129):211–216, 2013.
- [91] Andrew S Koivuniemi and Kevin J Otto. Asymmetric Versus Symmetric Pulses for Cortical Microstimulation. *IEEE Transactions on Neural Systems and Rehabilitation Engineering*, 19(5):468–476, 2011.
- [92] Andrew S Koivuniemi and Kevin J Otto. The Depth , Waveform and Pulse Rate for Electrical Microstimulation of the Auditory Cortex. In *Proceedings of the 34th Annual International Conference of the IEEE EMBS*, pages 2489–2492, 2012.
- [93] Takashi Daniel Yoshida Kozai and Alberto Luis Vazquez. Photoelectric artefact from optogenetics and imaging on microelectrodes and bioelectronics: New Challenges and Opportunities. *J. Mater. Chem. B*, 3(25):4965–4978, 2015.
- [94] Elliott D. Kozin and Daniel J Lee. Advances in Optogenetic-based Auditory Implants. *The Hearing Journal*, (September):8–10, 2016.
- [95] Alexis M. Kuncel and Warren M. Grill. Selection of stimulus parameters for deep brain stimulation. *Clinical Neurophysiology*, 115:2431–2441, 2004.

## Bibliography

---

- [96] S Kuwada, R Batra, and T R Stanford. Monaural and binaural response properties of neurons in the inferior colliculus of the rabbit: effects of sodium pentobarbital. *J Neurophysiol*, 61(2):269–282, 1989.
- [97] Mark Kuznetsov. VECSEL semiconductor lasers: A path to high-power, quality beam and UV to IR wavelength by design. In *Semiconductor Disk Lasers: Physics and Technology*, pages 1–71. 2010.
- [98] Ki Yong Kwon, Hyung Min Lee, Maysam Ghovanloo, Arthur Weber, and Wen Li. A wireless slanted optrode array with integrated micro leds for optogenetics. *Proceedings of the IEEE International Conference on Micro Electro Mechanical Systems (MEMS)*, pages 813–816, 2014.
- [99] S P Lacour, S Benmerah, E Tarte, J FitzGerald, J Serra, S McMahon, J Fawcett, O Graudejus, Z Yu, and B Morrison. Flexible and stretchable micro-electrodes for in vitro and in vivo neural interfaces. *Medical & Biological Engineering & Computing*, 48(10):945–954, 2010.
- [100] Stéphanie P. Lacour, Grégoire Courtine, and Jochen Guck. Materials and technologies for soft implantable neuroprostheses. *Nature Reviews Materials*, 1:16063, 2016.
- [101] Geoffrey W Lee, Fabio Zambetta, Xiaodong Li, and Antonio G Paolini. Utilising reinforcement learning to develop strategies for driving auditory neural implants. *Journal of Neural Engineering*, 13(4):046027, 2016.
- [102] Sang Yong Lee, Kwi Il Park, Chul Huh, Min Koo, Hyeon Gyun Yoo, Seungjun Kim, Chil Seong Ah, Gun Yong Sung, and Keon Jae Lee. Water-resistant flexible GaN LED on a liquid crystal polymer substrate for implantable biomedical applications. *Nano Energy*, 1:145–151, 2012.
- [103] Philip M. Lewis, Lauren N. Ayton, Robyn H. Guymer, Arthur J. Lowery, Peter J. Blamey, Penelope J. Allen, Chi D. Luu, and Jeffrey V. Rosenfeld. Advances in implantable bionic devices for blindness: A review. *ANZ Journal of Surgery*, 2016.
- [104] Yuhang Li, Yan Shi, Jizhou Song, Chaofeng Lu, Tae Il Kim, John a. Rogers, and Yonggang Huang. Thermal properties of microscale inorganic light-emitting diodes in a pulsed operation. *Journal of Applied Physics*, 113, 2013.
- [105] H. H. Lim, T. Lenarz, G. Joseph, R. D. Battmer, J. F. Patrick, and M. Lenarz. Effects of phase duration and pulse rate on loudness and pitch percepts in the first auditory midbrain implant patients: Comparison to cochlear implant and auditory brainstem implant results. *Neuroscience*, 154:370–380, 2008.
- [106] Hubert H. Lim and Thomas Lenarz. Auditory midbrain implant: Research and development towards a second clinical trial. *Hearing Research*, 322:212–223, 2015.

- [107] John Y Lin, Per Magne Knutsen, Arnaud Muller, David Kleinfeld, and Roger Y Tsien. ReaChR: a red-shifted variant of channelrhodopsin enables deep transcranial optogenetic excitation. *Nature neuroscience*, 16(10):1499–508, 2013.
- [108] John Y. Lin, Michael Z. Lin, Paul Steinbach, and Roger Y. Tsien. Characterization of engineered channelrhodopsin variants with improved properties and kinetics. *Biophysical Journal*, 96(5):1803–1814, 2009.
- [109] Szu-Te Lin, Mufaddal Gheewala, John C Wolfe, John a. Dani, and Wei-Chuan Shih. A flexible optrode for deep brain neurophotonics. *2011 5th International IEEE/EMBS Conference on Neural Engineering*, pages 700–703, 2011.
- [110] Michael E Llewellyn, Kimberly R Thompson, Karl Deisseroth, and Scott L Delp. Orderly recruitment of motor units under optical control in vivo. *Nature medicine*, 16(10):1161–1165, 2010.
- [111] Philipos P. Loizou. Speech Processing in. *Adv Otorhinolaryngol.*, 64:109–43, 2006.
- [112] Christopher J Long, Ian Nimmo-smith, David M Baguley, Martin O’Driscoll, Richard T Ramsden, Steven R Otto, Patrick R Axon, Robert P. Carlyon, Martin O Driscoll, Richard T Ramsden, Steven R Otto, Patrick R Axon, and Robert P. Carlyon. Optimizing the clinical fit of auditory brain stem implants. *Ear and hearing*, 26:251–62, 2005.
- [113] G Lovell and A E Refaie. Speech perception outcomes following auditory brainstem implantation in both tumour and non-tumour patients: A review. *Audiological Medicine*, 2012.
- [114] K A Ludwig, J D Uram, J Y Yang, D C Martin, and D R Kipke. Chronic neural recordings using silicon microelectrode arrays electrochemically deposited with a poly(3,4-ethylenedioxythiophene) (PEDOT) film. *Journal of Neural Engineering*, 3(1):59–70, 2006.
- [115] Xiliang Luo, Cassandra L. Weaver, David D. Zhou, Robert Greenberg, and Xinyan T. Cui. Highly stable carbon nanotube doped poly(3,4-ethylenedioxythiophene) for chronic neural stimulation. *Biomaterials*, 32(24):5551–5557, 2011.
- [116] Yvonne Hsu Lin Luo and Lyndon da Cruz. The Argus® II Retinal Prosthesis System. *Progress in Retinal and Eye Research*, 50:89–107, 2016.
- [117] Stefan J Mauger, Mohit N Shivdasani, Graeme D Rathbone, Rebecca E Argent, and Antonio G Paolini. An in vivo investigation of first spike latencies in the inferior colliculus in response to multichannel penetrating auditory brainstem implant stimulation. *Journal of neural engineering*, 7:036004, 2010.
- [118] MayfieldClinic. [www.mayfieldclinic.com](http://www.mayfieldclinic.com).

## Bibliography

---

- [119] Niall McAlinden, David Massoubre, Elliot Richardson, Erdan Gu, Shuzo Sakata, Martin D Dawson, and Keith Mathieson. Thermal and optical characterization of micro-LED probes for in vivo optogenetic neural stimulation. *Optics letters*, 38(6):992–4, 2013.
- [120] Jordan G McCall, Tae-il Kim, Gunchul Shin, Xian Huang, Yei Hwan Jung, Ream Al-Hasani, Fiorenzo G Omenetto, Michael R Bruchas, and John a Rogers. Fabrication and application of flexible, multimodal light-emitting devices for wireless optogenetics. *Nature protocols*, 8(12):2413–2428, 2013.
- [121] D B McCreery. Cochlear nucleus auditory prostheses. *Hearing Research*, 242(1-2):64–73, 2008.
- [122] D B McCreery, W F Agnew, T G H Yuen, and L Bullara. Charge-Density and Charge Per Phase as Cofactors in Neural Injury Induced by Electrical-Stimulation. *Ieee Transactions on Biomedical Engineering*, 37(10):996–1001, 1990.
- [123] D B McCreery, R V Shannon, J K Moore, and M Chatterjee. Accessing the tonotopic organization of the ventral cochlear nucleus by intranuclear microstimulation. *IEEE Trans Rehabil Eng*, 6(4):391–399, 1998.
- [124] C C McIntyre and W M Grill. Selective microstimulation of central nervous system neurons. *Annals of biomedical engineering*, 28:219–233, 2000.
- [125] Cameron C McIntyre and Warren M Grill. Extracellular stimulation of central neurons: influence of stimulus waveform and frequency on neuronal output. *Journal of neurophysiology*, 88:1592–1604, 2002.
- [126] Cameron C. McIntyre, Susumu Mori, David L. Sherman, Nitish V. Thakor, and Jerrold L. Vitek. Electric field and stimulating influence generated by deep brain stimulation of the subthalamic nucleus. *Clinical Neurophysiology*, 115:589–595, 2004.
- [127] Colette M Mckay, Mahan Azadpour, Deanne Jayewardene-aston, and Martin O Driscoll. Electrode Selection and Speech Understanding in Patients With Auditory Brainstem Implants. *Ear&Hearing*, pages 1–10, 2015.
- [128] Myles McLaughlin, Thomas Lu, Andrew Dimitrijevic, and Fan Gang Zeng. Towards a closed-loop cochlear implant system: Application of embedded monitoring of peripheral and central neural activity. *IEEE Transactions on Neural Systems and Rehabilitation Engineering*, 20(4):443–454, 2012.
- [129] K W Meacham, R J Giuly, L Guo, S Hochman, and S P DeWeerth. A lithographically-patterned, elastic multi-electrode array for surface stimulation of the spinal cord. *Biomedical Microdevices*, 10(2):259–269, 2008.
- [130] Jennifer R. Melcher and Nelson Y S Kiang. Generators of the brainstem auditory evoked potential in cat III: Identified cell populations. *Hearing Research*, 93:52–71, 1996.



- [131] Lotfi B Merabet, Joseph F Rizzo, Amir Amedi, David C Somers, and Alvaro Pascual-Leone. What blindness can tell us about seeing again: merging neuroplasticity and neuroprostheses. *Nat.Rev.Neurosci.*, 6(January):71–77, 2005.
- [132] A Mercanzini, K Cheung, D L Buhl, M Boers, A Maillard, P Colin, J C Bensadoun, A Bertsch, and P Renaud. Demonstration of cortical recording using novel flexible polymer neural probes. *Sensors and Actuators a-Physical*, 143(1):90–96, 2008.
- [133] P Merkus, R H Free, and M Sanna. Auditory brainstem implant indications. *Auris Nasus Larynx*, 40(1):113–114, 2013.
- [134] D R Merrill, M Bikson, and J G R Jefferys. Electrical stimulation of excitable tissue: design of efficacious and safe protocols. *Journal of Neuroscience Methods*, 141(2):171–198, 2005.
- [135] John C. Middlebrooks and Russell L. Snyder. Auditory prosthesis with a penetrating nerve array. *JARO - Journal of the Association for Research in Otolaryngology*, 8:258–279, 2007.
- [136] Ivan R Mineev, Pavel Musienko, Arthur Hirsch, Quentin Barraud, Nikolaus Wenger, Eduardo Martin Moraud, Jérôme Gandar, Marco Capogrosso, Tomislav Milekovic, Léonie Asboth, Rafael Fajardo Torres, Nicolas Vachicouras, Qihan Liu, Natalia Pavlova, Simone Duis, Alexandre Larmagnac, Janos Vörös, Silvestro Micera, Zhigang Suo, Grégoire Courtine, and Stéphanie P Lacour. Electronic dura mater for long-term multimodal neural interfaces. *Science*, 347:159–163, 2015.
- [137] A R Moller. Neurophysiologic basis for cochlear and auditory brainstem implants. *Am J Audiol*, 10(2):68–77, 2001.
- [138] Kate L Montgomery, Alexander J Yeh, John S Ho, Vivien Tsao, Shrivats Mohan Iyer, Logan Grosenick, Emily a Ferenczi, Yuji Tanabe, Karl Deisseroth, Scott L Delp, and Ada S Y Poon. Wirelessly powered, fully internal optogenetics for brain, spinal and peripheral circuits in mice. *Nature Methods*, 12(august):969–974, 2015.
- [139] Jean K Moore. The human auditory brain stem : A comparative view. *Hearing Research*, 29:1–32, 1987.
- [140] Tobias Moser. Optogenetic stimulation of the auditory pathway for research and future prosthetics. *Current Opinion in Neurobiology*, 34:29–36, 2015.
- [141] Michael a. Muniak, Alejandro Rivas, Karen L. Montey, Bradford J. May, Howard W. Francis, and David K. Ryugo. 3D model of frequency representation in the cochlear nucleus of the CBA/J mouse. *Journal of Comparative Neurology*, 521:1510–1532, 2013.
- [142] S Myllymaa, K Myllymaa, H Korhonen, J Toyras, J E Jaaskelainen, K Djupsund, H Tanila, and R Lappalainen. Fabrication and testing of polyimide-based microelectrode arrays for cortical mapping of evoked potentials. *Biosensors & Bioelectronics*, 24(10):3067–3072, 2009.

## Bibliography

---

- [143] NIH. <https://www.nidcd.nih.gov/health/cochlear-implants>.
- [144] K.S. Noij, E.D. Kozin, R. Sethi, P.V. Shah, A.B. Kaplan, B. Herrmann, A. Remenschneider, and D.J. Lee. Systematic review of nontumor pediatric auditory brainstem implant outcomes. *Otolaryngol. Head Neck Surg.*, 5(739-50), 153.
- [145] Donata Oertel and Eric D. Young. What's a cerebellar circuit doing in the auditory system? *Trends in Neurosciences*, 27(2):104–110, 2004.
- [146] Michael S Okun. Deep-brain stimulation for Parkinson's disease. *The New England journal of medicine*, 367:1529–38, 2012.
- [147] Amy L. Orsborn, Helene G. Moorman, Simon a. Overduin, Maryam M. Shanechi, Dragana F. Dimitrov, and Jose M. Carmena. Closed-loop decoder adaptation shapes neural plasticity for skillful neuroprosthetic control. *Neuron*, 82(6):1380–1393, 2014.
- [148] Pdraig E O'Suilleabhain, William Frawley, Cole Giller, and Richard B Dewey. Tremor response to polarity, voltage, pulsewidth and frequency of thalamic stimulation. *Neurology*, 60:786–90, 2003.
- [149] S R Otto, R V Shannon, E P Wilkinson, W E Hitselberger, D B McCreery, J K Moore, and D E Brackmann. Audiologic outcomes with the penetrating electrode auditory brainstem implant. *Otology & neurotology : official publication of the American Otological Society, American Neurotology Society [and] European Academy of Otology and Neurotology*, 29(8):1147–1154, 2008.
- [150] Liangqi Ouyang, Crystal L Shaw, Chin-Chen Kuo, Amy L Griffin, and David C Martin. In vivo polymerization of poly(3,4-ethylenedioxythiophene) in the living rat hippocampus does not cause a significant loss of performance in a delayed alternation task. *Journal of neural engineering*, 11(2):026005, April 2014.
- [151] Sung Il Park, Daniel S Brenner, Gunchul Shin, Clinton D Morgan, Bryan a Copits, Ha Uk Chung, Melanie Y Pullen, Kyung Nim Noh, Steve Davidson, Soong Ju Oh, Jangyeol Yoon, Kyung-In Jang, Vijay K Samineni, Megan Norman, Jose G Grajales-Reyes, Sherri K Vogt, Saranya S Sundaram, Kellie M Wilson, Jeong Sook Ha, Renxiao Xu, Taisong Pan, Tae-Il Kim, Yonggang Huang, Michael C Montana, Judith P Golden, Michael R Bruchas, Robert W Gereau, and John a Rogers. Soft, stretchable, fully implantable miniaturized optoelectronic systems for wireless optogenetics. *Nature biotechnology*, 33(November):1280–1286, 2015.
- [152] Sung Il Park, Gunchul Shin, Jordan G. McCall, Ream Al-Hasani, Aaron Norris, Li Xia, Daniel S. Brenner, Kyung Nim Noh, Sang Yun Bang, Dionnet L. Bhatti, Kyung-In Jang, Seung-Kyun Kang, Aaron D. Mickle, Gregory Dussor, Theodore J. Price, Robert W. Gereau, Michael R. Bruchas, and John a. Rogers. Stretchable multichannel antennas in soft wireless optoelectronic implants for optogenetics. *Proceedings of the National Academy of Sciences*, page 201611769, 2016.

- 
- [153] Ramin Pashaie, Polina Anikeeva, Jin Hyung Lee, Rohit Prakash, Ofer Yizhar, Matthias Prigge, Divya Chander, Thomas J. Richner, and Justin Williams. Optogenetic brain interfaces. *IEEE Reviews in Biomedical Engineering*, 7(c):3–30, 2014.
- [154] P Hunter Peckham and Kevin L Kilgore. Challenges and Opportunities in Restoring Function After Paralysis. *IEEE Transactions on Biomedical Engineering*, 60(3):602–609, 2013.
- [155] Ferruccio Pisanello, Leonardo Sileo, Ian a. Oldenburg, Marco Pisanello, Luigi Martiradonna, John a. Assad, Bernardo L. Sabatini, and Massimo De Vittorio. Multipoint-emitting optical fibers for spatially addressable in vivo optogenetics. *Neuron*, 82(6):1245–1254, 2014.
- [156] Marek Polak, Adrien a. Eshraghi, Omar Nehme, Syed Ahsan, Jose Guzman, Rafael E. Delgado, Jiao He, Fred F. Telischi, Thomas J. Balkany, and Thomas R. Van De Water. Evaluation of hearing and auditory nerve function by combining ABR, DPOAE and eABR tests into a single recording session. *Journal of Neuroscience Methods*, 134:141–149, 2004.
- [157] S.V. Puram, S.R. Barber, E.D. Kozin, P. Shah, A. Remenschneider, B.S. Herrmann, A-C. Duhaime, F.G. Barker, and D.J. Lee. Outcomes following pediatric auditory brainstem implant surgery: early experience in a north American center. *Otolaryngol. Head Neck Surg.*, 155(1):133–8, 2016.
- [158] D Purves, G J Augustine, D Fitzpatrick, W C Hall, A S LaMantia, J O McNamara, and L E White. *Neuroscience*, 2007.
- [159] Charlotte Py, P. Reverdy, L. Doppler, J. Bico, B. Roman, and C. N. Baroud. Capillarity induced folding of elastic sheets. *European Physical Journal: Special Topics*, 166:67–71, 2009.
- [160] S. Raspopovic, M. Capogrosso, F. M. Petrini, M. Bonizzato, J. Rigosa, G. Di Pino, J. Carpaneto, M. Controzzi, T. Boretius, E. Fernandez, G. Granata, C. M. Oddo, L. Citi, a. L. Ciancio, C. Cipriani, M. C. Carrozza, W. Jensen, E. Guglielmelli, T. Stieglitz, P. M. Rossini, and S. Micera. Restoring Natural Sensory Feedback in Real-Time Bidirectional Hand Prostheses. *Science Translational Medicine*, 6(222):222ra19–222ra19, 2014.
- [161] Frank Rattay. Analysis of Models for External Stimulation of Axons. *IEEE Transactions on Biomedical Engineering*, BME-33(10):974–977, 1986.
- [162] J P Rauschecker, R V Shannon, G. E. Loeb, J. P. Rauschecker, D. B. McCreery, R. V. Shannon, J. K. Moore, M. Chatterjee, R. V. Shannon, F.-G. Zeng, J. Wygonski, V. Kamath, M. Ekelid, M. a. Svirsky, a. M. Robbins, K. I. Kirk, D. B. Pisoni, R. T. Miyamoto, R. Klinke, a. Kral, S. Heid, J. Tillein, R. Hartmann, T. N. Wiesel, J. P. Rauschecker, C. Pantev, S. Rosen, a. Faulkner, L. Wilkinson, J. K. Moore, K. K. Osen, E. D. Young, D. Matthies, G. S. Brindley, W. S. Lewin, R. a. Normann, E. M. Maynard, P. J. Rousche, D. J. Warren, Q. Bui, K. D. Wise,

## Bibliography

---

- D. J. Anderson, T. D. Griffiths, S. Uppenkamp, I. Johnsrude, O. Josephs, R. D. Patterson, M. R. DeLong, and T. Wichmann. Sending sound to the brain. *Science (New York, N.Y.)*, 295(February):1025–9, 2002.
- [163] Retrosense. retrosense.com.
- [164] Sarah M Richardson-Burns, Jeffrey L Hendricks, Brian Foster, Laura K Povlich, Dong-Hwan Kim, and David C Martin. Polymerization of the conducting polymer poly(3,4-ethylenedioxythiophene) (PEDOT) around living neural cells. *Biomaterials*, 28(8):1539–52, March 2007.
- [165] C P Richter, S M Rajguru, A I Matic, E L Moreno, A J Fishman, A M Robinson, E Suh, and J T Walsh. Spread of cochlear excitation during stimulation with pulsed infrared radiation: inferior colliculus measurements. *J Neural Eng*, 8(5):56006, 2011.
- [166] D C Rodger, A J Fong, L Wen, H Ameri, A K Ahuja, C Gutierrez, I Lavrov, Z Hui, P R Menon, E Meng, J W Burdick, R R Roy, V R Edgerton, J D Weiland, M S Humayun, and Y C Tai. Flexible parylene-based multielectrode array technology for high-density neural stimulation and recording. *Sensors and Actuators B-Chemical*, 132(2):449–460, 2008.
- [167] S K Rosahl and S Rosahl. No Easy Target: Anatomic Constraints of Electrodes Interfacing the Human Cochlear Nucleus. *Neurosurgery*, 72:58–64, 2013.
- [168] T L Rose and L S Robblee. Electrical-Stimulation with Pt Electrodes .8. Electrochemically Safe Charge Injection Limits with 0.2 Ms Pulses. *Ieee Transactions on Biomedical Engineering*, 37(11):1118–1120, 1990.
- [169] Boris Rosin, Maya Slovik, Rea Mitelman, Michal Rivlin-Etzion, Suzanne N. Haber, Zvi Israel, Eilon Vaadia, and Hagai Bergman. Closed-loop deep brain stimulation is superior in ameliorating parkinsonism. *Neuron*, 72(2):370–384, 2011.
- [170] P J Rousche, D S Pellinen, D P Pivin, J C Williams, R J Vetter, and D R Kipke. Flexible polyimide-based intracortical electrode arrays with bioactive capability. *Ieee Transactions on Biomedical Engineering*, 48(3):361–371, 2001.
- [171] B Rubehn, C Bosman, R Oostenveld, P Fries, and T Stieglitz. A MEMS-based flexible multichannel ECoG-electrode array. *J Neural Eng*, 6(3):36003, 2009.
- [172] Birthe Rubehn, Steffen B E Wolff, Philip Tovote, Andreas Lüthi, and Thomas Stieglitz. A polymer-based neural microimplant for optogenetic applications: design and first in vivo study. *Lab on a chip*, 13(4):579–588, 2013.
- [173] Wim L C Rutten. Selective electrical interfaces with the nervous system. *Annual review of biomedical engineering*, 4:407–452, 2002.
- [174] A F Ryan, Z Furlow, N K Woolf, and E M Keithley. The Spatial Representation of Frequency in the Rat Dorsal Cochlear Nucleus and Inferior Colliculus. *Hearing Research*, 36(2-3):181–189, 1988.

- [175] David Ryugo. Auditory neuroplasticity, hearing loss and cochlear implants. *Cell and Tissue Research*, 361:251–269, 2014.
- [176] Melissa Saenz and Dave R M Langers. Tonotopic mapping of human auditory cortex. *Hearing Research*, 307:42–52, 2014.
- [177] Richard J. Salvi, Jian Wang, and Dalian Ding. Auditory plasticity and hyperactivity following cochlear damage. *Hearing Research*, 147:261–274, 2000.
- [178] Brett R. Schofield and Diana L. Coomes. Projections from auditory cortex contact cells in the cochlear nucleus that project to the inferior colliculus. *Hearing Research*, 206:3–11, 2005.
- [179] Lauren E. Schrock, Jonathan W. Mink, Douglas W. Woods, Mauro Porta, Dominico Servello, Veerle Visser-Vandewalle, Peter a. Silburn, Thomas Foltynie, Harrison C. Walker, Joohee Shahed-Jimenez, Rodolfo Savica, Bryan T. Klassen, Andre G. Machado, Kelly D. Foote, Jian Guo Zhang, Wei Hu, Linda Ackermans, Yasin Temel, Zoltan Mari, Barbara K. Changizi, Andres Lozano, M. Auyeung, Takanobu Kaido, Yves Agid, Marie L. Welter, Suketu M. Khandhar, Alon Y. Mogilner, Michael H. Pourfar, Benjamin L. Walter, Jorge L. Juncos, Robert E. Gross, Jens Kuhn, James F. Leckman, Joseph a. Neimat, and Michael S. Okun. Tourette syndrome deep brain stimulation: A review and updated recommendations. *Movement Disorders*, 30(00):448–471, 2015.
- [180] M S Schwartz, S R Otto, R V Shannon, W E Hitzelberger, and D E Brackmann. Auditory brainstem implants. *Neurotherapeutics*, 5(1):128–136, 2008.
- [181] Marc S. Schwartz and Eric P. Wilkinson. Auditory brainstem implant program development. *The Laryngoscope*, pages 1–7, 2016.
- [182] N Sethi, D Labar, L Ponticello, and J Torgovnick. Treatment of medically refractory epilepsy: A review of vagus nerve stimulator. *Internet J. Neurol*, 9(1):1–9, 2008.
- [183] R V Shannon. Advances in auditory prostheses. *Curr Opin Neurol*, 25(1):61–66, 2012.
- [184] R V Shannon and S R Otto. Psychophysical measures from electrical stimulation of the human cochlear nucleus. *Hear Res*, 47(1-2):159–168, 1990.
- [185] Robert V. Shannon. A Model of Safe Levels for Electrical Stimulation. *IEEE Transactions on Biomedical Engineering*, 39(4):424–426, 1992.
- [186] Robert K. Shepherd and Douglas B. McCreery. Basis of electrical stimulation of the cochlea and the cochlear nucleus. *Advances in Oto-Rhino-Laryngology*, 64:186–205, 2006.
- [187] M N Shivdasani, S J Mauger, G D Rathbone, and A G Paolini. Inferior colliculus responses to multichannel microstimulation of the ventral cochlear nucleus: implications for auditory brain stem implants. *J Neurophysiol*, 99(1):1–13, 2008.

## Bibliography

---

- [188] Andrew N. Smith, Matthew P. Christian, Samara L. Firebaugh, Garret W. Cooper, and Brian G. Jamieson. Predicting and managing heat dissipation from a neural probe. *Biomedical Microdevices*, 17:81, 2015.
- [189] Joseph T. Smith, Barry O'Brien, Yong Kyun Lee, Edward J. Bawolek, and Jennifer Blain Christen. Application of flexible OLED display technology for electro-optical stimulation and/or silencing of neural activity. *IEEE/OSA Journal of Display Technology*, 10(6):514–520, 2014.
- [190] Russell L. Snyder, John C. Middlebrooks, and Ben H. Bonham. Cochlear implant electrode configuration effects on activation threshold and tonotopic selectivity. *Hearing Research*, 235:23–38, 2008.
- [191] Jason J Song, Adrian Popescu, and Russell L Bell. Present and potential use of spinal cord stimulation to control chronic pain. *Pain physician*, 17:235–46, 2014.
- [192] G A Spirou, B J May, D D Wright, and D K Ryugo. Frequency Organization of the Dorsal Cochlear Nucleus in Cats. *Journal of Comparative Neurology*, 329(1):36–52, 1993.
- [193] T Stieglitz. Electrode materials for recording and stimulation. In K W Horch and G S Dhillon, editors, *Neuroprosthetics Theory and Practice*, volume 2, pages 475–516. 2004.
- [194] Joseph M. Stujenske, Timothy Spellman, and Joshua a. Gordon. Modeling the Spatiotemporal Dynamics of Light and Heat Propagation for In Vivo Optogenetics. *Cell Reports*, 12(3):525–534, 2015.
- [195] Josef Syka and Michael M. Merzenich. *Plasticity and Signal Representation in the Auditory System*. 2005.
- [196] S Takeuchi, D Ziegler, Y Yoshida, K Mabuchi, and T Suzuki. Parylene flexible neural probes integrated with microfluidic channels. *Lab on a Chip*, 5(5):519–523, 2005.
- [197] E J Tehovnik, A S Tolia, F Sultan, W M Slocum, and N K Logothetis. Direct and indirect activation of cortical neurons by electrical microstimulation. *J Neurophysiol*, 96(2):512–521, 2006.
- [198] R van den Brand. Restoring voluntary control of locomotion after paralyzing spinal cord injury. *Science*, 336:1182–1185, 2012.
- [199] a Vanhoestenbergh and N Donaldson. Corrosion of silicon integrated circuits and lifetime predictions in implantable electronic devices. *Journal of neural engineering*, 10:031002, 2013.
- [200] Rohit U Verma, Amélie a Guex, Kenneth E Hancock, Nedim Durakovic, Colette M McKay, Michaël C C Slama, M Christian Brown, and Daniel J Lee. Auditory responses to electric and infrared neural stimulation of the rat cochlear nucleus. *Hearing research*, 310:69–75, April 2014.

- [201] C Vincent. Auditory brainstem implants: how do they work? *Anat Rec (Hoboken)*, 295(11):1981–1986, 2012.
- [202] M Vosgueritchian, D J Lipomi, and Z A Bao. Highly Conductive and Transparent PEDOT:PSS Films with a Fluorosurfactant for Stretchable and Flexible Transparent Electrodes. *Advanced Functional Materials*, 22(2):421–428, 2012.
- [203] Jing Wang, Fabien Wagner, David a Borton, Jiayi Zhang, Ilker Ozden, Rebecca D Burwell, Arto V Nurmikko, Rick van Wagenen, Ilka Diester, and Karl Deisseroth. Integrated device for combined optical neuromodulation and electrical recording for chronic in vivo applications. *Journal of neural engineering*, 9(1):16001, 2012.
- [204] Taylor Ware, Dustin Simon, Keith Hearon, Clive Liu, Sagar Shah, Jonathan Reeder, Navid Khodaparast, Michael P. Kilgard, Duncan J. Maitland, Robert L. Rennaker, and Walter E. Voit. Three-dimensional flexible electronics enabled by shape memory polymer substrates for responsive neural interfaces. *Macromolecular Materials and Engineering*, 297:1193–1202, 2012.
- [205] J D Weiland and D J Anderson. Chronic neural stimulation with thin-film, iridium oxide electrodes. *Ieee Transactions on Biomedical Engineering*, 47(7):911–918, 2000.
- [206] Nikolaus Wenger, Eduardo Martin Moraud, Jerome Gandar, Pavel Musienko, Marco Capogrosso, Laetitia Baud, Camille G Le Goff, Quentin Barraud, Natalia Pavlova, Nadia Dominici, Ivan R Minev, Leonie Asboth, Arthur Hirsch, Simone Duis, Julie Kreider, Andrea Mortera, Oliver Haverbeck, Silvio Kraus, Felix Schmitz, Jack DiGiovanna, Rubia van den Brand, Jocelyne Bloch, Peter Detemple, Stéphanie P Lacour, Erwan Bézard, Silvestro Micera, and Grégoire Courtine. Spatiotemporal neuromodulation therapies engaging muscle synergies improve motor control after spinal cord injury. *Nature Medicine*, 22(2):5–7, 2016.
- [207] Justin C Williams and Timothy Denison. From optogenetic technologies to neuromodulation therapies. *Science translational medicine*, 5(177):177ps6, 2013.
- [208] W. J. Wilson. The relationship between the auditory brain-stem response and its reconstructed waveforms following discrete wavelet transformation. *Clinical Neurophysiology*, 115:1129–1139, 2004.
- [209] James Wright, Vaughan G. Macefield, Andr?? Van Schaik, and Jonathan C. Tapson. A review of control strategies in closed-loop neuroprosthetic systems. *Frontiers in Neuro-science*, 10(July):1–13, 2016.
- [210] F Wu, M. Im, and E. Yoon. A flexible fish-bone-shaped neural probe strengthened by biodegradable silk coating for enhanced biocompatibility. In *Transducers*, 2011.
- [211] Li Xu and Bryan E. Pfingst. Spectral and temporal cues for speech recognition: Implications for auditory prostheses. *Hearing Research*, 242:132–140, 2008.

## Bibliography

---

- [212] a N Yaroslavsky, P C Schulze, I V Yaroslavsky, R Schober, F Ulrich, and H J Schwarzmaier. Optical properties of selected native and coagulated human brain tissues in vitro in the visible and near infrared spectral range. *Physics in medicine and biology*, 47(12):2059–2073, 2002.
- [213] A Yazdan-Shahmorad, D R Kipke, and M J Lehmkuhle. Polarity of cortical electrical stimulation differentially affects neuronal activity of deep and superficial layers of rat motor cortex. *Brain Stimulation*, 4(4):228–241, 2011.
- [214] John Yeomans, Peter Prior, and Firth Bateman. Current-distance relations of axons mediating circling elicited by midbrain stimulation. *Brain Research*, 372:95–106, 1986.
- [215] Ofer Yizhar, Lief E Fenno, Thomas J Davidson, Murtaza Mogri, and Karl Deisseroth. Optogenetics in neural systems. *Neuron*, 71(1):9–34, 2011.
- [216] Eric D. Young and Donata Oertel. *The Cochlear Nucleus*. 2002.
- [217] S. Zeitler, E. Wendler-Kalsch, W. Preidel, and V. Tegeder. Corrosion of platinum electrodes in phosphate buffered saline solution. *Materials and Corrosion/Werkstoffe und Korrosion*, 48:303–310, 1997.
- [218] X. Zeng, D. L. Boiko, G. Cosendey, M. Glauser, J. F. Carlin, and N. Grandjean. Optically pumped long external cavity InGaN/GaN surface-emitting laser with injection seeding from a planar microcavity. *Applied Physics Letters*, 101, 2012.
- [219] Ziyang Zhu, Qing Tang, Fan Gang Zeng, Tian Guan, and Datian Ye. Cochlear-implant spatial selectivity with monopolar, bipolar and tripolar stimulation. *Hearing Research*, 283(1-2):45–58, 2012.



## Amélie Guex

Av. de Florissant 26  
1020 Renens  
amelie.guex@gmail.com  
077/429.92.44



### Strengths

- Biomedical engineer with a strong interest in neuroprostheses
- Enjoys multidisciplinary work and integration of knowledge from different fields
- Experience in auditory prostheses and electrical stimulation of neural tissue

## EDUCATION

### Swiss Federal Institute of Technology of Lausanne (EPFL)

PhD in Biomedical engineering and neuroprostheses	2012 – 2017
Master degree in Bioengineering, with minor in Biomedical Technologies 2011-2012: Master thesis at Harvard Medical School, Boston	2010 – 2012
Bachelor degree in Life Sciences and Technologies	2007 – 2010
Maturité, specialization in physics and mathematics	2002 – 2007

## EXPERIENCE

### PhD thesis : Laboratory for Soft Bioelectronic Interfaces, EPFL 2012 – 2017

- In this multidisciplinary project, my goal was to understand and develop guidelines to improve the outcomes of auditory brainstem implants. I developed a high density surface stimulation implant on a thin flexible substrate that generated highly selective activation of the auditory system. I also developed an algorithm for neural data analysis enabling the discrimination of the different components of auditory system activation, now also used in the other projects of the lab.
- This project was performed in close collaboration with the auditory brainstem implant research group, at the Massachusetts Eye and Ear Infirmary, Harvard Medical School, Boston.
- I also developed a process integrating SMD components on polyimide substrates into a chronic implantable device for optogenetic stimulation of neural tissue.

## SKILLS AND TECHNIQUES

### Microtechnologies

Cleanroom microfabrication techniques (photolithography, thin films deposition and etching)  
Flexible and stretchable electronics technologies (Polyimide, PDMS)

### Signal processing

Matlab-based processing and analysis of neural signals, spike post-processing algorithms

### Electrochemistry

Characterization of neural stimulation and recording electrodes with electrochemical impedance spectroscopy (EIS), cyclic voltammetry (CV) and voltage transients.

### Stimulation electrode coatings

Deposition and electrochemical characterization of iridium oxide and PEDOT conductive polymer

### Neural stimulation and recording

In vivo neural electrical and optical stimulation techniques (laser and LED-based)

Auditory evoked potentials (AEP), auditory brainstem responses (ABR), electroencephalography (EEG), electromyography (EMG) and multiunit neural recordings

### Computer literacy

Matlab, Java, ImageJ, C, C++, JMol, Adobe Illustrator, Clewin, Origin, Amira

## PROJECTS

### Auditory brainstem implant research group, Massachusetts Eye and Ear Infirmary, Harvard Medical School, Boston

2011 – 2012

- Master thesis supported by a *Bertarelli Foundation fellowship in neuroengineering and neuroprosthetics*
- The goal of this project was to characterize the auditory system responses to infrared neural stimulation of the auditory brainstem. I developed a stimulation protocol for in vivo infrared neural stimulation and a processing algorithm for direct multiunit recordings of auditory system activity, a new method in the lab at the time.

### Laboratory of Movement Analysis and Measurement, EPFL

2010

- Semester project : Matlab-based analysis of wearable accelerometer and gyroscope recordings resulting in objective assessment and prediction of risk of falling in elderly patients

## LANGUAGES

<b>French</b>	Native
<b>English</b>	Fluent
<b>German</b>	A2-A3

## ADDITIONAL INFORMATION

<b>Hobbies</b>	Music (piano, singing in a voice ensemble since 2008)
<b>Age</b>	29 years old
<b>Nationality</b>	Swiss

